

Solution-based Synthesis and Processing of Nanocrystalline ZrB₂-based Composites

A Dissertation
Presented to
The Academic Faculty

by

Yanli Xie

In Partial Fulfillment
of the Requirements for the Degree
Doctor of Philosophy

School of Materials Science and Engineering
Georgia Institute of Technology
December 2008

Solution-based Synthesis and Processing of Nanocrystalline ZrB₂-based Composites

Approved by:

Dr. Robert F. Speyer, Advisor
School of Materials Science and Engineering
Georgia Institute of Technology

Dr. Rosario A. Gerhardt
School of Materials Science and Engineering
Georgia Institute of Technology

Dr. Thomas H. Sanders, Jr., Advisor
School of Materials Science and Engineering
Georgia Institute of Technology

Dr. Kenneth Sandhage
School of Materials Science and Engineering
Georgia Institute of Technology

School of Materials Science and Engineering
Dr. Robert L. Snyder
Georgia Institute of Technology

Dr. John Z. Zhang
School of Chemistry and Biochemistry
Georgia Institute of Technology

Date Approved: Oct 22, 2008

ACKNOWLEDGEMENTS

I would like to express my deepest appreciation to several people. Without their support, this work would not have been possible.

First of all, I would like to thank my advisors, Professor Robert F. Speyer and Professor Thomas H. Sanders, Jr. for their guidance, knowledge, and support throughout this work. Also, I would like to thanks my committee members, Professor Robert L. Snyder, professor Kenneth Sandhage, Professor Rosario A. Gerhardt and Professor John Z. Zhang for their valuable suggestions and discussions.

I am grateful to Ms. Yolande Berta for guiding and helping me on the SEM works.

I also show my appreciate to the Air Force Office of Scientific Research (AFOSR Grant No. FA9550-04-1-0140; Program Manager: Dr. Joan Fuller) for the support for this project.

I greatly appreciate the friendship of all the other graduate students in our group, and my friends Runrun Duan, Zhe Cheng, Fei Peng, Zihao Bao, Yi Li and Zhaohui Yang in MSE for their kindness and encouragement which kept me going through the hard times in my life.

I also thanks Eva Liang, a graduate student of chemistry department, for her helping on the ICP analysis.

Finally, I thank my family for their love and support throughout my education. My parents and parents-in-law have been very thoughtful, caring, and encouraging over the years. I owe a lot to my daughter, Yibo Zhao. In the past 4 years, I do not take care of her and I am not a good mother. But thanks to my parents-in-law, they help me to look after my daughter and let her grow up happily.

TABLE OF CONTENTS

| | |
|--|------------|
| ACKNOWLEDGEMENTS | iii |
| LIST OF TABLES | ix |
| LIST OF FIGURES | x |
| SUMMARY | xv |
| CHAPTER 1 Introduction | 1 |
| 1.1 Synthesis | 3 |
| 1.1.1 Direct Reaction Using Elemental Metals or Metal Hydrides | 4 |
| 1.1.2 Carbothermal and Borothermal Reduction Reactions | 4 |
| 1.1.3 Preceramic Polymers | 8 |
| 1.1.4 Alkali Metal Reduction | 9 |
| 1.1.5 Other Methods | 10 |
| 1.2 Sintering of Zirconium Diboride | 10 |
| 1.2.1 Liquid phase formers [89]-[94] | 10 |
| 1.2.2 Solid solution formers [95]-[4] | 11 |
| 1.2.3 Reactive agents | 11 |
| 1.3 Enhancement of the Oxidation Resistance of ZrB_2 | 13 |
| 1.4 References | 16 |
| CHAPTER 2 EXPERIMENTAL PROCEDURES | 27 |
| 2.1 Synthesis of Nanocrystalline Powders by a Solution-based Method | 27 |
| 2.1.1 Zirconium Diboride (ZrB_2) | 27 |
| 2.1.1.1 Preparation of Dry Powder | 27 |
| 2.1.1.2 Pyrolysis | 28 |
| 2.1.1.3 Boro/carbothermal Reduction | 28 |
| 2.1.2 ZrB_2 - B_4C Composite | 30 |
| 2.1.2.1 Preparation of Boron Carbide (B_4C) Sol | 30 |
| 2.1.2.2 Preparation of ZrB_2 - B_4C Composite | 30 |
| 2.1.3 ZrB_2 - SiC Composite | 31 |
| 2.1.3.1 Preparation of Silicon Carbide (SiC) Sol | 31 |

| | | |
|---------|--|----|
| 2.1.3.2 | Preparation of ZrB ₂ -SiC Composite | 32 |
| 2.1.4 | ZrB ₂ -TaB ₂ and ZrB ₂ -TaB ₂ -SiC Composite | 32 |
| 2.1.4.1 | Preparation of ZrB ₂ -TaB ₂ Composite | 32 |
| 2.1.4.2 | Preparation of ZrB ₂ -TaB ₂ -SiC Composite | 34 |
| 2.1.5 | Preparation of ZrB ₂ -TaSi ₂ Composite | 34 |
| 2.2 | Pressureless Sintering of Pellets | 35 |
| 2.2.1 | Preparation for pellet P1-P5 of ZrB ₂ -B ₄ C and ZrB ₂ | 35 |
| 2.2.1.1 | Preparation of ZrB ₂ Powder Compact | 35 |
| 2.2.1.2 | Preparation of ZrB ₂ -B ₄ C Pellets | 37 |
| 2.2.2 | New Procedure for Preparing of Pellets | 38 |
| 2.2.2.1 | Ball-milling | 38 |
| 2.2.2.2 | Methanol Washing | 39 |
| 2.2.2.3 | Binder Addition | 39 |
| 2.2.2.4 | Green Body Preparation | 40 |
| 2.2.2.5 | Binder Burnout | 40 |
| 2.2.2.6 | Sintering | 40 |
| 2.3 | Characterization of Product Powders | 41 |
| 2.3.1 | Boron Determination | 41 |
| 2.3.1.1 | Boron Determination by ICP | 41 |
| 2.3.1.2 | Boron Determination by D-mannitol Titration | 43 |
| 2.3.2 | Particle Size Analysis using the LS 13 320 | 44 |
| 2.3.3 | Crystallite Size Determination by XRD line Broadening | 46 |
| 2.3.4 | Scanning Electron Microscopy | 48 |
| 2.3.5 | Bulk Density and Open Porosity Measurements by the Archimedes Method | 49 |
| 2.3.6 | True Density Measurement by Pycnometer | 49 |
| 2.4 | References | 54 |

CHAPTER 3 Research on the synthesis of ZrB₂ and ZrB₂-B₄C powder and their sinterability 55

| | | |
|-------|--|----|
| 3.1 | Synthesis of Nanocrystalline Zirconium Diboride by a Solution-based Method | 55 |
| 3.1.1 | Boron Source Determination | 55 |

| | | |
|---|--|------------|
| 3.1.1.1 | Triethyl Borate as Boron Source | 55 |
| 3.1.1.2 | Boric Acid as Boron Source | 56 |
| 3.1.2 | Preparation of Stoichiometric ZrB_2 Powder using a Solution-based Method | 57 |
| 3.1.2.1 | Preparation of ZrB_2 Sol | 57 |
| 3.1.2.2 | Heat Treatment for ZrB_2 Preparation | 61 |
| 3.1.2.3 | Chemical Analysis of the ZrB_2 Sample after Heat Treatment at 1400°C | 66 |
| 3.1.3 | Preparation of the $\text{ZrB}_2\text{-B}_4\text{C}$ Composite | 67 |
| 3.1.3.1 | Preparation of B_4C Sol | 67 |
| 3.1.3.2 | Preparation of $\text{ZrB}_2\text{-B}_4\text{C}$ composite | 68 |
| 3.2 | Study on the sinterability of ZrB_2 and $\text{ZrB}_2\text{-B}_4\text{C}$ Mixture | 72 |
| 3.2.1 | Sintering of ZrB_2 and $\text{ZrB}_2\text{-B}_4\text{C}$ in a Dilatometer | 72 |
| 3.2.1.1 | Green pellet preparation | 72 |
| 3.2.1.2 | Sintering of $\text{ZrB}_2\text{-3wt\%B}_4\text{C}$ pellet at 2050°C in a Dilatometer | 77 |
| 3.2.2 | Sinterability of ZrB_2 and $\text{ZrB}_2\text{-B}_4\text{C}$ Using a New Method | 81 |
| 3.2.2.1 | Synthesized Powder of ZrB_2 and $\text{ZrB}_2\text{-B}_4\text{C}$ for Sintering | 81 |
| 3.2.2.2 | Sintering | 82 |
| 3.3 | Conclusion | 85 |
| 3.4 | References | 92 |
| CHAPTER 4 Research on the synthesis of $\text{ZrB}_2\text{-TaB}_2$ and $\text{ZrB}_2\text{-TaB}_2\text{-B}_4\text{C}$ powder and their sinterability | | 94 |
| 4.1 | Synthesis of Nanocrystalline $\text{ZrB}_2\text{-TaB}_2$ based composite by a Solution-based Method | 94 |
| 4.1.0.3 | Preparation of $\text{ZrB}_2\text{-TaB}_2$ composite | 94 |
| 4.1.0.4 | Preparation of $\text{ZrB}_2\text{-TaB}_2\text{-B}_4\text{C}$ composite | 97 |
| 4.2 | Sintering of $\text{ZrB}_2\text{-TaB}_2$ and $\text{ZrB}_2\text{-TaB}_2\text{-B}_4\text{C}$ composites | 98 |
| 4.3 | Conclusion | 100 |
| 4.4 | References | 110 |
| CHAPTER 5 Research on the synthesis of $\text{ZrB}_2\text{-TaSi}_2$ and its sinterability | | 111 |
| 5.1 | Synthesis of Submicron $\text{ZrB}_2\text{-TaSi}_2$ Composite by a Solution-based Method | 111 |
| 5.2 | The Effect of Ball Milling on the Particle Size and Morphology of Particles | 114 |

| | | |
|--|---|------------|
| 5.3 | Sintering of $\text{ZrB}_2\text{-TaSi}_2$ Powder | 116 |
| 5.4 | Conclusion | 120 |
| 5.5 | References | 126 |
| CHAPTER 6 Research on the Synthesis of Nanocrystalline ZrB_2-based Composites | | 127 |
| 6.1 | Preparation of the Nanocrystalline ZrB_2 -based SiC Composite | 127 |
| 6.1.0.5 | Preparation of the Nanocrystalline ZrB_2 -based SiC Composite | 127 |
| 6.1.0.6 | Preparation of the $\text{ZrB}_2\text{-TaB}_2\text{-SiC}$ Composite | 129 |
| 6.2 | Synthesis ZrB_2 -based Composite by Adjusting the Precursor Adding Sequence | 133 |
| 6.3 | Preparation of the Nanocrystalline ZrB_2/ZrC or $\text{ZrB}_2/\text{ZrO}_2$ Composite by Solution-based Method | 135 |
| 6.3.1 | Synthesis of ZrB_2/ZrC or $\text{ZrB}_2/\text{ZrO}_2$ Composite by Adjusting the Initial Concentration of C/Zr and B/Zr | 135 |
| 6.3.2 | Synthesis of ZrB_2/ZrC or $\text{ZrB}_2/\text{ZrO}_2$ Composite by Adjusting the Initial Concentration of C/Zr | 136 |
| 6.3.2.1 | Synthesis dry powder | 136 |
| 6.3.2.2 | Heat-treatment of samples | 137 |
| 6.4 | Conclusions | 138 |
| 6.5 | References | 152 |
| CHAPTER 7 conclusions | | 153 |
| 7.1 | Nanocrystalline Powder Synthesis | 153 |
| 7.1.1 | Nanocrystalline ZrB_2 Powder Synthesis | 153 |
| 7.1.2 | Nanocrystalline $\text{ZrB}_2\text{-B}_4\text{C}$ Composite Synthesis | 154 |
| 7.1.3 | Synthesis of Nanocrystalline $\text{ZrB}_2\text{-TaB}_2$ Based Composite | 154 |
| 7.1.4 | Synthesis of Submicro-size $\text{ZrB}_2\text{-TaSi}_2$ Composite | 155 |
| 7.1.5 | Synthesis of Nanocrystalline Diboride-SiC Composite | 155 |
| 7.1.6 | Synthesis of other diboride-based Composites | 156 |
| 7.2 | Bulk Pellet Processing | 156 |
| 7.2.1 | Ball-milling | 157 |
| 7.2.2 | Methanol-washing | 157 |
| 7.2.3 | Binder | 157 |

| | | |
|-------|---|-----|
| 7.2.4 | CIP | 158 |
| 7.3 | Research on the Sinterability of Nanocrystalline Diboride Powders | 158 |
| 7.3.1 | Sinterability of ZrB_2 and $\text{ZrB}_2\text{-B}_4\text{C}$ Composite | 158 |
| 7.3.2 | Sintering of $\text{ZrB}_2\text{-TaB}_2$ and $\text{ZrB}_2\text{-TaB}_2\text{-B}_4\text{C}$ Composite | 158 |
| 7.3.3 | Sintering of $\text{ZrB}_2\text{-TaSi}_2$ Composite | 158 |

LIST OF TABLES

| | | |
|----------------|---|-----|
| Tab 2.1 | XRD peak widths of single crystal silicon. | 47 |
| Tab 2.2 | ZrB ₂ crystallite size determination by XRD diffraction line broadening (ZrB ₂ -SiC composite heat-treated at 1400° for 2 h). | 48 |
| Tab 3.1 | Yield of triethyl borate in different solvents. | 55 |
| Tab 3.2 | Yield of boric acid in different solvents | 56 |
| Tab 3.3 | Chemical analysis results for ZrB ₂ sample heat treated at 1400°C-2 h. . . . | 66 |
| Tab 3.4 | Heat-treatment results for sample ZB-BC1 (Crystal size determined by XRD line broadening). | 70 |
| Tab 3.5 | Dimension and density of pellets (P1:pressure-150 MPa; P4-pressure-300 MPa; P5-pressure-450 MPa. where, ϕ is the diameter of pellets, δ is the thickness of pellets. | 75 |
| Tab 3.6 | Dimension and bulk density of ZrB ₂ and ZrB ₂ -B ₄ C pellets using new processing method where, ϕ is the diameter of pellets, δ is the thickness of pellets. | 83 |
| Tab 3.7 | Archimedes density measurement of ZrB ₂ and ZrB ₂ -B ₄ C pellets sintered at 2020°C for 1 h in M11 furnace where, ϕ is the diameter of pellets, δ is the thickness of pellets. | 84 |
| Tab 4.1 | Dimension and bulk density of ZrB ₂ -TaB ₂ and ZrB ₂ -TaB ₂ -B ₄ C pellets using new processing method where, ϕ is the diameter of pellets, δ is the thickness of pellets. | 103 |
| Tab 4.2 | Archimedes density measurement of ZrB ₂ -TaB ₂ and ZrB ₂ -TaB ₂ -B ₄ C pellets sintered at 2020°C for 1 h in M11 furnace where, ϕ is the diameter of pellets, δ is the thickness of pellets. | 106 |
| Tab 4.3 | Lattice parameter for ZrB ₂ and TaB ₂ | 106 |
| Tab 5.1 | The Yields for ZrB ₂ -TaSi ₂ Heat Treatments | 114 |
| Tab 5.2 | Dimensional density of ZrB ₂ -TaSi ₂ -green and pellet after CIP where, ϕ is the diameter of pellets, δ is the thickness of pellets. | 118 |
| Tab 5.3 | Archimedes density measurement of ZrB ₂ -TaSi ₂ pellets sintered at 2020°C for 30 min in M11 furnace. | 119 |
| Tab 6.1 | Observations for synthesizing of ZrB ₂ with different precursor adding sequence | 134 |
| Tab 1 | Reference ICDD card number. | 160 |

LIST OF FIGURES

| | | |
|-----------------|---|----|
| Fig 1.1 | Thermodynamic calculation results for reactions (data from NIST-JANAF Thermochemical Tables [9]). | 5 |
| Fig 2.1 | Flow chart for synthesis of ZrB_2 from solution-based precursors. | 27 |
| Fig 2.2 | Flow chart for synthesis of $\text{ZrB}_2\text{-B}_4\text{C}$ composite. | 31 |
| Fig 2.3 | Flow chart for synthesis of $\text{ZrB}_2\text{-SiC}$ composite. | 32 |
| Fig 2.4 | Flow chart for synthesis of sample $\text{ZrB}_2\text{-TaB}_2$ composite. | 33 |
| Fig 2.5 | SEM Photo of commercial TaSi_2 mixed with synthesized ZrB_2 -based solution. | 35 |
| Fig 2.6 | Particle size distribution of ZrB_2 after and before spex-mill (measured by LS 13 320). | 36 |
| Fig 2.7 | Particle Size Distribution of $\text{ZrB}_2\text{-B}_4\text{C}$ powder (measured by LS 13 320) after ball milling 48 h and methanol washing 30min twice. | 37 |
| Fig 2.8 | Illustration for ICP plasma formation. | 42 |
| Fig 2.9 | Schematic of optical system for particle size analysis. (The figure is reproduced from reference [6]). | 44 |
| Fig 2.10 | XRD pattern of ZrB_2 powder (heat-treated at 1400°C for 2 h) before and after background subtraction. | 51 |
| Fig 2.11 | Lorentz fit for the peak of ZrB_2 powder at diffraction angle of 41.657° | 52 |
| Fig 2.12 | Photo of archimedes density measurement set-up. | 53 |
| Fig 3.1 | TG-DSC measurement of the thermal decomposition of H_3BO_3 in low temperature range. | 58 |
| Fig 3.2 | Reaction for precursor synthesis. | 59 |
| Fig 3.3 | FTIR spectra for (a) starting material (Zr-propoxide) and material after being refluxed, (b) material after refluxing and a commercial Zracac. | 60 |
| Fig 3.4 | XRD patterns for as dried (120°C) and heat treated ZrB_2 powders ($800\text{-}1400^\circ\text{C}$ for 2 h, $\text{B/Zr} = 3$, $\text{C/Zr} = 5.0$). The sample was first pyrolyzed at $800\text{-}1100^\circ\text{C}$ in a alumina tube furnace with a heating rate of 5°C/min . The pyrolyzed powder was then further heat-treated in a graphite furnace at higher temperatures of $1200\text{-}1400^\circ\text{C}$ (80°C/min to a temperature 75°C lower than final temperature, then 40°C/min to a temperature 35°C lower than final temperature, 20°C/min to a temperature 15°C lower, and 5°C/min to a temperature 5°C lower, and finally 1°C/min to the terminal temperature). | 62 |
| Fig 3.5 | Plot of weight loss vs. temperature for an 800°C -pyrolyzed sample. | 63 |
| Fig 3.6 | Plots of the m- ZrO_2 , t- ZrO_2 , and ZrB_2 crystallite sizes vs. heat treatment temperature (based on XRD line broadening). | 64 |

| | | |
|-----------------|--|----|
| Fig 3.7 | SEM photomicrograph of ZrB_2 sample heat-treated at 1400°C for 2 h in an alumina tube furnace. | 65 |
| Fig 3.8 | SEM photomicrograph of ZrB_2 samples heat-treated at 1400°C for 2 h in a graphite tube furnace. | 65 |
| Fig 3.9 | XRD patterns for B_4C powder after heat treatment at 1400°C or 1600°C for 2 h. (Initial compositions are indicated in the figure). | 68 |
| Fig 3.10 | XRD patterns for $\text{ZrB}_2\text{-B}_4\text{C}$ powder after boro/carbothermal reduction. Specimens were soaked at 180°C for 2h to eliminate moisture, heated at $5^\circ\text{C}/\text{min}$ to 800°C , and soaked 2h for pyrolysis. Specimens were then placed in a graphite furnace and then heated to a) 1300°C or b) 1400°C and soaked for 2h. | 69 |
| Fig 3.11 | SEM photo and EDS of $\text{ZrB}_2\text{-1wt}\%\text{B}_4\text{C}$ sample heat-treatment at 1400°C for 2 h in a graphite tube furnace. | 71 |
| Fig 3.12 | XRD pattern for $\text{ZrB}_2\text{-B}_4\text{C}$ powder after ball milling 48 h and methanol washing 30min twice. | 73 |
| Fig 3.13 | SEM of the cross-section of $\text{ZrB}_2\text{-3 wt}\%\text{B}_4\text{C}$ green pellet (150 MPa, 1 min) fracture. | 74 |
| Fig 3.14 | XRD pattern of ZrB_2 ($1300^\circ\text{C}\text{-2h-M11}$) after and before spex-mill. | 76 |
| Fig 3.15 | Dimension changes of $\text{ZrB}_2\text{-B}_4\text{C}$ (the pressure for pellets P1, P4, and P5 are 150, 300 and 450 MPa, respectively) and ZrB_2 (ZB8, which is first sintered in M11 before load into dilatometer) during sintering at 2050°C in dilatometer. | 77 |
| Fig 3.16 | SEM photo of pellets sintered at 2050°C in a dilatometer. (a) $\text{ZrB}_2\text{-3 wt}\%\text{B}_4\text{C}$, sintered at 2050°C for 73 min; (b) ZrB_2 , sintered at $1600^\circ\text{C}\text{-2 h}\text{-}1950^\circ\text{C}\text{-2 h}$ in the M11, then 2050°C for 250 min in the dilatometer. | 78 |
| Fig 3.17 | XRD pattern of pure ZrB_2 after sintering at 2050°C in the dilatometer. | 79 |
| Fig 3.18 | XRD pattern of $\text{ZrB}_2\text{-B}_4\text{C}$ after sintering at 2050°C in the dilatometer(the pellet Pa, P4 and P5 are all prepared by dry-pressing but the pressure are 150 MPa, 300 MPa and 450 MPa, respectively). | 80 |
| Fig 3.19 | SEM photo of ZrB_2 powder heat-treated at 1400°C | 82 |
| Fig 3.20 | SEM photo of $\text{ZrB}_2\text{-B}_4\text{C}$ powder heat-treated at 1400°C | 83 |
| Fig 3.21 | SEM micrograph of ZrB_2 and $\text{ZrB}_2\text{-B}_4\text{C}$ pellets after sintering at 2020°C for 1 h in the M11 furnace. | 87 |
| Fig 3.22 | Partial pressure of oxygen during the oxidization of Zr, B and ZrB_2 in flowing argon with oxygen partial pressure of 10^{-6} with temperature from thermal calculation (data from NIST-JANAF Thermochemical Tables [9]). | 88 |
| Fig 3.23 | XRD Pattern of ZrB_2 powder heat-treated at 1400°C for 2 h used for preparaing of a pellet, and the pellet after sintering at 2020°C for 1 h in the M11 furnace. | 89 |

| | | |
|-----------------|--|-----|
| Fig 3.24 | XRD Pattern of $\text{ZrB}_2\text{-B}_4\text{C}$ powder heat-treated at 1400°C for 2 h used for preparing of pellet. | 90 |
| Fig 3.25 | XRD pattern of $\text{ZrB}_2\text{-B}_4\text{C}$ pellet and powder sintered at 2020°C for 1 h in M11 furnace. | 91 |
| Fig 4.1 | Weight loss vs. temperature for a $\text{ZrB}_2\text{-TaB}_2$ composite. | 95 |
| Fig 4.2 | XRD patterns for $\text{ZrB}_2\text{-TaB}_2$ heat-treated from 600°C to 1800°C for 2h. . . | 96 |
| Fig 4.3 | SEM micrograph of $\text{ZrB}_2\text{-TaB}_2$ heat-treated at (a) 1300°C -2 h. (b) 1600°C -2 h. (c) 1600°C -2 h-backscatter | 101 |
| Fig 4.4 | Plot of crystallite sizes (determined from XRD measurements) vs. heat treatment temperature for $\text{ZrB}_2\text{-TaB}_2$ composite. | 102 |
| Fig 4.5 | Weight loss vs. temperature for a $\text{ZrB}_2\text{-TaB}_2\text{-B}_4\text{C}$ composite. | 102 |
| Fig 4.6 | XRD patterns for $\text{ZrB}_2\text{-TaB}_2\text{-3wt}\%\text{B}_4\text{C}$ heat-treated from 1250°C to 1600°C for 2h. | 103 |
| Fig 4.7 | SEM micrograph of $\text{ZrB}_2\text{-TaB}_2\text{-3 wt}\%\text{B}_4\text{C}$ heat-treated at 1300°C (heating at $80^\circ\text{C}/\text{min}$ to 1225°C , $40^\circ\text{C}/\text{min}$ to 1265°C , $20^\circ\text{C}/\text{min}$ to 1285°C , $5^\circ\text{C}/\text{min}$ to 1295°C , $2^\circ\text{C}/\text{min}$ to 1299°C , and $1^\circ\text{C}/\text{min}$ to 1300°C) for 2 h. | 104 |
| Fig 4.8 | SEM micrograph of $\text{ZrB}_2\text{-TaB}_2\text{-3 wt}\%\text{B}_4\text{C}$ heat-treated at 1400°C , 1500°C , 1600°C for 2 h. | 105 |
| Fig 4.9 | XRD patterns for $\text{ZrB}_2\text{-TaB}_2\text{-3 wt}\%\text{B}_4\text{C}$ powder and pellet sintered at 2020°C for 2h. | 106 |
| Fig 4.10 | XRD patterns for $\text{ZrB}_2\text{-TaB}_2$ powder and pellet sintered at 2020°C for 2h. | 107 |
| Fig 4.11 | SEM micrograph for $\text{ZrB}_2\text{-TaB}_2$ and $\text{ZrB}_2\text{-TaB}_2\text{-B}_4\text{C}$ pellets sintered at 2020°C for 2h (crosssection of fractured pieces). | 108 |
| Fig 4.12 | EDS spectra of $\text{ZrB}_2\text{-TaB}_2\text{-B}_4\text{C}$ pellet sintered at 2020°C for 2h. | 109 |
| Fig 5.1 | XRD patterns for $\text{ZrB}_2\text{-TaSi}_2$ pyrolyzed at 850°C and further heat-treated at 1300, 1400°C for 2h. | 113 |
| Fig 5.2 | SEM micrograph of $\text{ZrB}_2\text{-TaSi}_2$ pyrolyzed at 850°C in Lindberg furnace for 2 h. | 115 |
| Fig 5.3 | SEM micrograph of $\text{ZrB}_2\text{-TaSi}_2$ heat treated at 1300°C in the M11 furnace for 2 h (heating at $80^\circ\text{C}/\text{min}$ to 1225°C , with successively slower rates as 1300°C was approached). | 116 |
| Fig 5.4 | SEM micrograph of $\text{ZrB}_2\text{-TaSi}_2$ heat treated at 1400°C in M11 furnace for 2 h (heating at $80^\circ\text{C}/\text{min}$ to 1325°C , with successively slower rates as 1400°C was approached). | 117 |
| Fig 5.5 | SEM micrograph of $\text{ZrB}_2\text{-TaSi}_2$ powder after ball-milling for 10 h, 40 h and 60 h. | 121 |

| | | |
|-----------------|--|-----|
| Fig 5.6 | (a) SEM micrograph of $\text{ZrB}_2\text{-TaSi}_2$ powder after ball-milling for 60 h (b) SEM micrograph of $\text{ZrB}_2\text{-TaSi}_2$ powder after ball-milling for 60 h and sonication for 60 min. | 122 |
| Fig 5.7 | SEM micrograph of the crosssection of fractured $\text{ZrB}_2\text{-TaSi}_2$ pellet heat treated 2020°C for 1h. (a) Pellet on ZrB_2 substrate. (b) Pellet buried in B_4C powder. (c) magnification of b. | 123 |
| Fig 5.8 | XRD patterns for $\text{ZrB}_2\text{-TaSi}_2$ powder and pellet heat treated 2020°C for 1h. (a) Pellet on graphoil. (b) Pellet on ZrB_2 substrate. (c) Pellet buried in B_4C powder. (For the peaks at diffraction angle of ~ 29 and 48°), no ICDD card match them. They may be solid solution between ZrB_2 , TaB_2 or TaSi_2 . . . | 124 |
| Fig 5.9 | XRD patterns for $\text{ZrB}_2\text{-TaSi}_2$ powder and pellet heat treated 2020°C for 1h (For the peaks at diffraction angle of ~ 29 and 48°), no ICDD card match them. They may be solid solution between ZrB_2 , TaB_2 or TaSi_2 | 125 |
| Fig 6.1 | XRD pattern for $\text{ZrB}_2\text{-20 vol\% SiC}$ heat-treated at 1100°C or 1400°C for 2h. | 128 |
| Fig 6.2 | SEM photo of $\text{ZrB}_2\text{-SiC}$ sample heat-treated at 1400°C for 2 h in an alumina tube furnace. | 129 |
| Fig 6.3 | XRD patterns for $\text{ZrB}_2\text{-TaB}_2\text{-SiC}$ heat-treated from 700°C and 1800°C for 2h. | 130 |
| Fig 6.4 | Plot of weight loss vs. temperature for $\text{ZrB}_2\text{-TaB}_2\text{-SiC}$ composite. | 132 |
| Fig 6.5 | Plot of crystallite sizes (determined from XRD measurements) vs. heat treatment temperature for $\text{ZrB}_2\text{-TaB}_2\text{-SiC}$ composite. | 133 |
| Fig 6.6 | SEM micrograph and EDS pattern of $\text{ZrB}_2\text{-TaB}_2\text{-SiC}$ heat-treated at 1600°C (heating at $80^\circ\text{C}/\text{min}$ to 1525°C , with successively slower rates as 1600°C was approached) for 2 h. Indicated phases are based on EDS analysis. . . . | 140 |
| Fig 6.7 | Backscatter SEM micrograph of $\text{ZrB}_2\text{-TaB}_2\text{-SiC}$. (a) Heat-treated at 1300°C for 2 h. (b) Heat-treated at 1800°C for 2 h. | 141 |
| Fig 6.8 | XRD patterns of ZrB_2 samples heat-treated at 1300°C for 2 h in M11 furnace with different precursor adding sequence as follows: (a) Reflux - hydrolysis - addition of boric acid - addition of phenolic. (b) Reflux - addition of boric acid - hydrolysis - addition of phenolic. (c) Reflux - addition of boric acid - addition of phenolic - hydrolysis. (d) Reflux - (addition of boric acid and phenolic mixture) - hydrolysis. (e) Reflux - hydrolysis - (addition of boric acid and phenolic mixture). | 142 |
| Fig 6.9 | XRD pattern for two compositions heat-treated at 1300°C for 2 h (a. $\text{B}/\text{Zr} = 6.0$, $\text{C}/\text{Zr} = 4.0$; b. $\text{B}/\text{Zr} = 2.2$, $\text{C}/\text{Zr} = 6$). | 143 |
| Fig 6.10 | XRD for phase development of sample ZrB_2 as a function of soaking temperature ($\text{B}/\text{Zr} = 2.2$, $\text{C}/\text{Zr} = 6$). | 143 |
| Fig 6.11 | SEM photomicrograph of $\text{ZrB}_2\text{-ZrC}$ sample heat-treated at 1400°C for 2 h in a graphite-tube furnace. | 144 |

| | | |
|-----------------|--|-----|
| Fig 6.12 | SEM photomicrograph of $\text{ZrB}_2\text{-ZrC}$ sample heat-treated at 1300°C , 1400°C and 1500°C for 2 h in a graphite-tube furnace. | 145 |
| Fig 6.13 | SEM photomicrograph of $\text{ZrB}_2\text{-ZrC}$ sample heat-treated at 1600°C and 1950°C for 2 h in a graphite-tube furnace. | 146 |
| Fig 6.14 | Plot of weight loss vs. temperature for ZrB_2 composite ($\text{B/Zr} = 2.2$, $\text{C/Zr} = 6$). | 147 |
| Fig 6.15 | XRD pattern of ZrB_2 sample with different initial C/Zr heat-treated at 1300°C for 2 h in M11 furnace. (e) $\text{C/Zr} = 5.0$ (b) $\text{C/Zr} = 4.5$. (c) $\text{C/Zr} = 5.5$ | 148 |
| Fig 6.16 | XRD pattern of ZrB_2 sample (with initial $\text{C/Zr} = 4.5$) heat-treated at 1300°C for (a) 2 h. (b) 4 h. (c) 8 h in a graphite-tube furnace. | 149 |
| Fig 6.17 | SEM photomicrograph of $\text{ZrB}_2\text{-ZrC}$ sample heat-treated at 1300°C for 2 h and 4 h in a graphite-tube furnace. | 150 |
| Fig 6.18 | XRD pattern of ZrB_2 sample (with initial $\text{C/Zr} = 5.5$) heat-treated at 1300°C for (a) 2 h. (b) 4 h. (c) 8 h in a graphite-tube furnace. | 151 |

SUMMARY

Zirconium- and tantalum-based diborides, and diboride/carbide composites are of interest for ultra-high temperature applications requiring improved thermomechanical and thermochemical stability. This thesis focuses on the synthesis, processing and sintering of nanocrystalline powders with Zr- and Ta-based diboride/carbide/silicide compositions. A solution-based processing method was developed to prepare reactive mixtures that were precursors for ZrB₂-based powders. The precursors reacted to form the ceramic powders after suitable pyrolysis and borothermal/carbothermal reduction heat treatments. Single-phase ZrB₂ powders were prepared with initial composition of C/Zr = 4.8 and B/Zr = 3.0. ZrB₂-based composite powders with ZrC, ZrO₂, TaB₂, TaC, SiC, TaSi₂ and B₄C were prepared with particle sizes of 10-500 nm for different phases based SEM micrographs. The composite powders were highly sinterable with proper processing methods developed to avoid and remove oxide impurities. The relative densities of ZrB₂/B₄C, ZrB₂/TaB₂, ZrB₂/TaB₂/B₄C, ZrB₂/TaSi₂ were in the range of 91%-97% after pressureless sintering at 2020°C for 1 h or 30 min.

CHAPTER 1

Introduction

In recent years, a renewed interest has developed in the diborides of group IV, and V transition metals (e.g., Zr, Hf, Ta). The thermal and chemical stability of these compounds makes them candidates for use in the extreme environments associated with hypersonic flight (1400°C and above in air), atmospheric re-entry (2000°C and above), and rocket propulsion (3000°C and above). These materials have melting temperatures above 3000°C, retain their strength at temperatures above 1200°C, exhibit good thermal shock resistance, and can be modified with additives such as SiC to promote oxidation resistance. In particular, ZrB₂-SiC and HfB₂-SiC with volume ratios of 80:20 were found to be the most efficient ultrahigh temperature ceramics (UHTCs) for this application because the SiC phase enhances the oxidation resistance without adversely affecting other critical properties such as the high-temperature strength. Therefore, they are candidates for wing leading edges and other components in thermal protection systems [1]-[4].

The main deficiencies of these composites are difficulties associated with their extreme processing conditions. Currently, they are fabricated in either pellet or plate geometries using uniaxial hot-pressing, which requires typical sintering temperatures of 1850 to 2250°C under pressures of 7 to 35 MPa. The components processed by hot pressing are typically axi-symmetric with simple shape, thus requiring significant amounts of machining, with its associated cost to fabricate parts such as those designed for a leading-edge application. A pressureless-sintering process with the capability to obtain near-net-shape configurations would decrease the component fabrication costs, making these materials more attractive for aerospace applications. However, some major problems have limited their use:

1. What synthesis routes can be used to produce diborides with a controlled particle size and properties?

ZrB₂ and TaB₂ are usually synthesized by reacting powder mixtures of (1) metal oxides and elemental B, or (2) metal oxides with B₄C/B₂O₃, and carbon. In most cases, high temperatures are required for the diboride-forming reactions because the powders are mixed together on a relatively coarse scale. This also leads to metal diboride products with relatively large particle sizes. Hence, hot pressing of these particles is usually necessary to produce bulk objects with high relative densities.

Pre-ceramic polymer precursors that are prepared by solution-based processing methods are a potential way to attenuate this problem, which offers several advantages over other synthesis routes. First, the composition of pre-ceramic polymers can be tailored by changing the composition of the polymer itself, or by blending two or more different polymers with different elemental backbones prior to concentration and pyrolysis. Pre-ceramic polymers also offer increased control over microstructure development compared to standard powder processing. The pyrolysis time, temperature, and atmosphere can be altered to control the grain size and phase distribution in the resulting product, which in turn will factor into the properties of the resulting materials [3]-[7].

2. What limits the ability of these materials to reach full density during sintering and to reach full density via a cost-effective and shape-preserving method?

ZrB₂, TiB₂, and TaB₂ have strong covalent bonding and low self-diffusion coefficients, which has been attributed to be the cause of their difficulty in sintering; hence, hot-pressing has been typically used to densify such materials. However, hot pressing is limited to the formation of simple geometries and moderate sizes. Fabrication of components with complex shapes requires diamond machining, which is expensive and time-consuming. The development of a pressureless sintering process would enable the fabrication of components to near-net shape using standard powder processing methods [8].

The typical sintering aids which form a liquid-phase during sintering must be avoided

to minimize the potential impact on the high temperature mechanical behavior. However, reactive agents can act as densification aids by reacting with impurities that inhibit densification. Baik [5] found that oxides have been shown to inhibit the sintering of TiB_2 and a reactive agent such as carbon can be used to reduce the oxygen content, hence improving the densification of TiB_2 . Similarly, possible reactive additives, such as B_4C , can be used as sintering aids for ZrB_2 and TaB_2 .

3. How do composition and crystal structure affect the properties of diborides? What are the effects of grain size, and second or third phases on them?

Composition and crystal structure may affect melting temperature, densification kinetics, and creep resistance. Grain size and distribution of second phases affect strength and oxidation resistance. For example, additions of silicon carbide and tantalum silicide or tantalum boride to zirconium diboride can enhance oxidation resistance and limit grain growth [10]-[1]. Boron carbide is another addition used to react with oxides (e.g. ZrO_2) during sintering to enhance densification [8]. However, how these additives affect the densification kinetics and oxidation are unclear.

Moreover, the present method to introduce these additives is by mixing of powdered additives with zirconium diboride powders, which does not yield uniform dispersions. A solution-based precursor method can facilitate a more homogeneous mixture, but the relationship among the characteristics of the precursors, the processing, and the microstructure and properties of sintered specimens is not well established [4].

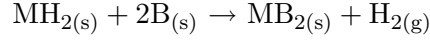
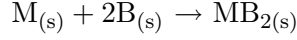
The work of this thesis is to resolve at least some of the aforementioned problems. New processing methods have been developed and multi-phase powders were developed to improve sinterability and oxidation resistance.

1.1 *Synthesis*

Synthesis methods used to produce high-temperature metal diboride powders are reviewed below. Advantages and disadvantages of different methods are identified in order to provide a rationale for the techniques used in this research.

1.1.1 Direct Reaction Using Elemental Metals or Metal Hydrides

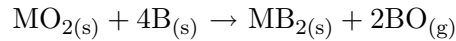
Metal diboride (MB_2) compounds can be formed by direct reaction between the elements or from metal hydrides:



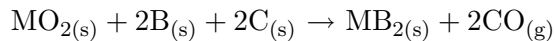
Synthesis of metal diborides by direct reaction between elements generally requires relatively high reaction temperatures because normally the reactant powders (i.e., at least the metals) usually have coarse particle sizes. Many metals oxidize easily and the extent of oxidation increases as the powder specific surface area increases. In fact, metals of particular interest for the proposed study (i.e., Hf and Zr) are pyrophoric (ignite spontaneously) when particle sizes are sufficiently small. Hence, metal powders are usually produced with a relatively coarse particle size. However, the combination of large starting particle sizes and high reaction temperatures results in reaction products with coarse particles sizes as well. In SHS (self-propagating-high-temperature synthesis) processing, the reaction product may also have non-uniform microstructural characteristics (i.e., non-uniformity in phases, particles sizes, etc.) because of temperature non-uniformities as the combustion wave propagates through the sample. Furthermore, the temperatures produced during combustion synthesis are sometimes high enough to cause local melting. Based on the above considerations, direct reaction between elements does not appear to be a particularly favorable route for producing nanocrystalline metal diborides [19]-[32].

1.1.2 Carbothermal and Borothermal Reduction Reactions

Metal diborides can be synthesized by reaction between a metal oxide and boron (borothermal reduction) [24], [33]-[37]:



The reaction temperatures are generally lowered by having carbon present, such that the overall boro/carbothermal reaction is given by [38]:



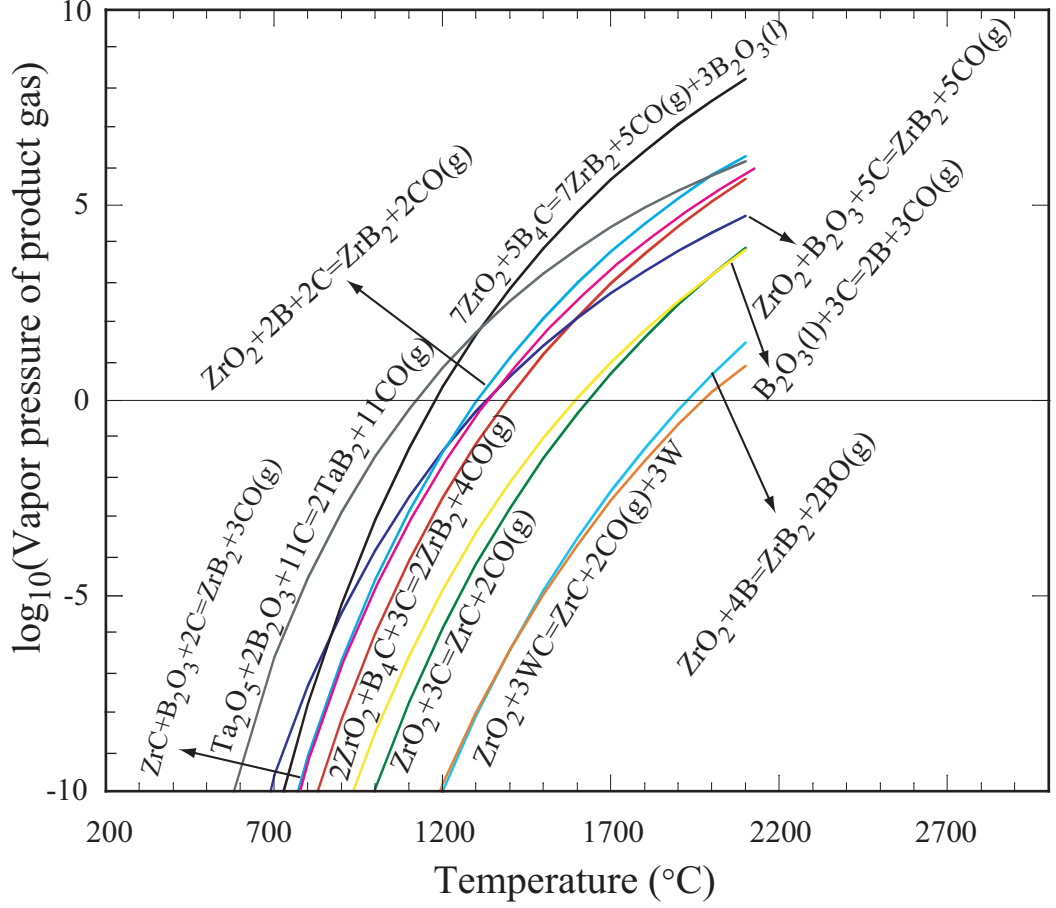
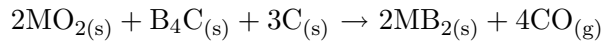


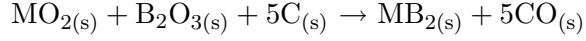
Fig 1.1: Thermodynamic calculation results for reactions (data from NIST-JANAF Thermochemical Tables [9]).

The temperature above which this reaction becomes thermodynamically favorable decreases from $\sim 2000^\circ\text{C}$ without carbon to $\sim 1400^\circ\text{C}$ with carbon, as shown in Figure 1.1. The typical reaction environment for those reactions is in flowing Ar gas, thus the product pressure cannot build up over 1 atm. Therefore, if the equilibrium pressure is above 1 atm, that is, above the zero line in Figure 1.1, we can assume the reaction goes to 100% products, i.e., products are strongly favored. However, under the zero line, reactants are favored.

A similar approach involves using boron carbide powders instead of elemental boron [39]-[43], but the disadvantage of this method is that B_4C powders are relatively expensive, especially if the particle size is small:

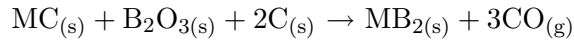


However, boria can be used as boron source, which is less expensive than boron carbide or boron [44, 45]:



Excess boria is generally required for the above reaction because of boria volatilization at elevated temperatures (boiling point of B_2O_3 , i.e. 1 atm vapor pressure, is 1860°C [43]). Another concern in using boria is that it melts at low temperature (450°C). Homogeneous products with fine particle size have been reported [43],[46]-[47] using this fabrication route.

Metal carbides have been observed as intermediate reaction products during metal diboride synthesis because of preferential carbothermal reduction of the metal oxide by carbon. However, the metal diboride is formed eventually if sufficient boron is available, i.e., according to the reaction:



There has been limited investigation to identify key factors affecting the reaction sequence during metal diboride synthesis, but presumably the reactant characteristics (e.g., particle sizes), heating conditions, and heat-treatment atmosphere are significant variables in the process.

In conventional processing methods, relatively high temperatures are required to produce metal diborides by boro/carbothermal reduction because coarse powder mixtures are used as reactants [19],[23],[48]-[51], which results in reaction products with large particle sizes. Therefore, densification of bulk ZrB_2 objects to high relative densities is invariably carried out by hot pressing.

Many methods have been developed in recent years to prepare metal diborides by boro/carbothermal reduction reactions using starting materials that allow for a finer scale of mixing of the reactants in comparison to the conventional processes. Many of these studies have focused on producing powders with smaller crystallite sizes and less aggregation, reducing the temperatures required for reaction (which in turn reduces the product particle size). Those methods can be classified as “fine particle” or “colloidal processing” routes, “chemical solution routes,” or a hybrid of the first two approaches.

Fine particle/colloidal processing routes involve mixing together particles of metal oxide, boron or elemental boron and carbon. The distinction from the typical industrial process is that at least one of the components is colloidal in size (nominally $< 1\ \mu\text{m}$, but much finer sizes have been used in some cases). Particles are usually combined initially in a liquid medium (e.g., colloidal suspensions or sols are first prepared) since this may result in more homogeneous mixing of the components (i.e., compared to mixing of dry powders).

“Chemical solution processing” routes refer to methods in which one or all of the components (i.e., metal-bearing, boron-bearing and carbon-bearing) are solubilized in a liquid processing medium. Soluble sources that are used to provide boron including boric acid and boron alkoxides. Numerous soluble carbon-bearing materials have been used to produce metal carbides, including phenolic resins, furfuryl alcohol, sugar, corn starch, petroleum pitch, polyacrylonitrile (PAN) polymers, cellulose acetate polymers, diols, etc. Common soluble metal/metal oxide-bearing materials are metal alkoxides, metal diketonates, metal carboxylates, etc. Metal-organic compounds are usually subjected to hydrolysis/condensation reactions to produce “polymeric” or “colloidal” metal-oxide precursors[52]-[73]. Depending on the reaction conditions, the metal-organic compound may also be a source for some of the carbon for the carbothermal reduction reaction.

The most important advantage of solution-processing methods is that more intimate mixing of components (atomic-scale or at least molecular-scale mixing) can be achieved. However, it should be noted that preparation of solutions with atomic- or molecular-scale mixing does not necessarily ensure that the same scale of mixing will be maintained during subsequent processing steps. It is necessary to remove the liquid medium in a manner that avoids segregation of components. For example, molecular-scale mixing in the solutions may be maintained by first gelling the solutions prior to solvent removal. Another potential advantage for some types of solution processing is that the cost of materials may be relatively low (especially for some external carbon sources).

1.1.3 Preceramic Polymers

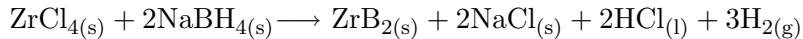
The use of preceramic polymers for synthesizing metal borides is presented here as a separate section. However, there is overlap with the previous section because carbothermal and borothermal reduction reactions may still play a role in the formation of the carbides and diborides. This will become evident from the information presented below.

More recently, significant achievements have also been made in the development of organoboron polymers as precursors for boron carbide-based or metal diboride-based ceramics [74]-[79]. In contrast, preceramic polymers have not been prepared that directly decompose upon pyrolysis to carbide or diboride ceramics based on Zr and Hf. However, the organosilicon and organoboron preceramic polymers would still be useful for synthesizing the composite powders of interest for this work. The organosilicon polymers can be used as a molecular source for incorporating SiC additions into the transition metal carbide/diboride composite powders. The organoboron polymers can be used as a molecular source for the boron needed in the synthesis of the transition metal diborides.

The potential advantages of using preceramic polymers for metal carbide synthesis include lower reaction temperatures and finer crystallite sizes. This is because the polymer contains direct metal-carbon (M-C) bonds. It should be noted, however, there are difficulties in achieving compositional control for boron carbide-based ceramics prepared from organoboron polymers[80]. For example, Su and Sneddon found that a decaborane-dicyanopentane polymer formed boron carbide upon pyrolysis, but the ceramic product also contained nitrogen (i.e., a B-C-N ceramic was formed) and a significant excess of graphitic carbon[80]. Nevertheless, they found this polymer to be useful in forming various transition metal diborides, including ZrB_2 and HfB_2 [80]. They prepared mixtures in which transition metal oxide powders were dispersed in organoboron polymer solutions. The suspensions were dried to remove the solvent and then heat treated at $>1400^\circ\text{C}$ to form the metal diborides via borothermal and carbothermal reduction reactions.

1.1.4 Alkali Metal Reduction

Transition metal diborides can be synthesized by alkali metal reduction of metal halides. The initial step involves a solution-phase reaction of an alkali metal borohydride (e.g., NaBH_4 , LiBH_4) with transition metal chlorides in order to produce transition metal borohydrides or their derivatives.

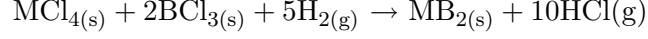


The product can be decomposed at low temperature to form amorphous transition metal diboride powders. Crystalline powders with crystallite sizes as small as ~ 5 nm can be formed at temperatures as low as 800°C [81]-[86].

The alkali metal reduction routes for the synthesis of transition metal metal diborides have two important advantages: (1) The processing temperatures for forming crystalline products are low (i.e., often $< 1000^\circ\text{C}$). (2) It is possible to produce powders with very small crystallite sizes. However, there are some difficulties associated with these methods: (1) Synthesis is carried out using materials which have safety and/or environmental concerns (i.e., alkali metal compounds, organic solvents, etc.) (2) Rigorous control is required for the atmosphere used during processing. This is not only because of safety and environmental concerns, but also because both precursors and intermediate products are air and/or moisture sensitive. Hence, inadequate control over the atmosphere during synthesis will result in formation of metal oxide/hydroxide particles, rather than metal carbides or diborides. Furthermore, even the crystallized metal carbide or metal boride powder formed after elevated heat treatment may be air and/or moisture sensitive as a result of their very small crystallite sizes (and high specific surface areas). (3) It is necessary to remove the alkali halides (e.g., LiCl , NaCl) that are byproducts of the solution-based reaction. Since the reaction products are usually moisture-sensitive, the alkali halides are often removed by sublimation at elevated temperature.

1.1.5 Other Methods

A common vapor-phase method for forming metal diborides is hydrogen reduction of metal chlorides, as shown by the reaction equilibria below. Both coatings and fine powders have been prepared by such reactions[87]-[88].



Disadvantages of vapor-phase methods for powder preparation are the relatively high cost and the safety concerns in using hazardous and corrosive gases. In addition, powders prepared by vapor-phase reactions tend to be highly aggregated. The latter problem can be mitigated by maintaining dilute reactant concentrations in the gas stream, but such an approach makes the process less practical to scale up.

1.2 *Sintering of Zirconium Diboride*

Because of its high melting temperature, low self-diffusion coefficient and its tendency to undergo abnormal grain growth during sintering, ZrB_2 has been typically densified by hot-pressing at temperatures higher than 1600°C and ~ 30 MPa pressure. However, hot pressing can only process samples with simple shapes and moderate sizes. The barrier to densification for pressureless sintering is the highly coarsened microstructure of particles, while hot pressing is less vulnerable to this problem because of the increasing driving force for densification induced by pressure. This pressure-assisted densification is generally done at lower temperatures where abnormal grain growth would be suppressed [89]-[106].

Potential sintering additives to enhance the densification of metal diborides can be classified into three categories:

1.2.1 Liquid phase formers [89]-[94]

The typical candidate additives to forming liquid phase during diboride sintering are: a) iron, nickel cobalt and their alloys; b) high melting-point metals, such as Mo, W, Zr Nb and Cr; c) chromium alloys. Those additives promote liquid phase formation, hence improving mass transfer and enhancing densification. However, the grains resulting from liquid

phase sintering are always large and the additives always have lower melting temperatures compared to metal diboride, which deteriorates the high temperature mechanical behavior.

1.2.2 Solid solution formers [95]-[4]

ZrB₂ can form a solid solution with other transition metal (Ti, Hf, Ta, Nb, Mo) borides over a wide range of compositions, which suppresses grain growth, removes most pores, and results in improvements in densification. Wantanate [4] reported that the addition of 5 wt% TaB₂ led to an increase in the relative density of hot pressed TiB₂-CoB composites. The reason is that a part of TiB₂ and TaB₂ may dissolve into melted CoB when heated at 1800°C and formed solid solution. Those solid solution may precipitate on the surfaces of TiB₂ grain and suppress grain growth.

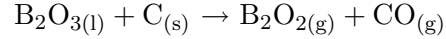
1.2.3 Reactive agents

Possible reactive additives for ZrB₂ are nitrides (Si₃N₄, AlN) [97, 98], carbon and carbides (WC, SiC, B₄C etc.), which act as densification aids by reacting with impurities that inhibit sintering [99, 8]. Oxide is the main impurity that inhibits sintering of diborides by inducing extensive crystal coarsening [5, 101]. For hot pressing, the maximum attainable densities are dependent on the oxygen content and limited by exaggerated grain size, where the relation between grain size and relative density follows the behavior expected when coarsening is controlled by evaporation and condensation kinetics. While the oxygen contamination in the form of B₂O₃ can accelerate the vapor-phase transport, thus results in coarse particles. For pressureless sintering, the maximum relative densities are influenced by particle coarsening, which is controlled by surface diffusion. In this case, the influence of oxygen contamination (such as ZrO₂, B₂O₃ had been evaporated at temperature before the pressureless sintering begun) is increase the surface diffusion coefficient [5, 6, 7].

Baik [5] suggests that the oxygen content in TiB₂ must be less than 0.5 wt% for full densification or add a reactive reagent, such as carbon, that can reduce the oxygen impurity content, hence facilitating densification. The relative density for TiB₂ containing 0.7% oxygen with 2 wt% carbon after hot-pressing at 1700°C for 2 h under 35 MPa was 99% with a grain size of 10 μm, while the density of TiB₂ produced under the same conditions

but no carbon addition was only 96% with a coarse grain size of $\sim 70 \mu\text{m}$. The effect of Si_3N_4 was similar to carbon and can also decrease the oxygen content for hot-pressed samples [97]. However, both carbon and Si_3N_4 are not effective in removing oxygen for pressureless sintering, as explained below.

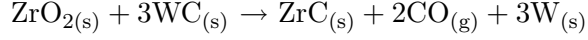
The oxygen in metal diborides exists in two forms: boria and metal oxide. Different forms of oxygen behave differently during pressureless sintering and hot-pressing due to the distinct temperature ranges required for significant densification to be achieved with the two processing methods. Boron oxide can evaporate at $1400\text{-}1600^\circ\text{C}$ without vacuum, or at lower temperature of 1300°C with vacuum [8, 5]. During hot-pressing, significant densification starts at lower temperature of $1200\text{-}1400^\circ\text{C}$ for TiB_2 , at which the boron oxide hasn't been removed from the system. Therefore, the high vapor pressure of boria in the system can adversely affect the overall densification. However, the carbon introduced during milling can remove B_2O_3 as CO gas at temperatures ($<1000^\circ\text{C}$) below which densification starts, hence enhancing the sintering of TiB_2 [5].



In the case of pressureless sintering, densification starts at much higher temperature ($>1600^\circ\text{C}$), where most B_2O_3 had been removed; the oxygen impurity remaining in the system is in the form of metal oxide, which cannot be removed by carbon or Si_3N_4 (by the reduction of the metal oxide to form CO and BN gas) at such temperatures. However, adding carbides, such as SiC, WC and B_4C , can remove the metal oxide during pressureless sintering as well as hot-pressing [8, 5], [6]-[105].

Torizuka [106] studied the effect of SiC on the densification of TiB_2 . The results showed that the relative density of TiB_2 without SiC was 62% after sintering at 1700°C , while the relative density was 89% with the addition of 1.5 wt% SiC, and 96% with a content of 2.5 wt% SiC. However, SiC cannot react with ZrO_2 even at a high temperature of 2100°C , according to our thermodynamic calculation (shown in Figure 1.1), but rather facilitates sintering by suppressing grain growth because it sits between the grains of ZrB_2 as a barrier of second phase. The important reactive additives to enhance sintering of ZrB_2 are WC

and B_4C , which react with ZrO_2 and oxygen is removed as gas phase of CO or B_2O_3 .



Among the above additives, WC forms a second phase in the solid product which may affect the properties of the diboride. However, the solid product for B_4C is ZrB_2 , which does not bring impurity to the product. Therefore, B_4C was used as the additive to improve the sintering property of diborides.

1.3 Enhancement of the Oxidation Resistance of ZrB_2

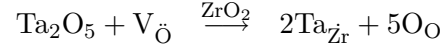
Because of its excellent and unique combination of properties, such as high melting point, high elastic modulus, high electrical and thermal conductivity, good thermal shock and wear resistance, and good chemical inertness, zirconium diboride (ZrB_2) is a candidate for numerous applications in high-temperature environments with aggressive gases and possible corrosive deposits, especially on supersonic and hypersonic vehicles. As a result, the components made from ZrB_2 will be frequently exposed to very hot and hostile environments; high-temperature stability, especially resistance to oxidation, is a key criterion for these applications. The mechanical and physical properties of monolithic zirconium diboride may be inadequate for some applications. However, its resistance to ablation/oxidation can be improved by introducing second phases, such as SiC , Si_3N_4 , and TaB_2 [10]-[15], [107, 108].

The oxidation resistance of ZrB_2 is dependent on the properties of the oxide layer formed on the surface exposed to air. The main reaction products from the oxidation of ZrB_2 are zirconia and amorphous boria (B_2O_3). In the initial stage of oxidation, boria fills all of the porosity and interparticle spaces of zirconia forming a continuous coating which prevents the diffusion of oxygen to interior ZrB_2 and provides oxidation protection [13]. Unfortunately, boron oxide has an unusually low melting point ($450^\circ C$) and a high vapor pressure, so at high temperature it quickly vaporizes [107]. As a result, the primary protective oxidation barrier ZrB_2 is the zirconium oxide scale plus any residual B_2O_3 , which is not a continuous layer and can not prevent the inward diffusion of oxygen. Perfect zirconium oxide may be a good

oxygen barrier, but it becomes nonstoichiometric by forming oxygen lattice vacancies under low oxygen partial pressure conditions. It is also readily modified by aliovalent cations of lower valence to form oxygen lattice vacancies. Oxygen lattice vacancies allow rapid oxygen ion transport through the scale and cannot protect the matrix from oxidation [3, 4].

The addition of SiC to ZrB_2 leads to the formation of a protective layer of borosilicate glass with lower vapor pressure and higher viscosity, hence improving the oxidation resistance of ZrB_2 [10]-[15] and increase the oxidation resistance temperature from 1200°C to 1500°C . The effect of this borosilicate glass is to improve resistance to oxidation by acting as a barrier against the inward diffusion of oxygen more efficiently than B_2O_3 and ZrO_2 . However, with the thickness of SiO_2 -rich glass layer (oxidation layer) increasing, the oxygen transport decreases, and the O_2 pressure beneath the glass layer decreases, and SiO_2 transforms to SiO , which results in the increasing of P_{SiO} and finally leads to the rupture of the glass layer (active oxidation) [14, 1]. As a result, most of the B_2O_3 and SiO_2 that formed the borosilicate protective layer will be lost by evaporation or active oxidation at very high temperatures in a flowing environment. This results in the same problem encountered as mentioned above for pure ZrB_2 . However, this mechanism appears as a hypothesis without experimental verification.

Another problem with ZrO_2 is its phase instability. At high temperatures, ZrO_2 is tetragonal. Upon cooling to room temperature it transforms to a monoclinic structure with a significant volume expansion, hence leading to cracking and spalling. One approach to resolve the oxygen transport problem and the cracking issue is to modify the scale with a cation with higher valence compared to Zr^{4+} , which can stuff oxygen into the lattice and increase scale adhesion. Thus, the substituting cations must have higher valence and can form a refractory oxide. The best candidates are niobium and tantalum. However, the melting point for niobium pentoxide is only 1460°C . That leaves tantalum, with a pentoxide melting point of 1880°C , as the only candidate being added to zirconium diborides. Additions can be either as the element, carbide, silicide or boride[3]-[4]. Ta additions result in substitution of Ta on the Zr site in ZrO_2 , reducing the concentration of oxygen vacancies in the ZrO_2 through following reaction:



The resultant lower concentration of oxygen vacancies, decreases oxygen transport through the growing oxide scale, and thus lowers the oxidation rate of Ta-doped ZrB₂[1]. The experimental results showed that adding TaB₂ to ZrB₂-20 vol% SiC can improve the oxidation resistance of this material up to 1570°C, while adding 20 vol% TaSi₂ can improve its oxidation resistance at 1627°C in air [10]-[1].

REFERENCES

1.4 References

- [1] K. Upadhyaya, J. M. Yan, and W. P. Hoffman, “Materials for Ultrahigh Temperature Structural Applications,” *Am. Ceram. Soc. Bull.*, **76** 51-56 (1997).
- [2] R. W. Newman, “Oxidation-Resistant High-Temperature Materials,” *Johns Hopkins APL Technical Digest*, **14** [1] 24-28 (1993).
- [3] S. R. Levine, E. J. Opila, “Tantalum Addition to Zirconium Diboride for Improved Oxidation Resistance,” NASA/TM-2003-212483
- [4] S. R. Levine, E. J. Opila, R. C. Robinson, J. A. Lorincz, “Characterization of an Ultra-High Temperature Ceramic Composite,” NASA/TM-2004-213085
- [5] Z. Hu, M. D. Sacks, G. A. Staab, C. A. Wang, and A. Jain, “Solution-Based Processing of Nanocrystalline ZrC,” *Ceram. Eng. Sci. Proc.*, **23**[4] 711-717 (2002).
- [6] A. Jain, M. D. Sacks, C. A. Wang, M. Middlemas, and Z. Cheng, “Processing of Nanocrystalline Zirconium Carbide Powders,” *Ceram. Eng. Sci. Proc.*, **24**[A] 41-49 (2003).
- [7] A. Jain, M. D. Sacks, and C. A. Wang, “Preparation of Nanocrystalline Zirconium Carbide Powders by Carbothermal Reduction,” *Ceram. Trans.*, 37-46 (2003).
- [8] S. C. Zhang, G. E. Hilmas, W. G. Fahrenholtz, “Pressureless Densification of Zirconium Diboride with Boron Carbide Additions,” *J. Am. Ceram. Soc.*, in press, (2006).
- [9] S. Baik, P. F. Becher, “Effect of Oxygen Contamination on Densification of Titanium Diboride,” *J. Am. Ceram. Soc.*, **70** [8] 527-30 (1987).

- [10] I. G. Talmy, J. A. Zaykoski, M. M. Opeka, S. Dallek, "Oxidation of ZrB₂ Ceramics Modified With SiC and Group IV-VI Transition Metal Diborides," *Elec. Chem. Soc. Proc.*, **12** 144-158 (2001).
- [11] W. C. Tripp, "Effect of an SiC Addition on the Oxidation of ZrB₂," *Am. Ceram. Soc. Bull.*, **52** [8] 1606-10 (1973).
- [12] D. M. Van-Wie, D. G. Drewry Jr., D. E. King, and C. M. Hudson, "The Hypersonic Environment: Required Operating Conditions and Design Challenges," *J. Mater. Sci.*, **39** 5915-5924 (2004).
- [13] I. G. Talmy, J. A. Zaykoski, and M. A. Opeka, "Properties of Ceramics in the ZrB₂/ZrC/SiC System Prepared by Reactive Processing," *Ceram. Eng. Sci. Proc.*, **19** [3] 105-112 (1998).
- [14] E. J. Opila, M. C. Halbig, "Oxidation of ZrB₂-SiC," *Elec. Chem. Soc. Proc.*, **12** 221-228 (2002).
- [15] S. R. Levine, E. J. Opila, M. C. Halbig, J. D. Kiser, M. Singh, J. A. Salem, "Evaluation of Ultra-high Temperature Ceramics for Aeropropulsion Use," *J. Euro. Ceram. Soc.*, **22** 2757-2767 (2002).
- [16] E. Opila, S. Levine, J. Lorincz, "Oxidation of ZrB₂- and HfB₂-based Ultra-high Temperature Ceramics: Effect of Ta Additions," *J. Mater. Sci.*, **39** 5969-5977 (2004).
- [17] M. Opeka, I. Talmy, J. Zaykoski, "Oxidation-based Materials Selection for 2000°C + Hypersonic Aerosurfaces: Theoretical Considerations and Historical Experience," *J. Mater. Sci.*, **39** 5887 - 5904 (2004).
- [18] "Nist-Janaf Thermochemical Tables" *J. Phys. Chem. Ref. Data*, monograph 9.
- [19] L. E. Toth, *Transition Metal Carbides and Nitrides*, Academic Press, New York, 1971.
- [20] A. J. Perry, "The Refractories HfC and HfN - A Survey. I. Basic Properties," *Powder Metall. Int.*, **19** [1] 29-35 (1987).

- [21] A. J. Perry, "The Refractories HfC and HfN - A Survey. II. Phase Relationships," *Powder Metall. Int.*, **19** [2] 32-36 (1987).
- [22] M. M. Opeka, I. G. Talmy, E. J. Wuchina, J. A. Zaykosi, and S. J. Causey, "Mechanical, Thermal, and Oxidation Properties of Refractory Hafnium and Zirconium Compounds," *J. Eur. Ceram. Soc.*, **19** 2405-2414 (1999).
- [23] S. T. Oyama, *The Chemistry of Transition Metal Carbides and Nitrides*, Blackie Academic & Professional, Glasgow, UK, (1996).
- [24] T. Lundstrom, "Transition Metal Borides," in *Boron and Refractory Borides*, edited by V.I. Matkovich, Springer-Verlag, Berlin, 351-376 (1977).
- [25] T. Matsudaira, H. Itoh, S. Naka, and H. Hamamoto, "Synthesis of Niobium Boride Powder by Solid State Reaction Between Niobium and Amorphous Boron," *J. Less-Common Metals*, **155** 207-214 (1989).
- [26] S. D. Dunmead, Z. A. Munir, and J. B. Holt, "Temperature Profile Analysis in Combustion Synthesis: II, Experimental Observations," *J. Am. Ceram. Soc.*, **75** [1] 180-188 (1992).
- [27] A. G. Merzhanov, "Self-Propagating High-Temperature Synthesis: Twenty Years of Search and Findings," in *Combustion and Plasma Synthesis of High-Temperature Materials*, edited by Z. A. Munir and J. B. Holt, VCH Publ., New York, 1-53 (1990).
- [28] Z. A. Munir and U. A. Tamburini, "Self-Propagating Exothermic Reactions: The Synthesis of High-Temperature Materials by Combustion," *Mater. Sci. Rept.*, **3** [7-8] 277-365 (1989).
- [29] J. W. McCauley, "A Historical and Technical Perspective of SHS," *Ceram. Eng. Sci. Proc.*, **11** [9-10] 1137-1181 (1990).
- [30] V. Hlavacek and J. A. Puszynski, "Chemical Engineering Aspects of Advanced Ceramic Materials," *Indust. Eng. Chem. Res.*, **35** 349-377 (1996).

- [31] J. B. Holt and S. D. Dunmead, "Self-Heating Synthesis of Materials," *Annual. Rev. Mater. Sci.*, **21** 305-334 (1991).
- [32] J. F. Crider, "Self-Propagating High-Temperature Synthesis: A Soviet Method for Producing Ceramic Materials," *Ceram. Eng. Sci. Proc.*, **3** [9-10] 519-528 (1982).
- [33] P. Peshev and G. Blizanakov, "On the Borothermic Preparation of Titanium, Zirconium, and Hafnium Diborides," *J. Less-Common Metals*, **14** 23-32 (1968).
- [34] G. Blizanakov and P. Peshev, "The Preparation of Cerium, Praseodymium, and Neodymium Hexaborides," *J. Less-Common Metals*, **7** 441-446 (1964).
- [35] P. Peshev, G. Blizanakov, and L. Leyarovska, "On the Preparation of Some Chromium, Molybdenum, and Tungsten Borides," *J. Less-Common Metals*, **13** 241-247 (1967).
- [36] P. Peshev, L. Leyarovska, and G. Blizanakov, "On the Borothermic Preparation of Vanadium, Niobium, and Tantalum Borides," *J. Less-Common Metals*, **15** 259-267 (1968).
- [37] L. Bartons and D. Nicholls, "The Hydrogenation of Boron Monoxide to Diborane and the Reactions of Boron and Boron Carbide with Titanium and Zirconium Dioxides," *J. Inorg. Nucl. Chem.*, **28** 1367-1372 (1966).
- [38] Z. Jiang and W. E. Rhine, "Preparation of Titanium Diboride from Titanium Alkoxide and Boron Powder," *Chem. Mater.*, **4** [3] 497-500 (1992).
- [39] C. T. Baroch and T. E. Evans, "Production of Zirconium Diboride from Zirconia and Boron Carbide," *J. Metals*, **7** 908-911 (1955).
- [40] H. Zhao, Y. He, and Z. Jin, "Preparation of Zirconium Boride Powder," *J. Am. Ceram. Soc.*, **78** [9] 2534-2536 (1995).
- [41] J. K. Walker, "Synthesis of TiB_2 by the Borothermic/Carbothermic Reduction of TiO_2 with B_4C ," *Adv. Ceram. Mater.*, **3** [6] 601-604 (1988).

- [42] J. Kim and C. H. McMurty, "TiB₂ Powder Production for Engineered Ceramics," *Ceram. Eng. Sci. Proc.*, **6** [9-10] 1313-1320 (1985).
- [43] A. W. Weimer, R. P. Roach, C. N. Haney, W. G. Moore, and W. Rafaniello, "Rapid Carbothermal Reduction of Boron Oxide in a Graphite Transport Reactor," *AICHE J.*, **37** [5] 759-768 (1991).
- [44] H. Blumenthal, "Production of Transition Metal Diborides and their Solid Solutions from Metal Oxides and Boron Oxide," *Powder Met. Bull.*, **7** [3-6] 79-81 (1956).
- [45] A. I. Karasev, "Preparation of Zirconium Diboride by the Carbothermic Reduction of Mixtures of Zirconium and Boron Oxides," *Poroshkovaya Met.*, **11** [131] 80-84 (1973).
- [46] Maeda, T. Yoshikawa, K. Kusakabe, and S. Morooka, "Synthesis of Ultrafine NbB₂ Powder by Rapid Carbothermal Reduction in a Vertical Tubular Reactor," *J. Alloys and Compounds*, **215** 127-134 (1994).
- [47] T. Saito, T. Fukuka, H. Maeda, K. Kusakabe, and S. Morooka, "Synthesis of Ultrafine TiB₂ Particles by Rapid Carbothermal Reduction in a Particulate Transport Reactor," *J. Mater. Sci.*, **32** 3933-3938 (1997).
- [48] C. E. Curtis, L. M. Doney, and J. R. Johnson, "Some Properties of Hafnium Oxide, Hafnium Silicate, Calcium Hafnate, and Hafnium Carbide," *J. Am. Ceram. Soc.*, **37** [10] 458-465 (1954).
- [49] P. G. Cotter and J. A. Kohn, "Industrial Diamond Substitutes: I, Physical and X-ray Study of Hafnium Carbide," *J. Am. Ceram. Soc.*, **37** [9] 415-420 (1954).
- [50] V. I. Zhelankin, V. S. Kutsev, and B. F. Ormont, "Equilibrium in Reactions for Reduction of ZrO₂ and V₂O₃ by Carbon at High Temperatures," *Zh. Neorg. Khim.*, **3** [5] 1237-1240 (1958).
- [51] S. K. Sarkar, A. D. Miller, and J. I. Mueller, "Solubility of Oxygen in ZrC," *J. Am. Ceram. Soc.*, **55** [1] 628-630 (1972).

- [52] H. Martin, R. Ecke, and E. Muller, "Synthesis of Nanocrystalline Silicon Carbide Powder by Carbothermal Reduction," *J. Eur. Ceram. Soc.*, **18** 1737-1742 (1998).
- [53] H. Tanaka and Y. Kurachi, "Synthesis of β -SiC Powder from Organic Precursor and its Sinterability," *Ceram. International*, **14** 109-115 (1988).
- [54] K. Ono and Y. Kurachi, "Kinetic Studies on β -SiC Formation from Homogeneous Precursors," *J. Mater. Sci.*, **26** 388-392 (1991).
- [55] D. Huang and Y. Ikuhara, "Characterization of β -Silicon Carbide Powders Synthesized by the Carbothermal Reduction of Silicon Carbide Precursors," *J. Am. Ceram. Soc.*, **81** 3173-3176 (1998).
- [56] Y. Sugahara, Y. Takeda, K. Kuroda, and C. Kato, "Carbothermal Reduction Process of Precursors Derived from Alkoxides for Synthesis of Boron-Doped SiC Powder," *J. Mater. Sci. Lett.*, **8** 944-946 (1989).
- [57] Y. Sugahara, Y. Takeda, K. Kuroda, and C. Kato, "The Preparation of Boron-Doped Silicon Carbide Powder by the Carbothermal Reduction of Oxides Derived from the Hydrolyzed Methyl Triethoxysilane," *J. Non-Cryst. Solids*, **100** 542-546 (1988).
- [58] G. C. Wei, C. R. Kennedy, and L. A. Harris, "Synthesis of Sinterable SiC Powders by Carbothermic Reduction of Gel-Derived Precursors and Pyrolysis of Polycarbosilane," *Am. Ceram. Soc. Bull.*, **63** [8] 1054-1061 (1984).
- [59] I. Hasegawa, T. Nakamura, S. Motojima, and M. Kajiwara, "Silica Gel-Phenolic Resin Hybrid Fibres: New Precursors for Continuous β -Silicon Carbide Fibres," *J. Mater. Chem.*, **5** [1] 193-194 (1995).
- [60] I. Hasegawa, T. Nakamura, S. Motojima, and M. Kajiwara, "Synthesis of Silicon Carbide Fibers by Sol-Gel Processing," *J. Sol-Gel Sci. Tech.*, **8** 577-579 (1997).
- [61] A. W. Weimer, W. G. Moore, R. P. Roach, J. E. Hitt, R. S. Dixit, and S. E. Pratsinis, "Kinetics of Carbothermal Reduction Synthesis of Boron Carbide," *J. Am. Ceram. Soc.*, **75** [9] 2509-2514 (1992).

- [62] I. Hasegawa, Y. Fukuda, and M. Kajiwara, "Inorganic-Organic Hybrid Route to Synthesis of ZrC and Si-Zr-C Fibres," *Ceram. Int.*, **25** 523-527 (1999).
- [63] Y. Kurokawa, S. Kobayashi, M. Suzuki, M. Shimazaki, and M. Takahashi, "Preparation of Refractory Carbide Fibers by Thermal Decomposition of Transition Metal (Ti, Zr, Hf, Nb, Ta) Alkoxide-Cellulose Precursor Gel Fibers," *J. Mater. Res.*, **13** [3] 760-765 (1998).
- [64] Z. Jiang and W.E. Rhine, "Preparation of TiN and TiC from a Polymer Precursor," *Chem. Mater.*, **3** 1132-1137 (1991).
- [65] D. R. Stanley, J. D. Birchall, J. N. K. Hyland, L. Thomas, and K. Hodgetts, "Carbothermal Synthesis of Binary (MX) and Ternary (M1,M2,X) Carbides, Nitrides and Borides from Polymeric Precursors," *J. Mater. Chem.*, **2** [2] 149-156 (1992).
- [66] H. Preiss, B. Meyer, and C. Olschewski, "Preparation of Molybdenum and Tungsten Carbides from Solution Derived Precursors," *J. Mat. Sci.*, **33** 712-722 (1998).
- [67] C. A. Wang, M. D. Sacks, G. A. Staab, and Z. Cheng, "Solution-Based Processing of Nanocrystalline SiC," *Ceram. Eng. Sci. Proc.*, **23** [4] 701-709 (2002).
- [68] Z. Cheng, C. A. Wang, and M. D. Sacks, "Synthesis of Nanocrystalline Silicon Carbide Powders," *Ceram. Eng. Sci. Proc.*, **24** [A], 23-32 (2003).
- [69] Z. Cheng, M. D. Sacks, C. Wang, and Z. Yang, "Preparation of Nanocrystalline Silicon Carbide Powders by Carbothermal Reduction," *Ceram. Trans.*, 15-25 (2003).
- [70] H. Preiss, E. Schierhorn, K. W. Brzenzinka, "Synthesis of Polymeric Titanium and Zirconium Precursors and Preparation of Carbide Fibers and Films," *J. Mater. Sci.*, **33** 4697-4706 (1998).
- [71] E. L. Sham, E. M. Farfan-Torres, S. Bruque-Gamez, and J. J. Rodriguez-Jimenez, "Synthesis of ZrC/ZrO₂ by Pyrolysis of Modified Zirconium Alkoxide Precursors," *Solid State Ionics*, **63-65** 45-51 (1993).

- [72] C. A. Wang and M. D. Sacks, "Processing of Nanocrystalline Hafnium Carbide Powders," *Ceram. Eng. Sci. Proc.*, **24** [A] 33-40 (2003).
- [73] C. A. Wang, M. D. Sacks, and Z. Yang, "Preparation of Nanocrystalline Hafnium Carbide Powders by Carbothermal Reduction," *Ceram. Trans.*, 27-36 (2003).
- [74] J. Green, M. M. Fein, N. Mayes, G. Donovan, M. Israel, and M. S. Cohen, "Polymers from Decaborane," *Polym. Lett.*, **2** 987-989 (1964).
- [75] W. S. Rees Jr. and D. Seyferth, "High-Yield Synthesis of B₄C/BN Ceramic Materials by Pyrolysis of Polymeric Lewis Base Adducts of Decaborane(14)," *J. Am. Ceram. Soc.*, **71** [4] C-194 - C-196 (1988).
- [76] D. Seyferth, N. Bryson, D. P. Workman, and C. A. Sobon, "Preceramic Polymers as "Reagents" in the Preparation of Ceramics," *J. Am. Ceram. Soc.*, **74** [10] 2687-2689 (1991).
- [77] M. G. L. Mirabelli and L. G. Sneddon, "Synthesis of Boron Carbide via Poly(vinylpentaborane) Precursors," *J. Am. Chem. Soc.*, **110** 2205-3307 (1988).
- [78] M. J. Pender and L. G. Sneddon, "Polyalkenyldecaboranes: New Polymeric Precursors to Boron Carbide Ceramics," *ACS Polym. Prepr.*, **41** 551-552 (2000).
- [79] M. J. Pender, K. M. Forsthoefel, and L. G. Sneddon, "The Design, Synthesis, and Application of Group 13 Molecular and Polymeric Precursors to Advanced Ceramics," in *Group 13 Chemistry: From Fundamentals to Applications*, edited by P. J. Shapiro and D. A. Atwood, American Chemical Society, Washington, D.C., 168-180 (2002).
- [80] K. Su and L. G. Sneddon, "A Polymer Precursor Route to Metal Borides," *Chem. Mater.*, **5** 1659-1668 (1993).
- [81] J. A. Jensen, J. E. Gozum, D. M. Polina, "Titanium, Zirconium, and Hafnium Tetrahydroborates as "Tailored" CVD Precursors for Metal Diboride Thin Films," *J. Am. Chem. Soc.*, **110** 1643-1644 (1988).

- [82] J. D. MacKenzie and D. R. Ulrich, *Ultrastructure Processing of Advanced Ceramics*, edited by John Wiley, New York, 901-906,(1988).
- [83] G. W. Rice and R. L. Woodin, "Zirconium Borohydride as a Zirconium Boride Precursor," *J. Am. Ceram. Soc.*, **71** [4] C-181 - C-183 (1988).
- [84] G. N. Glavee, K. J. Klabunde, C. M. Sorensen, and G. C. Hadjapanayis, "Borohydride Reductions of Metal Ions. A New Understanding of the Chemistry Leading to Nanoscale Particles of Metals, Borides, and Metal Borates," *Langmuir*, **8** 771-773 (1992).
- [85] L. Chen, Y. Gu, Z. Yang, and Y. Tai, "Preparation and Some Properties of Nanocrystalline ZrB_2 Powders," *Scripta Materialia*, **50** 959-961 (2004).
- [86] S. E. Bates, W. E. Buhro, and K. F. Kelton, "Synthesis of Titanium Diboride (TiB_2) Nanocrystallites by Solution-Phase Processing," *J. Mater. Res.*, **10** [10] 2599-2612 (1995).
- [87] H. R. Baumgartner and R. A. Steiger, "Sintering and Properties of Titanium Diboride Made from Powder Synthesized in a Plasma-Arc Heater," *J. Am. Ceram. Soc.*, **67** [3] 207-212 (1984).
- [88] H. O. Pierson, E. Randich, and D. M. Mattox, "The Chemical Vapor Deposition of TiB_2 on Graphite," *J. Less-Common Metals*, **67** 381-388 (1979).
- [89] F. Monteverde, A. Bellosi, and S. Guicciardi, "Processing and Properties of Zirconium Diboride-based Composites," *J. Eur. Ceram. Soc.*, **22** 279-288 (2002).
- [90] M. Einarsrud, E. Hagen, G. Pettersen, and T. Grande, "Pressureless Sintering of Titanium Diboride with Nickel, Nickel Boride, and Iron Additives," *J. Am. Ceram. Soc.*, **80** [12] 3013-20 (1997).
- [91] S. K. Woo, C. H. Kim, and E. S. Kang, "Fabrication and Microstructure Evaluation of $ZrB_2/ZrC/Zr$ Composites by Liquid Infiltration," *J. Mater. Sci.*, **29** 5309-5315 (1994).

- [92] S. K. Mishra, S. K. Das, A. K. Ray, and P. Ramachandrarao, "Effect of Fe and Cr Addition on the Sintering Behavior of ZrB_2 Produced by SHS," *J. Am. Ceram. Soc.*, **85** [11] 2846-2848 (2002).
- [93] P. S. Kisliy, M. A. Kuzenkora, and O. V. Zaveruha, "On the Sintering Process of Zirconium Diboride with Tungsten," *Physics of Sintering*, **3** [1] 29-44 (1971).
- [94] E. S. Kang, C. W. Jang, C. H. Lee, and C. H. Kim, "Effect of Iron and Boron Carbide on the Densification and Mechanical Properties of Titanium Diboride Ceramics," *J. Am. Ceram. Soc.*, **72** [10] 1868-72 (1989).
- [95] W. A. Zdaniewski, "Solid Solution Effect on Properties of Titanium Diboride," *J. Am. Ceram. Soc.*, **70** [11] 793-797 (1987).
- [96] T. Watanabe and S. Kouno, "Mechanical Properties of TiB_2 -CoB-metal Boride Alloys," *Am. Ceram. Soc. Bull.*, **61** [9] 970-973 (1982).
- [97] F. Monteverde, A. Bellosi, "Effect of the Addition of Silicon Nitride on Sintering Behaviour and Microstructure of Zirconium Diboride," *Scripta Materialia*, **46** 223-228 (2002).
- [98] F. Monteverde, A. Bellosi, "Beneficial of Effects of AlN as Sintering Aid on Microstructure and Mechanical Properties of Hot-pressed ZrB_2 ," *Adv. Eng. Mater.*, **5** [7] 508-12 (2003).
- [99] T. Graziani, A. Bellosi, "Sintering and Characterization of TiB_2 - B_4C - ZrO_2 Composites," *Mater. Manu. Proc.*, **9** [4] 781-802 (1994).
- [100] A. L. Chamberlain, W. G. Fahrenholtz, and G. E. Hilmas, "High-strength Zirconium Diboride-based Ceramics," *J. Am. Ceram. Soc.*, **87** [6] 1170-1172 (2004).
- [101] S. L. Doie, S. Prochaka, and R. H. Doremus, "Microstructural Coarsening During Sintering of Boron Carbide," *J. Am. Ceram. Soc.*, **72** [6] 51-56 (1989).

- [102] M. F. Yan, U. Chowdhry, and R. M. Cannon, "Conditions for Discontinuous Grain Growth with Pore Entrapment or Pore Coarsening," *Am. Ceram. Soc. Bull.*, **57** [3] 316 (1978).
- [103] M. F. Yan, "Microstructural Control in the Processing of Electronic Ceramics," *Mater. Sci. Eng.*, **48** 53-72 (1981).
- [104] R. M. Williams, B. N. Juterbock, C. R. Peters, and T. J. Whalen, "Forming and Sintering Behavior of B- and C-doped α - and β -SiC," *Communication of the American Ceramic Society*, [4] C-62-64 (1984).
- [105] H. W. Kim, Y. H. Koh, H. E. Kim, "Reaction Sintering and Mechanical Properties of B₄C with Addition of ZrO₂," *J. Mater. Res.*, **15** [11] 2431-34 (2000).
- [106] S. Torizuka, K. Sato, H. Nishio, and T. Kishi, "Effect of SiC on Interfacial Reaction and Sintering Mechanism of TiB₂," *J. Am. Ceram. Soc.*, **78** [6] 1606-10 (1995).
- [107] F. Monteverdez and A. Bellosi, "Oxidation of ZrB₂-Based Ceramics in Dry Air," *J. Elec. Chem. Soc.*, **150** [11] B552-B559 (2003).
- [108] G. Laudisio, K. G. Nickel, and C. Berthold, "Oxidation Behavior and Electroconductive Properties of Si₃N₄ Doped ZrB₂," *Elec. Chem. Soc. Proc.*, **16** 387-397 (2003).
- [109] J. L. Blumenthal, M. J. Santy, and E. A. Burns, "Kinetics Study of High-temperature Carbon-silica Reactions in Charred Silica-reinforced Phenolic Resins," *J. AIAA*, **4** [6] 1053-1057 (1966).
- [110] V. M. Kevorkijan, M. Komac, and D. Kolar, "Low Temperature Synthesis of Sinterable SiC Powders by Carbothermic Reduction of Colloidal SiO₂," *J. Mater. Sci.*, **27** [10] 2705-2712 (1992).
- [111] A. W. Weimer, K. J. Nilson, G. A. Cochran and R. P. Roach, "Kinetics of Carbothermal Reduction Synthesis of Beta Silicon Carbide," *J. AICHE*, **39** [3] 493-503 (1993).

CHAPTER 2

EXPERIMENTAL PROCEDURES

2.1 Synthesis of Nanocrystalline Powders by a Solution-based Method

2.1.1 Zirconium Diboride (ZrB_2)

2.1.1.1 Preparation of Dry Powder

Solution-based synthesis is a good method to achieve intimate mixing of reactants and thus can obtain fine scale mixing of product powders. All of our samples were synthesized via a solution-based method. The flow chart for synthesis of ZrB_2 is illustrated in Figure 2.1.

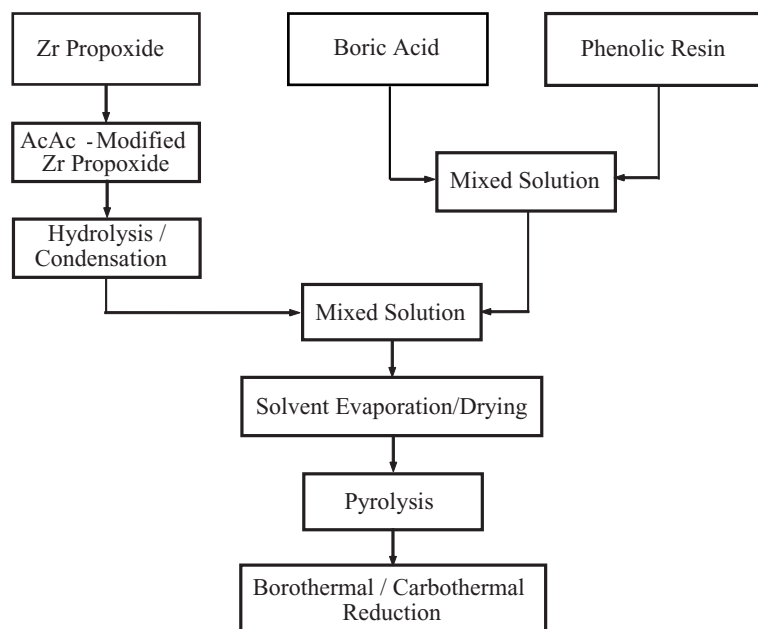


Fig 2.1: Flow chart for synthesis of ZrB_2 from solution-based precursors.

The starting Zr-containing material was a zirconium n-propoxide/n-propanol solution (i.e., 70 wt% $\text{Zr}(\text{OC}_3\text{H}_7)_4$ in n-propanol, Alfa Aesar, Ward Hill, MA). The zirconium n-propoxide was mixed with “acacH” (i.e., 2,4-pentanedione, Alfa Aesar, Ward Hill, MA) using molar ratios of 3:1, and 2-propanol was used as a mutual diluent. The resulting

solutions were refluxed (solution was heated and the vapor formed was condensed and returned to the system to be heated again) at temperatures in the range of 170-195°C for 2 h. After refluxing, much of the solvent (about 2/3) was evaporated (to remove residual propanol and residual “acacH”) and then 2-propanol was added back to the sol. The refluxed Zr-containing precursors were partially hydrolyzed (the decomposition of organic compounds by interaction with water) at 50°C for 2 h under acidic conditions with a HNO₃/Zr molar ratio of 0.27 and an H₂O/Zr molar ratio of 24.

A boric acid (H₃BO₃, Fisher Scientific, Fair Lawn, NJ) in water solution with concentration of 4 wt% was prepared as boron source to make a B/Zr ratio of 3. 2-propanol was then added to dilute the boric acid solution with a propanol/H₂O ratio of 3.

20 wt% phenol-formaldehyde resin (“novolac” type, Georgia Pacific, Atlanta, GA) in 2-propanol solution was added to above boric acid solutions to increase the C/Zr ratio (4.8-6.0) in the powders used for carbothermal reduction. The mixture of boric acid and phenolic resin was added to hydrolyzed solutions. The solutions were initially concentrated by rotary evaporation and then dried to powders at 120-140°C (2 h).

2.1.1.2 Pyrolysis

The dried powders were subsequently pyrolyzed at temperatures in the range of 800-1100°C (2 h) in a flowing argon atmosphere with oxygen partial pressure of 10⁻⁵-10⁻⁶ to produce zirconia/boria/carbon mixtures. The heating rate for all pyrolysis experiments was 5°C/min with a hold of 2 h at the maximum temperature. The experiments were performed in a flowing argon (75 ml/min) atmosphere. The weight losses that occurred during pyrolysis were monitored. The furnace used for pyrolysis is an alumina tube furnace (Model 55031, Lindberg, Watertown, WI). The furnace was naturally cooled to room temperature by shutting off the power of furnace after holding at the desired temperature.

2.1.1.3 Boro/carbothermal Reduction

Pyrolyzed powders were subsequently heat-treated at temperatures in the range of 1200-1800°C (2 h) for carbo/borothermal reduction reaction in a water cooled “M11” furnace (Model M11, Centorr Vacuum Systems, Nashua, NH) under flowing argon (Ar, >99.999%,

Airgas, Randor, PA) atmosphere (oxygen partial pressure : 10^{-5} - 10^{-6}) with a flowing rate of 500 ml/min. The heating element, insulation and furnace gas-flow tube were all made of graphite and the temperature was measured at the center of the furnace tube by a Type C (95%W/5%Re vs. 74%W/26%Re, Flow Autoclave Systems Inc., Columbus, OH) thermocouple with a Mo sheath. The heating rate was 80°C/min to 75°C lower than the final temperature, then 40°C/min to 35°C lower than the final temperature, 20°C/min to a temperature 15°C lower, and 5°C/min to 5°C lower, and finally 1°C/min to the soak temperature, and hold for a desired time, such as 2 h. Graphoil (electrically conductive grade, graphoil, UCAR Carbon Company Inc., Cleveland, OH) was used as containers for samples heat-treated at temperature lower than 1500°C, while ZrB₂ pellets sintered at 1950°C was used as substrate for samples heat-treated at temperature higher than 1500°C. The furnace was programmed to cool to room temperature at a rate of 40°C/min. The weight loss of all samples was recorded.

The B/Zr ratios in some of the heat-treated samples were determined by the D-mannitol titration method, and the C/Zr ratio was then calculated from weight losses that occurred upon oxidation (1100°C, 1 h) in air (i.e., in order to remove carbon by oxidative combustion). The B/Zr ratio was also determined by inductively coupled plasma (ICP) as a comparison with our titration results.

X-ray diffraction, XRD (Model PW1800, Philips Analytical, Netherlands or Model X'pert PRO Alpha-1 PANalytical, Netherlands), was used to determine the phases present. The crystallite sizes of ZrB₂ and ZrO₂ were calculated from the broadening of the XRD peaks (Model PW1800, Philips Analytical, Netherlands) using the Scherrer equation.

The sintering behavior was evaluated using a ZrB₂ powder prepared by boro/carbo-thermal reduction at 1400°C. The powder was first ball-milled in methanol(ACS grade, 99.8%, VWR, West Chester, PA) for 48 h using B₄C as media (B₄C media is the fracture of B₄C plate (4×4 inch we densified, which were first ball-milling in methanol for 40 h to remove the sharp corner and edges, and then cleaned and dried. The size of the media is around 5 mm-10 mm) to break up aggregates, and then was washed in methanol (sonicated for 60 min), repeated 4-6 times to remove boron oxide on the powder surface. The powder was

mixed with approximately 10 vol% organic binder (polyvinyl alcohol/polyethylene glycol mixture), and then dried in a 60°C oven for 3 h. The powder agglomerates were broken up using a spatula and ground in alumina mortar. The powder was then put through a 120 mesh (90 μm) sieve. Dry pressing was performed in a 6.44 mm steel die at ~ 150 MPa. The binder was removed by heat treatment at 1150°C (1 h in argon). Samples were then sintered at temperatures in the range of 1750-2050°C in helium. The bulk densities of the samples were determined based on the weight and geometric dimensions of the cylinder-shaped samples. In addition, the bulk density and open porosity were determined for some samples using the Archimedes displacement method with distilled water as the suspending liquid. Relative (percentage) densities were calculated using a solid (“true”) density value calculated according to the composition of samples. The true density for some selected sample was measured by pycnometer (Model MVP-1, Quantachrome Corporation).

The gas adsorption/condensation method (Model ASAP 2000, Micromeritics, Norcross, GA) was used to determine the powder porosity characteristics based on the BET model.

2.1.2 ZrB₂-B₄C Composite

2.1.2.1 Preparation of Boron Carbide (B₄C) Sol

A 3.85 wt% boric acid (H₃BO₃, Fisher Scientific, Fair Lawn, NJ) in water solution was first prepared as a boron source, and then was diluted by 2-propanol to make a ratio of H₂O/2-propanol of 4. A 20 wt% phenol-formaldehyde resin (“novolac” type, Georgia Pacific, Atlanta, GA) in 2-propanol solution was used as carbon source, which was added to above boric acid/H₂O/2-propanol solution to make B/C ratio to 6/7. The mixture was strongly stirred and then stabilized for 2 h.

2.1.2.2 Preparation of ZrB₂-B₄C Composite

The B₄C sols were added to ZrB₂ sols to make the weight percent of B₄C in the range of 1-5 wt%. The mixtures of ZrB₂/B₄C sols were initially concentrated at 35°C by rotary evaporation and then vacuum dried at 140°C for 2 h to ensure removal of all solvent and to produce a porous, brittle powder. The dried material was gently crushed and ground using an alumina mortar and pestle. The ground material was sieved through 150 mesh sieve. The

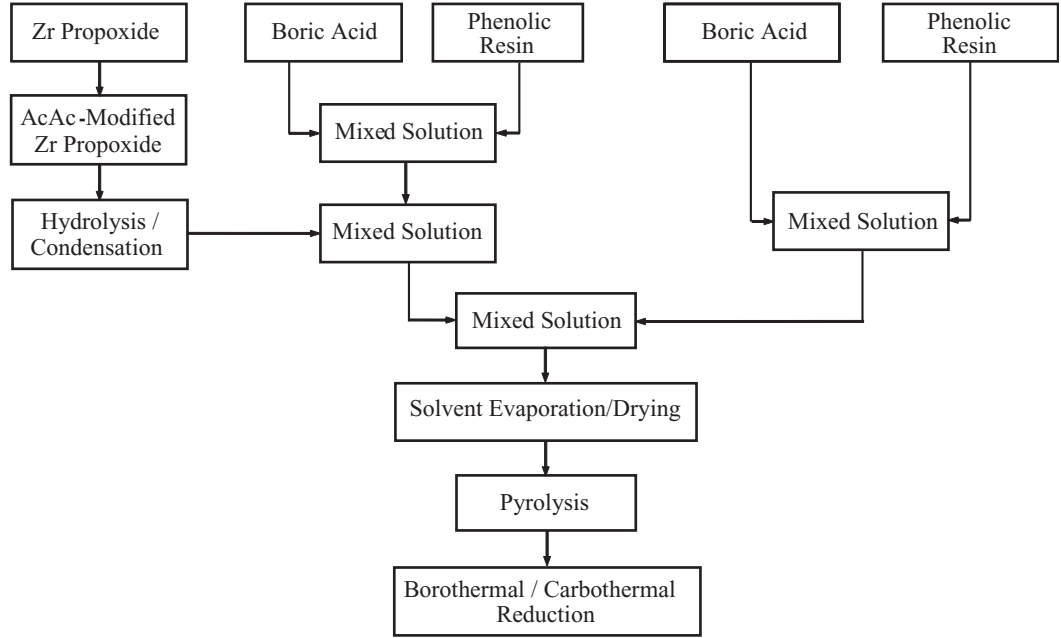


Fig 2.2: Flow chart for synthesis of $\text{ZrB}_2\text{-B}_4\text{C}$ composite.

sieved powder was pyrolyzed at 800-1100°C (2 h, heating rate was 5°C/min) in a flowing argon atmosphere with oxygen partial pressure of 10^{-6} . This resulted in the removal of volatile decomposition products from the precursor materials and the development of fine-scale zirconia/boria/carbon mixtures. The synthesis flow chart is shown in Figure 2.2. The pyrolyzed samples were then heat treated in the range of 1300-1600°C in flowing argon (with oxygen partial pressure of 10^{-6}) in order to carry out the carbothermal reduction reaction to produce $\text{ZrB}_2\text{-B}_4\text{C}$ composite. The weight losses resulting from these heat treatments were recorded.

2.1.3 $\text{ZrB}_2\text{-SiC}$ Composite

2.1.3.1 Preparation of Silicon Carbide (SiC) Sol

The starting Si-containing material was tetraethoxysilane (TEOS, $[\text{Si}(\text{OC}_2\text{H}_5)_4]$, Alfa Aesar, Ward Hill, MA), which was added to a phenol-formaldehyde resin solution to form a C/Si ratio of 2. 2-propanol was used as a mutual solvent. Mixed TEOS/phenolic resin solutions were heated at 65°C for 1 h using acidic conditions with a HNO_3 /TEOS molar ratio of 0.01 and relatively low water content (H_2O /TEOS molar ratio of ~ 2).

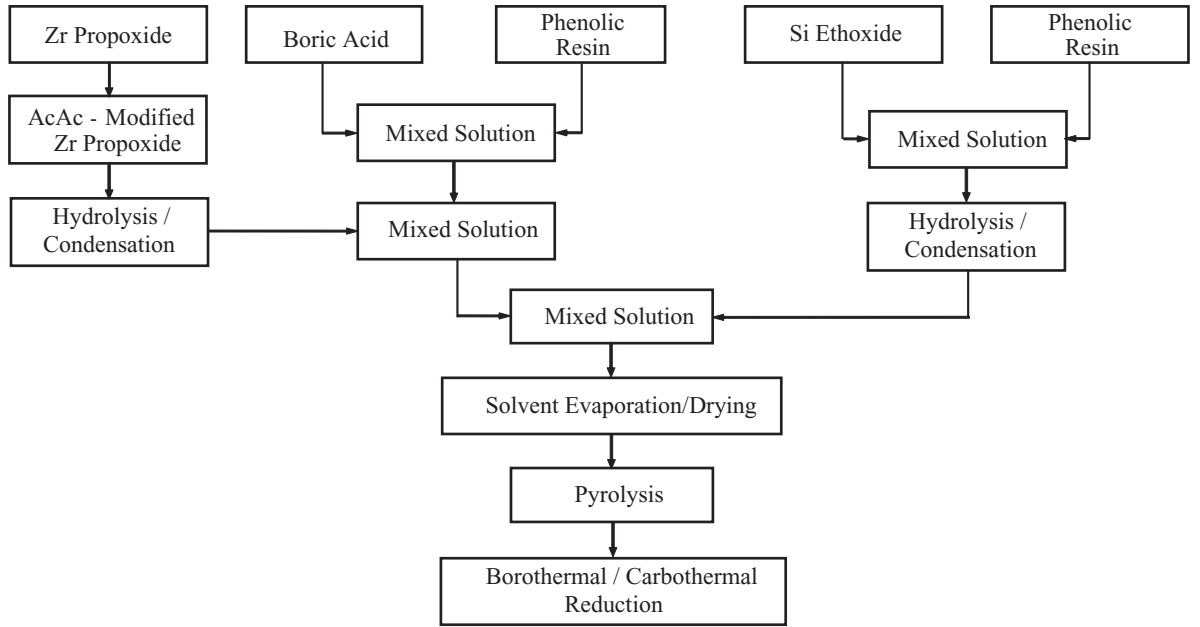


Fig 2.3: Flow chart for synthesis of $\text{ZrB}_2\text{-SiC}$ composite.

2.1.3.2 Preparation of $\text{ZrB}_2\text{-SiC}$ Composite

SiC sol was added to ZrB_2 sol to make an intended final composition of 20 vol% SiC . The mixtures of ZrB_2/SiC sol was then processed in a fashion identical to the synthesis of ZrB_2 , except that the gels were vacuum dried at low temperature ($\sim 40\text{-}70^\circ\text{C}$) for 24 h and then dried at 140°C for 2 h. The powder was pyrolyzed at $800\text{-}1100^\circ\text{C}$ (2 h) in a flowing argon atmosphere with oxygen partial pressure of $10^{-5}\text{-}10^{-6}$ to remove the volatile decomposition products from the precursor materials and developed a mixture of fine-scale zirconia/boria/silica/carbon. The synthesis flow chart is shown in Figure 2.3. The pyrolyzed samples were then heat treated in the range of $1300\text{-}1600^\circ\text{C}$ in flowing argon in order to carry out the borothermal/carbothermal reduction reaction to produce the $\text{ZrB}_2\text{-SiC}$ composite.

2.1.4 $\text{ZrB}_2\text{-TaB}_2$ and $\text{ZrB}_2\text{-TaB}_2\text{-SiC}$ Composite

2.1.4.1 Preparation of $\text{ZrB}_2\text{-TaB}_2$ Composite

Figure 2.4 shows a processing flow diagram of the method to prepare $\text{ZrB}_2/\text{TaB}_2$ composite. The starting Ta-containing material was a tantalum ethoxide solution (i.e., 99.99 wt% $\text{Ta}(\text{OC}_2\text{H}_5)_5$ in ethanol, HC Stark). The tantalum ethoxide was mixed with “acacH”

using molar ratios of 3:1 and 1-propanol was used as a mutual diluent. Zirconium n-propoxide/acacH solution was prepared by the same method.

Tantalum ethoxide/acacH solution was added to zirconium propoxide/acacH solution to make a Zr/Ta ratio of 3. The resulting solutions were initially refluxed at temperatures $\sim 195^\circ\text{C}$ for 2 h, and then partially hydrolyzed (at 50°C for 2 h) under acidic conditions with a HNO_3/Zr molar ratio of 0.27 and an $\text{H}_2\text{O}/\text{Zr}$ molar ratio of 24.

The following steps were the same as the synthesis of pure ZrB_2 , and the synthesis flow chart is shown in Figure 2.4. The dry powder was first pyrolyzed at 800°C (some

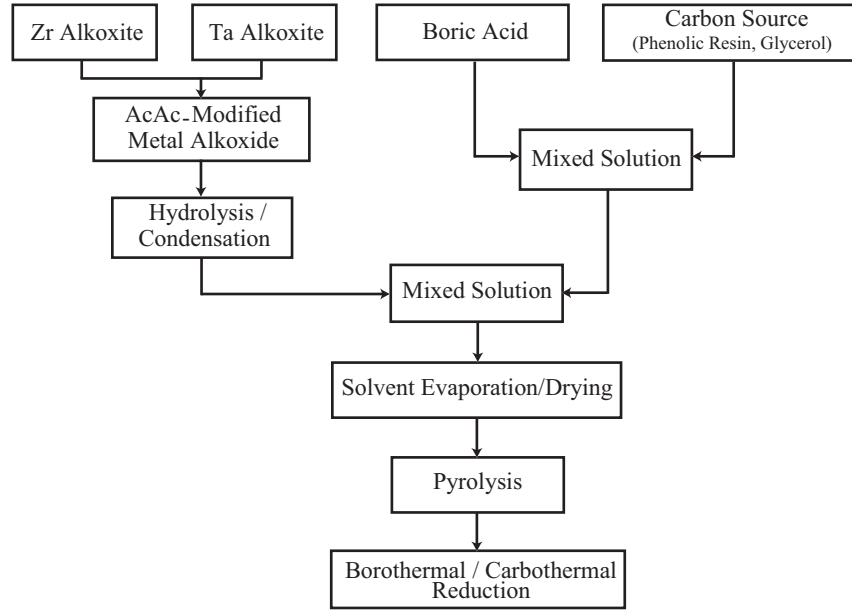


Fig 2.4: Flow chart for synthesis of sample $\text{ZrB}_2\text{-TaB}_2$ composite.

samples were pyrolyzed in the range of $600\text{-}1100^\circ\text{C}$ to obtain the data of weight loss with increasing of temperature) to obtain fine-scale mixtures of $\text{ZrO}_2/\text{Ta}_2\text{O}_5/\text{B}_2\text{O}_3/\text{carbon}$, and then pyrolytic powders were heat treated at $1300\text{-}1400^\circ\text{C}$ (some samples were heat-treated in the range of $1150\text{-}1800^\circ\text{C}$ to obtain the weight loss with temperature) in flowing argon (with oxygen partial pressure of 10^{-6}) in order to carry out the borothermal/carbothermal reduction reaction to produce the $\text{ZrB}_2\text{-TaB}_2$ composite. The weight losses resulting from these heat treatments were recorded.

2.1.4.2 Preparation of ZrB₂-TaB₂-SiC Composite

The solutions of ZrB₂-TaB₂ and SiC were initially prepared according to aforementioned methods, and then SiC sol was added to the ZrB₂-TaB₂ sol to make it 20 vol%. The solutions were then processed identical to the synthesis of ZrB₂, but the powder was vacuum dried at a temperature profile of \sim (50°C-24 h-130°C-2 h). The products of pyrolyzed powder (800-1100°C, 2 h, in a flowing argon atmosphere with oxygen partial pressure of 10^{-5} - 10^{-6}) were fine-scale zirconia/tantania/boria/silica/carbon mixtures. The pyrolyzed samples were then heat treated in the range of 1300-1800°C in flowing argon with oxygen partial pressure of 10^{-6} in order to carry out the borothermal/carbothermal reduction reaction to produce a ZrB₂-TaB₂-SiC composite. The weight losses resulting from these heat treatments were recorded and the powder samples were characterized in the same way as the pure ZrB₂ sample.

2.1.5 Preparation of ZrB₂-TaSi₂ Composite

0.06 mol ZrB₂-based solution was synthesized in the same way as before with a molar ratio of C/Zr = 4.8, B/Zr = 3.0.

3.8g (0.016 mol) TaSi₂ (99.5% pure, -325mesh, CERAC, Milwaukee, WI) (the molar ratio of Zr/Ta=3.75) powder was ball-milled in 2-propanol for 8 h using B₄C as media, and the TaSi₂ slurry was added to the above 0.06 mol ZrB₂-based solution and strong stirring for 1 h. The particle size range of TaSi₂ added to the system was 200 nm-1.2 μ m according to the electron micrograph shown in Figure 2.5. The mixed slurry was initially concentrated by rotary evaporation and then dried at 120°C for 3 h.

The dry powder was first pyrolyzed at 800°C to obtain fine-scale mixtures of TaSi₂/ZrO₂/-B₂O₃/carbon, and then pyrolytic powders were heat treated at 1300-1400°C in flowing argon in order to carry out the borothermal/carbothermal reduction reaction to produce the ZrB₂-TaSi₂ composite. The weight losses resulting from these heat treatments were recorded.

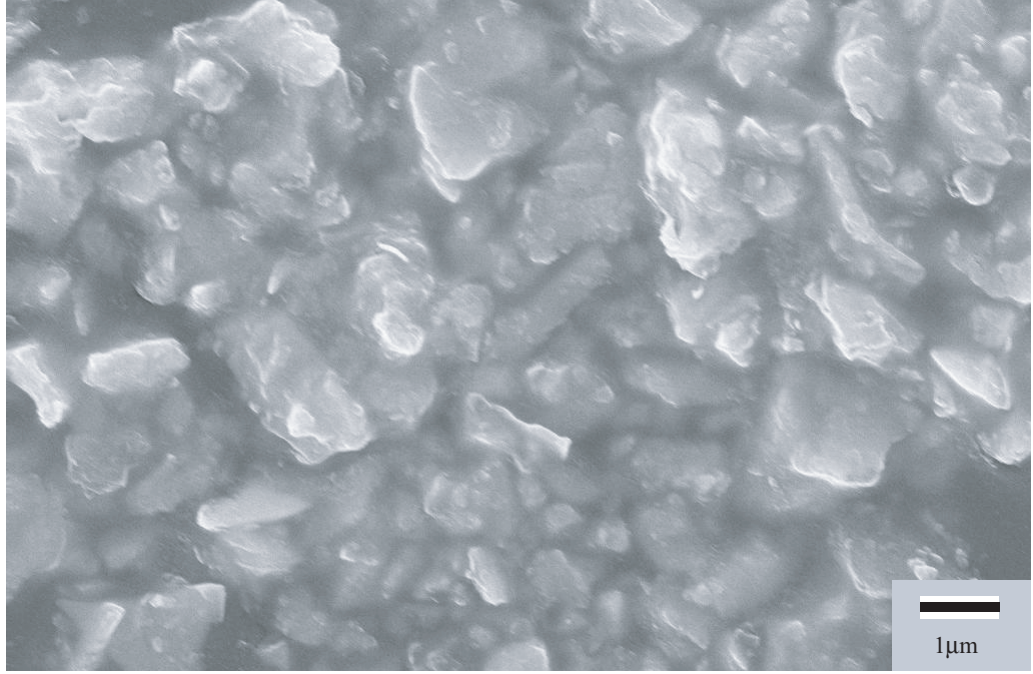


Fig 2.5: SEM Photo of commercial TaSi₂ mixed with synthesized ZrB₂-based solution.

2.2 Pressureless Sintering of Pellets

2.2.1 Preparation for pellet P1-P5 of ZrB₂-B₄C and ZrB₂

2.2.1.1 Preparation of ZrB₂ Powder Compact

The initial composition of the pure ZrB₂ powder used was C/Zr = 5 and B/Zr = 3.0. Dry powder was first pyrolyzed at 1100°C for 2h, and then heat-treated at 1300°C for 2h for carbo/borothermal reduction in flowing argon (partial pressure of oxygen is 10⁻⁶) with a flow rate of ~220 ml/min. The powder after boro/carbothermal reduction reaction was then spex milled for 30 min.

(i) Milling

The purpose of milling was to break the loose agglomerates in ZrB₂ powder after boro/carbothermal reduction, which was done on the spex milling unit in Prof. Thadhani's lab (MSE, Georgia Institute of Technology). ~500 mg of the reacted powder was put into a small milling vessel (coated with WC) with volume of 5 ml. The milling media used in this work was one zirconia ball with diameter of 1.05 cm. The vessel was removed from the milling unit every 2 minutes and the powder was then carefully removed from the inner wall of the vessel.

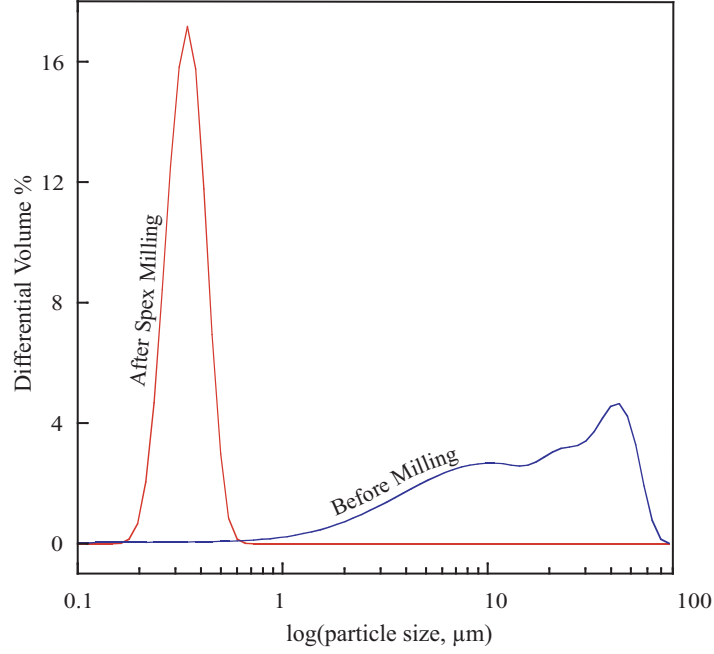


Fig 2.6: Particle size distribution of ZrB_2 after and before spex-mill (measured by LS 13 320).

The total milling time was 30 min. The particle size distributions of samples before and after milling were then measured by the LS 13 320 particle size analyzer and the results are shown in Figure 2.6. The mean size of agglomerates of particle decreased from $21.80 \mu\text{m}$ before spex-milling to $0.35 \mu\text{m}$ after milling. The phase before and after milling was also analyzed by XRD.

(ii) Green pellet preparation

The green pellet was prepared by dry pressing in a 6.44 mm diameter die at 150 MPa for 1 min. Then the pellet was first pyrolyzed at 1150°C for 2 h with a heating rate of $5^\circ\text{C}/\text{min}$ in flowing argon to remove organic, and then sintered in M11 furnace at a temperature profile of: 1350°C -2h- 1600°C -2h to remove boria and 1950°C -3h in flowing argon with oxygen partial pressure of 10^{-6} . The pellet was then sintered in the dilatometer at higher temperature of 2050°C (heating rate was the same as above ZrB_2 -3 wt% B_4C sample, that is $10^\circ\text{C}/\text{min}$; and was held until the expansion rate was below $0.005 \text{ } \%/ \text{min}$).

2.2.1.2 Preparation of $\text{ZrB}_2\text{-B}_4\text{C}$ Pellets

The composite of $\text{ZrB}_2\text{-B}_4\text{C}$ used for sintering was heat-treated at 1400°C for 2 h with initial composition of $\text{C/Zr} = 4.8$, $\text{B/Zr} = 3.0$ for ZrB_2 sol, and $\text{B/C} = 6/7$ for B_4C sol. The powder was first ball-milled for 48 h (in methanol, and ZrO_2 was used as media) and then methanol washed for 30 min (twice).

(i) Ball milling and methanol washing of powder

$\text{ZrB}_2\text{-B}_4\text{C}$ samples (total amount: ~ 1.2 g) were dispersed in methanol in a 20 ml vinyl bottle for ball milling with zirconium oxide as the milling media. After milling for 48 h, the suspension was transferred to a 100 ml flask and sonicated for 30 min. The suspension was then dried through rotary evaporation. Methanol was added back to the flask, and sonicated for another 30 min, and the suspension was put into oven at $\sim 80^\circ\text{C}$ overnight to let the methanol evaporate. The purpose of above methanol washing step was to remove the B_2O_3 on the particle surfaces. The dry powder was taken out from the flask and ground in mortar until they passed through 170 mesh sieve. The phase and particle size distribution before and after milling and methanol washing were analyzed by XRD and a LS 13 320 (Beckman Coulter Inc., measuring range is 40 nm-2000 μm) particle size analyzer, respectively.

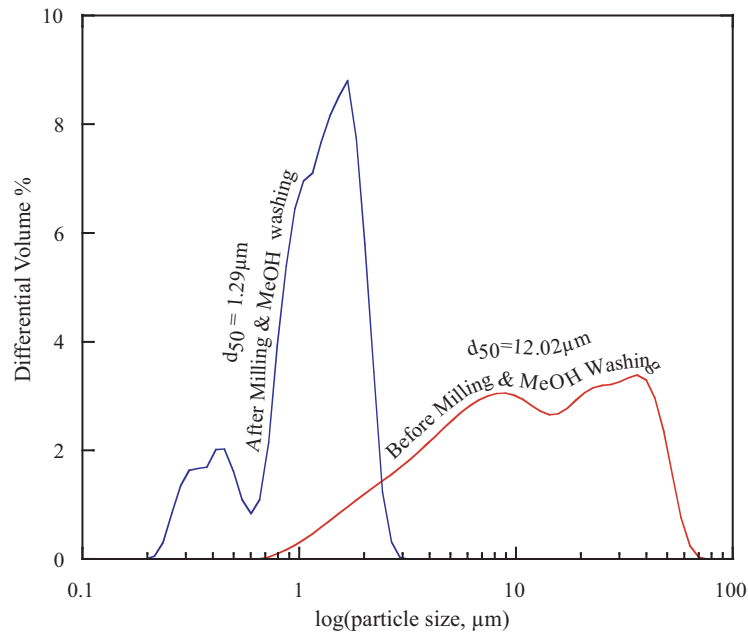


Fig 2.7: Particle Size Distribution of $\text{ZrB}_2\text{-B}_4\text{C}$ powder (measured by LS 13 320) after ball milling 48 h and methanol washing 30min twice.

Figure 2.7 shows the particle size distribution of $\text{ZrB}_2\text{-B}_4\text{C}$ after ball-milling 48 h and methanol washing 60 min. It shows that ball-milling and methanol washing were efficient methods of breaking up agglomerates; the average size of agglomerate was decreased from $12.02\ \mu\text{m}$ to $1.29\ \mu\text{m}$ (analyzed by LS 13 320) after ball-milling and methanol washing.

(ii) Green pellet preparation

Three pellets were prepared by dry pressing at different pressures. Approximately 260 mg of the above $\text{ZrB}_2\text{-3 wt\% B}_4\text{C}$ powder (without binder) was poured into a 6.44 mm diameter die for each pellet and then pressed at 150 MPa (Pellet 1, labeled as P1), 300 MPa (P4), 450 MPa (P5) for 1 min. The dimensions were measured and the green dimensional density was calculated. Then the pellets were heated at $10^\circ\text{C}/\text{min}$ to 2050°C and held at that temperature until the expansion rate was below $0.005\ \%/ \text{min}$ (shown on the controlling computer).

2.2.2 New Procedure for Preparing of Pellets

2.2.2.1 Ball-milling

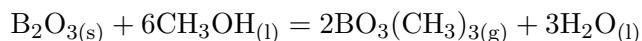
The old method to prepare pellets did not yield high green densities and some oxide impurities, such as ZrO_2 , were introduced into the system during the milling procedure, which may inhibit densification of pellets. A new method was used to avoid such problems.

Approximately 12-18 g B_4C medias (fractures from densified B_4C plate and milled for hours to remove sharp edges, which were then cleaned, dried and used as milling media) was added to a 50 ml vial, and then $\sim 6\ \text{g}$ ZrB_2 powder was added to the same vial. 25-30 ml methanol (ACS grade 99.8%, VWR, West Chester, PA) was added to the vial as a diluting solution. This procedure was done in a glove box under argon atmosphere to avoid introducing oxygen into the system. The 50 ml vial was sealed and then put into a 500 ml polyethylene (PE) bottle which was stuffed with Kimwipe paper to hold the 50 ml vials in their position. The PE bottle was then placed on a milling machine for 60 h to break up the agglomerates.

2.2.2.2 Methanol Washing

The purpose of methanol washing is removing the boron oxide (which may inhibit the densification of ZrB_2) from the system. B_2O_3 reacted with methanol and formed $\text{BO}_3(\text{CH}_3)_3$, which is a gas and be removed from the system by vacuum when connected to rotary evaporator.

The suspension in the 50 ml vial after ball-milling for 60 h was transferred to a 200 ml flask in glove box, and then the flask was connected to the rotary evaporator to remove the solvent at 35°C . Methanol was then added back to the flask with almost dried powder in Glove box, and then the suspension was sonicated (Model VC600, Sonics and Materials Inc., Danbury, CT) for 40 min at 600 watts and 20 kHz frequency. The flask was then connected to rotary evaporator to remove the solvent. This procedure was repeated for 6 times to eliminate the boron oxide on the surface of powder and also break up agglomerates and obtain more uniform powders.



2.2.2.3 Binder Addition

The powder after methanol washing was then further dried in a vacuum oven at 120°C for 3 h and then binder was added to the system which was used to facilitate the dry pressing operation. The binder used to improve strength of pellet was made of 0.02 g/ml polyvinyl alcohol-polyvinyl acetate copolymer (PVA, 99-100 hydrolyzed, with a molecular weight of 11000) and 0.1 g/ml polyethylene glycol (PEG, with molecular weight of 12000). A 40 % solution of Darven 821A (ammonium polyacrylate) was a deflocculant and used to disperse ceramic suspensions to minimize the water content. The polyacrylic acid negatively charged along their length and attach to clay particles and cause them to repel each other. The amounts of binder compared with the weight of dry powder were 3.46 wt% PVA, 0.69 wt% PEG, 0.52 wt% Darven 821A and 60.71 wt% water. All those solutions were added into the dry powder in a 50 ml vinyl bottle in the glove box. The bottle was sealed and put into a 500 ml polyethylene bottle for 6 h ball-milling for better mixing results. The solvents was removed by rotary evaporator after ball milling and then dried in a vacuum oven at 120°C

for 3 h. The dry powder was then ground in an alumina mortar and sieved through a 120 mesh screen.

2.2.2.4 Green Body Preparation

The sieved powders were used to form powder compacts by uniaxial dry pressing. ~ 400 mg powder was put into a stainless steel die with a diameter of 6.4 mm. The die sets were first cleaned using paper tissue, and the inside surfaces were lubricated by a stearic acid/acetone solution which was applied by using a cotton swab. The die with powder was then compacted at 300 MPa for 30 s using a manually operated hydraulic press (Model 3925, Carver Inc., Wabash, IN).

The dimension and weight of the green pellet was measured and the dimension density was calculated, which were normally with relative density of ~ 40 -50 %. The green pellet was then cold isostatic pressed (CIP) at 45000 PSI for 30 s, which increased the relative green density to ~ 55 -60%.

2.2.2.5 Binder Burnout

The pellets after CIP were first heat-treated in a flowing argon atmosphere ($P(\text{O}_2) = 10^{-6}$) to remove the organic binder. The pellets were put on a graphoil boat and loaded into an alumina tube furnace (Model 55031, Lindberg, Watertown, WI). The valve on the downstream end was first closed and the furnace was evacuated to 25 mtorr by a mechanical vacuum pump. Argon was back filled to nearly 1 atm and this procedure was repeated 4 times. The valve on the downstream end was then opened and the argon flow rate was 100 ml/min. The heating rate for debinding was $0.2^\circ\text{C}/\text{min}$ to 500°C , holding for 24 h.

2.2.2.6 Sintering

The pellets after debinding were then sintered at 2020°C for 1 h. For ZrB_2 - TaSi_2 samples, they were only held at 2020°C for 30 min. The heating rate for sintering was $50^\circ\text{C}/\text{min}$ to 1900°C , 20°C to 2000°C , and $5^\circ\text{C}/\text{min}$ to 2020°C . The sintering experiments were operated in a graphite tube furnace M11 (Model M11, Centorr Vacuum Systems, Nashua, NH) with a flowing argon (the oxygen partial pressure in the argon is $\sim 10^{-6}$) rate of 500 ml/min. The

temperature was controlled by pyrometer positioned on the downstream end of the furnace.

2.3 Characterization of Product Powders

2.3.1 Boron Determination

2.3.1.1 Boron Determination by ICP

50 mg ZrB_2 powder was put into the pressure acid digestion bomb (PARR) vessel (inner volume 23 ml), and 2.5 ml H_2SO_4 (volume ratio of $\text{H}_2\text{SO}_4/\text{H}_2\text{O}=1:1$) and 0.5 ml HNO_3 (69-70% in water) was then added to it. The PARR vessel was covered and held 3 h at 70°C . The PARR was taken out from the oven and 0.25 ml HF (49% in water) was added to the vessel after it had been cooled down to room temperature. The PARR was then held at 150°C for 20 h or longer until all powder was dissolved. The solution was transferred to a 50 ml flask and diluted to the mark of the flask. This solution was then sent to the Institute of Papers Science and Technology of GeorgiaTECH for inductively coupled plasma (ICP) analysis.

Inductively Coupled Plasma (ICP) is an analytical technique used for the detection of trace metals in samples. The primary goal of ICP is to get elements to emit characteristic wavelength specific light which can then be measured [1]- [3].

An ICP requires that the elements analyzed to be dissolved in solution. The nebulizer transforms the aqueous solution into an aerosol. The light emitted by the atoms of an element in the ICP must be converted to an electrical signal that can be measured quantitatively. This is accomplished by resolving the light into its component radiation (nearly always by means of a diffraction grating) and then measuring the light intensity with a photomultiplier tube at the specific wavelength for each element line. The light emitted by the atoms or ions in the ICP is converted to electrical signals by the photomultiplier in the spectrometer. The intensity of the electron signal is compared to previous measured intensities of known concentration of the element and a concentration is computed. The standard solution are: Zirconium(0.999g/ml, custom-grade standard, Inorganic Ventures, Inc. Lakewood, NJ), Silicon (1000 μg /ml, ICP-014, ULTRA scientific, N. Kingstone, RI) and Boron (1000 μg /ml, ICP-005, ULTRA scientific, N. Kingstone, RI). Each element will

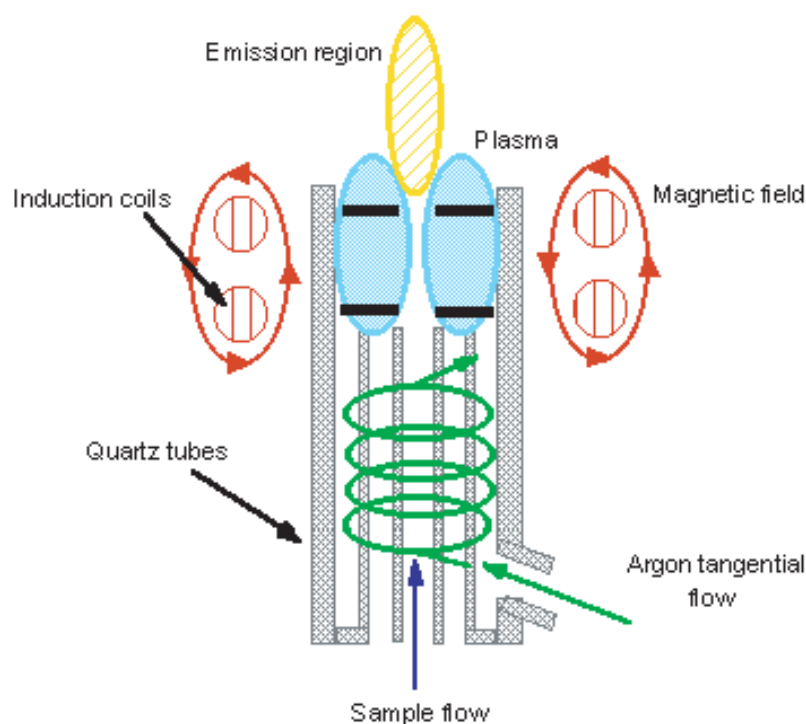


Fig 2.8: Illustration for ICP plasma formation.

have many specific wavelengths in the spectrum which could be used for analysis. Thus, the selection of the best line the analytical application in hand requires considerable experience of ICP wavelengths [5].

ICP hardware shown as in Figure 2.8 is designed to generate plasma, which is a gas in which atoms are present in an ionized state. The basic set up of an ICP consists of three concentric tubes, most often made of silica. These tubes, termed outer loop, intermediate loop, and inner loop, collectively make up the torch of the ICP. The torch is situated within a water-cooled coil of a radio frequency (r.f.) generator. As flowing gases are introduced into the torch, the r.f field is activated and the gas in the coil region is made electrically conductive. This sequence of events forms the plasma. When the sample aerosol punch through the plasma, the high temperature plasma will remove the solvent from the aerosol, leaving the sample as microscopic salt particles, which was first decomposed into a gas of individual molecules (vaporization), and then dissociated into atoms. The atom was excited and ionized, and one of its electrons was promoted to a higher energy level and exit

its characteristic radiation. The light spectra emitted by the excited atoms and ions in the plasma is measured to obtain information about the sample.

2.3.1.2 Boron Determination by D-mannitol Titration

A 20-50 mg sample in an alumina boat was oxidized at 1100°C in the Lindberg alumina tube furnace for 1 h in flowing compressed air (with a flow rate of 75 ml/min), and was then dissolved in boiling water (boiling maintained for 1.5 h). The slurry was filtrated through nylon filter paper under pressure while cooling down to room temperature, and the clear solution was transferred to a 250 ml conical flask with stirring bar. 4-6 drops methyl purple indicator was added to the solution, and the color of the solution became green. 10% H₂SO₄ was added to the solution and make the solution just acid enough to appear as methyl purple (pink), and then 0.1 N NaOH was added to adjust the pH to its green end point.

0.5 ml phenolphthalein indicator and 3 g D-mannitol were added to the solution, and titrated it with CO₂ free ~0.1 N NaOH solution to the pink phenolphthalein end point. After adding mannitol, the solution is in pink color, with the addition of NaOH, solution color gradually changes to green, titration ends when solution color turns into pink again [4].

A blank sample (only de-ionized water was used) was titrated identical as before. The amount of boron can be calculated according to following equation:

$$\text{Boron amount} = (A - B)(N), \text{ mmol}$$

where A = volume of NaOH used for sample, ml

B = volume of NaOH used for blank, ml

N = normality of NaOH, 0.1N

$$\text{Zr amount} = (\text{weight of sample-boron amount} \times 69.62/2)123.22, \text{ mmol}$$

In this method, the oxidized powder was not dispersed uniformly in the boat. As a result, if we only collect the powder in the boat, some boria will be lost, resulting in a low detected boron content. Therefore, both of the sample and boat were placed in boiling water to collect all boria.

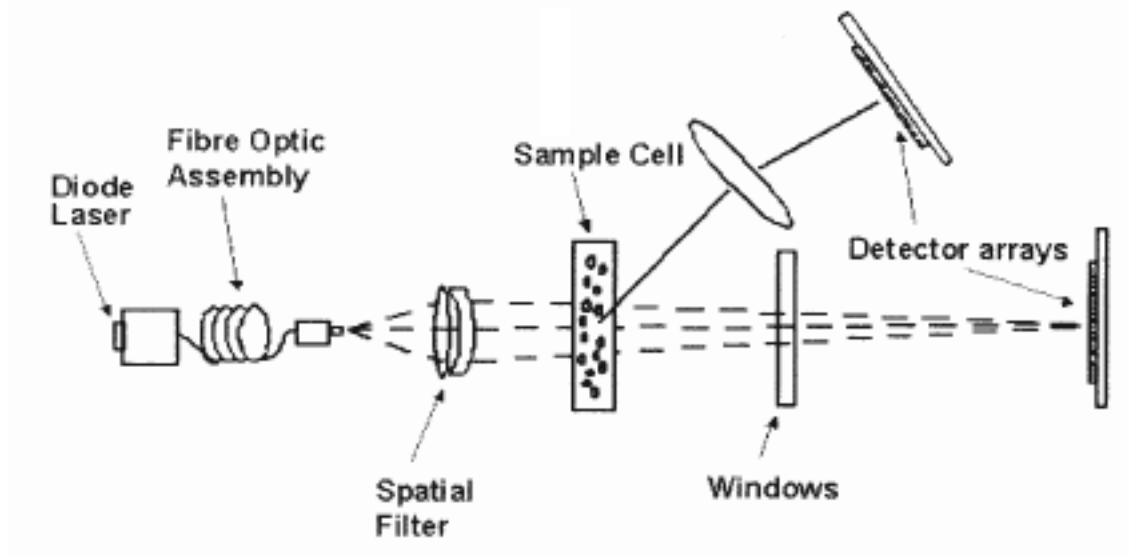


Fig 2.9: Schematic of optical system for particle size analysis. (The figure is reproduced from reference [6]).

2.3.2 Particle Size Analysis using the LS 13 320

The LS 13 320 particle size analyzer (Beckman Coulter Inc., Miami, FL) measures particle size distributions by measuring the pattern of light scattered by the particles in the sample. A schematic of the instrument for the LS 13 320 is shown in Figure 2.9. The basic components of the systems are a monochromatic source of illumination-diode laser, a spatial filter to focus the light beam, a sample chamber to hold the sample and allow the sample interact with the light beam, and an array of photodetectors that record the intensity patterns for the light scattered by the particles.

The pattern of scattered light is called a scattering pattern or scattering function, which is formed by light intensity as a function of scattering angle and affected by particle dimension, particle refractive index, medium refractive index, light wavelength, polarization, particle concentration and particle-particle interaction. Some variables, such as particle refractive index and wavelength are constant for a particular measurement. Optimum range of sample concentration was used to obtain enough scattering light intensity and minimize the noise, particle-particle interaction and multi-scattering.

Fraunhofer theory is simple and do not need know the refractive index of sample, The angle for the first minimum of scattering intensity is simply related to the size by following

equation:

$$\sin\theta = 1.22 \times \lambda/d$$

However, it can only be used for particles that are 1) much larger than the wavelength of the incident light and nontransparent.

When the particle sizes are smaller than the incident light wavelength, a more complex theory - Mie theory need to be used and the refractive index of the sample was needed and its only applicable to spheres. The Mie theory was required for most of the powders characterized in this study and the refractive index we used for ZrB_2 is 1.46.

Measurements of particle size distributions via the light scattering are carried out using dilute particle/liquid suspensions. The concentration is sufficient to provide enough scattered light to reach the detectors with adequate signal-to-noise ratio, but low enough to minimize particle-particle interactions and multiple light scattering. In the LS 13 320 instrument, the suspensions are loaded into a “liquid module” which consists of a sample cell and a circulation system. The sample cell allows the particles in the suspension to be exposed to the illuminating source. The circulation system has a pump which allows the cell to be filled and rinsed automatically. It also keeps particles suspended in the liquid.

The starting materials for preparing the diluted suspension are dry powder of samples needed to be analyzed and D.I. water adjusted to different pH values. Specific amounts (normally ~ 5.0 - 10.00 mg for fine powder, and ~ 30 - 50 mg for coarse powder) were added into ~ 20 ml pH 9.50 (pH was adjusted by adding NH_4OH to D.I. water), D.I. water (D.I. water with pH = 7), pH = 3.5 (adjusted by adding HNO_3) or other pH value. D.I. water with different pH were first used to disperse dry powder to find the pH that the powder was well dispersed and no flocculation occurred during the measurement. The mixture of powder and water was then sonicated (Model VC600, Sonics and Materials Inc., Danbury, CT) for 20 minutes to obtain a well-dispersed suspension. For proper dispersion, the solvent should wet well on the sample and no obvious agglomerates form after sonication.

Prior to the measurements, the liquid module was first rinsed twice with water, which has the same pH value as the water used to disperse the sample, and then filled with the

same water. De-bubbling, alignment, background measurement must be done before measuring the particle size. A de-bubbling step is used to remove the air bubbles from the DI water in the liquid module. Bubbles need to be eliminated because they produce a light scattering pattern that causes incorrect analysis of the particle size distribution for the samples. The alignment aligns the laser beam at the center of the detector array because the laser beam must be precisely positioned to accurately measure the light intensity as a function of scattering angle. The background measurement recorded the light scattering pattern from the liquid and glass sample cell (i.e., with no particles present). It is automatically subtracted from the light scattering pattern of the samples. The diluted powder suspension is then added to the liquid module by using a pipette drop by drop until the desired amount, as indicated by the instrument software. The measurements were repeated and the average data of two results are reported.

2.3.3 Crystallite Size Determination by XRD line Broadening

The crystallite sizes of powders after heat-treatment (pyrolysis or boro/carbothermal reduction) were determined using XRD (Model PW1800, Philips Analytical, Netherlands) data that was collected for phase analysis. The radiation used for the XRD analysis was the $\text{CuK}\alpha$ line with an average wavelength of 1.54184, which was comprised of the $\text{K}\alpha_1$ ($\lambda = 1.54056$) and $\text{K}\alpha_2$ ($\lambda = 1.54439$) double line. XRD data was collected using continuous scan with a step size of 0.02° and scan speed of 0.4 sec/step. The scanning range for 2θ angles was between 20° and 100° .

The crystallite sizes were determined from the broadening of the XRD diffraction lines using the Scherrer equation:

$$D_{hkl} = 0.9\lambda/\beta_{hkl}\cos\theta$$

where D_{hkl} is the thickness of the crystal measured in a direction perpendicular to the (hkl) reflecting planes, λ is the radiation wavelength, θ is the Bragg angle, and β_{hkl} is the true width of the diffraction line at a height where the intensity is one-half of the maximum intensity. Before the determination of half width, the α_2 stripping must be performed first to obtain the true line shape contributed by the $\text{CuK}\alpha_1$ line, whose wavelength is 1.5406Å

(0.15406 nm). Background subtraction was also necessary to obtain the true height of the diffraction line.

Figure 2.10 shows the XRD pattern before and after the automated background subtraction using Powder 2.0 software (Version E 1999-03-03, Bucharest, Romania).

β_{hkl} can be corrected by considering the instrumental broadening b , which was determined from the peak broadening that occurred using a single crystal silicon wafer. The results for peak width from Si XRD pattern are listed in Table 2.1.

Tab 2.1: XRD peak widths of single crystal silicon.

| | | | | | |
|-----------|--------|--------|--------|--------|-------|
| 2θ | 28.667 | 47.524 | 56.331 | 69.346 | 76.57 |
| Width | 0.058 | 0.069 | 0.089 | 0.093 | 0.123 |

Linear interpolation was used to obtain the b values for any angles within the different diffraction angle ranges. The equation used to calculate b are:

$$28.667^\circ < 2\theta < 47.524^\circ \quad b = [0.000583 \times (2\theta - 28.667)] + 0.058$$

$$47.524^\circ < 2\theta < 56.331^\circ \quad b = [0.002270 \times (2\theta - 47.524)] + 0.069$$

$$56.331^\circ < 2\theta < 69.346^\circ \quad b = [0.000307 \times (2\theta - 56.331)] + 0.089$$

$$69.346^\circ < 2\theta < 76.570^\circ \quad b = [0.004150 \times (2\theta - 69.346)] + 0.093$$

$$2\theta > 76.570^\circ \quad b = [0.004150 \times (2\theta - 76.570)] + 0.123$$

After correction, the β_{hkl} can be obtained from the following equation: $\beta_{hkl} = B - b$

where β is the measured width of the sample XRD diffraction line (or Full Width at Half Maximum, FWHM) by performing lorentz fit on chosen peaks of each phase using origin software (version 6.1, OriginLab Corporation, Northampton, MA). Figure 2.11 shows the Lorentz fit for the ZrB_2 peak at diffraction angle of 41.657° .

And then, the crystallite size D_{hkl} (in nm) is given by:

$$D_{hkl} = 0.9 \times 0.15406 / (\beta - b) \times \cos\theta$$

Some significant peak of the phase was chosen for calculating the crystallite size of this phase, and then the average value was obtained as the crystallite size. The calculate

results for ZrB_2 phase in sample $\text{ZrB}_2\text{-SiC}$ composite heat-treated at 1400°C were listed in Table 2.2.

Tab 2.2: ZrB_2 crystallite size determination by XRD diffraction line broadening ($\text{ZrB}_2\text{-SiC}$ composite heat-treated at 1400° for 2 h).

| 2θ | β width of half | H width of single crystal Si | $\beta - H$ | crystallite size nm |
|-----------|--------------------------|---------------------------------|-------------|------------------------|
| 32.757 | 0.20131 | 0.060 | 0.141 | 61.4 |
| 41.813 | 0.23672 | 0.066 | 0.171 | 51.9 |
| 58.319 | 0.25537 | 0.090 | 0.166 | 57.3 |

The average size of ZrB_2 crystal grains is 56.9 nm with standard deviation of 4.7 nm.

2.3.4 Scanning Electron Microscopy

Scanning electron microscopy was used to observe the particle sizes and morphologies of powder samples. The initial step in the sample preparation process was to put some double-sided adhesive-coated graphite tape (S T R Tape, Shinto Paint Company, Japan) onto a cylindrical aluminum-mounting block.

For dry powder which was first dispersed on a weighting paper, and a glass slide was pressed on it to obtain a thin layer of powder, and then the slide with the powder sample of interest was slightly pressed on the tape to transfer the thin layer of powder onto the tape. For suspensions, a drop of slurry was taken out by pipette and then was diluted by methanol. One drop of diluted slurry was dripped on the tape and let the solvent evaporate in air. The whole sample mount was then coated with a thin layer of gold-palladium by sputtering with a gold-palladium target. The sputter coater (Sputter Coater, International Scientific Instruments, England) chamber was evacuated to 0.09 torr. The coater was operated at ~ 20 mA current (1.2 kilovolts) for 2 min in order to coat the sample. The gold-palladium coating prevented the accumulation of charge on the sample during SEM observations.

The experiments were performed by using a field emission SEM (Model 1530, LEO, Thornwood, NY). The acceleration voltage used for normal observation was in the range of 10-20 kV, while the voltage for backscattering observation is 30 kV.

2.3.5 Bulk Density and Open Porosity Measurements by the Archimedes Method

The Archimedes method was used to determine density and porosity of the sintered samples. The pellet was first dried in an air oven at 70°C for 1 h. The dry weight was measured and the pellet was placed in a beaker with water. The beaker was then put onto a heating plate and water was boiled for at least 1 h to promote complete infiltration of water into the pores. The beaker was then removed from the heating plate and cooled to room temperature, taking care that the pellet remained submerged completely under water in the beaker. The suspended weight was recorded by using the density accessory kit set-up (Mettler-Toledo, Inc., 1900 Polaris Parkway, Columbus, OH) as shown in Figure 2.12.

The sample was then taken out of water and the sample surfaces were wiped off by using a Kimwipe paper (Kimberly-Clark, Roswell, GA). The pellet was then immediately placed in a previously weighed vial and the vial was quickly sealed. The vial (with the sample) was weighed and the saturated weight of the sample was determined. This procedure was used in order to minimize changes in the saturated weight of the sample as a result of evaporation of water from the near-surface region of the sample.

The temperature of the water was recorded to the nearest 0.1°C and the density of the water at that temperature was obtained by standard tabulations of water densities. The bulk volume (BV), percentage open porosity (%OP), and the bulk density (BD) for the pellet were then calculated by using the following equations:

$$BV = (SaW - SuW)/DL$$

$$\%OP = ((SaW - DW)/(SaW - SuW))100$$

$$BD = DW/BV$$

where SaW is the saturated weight, SuW is the suspended weight, DL is the density of liquid, and DW is the dry weight.

2.3.6 True Density Measurement by Pycnometer

The same powder used for preparing pellets was heat-treated under the same temperature profile as the sintered pellet, and then the density of the powder was measured using a

pycnometer.

The apparatus used to measuring the density is a density bottle of 10 ml with stopper having a capillary hole. The bottle was first cleaned and dried and the dry weight of the bottle with stopper was measured (W1). ~1-2 g powder (the same powder used for pellet preparation) heat-treated at the same sintering temperature profile was added to the bottle and the weight of the powder and bottle with stopper was measured (W2). D.I. Water was added to fill the bottle completely and the stopper was put on, and then the outside of the bottle was wiped and dried by paper tissue. The weight of bottle with the contents was determined (W3). The bottle was emptied and cleaned, and then only D.I. water was filled into the bottle and the weight was measured as W4.

The density of the powder now can be calculated using the following equation:

$$TD = (W2 - W1)/((W4 - W1) - (W3 - W2))$$

Relative density, RD, (i.e., percentage of the theoretical density of the solid material) were calculated by using the following equation:

$$RD = (BD/TD)100$$

where BD is the bulk density and TD is the true (theoretical) density of the pore-free solid. The bulk density was obtained either by using the geometric dimensions of the sample or the Archimedes method. TD was measured using pycnometer or be calculated as follows:

For example, the composite of ZrB_2 with 3 wt% B_4C , the density of powder can be calculated using the equation:

$$TD = 100/(97/D1 + 3/D2)$$

Where TD is the density of mixed powder, D1 is the density of pure ZrB_2 powder, D2 is the density of pure B_4C powder.

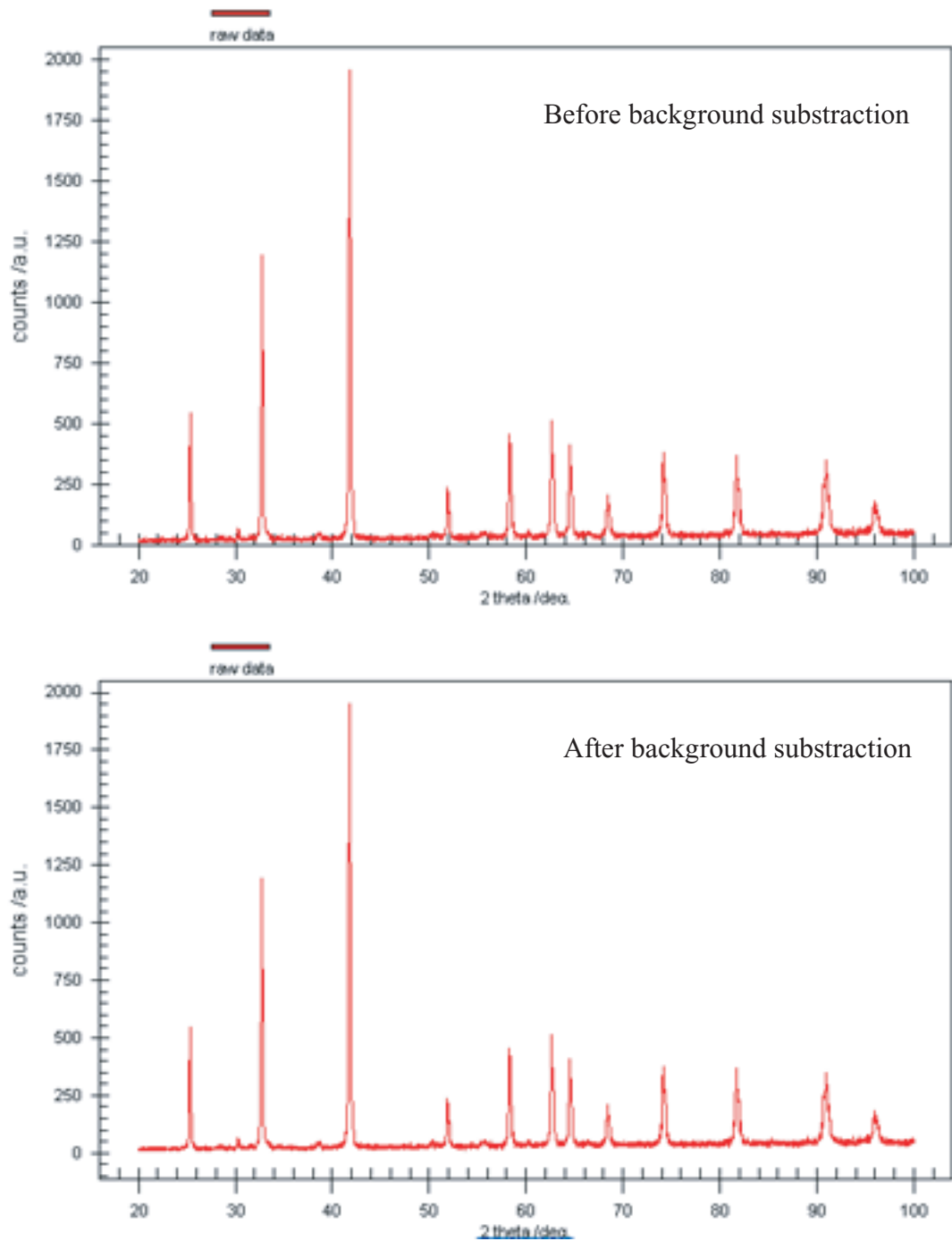


Fig 2.10: XRD pattern of ZrB_2 powder (heat-treated at 1400°C for 2 h) before and after background subtraction.

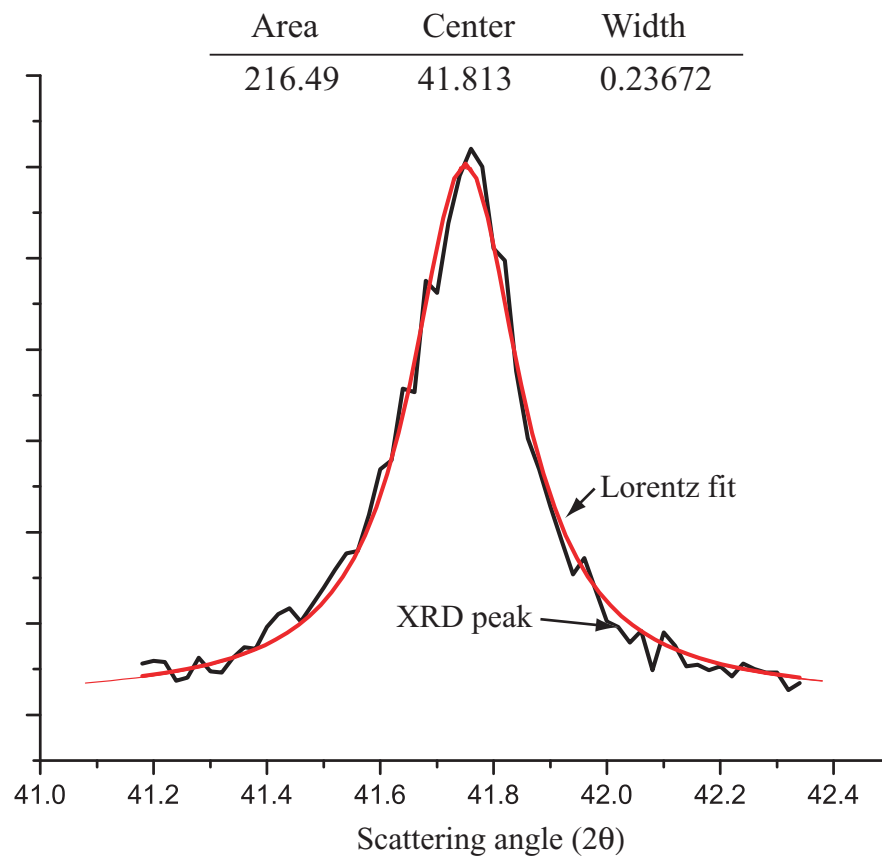


Fig 2.11: Lorentz fit for the peak of ZrB_2 powder at diffraction angle of 41.657° .

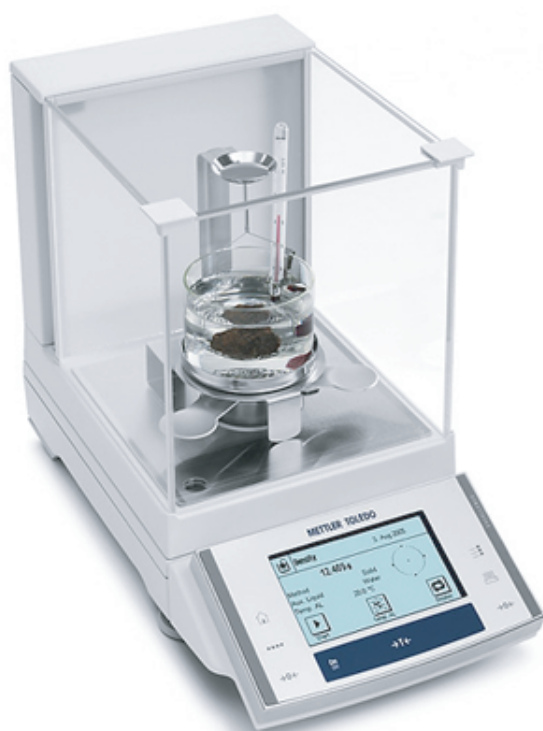


Fig 2.12: Photo of archimedes density measurement set-up.

REFERENCES

2.4 References

- [1] B. Docekal, J. A. C. Broekaert, and T. Graule, "Determination of Impurities in Silicon Carbide Powders," *J. Anal. Chem.*, **342** 113-117 (1992).
- [2] S. Mann, D. Geilenberg, J. A. C. Broekaert, and M. Jansen, "Digestion Methods for Advanced Ceramic Materials and Subsequent Determination of Silicon and Boron by Inductively Plasma Atomic Emission Spectrometry," *J. Anal. atomic Spectrometry*, **12** 975-979 (1997).
- [3] F. Yokota, H. Morikawa, and T. Ishizuka, "Determination of Impurities in Zirconium Disilicide and Zirconium Diboride by Inductively Coupled Plasma Atomic Emission Spectrometry," *Analyst*, **119** [5] 1023-1027 (1994).
- [4] F. D. Snell, C. L. Hilton, *Encyclopedia of Industrial Chemical Analysis*, Interscience Publishers, New york, **7** 384-405.
- [5] C. B. Boss, K. J. Fredeen, *Concepts, Instrumentation, and Techniques in Industively Coupled Plasma Optical Emission Spectrometry*, The Perkin-Elmer Corporation
- [6] LS 13 320 particle size analyzer manual book, Beckman Coulter, Inc.

CHAPTER 3

Research on the synthesis of ZrB_2 and $\text{ZrB}_2\text{-B}_4\text{C}$ powder and their sinterability

3.1 Synthesis of Nanocrystalline Zirconium Diboride by a Solution-based Method

3.1.1 Boron Source Determination

3.1.1.1 Triethyl Borate as Boron Source

Triethyl borate was initially used as the boron source for the synthesis of metal diboride. In the experiment, addition of the triethyl borate was done before or after reflux. However, no metal diboride was formed through borothermal reduction in either case. Therefore, a series of experiments were conducted to determine how boron was lost from the system.

Three solvents (ethanol, 2-propanol, and 1-butanol) were used in the test. Triethyl borate (10 wt%) was dissolved into the solvents. 10 wt% water was slowly added into the solution at a $\text{H}_2\text{O}/\text{B}$ molar ratio of 24. pH was adjusted by adding 1 M HNO_3 or 1 M NH_4OH . The solution was then put into 50°C oven for hydrolysis for 2 h. After hydrolysis, the solution was concentrated on rotary evaporator at 35°C . Experimental results are summarized in Table 3.1.

Tab 3.1: Yield of triethyl borate in different solvents.

| Solvent | EtOH | 2-propanol | 1-butanol |
|-------------------------------|------|------------|-----------|
| B/Solvent (wt%) | 1:9 | 1:9 | 1:9 |
| $\text{H}_2\text{O}/\text{B}$ | 24 | 24 | 24 |
| pH value | 9.92 | 9.42 | 9.59 |
| Yield after evaporation | 0 | 0 | 0 |

Also, triethyl borate was added directly into water and no precipitate was found, and yield after vacuum evaporation is zero. Therefore, triethyl borate is not suitable for use as B source in this synthesis, since in solution, the boron it contributes is part of a volatile

species.

3.1.1.2 Boric Acid as Boron Source

Boric acid (H_3BO_3) has a solubility of ~ 56 g in 1000 ml cold water or cold alcohol (~ 250 g/1000 ml in boiling water or boiling alcohol). A few experiments were conducted to examine the possibility of using boric acid as boron source in our experiments. These experiments are similar to those for triethyl borate. Ethanol, 2-propanol, and 1-butanol were still used as solvents. 4.6 wt% boric acid/water solution was added into these solvents with strong stirring, and the mixture was then evaporated on rotary evaporator at low temperature of 35°C until dry. Dried powder was first put into vacuum furnace at $120\text{-}130^\circ\text{C}$ for 2 h, and then the temperature was increased to 180°C to make sure that the sample decomposed completely. The yield of each sample was calculated and summarized in Table 3.2.

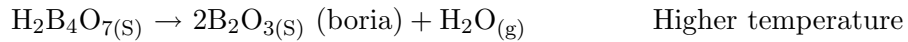
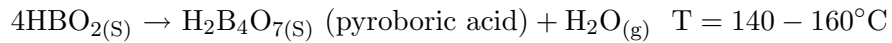
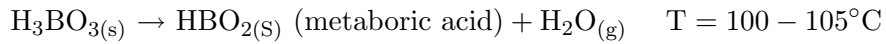
Tab 3.2: Yield of boric acid in different solvents

| Solvent | EtOH | 2-propanol | 1-butanol |
|--|------|---------------|---------------|
| B/Solvent (wt%) | 1:9 | 1:9 | 1:9 |
| $\text{H}_2\text{O}/\text{B}$ | 22 | 22 | 22 |
| pH value | 6.02 | 6.08 | 6.08 |
| B Yield after dry- 120°C | 0 | 99.8 ± 0.1 | 96.5 ± 0.1 |
| B Yield after dry- 180°C | 0 | 99.2 ± 0.1 | 96.2 ± 0.1 |

As can be seen from the table, the boron yield after dry in ethanol is 0 and boric acid was totally lost during evaporation when dissolved into ethanol, probably due to the formation of volatile ethyl borate. For 2-propanol and 1-butanol, the yield of boron after drying at $120\text{-}130^\circ\text{C}$ is nearly 100%, indicating that there is no significant loss of boron during evaporation. Table 3.2 also showed that the yields of boron between 120°C drying and 180°C drying are essentially the same, which suggested that boric acid already decomposed into boria by drying at $120\text{-}130^\circ\text{C}$ for 2h in the vacuum oven. From the above discussion, boric acid showed good retention upon heat treatment in 2-propanol and 1-butanol solvent systems. Therefore, boric acid can be used as boron-bearing source for metal boride synthesis. In our synthesis, 2-propanol was used as solvent.

More experiments were done to understand the thermal decomposition of H_3BO_3 in

TG-DSC (Netzsch Geratebau, STA 409) if boric acid is used as boron-bearing source for ZrB_2 synthesis. As-received boric acid powder was heat-treated at 105, 150, and 250°C for 2h in flowing argon (partial pressure of oxygen is $\sim 10^{-6}$), and the yields were calculated, which were 70.2%, 58.8%, and 56.2%, respectively. Thermal decomposition of boric acid proceeds according to following reactions:



The yields of boric acid decomposed into metaboric acid, pyroboric acid, and boria from the above three reactions were calculated, which are 70.87%, 63.59% and 56.31% respectively.

Figure 3.1 shows the TG-DSC recording of the thermal decomposition of H_3BO_3 in the temperature range from 25°C to 300°C with a slow heating rate (0.5°C/min). It is observed from the plots that there are three stages in the decomposition, with endotherms peaked at 100.4°C, 117.3°C and 150.1°C. The peak at 100.4°C corresponds to the first reaction that formed metaboric acid, and 150.1°C corresponds to the second reaction that formed pyroboric acid. It seems that there is one more decomposition step between the above two reactions, which is shown as a 117.3°C peak. For example, HBO_2 can decompose into $\text{H}_4\text{B}_4\text{O}_6$, and $\text{H}_4\text{B}_4\text{O}_6$ and then further decompose into $\text{H}_2\text{B}_4\text{O}_7$ [1]. The decomposition step to boria (the third reaction) does not show an endothermic peak in Figure 3.1-b, probably because it's a gradual process with relatively wide temperature range.

3.1.2 Preparation of Stoichiometric ZrB_2 Powder using a Solution-based Method

3.1.2.1 Preparation of ZrB_2 Sol

In general, Zr-propoxide undergoes more rapid hydrolysis/condensation reactions than the corresponding Zracac (zirconium pentanedionate), and this may result in uncontrolled precipitation of relatively large precursor particles. Therefore, Zirconium n-propoxide was first refluxed (195°C, 2 h) with 2,4 pentanedione (acacH) in order to partially or fully convert

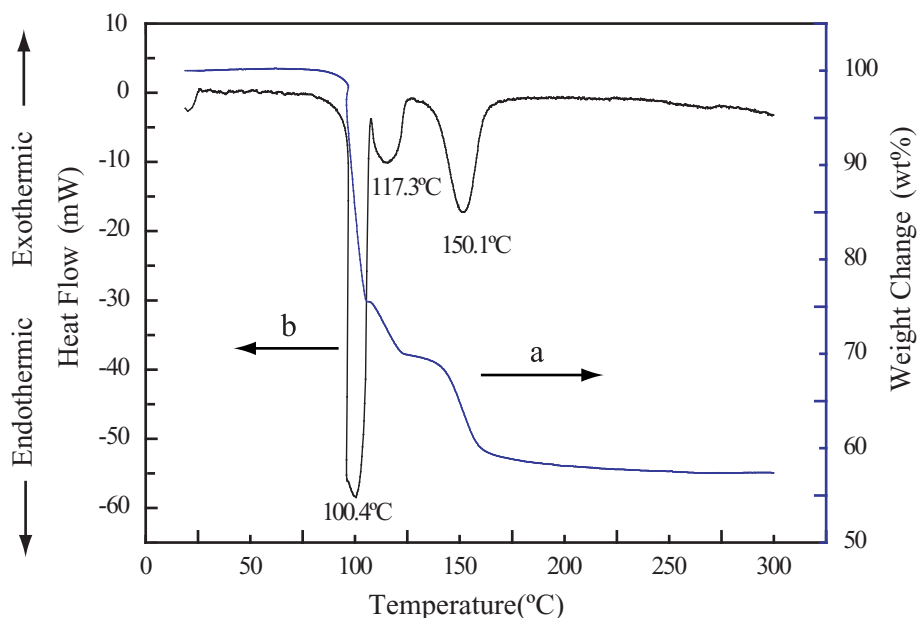


Fig 3.1: TG-DSC measurement of the thermal decomposition of H_3BO_3 in low temperature range.

the zirconium alkoxy groups to a chelated zirconium diketonate (Zracac) structure [5, 3]. The reaction is shown in Figure 3.2 (top two reactions show the same reaction, but reaction 2 displays the structure of the organic compounds). The primary reason for carrying out the replacement reaction is to produce a soluble Zr-organic precursor that allows for greater control over the hydrolysis and condensation reactions that are carried out in a subsequent processing step (also shown in Figure 3.2). Zirconium diketonate (Zracac) is more resistant to hydrolysis compared to the corresponding zirconium propoxide [3], which provides an advantage in subsequent processing because it allows for better control over the C/Zr ratio that is obtained after the high temperature heat treatments.

Figure 3.3a shows Fourier transform infrared spectroscopy (FTIR) spectra obtained from the starting material (Zr-propoxide) and material after refluxing, while Figure 3.3b shows the FTIR spectra of material after refluxing and a commercial Zracac. The figure illustrates that Zr-propoxide reacted with AcAcH and formed Zracac. This is indicated by the close agreement of the spectral results from our self-synthesized sample with a commercial source (shown in Figure 3.3b) and coincident with previous work of Sacks [5].

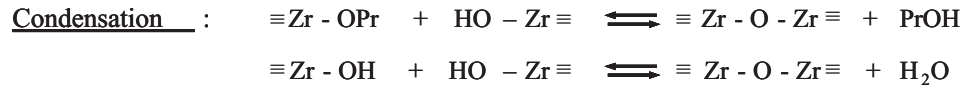
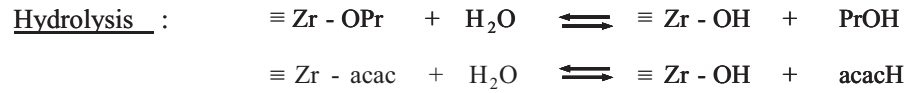
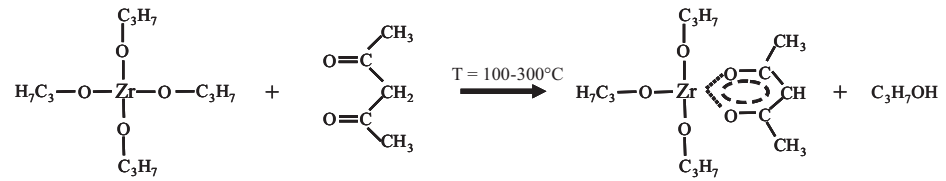


Fig 3.2: Reaction for precursor synthesis.

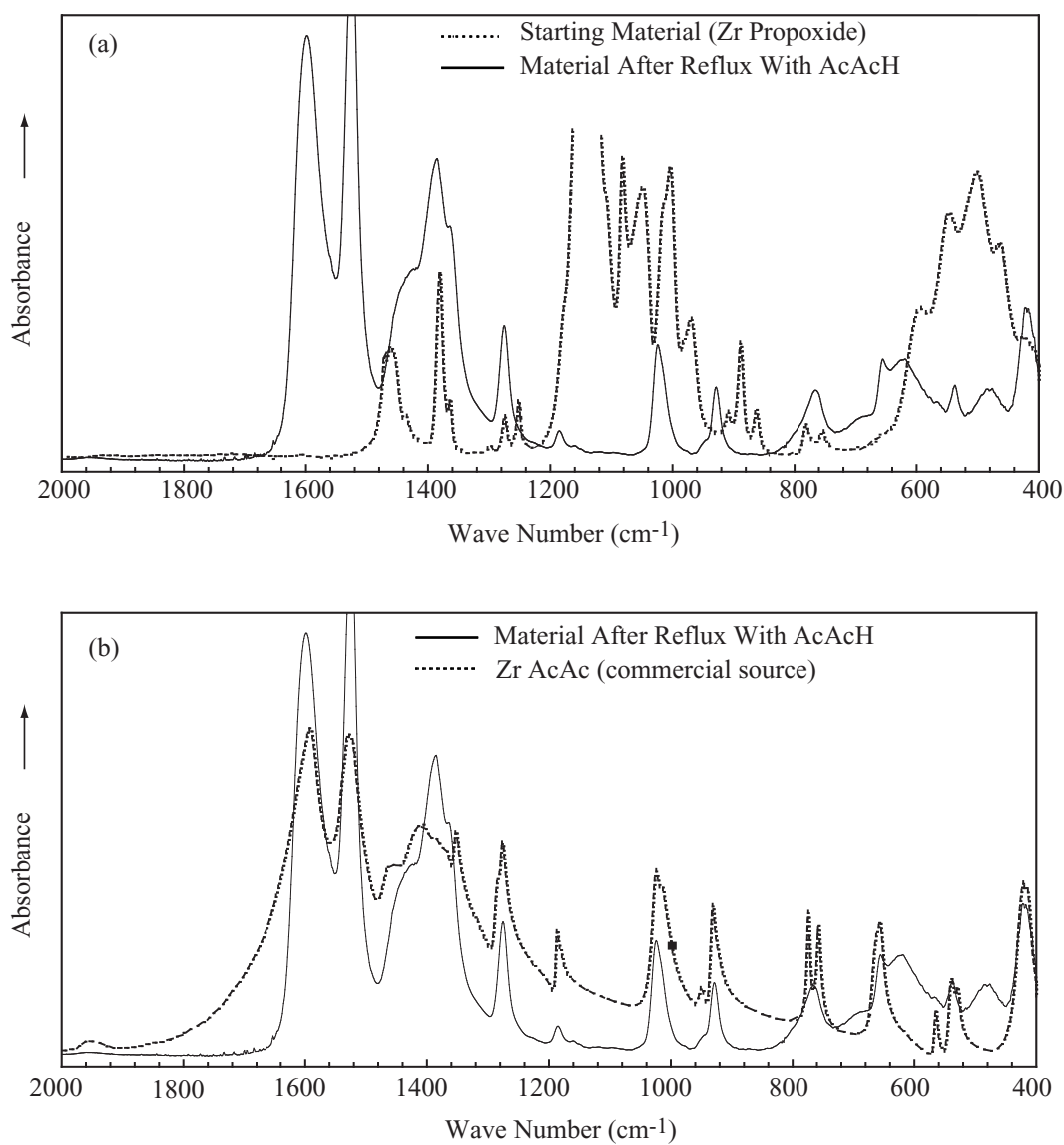
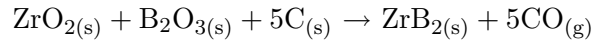


Fig 3.3: FTIR spectra for (a) starting material (Zr-propoxide) and material after being refluxed, (b) material after refluxing and a commercial Zracac.

The next solution processing step was to hydrolyze the Zr-organic precursor through the addition of water. Hydrolysis was required to initiate condensation reactions which, in turn, leads to the build-up of sol species with a three-dimensional structure. Phenolic resin was then added to above solution to increase the C/Zr ratio in the powders used for carbothermal reduction, and boric acid (H_3BO_3 , Alfa Aesar, Ward Hill, MA) was added according to the B/Zr ratio designed for borothermal reduction. After strong stirring, the mixed sols were first concentrated and dried, and then pyrolyzed to decompose the precursors and produce a fine-scale $\text{ZrO}_2/\text{B}_2\text{O}_3/\text{C}$ mixture. ZrB_2 was then produced by borothermal/carbothermal reduction reactions.

3.1.2.2 Heat Treatment for ZrB_2 Preparation

An idealized reaction to produce stoichiometric ZrB_2 by carbothermal/borothermal reduction involves reacting carbon and zirconium in a 5:1 molar ratio. However, the ideal molar ratio of boron to zirconium is $\sim 3:1$ instead of 2:1 as shown in the reaction. Excess boria is required to obtain stoichiometric ZrB_2 because of boria volatilization at elevated temperatures (boiling point of B_2O_3 , i.e. 1 atm vapor pressure, is 1860°C [43]; melting point is 450°C).



$$\Delta G = -44.58 \text{ kJ/mol, at } 1700 \text{ K}$$

Figure 3.4 shows X-ray diffraction (XRD) patterns for a dried precursor powder (prepared by solution processing) and powder samples that were heat treated for 2 h at 800-1400°C in flowing argon. The as-dried precursor was XRD-amorphous. In contrast, the XRD patterns for the pyrolyzed powder after heat-treatment at 800 and 1100°C show monoclinic zirconia (m- ZrO_2) with a trace of tetragonal zirconia (t- ZrO_2). Boria and carbon were also present in the pyrolyzed sample, but these phases were amorphous since they were not detected by XRD. No significant change was observed between samples heat treated at 800°C and 1100°C.

The initial formation of ZrB_2 was observed in the sample that was heat treated at 1200°C for 2 h, and the intensity of t- ZrO_2 increased compared with m- ZrO_2 . ZrB_2 became

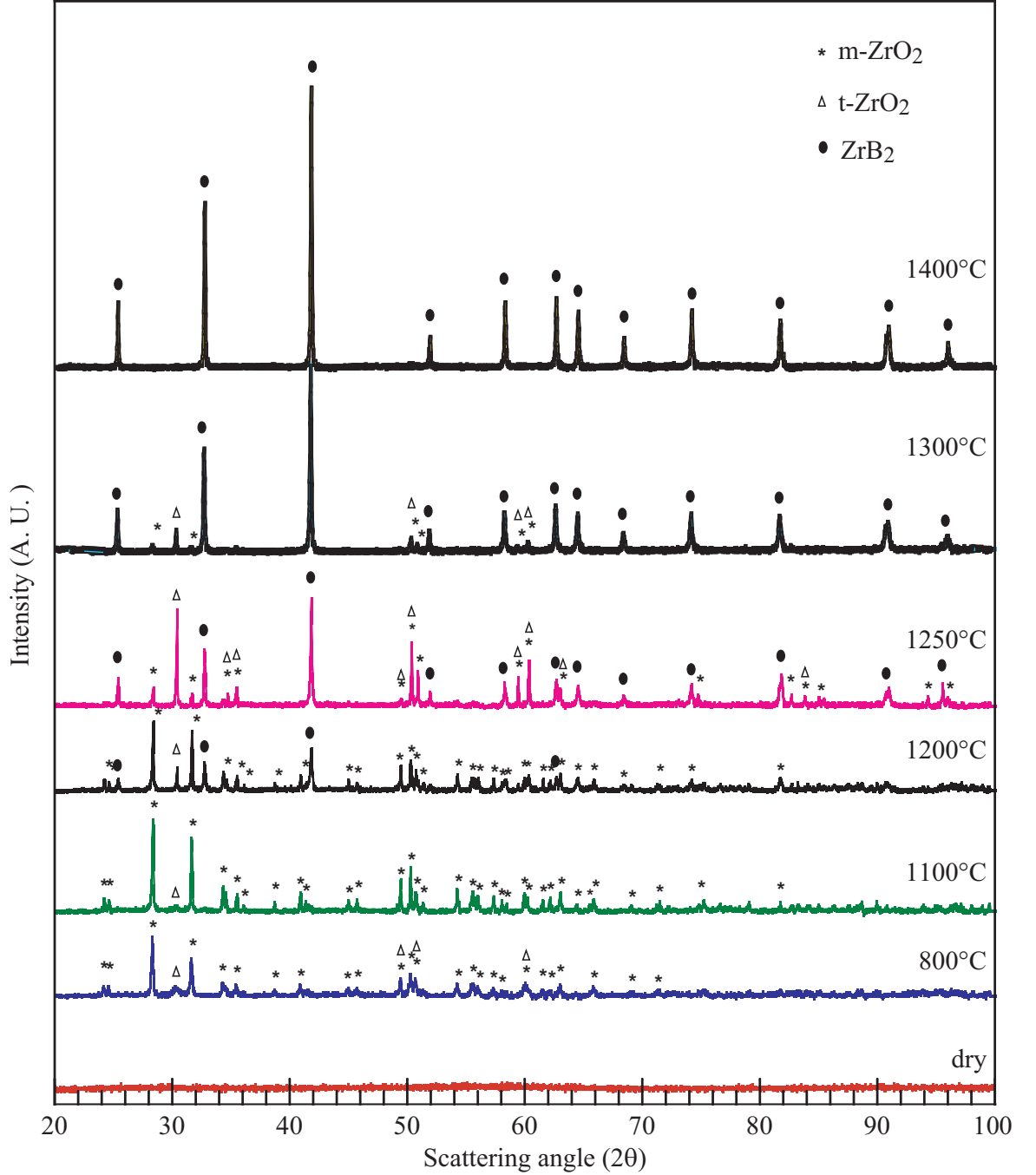


Fig 3.4: XRD patterns for as dried (120°C) and heat treated ZrB_2 powders (800-1400°C for 2 h, $\text{B}/\text{Zr} = 3$, $\text{C}/\text{Zr} = 5.0$). The sample was first pyrolyzed at 800-1100°C in a alumina tube furnace with a heating rate of 5°C/min. The pyrolyzed powder was then further heat-treated in a graphite furnace at higher temperatures of 1200-1400°C (80°C/min to a temperature 75°C lower than final temperature, then 40°C/min to a temperature 35°C lower than final temperature, 20°C/min to a temperature 15°C lower, and 5°C/min to a temperature 5°C lower, and finally 1°C/min to the terminal temperature).

the predominant phase after heat-treatment at 1250°C, although a substantial amount of m-ZrO₂ and t-ZrO₂ were still present. ZrB₂ was the dominant phase after heat-treatment at 1300°C with a trace of m-ZrO₂ and t-ZrO₂. Finally, ZrB₂ became the only crystalline phase in the sample heat treated at 1400°C. The weight loss in Figure 3.5 showed that the borothermal/carbothermal reduction was completed at 1400°C because the weight loss between 1300°C and 1400°C was small.

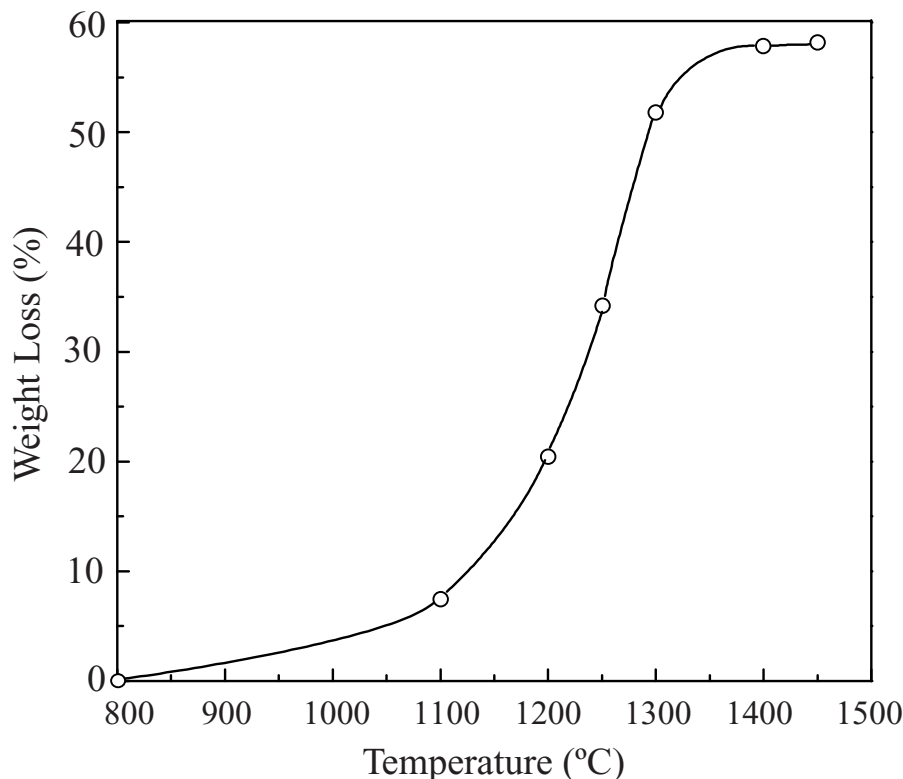


Fig 3.5: Plot of weight loss vs. temperature for an 800°C-pyrolyzed sample.

Figure 3.6 shows the average crystallite sizes (determined by XRD line broadening from Figure 3.4) for each phase (m-ZrO₂, t-ZrO₂, and ZrB₂) as a function of heat treatment temperature. The crystallite sizes for the t-ZrO₂ and m-ZrO₂ phases obtained at 800°C were ~16 nm and ~60 nm, respectively, which suggests that a fine-scale mixture was produced in the pyrolyzed material. The t-ZrO₂ crystallites remained relatively small (~20 nm) in the pyrolyzed samples (800-1100°C). Rapid crystallite growth began with the onset of the carbothermal/borothermal reduction above 1100°C. The crystallite sizes for t-ZrO₂ increased from ~80 nm at 1200°C to over 160 nm at 1300°C, while the crystallite size of

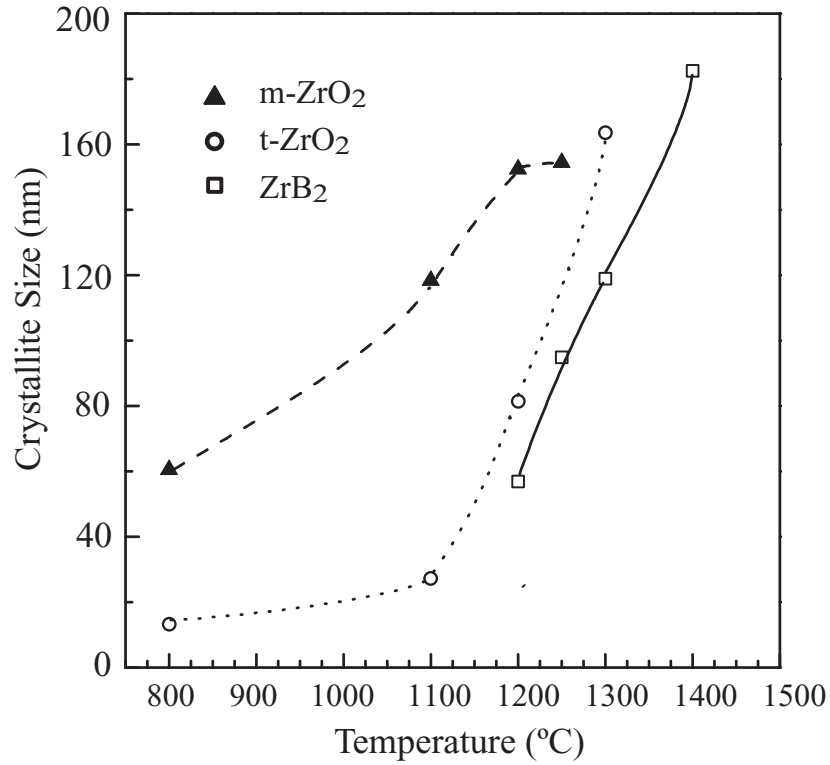


Fig 3.6: Plots of the m-ZrO₂, t-ZrO₂, and ZrB₂ crystallite sizes vs. heat treatment temperature (based on XRD line broadening).

ZrB₂ increased from ~50 nm at 1200°C to over 180 nm at 1400°C.

However, the crystallite size calculated from XRD line broadening is different from those measured from SEM photomicrograph because the particle size obtained from SEM maybe polycrystal. Figure 3.7 shows the SEM photomicrographs of a sample (initial composition was C/Zr = 5.0, B/Zr = 3.0) heat-treated in a alumina-tube furnace with argon flow rate of 150 ml/min, from which we can find that the particle size distribution is 30 nm-1 μ m. Figure 3.8 shows SEM photomicroscope of a sample with same composition but heat-treated in a graphite tube furnace with an argon flow rate of 230 ml/min and the ranges of particle sizes are 20 nm-550 nm.

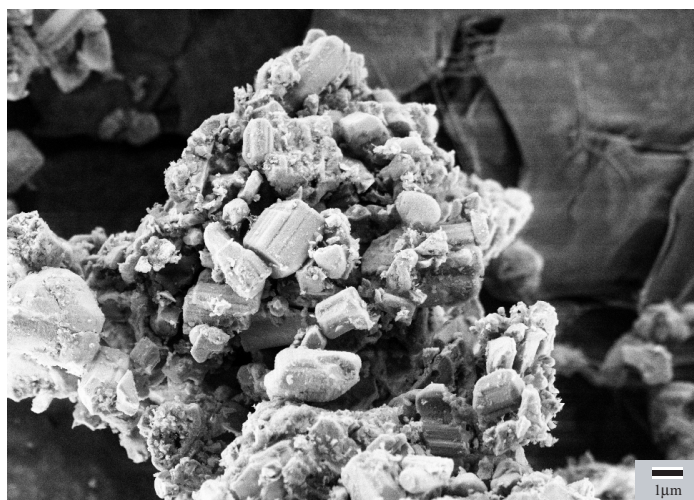


Fig 3.7: SEM photomicrograph of ZrB₂ sample heat-treated at 1400°C for 2 h in an alumina tube furnace.

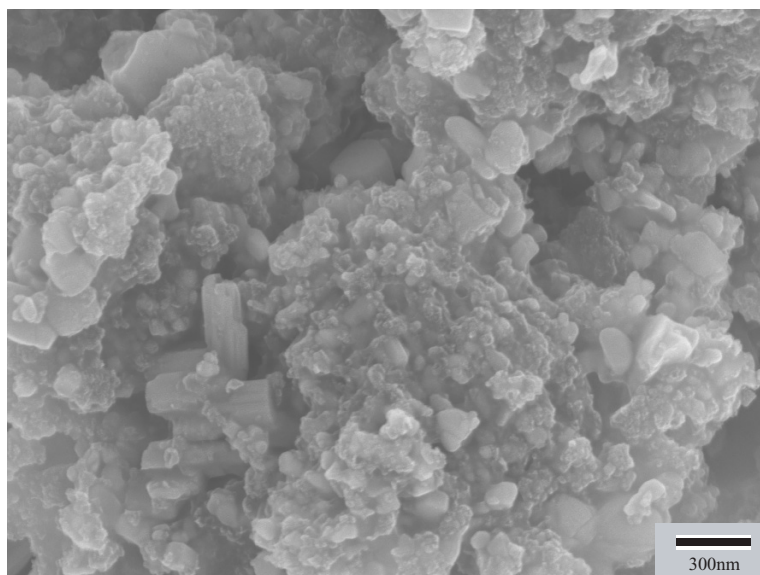


Fig 3.8: SEM photomicrograph of ZrB₂ samples heat-treated at 1400°C for 2 h in a graphite tube furnace.

3.1.2.3 Chemical Analysis of the ZrB_2 Sample after Heat Treatment at 1400°C

The ZrB_2 powder after heat treatment at 1400°C was dissolved in acid by PARR digestion at 150°C for 20 h. Then the solution was diluted for ICP analysis. Table 3.3 shows the results determined by ICP and by D-mannitol titration method (analyzed by ourselves). For D-mannitol titration method, the sample was first oxidized at 1100°C for 1 h in flowing air (weight gain is 162.6% for this sample), and then the powder was dissolved in water for titration by NaOH.

Tab 3.3: Chemical analysis results for ZrB_2 sample heat treated at 1400°C -2 h.

| | B, mmol | Zr, mmol | B/Zr ratio |
|-----------|--------------------|---------------------|-------------------|
| ICP | 0.1906 ± 0.002 | 0.09209 ± 0.002 | 2.069 ± 0.002 |
| Titration | 0.6599 ± 0.02 | 0.3306 ± 0.02 | 1.996 ± 0.02 |

The molar amount of B and Zr determined by different methods was distinct because the solution was diluted differently, but the B/Zr ratio is similar. The ratio of boron to zirconium ($\text{B/Zr} = 2.069$) determined by D-mannitol titration was lower than the ratio of $\text{B/Zr} = 1.996$ determined by ICP. This is reasonable because some boria evaporates during the oxidation.

Carbon content for this sample can be calculated from the yield of oxidation and B/Zr ratio determined by ICP. For this sample prepared at 1400°C -2 h, the oxidation yield is 162.6% (1100°C , 2 h, in flowing air) and the B/Zr ratio is 2.069, which shows a small boron excess. The XRD pattern in Figure 3.4 shows that there is no ZrO_2 phase observed for the sample heat-treated at 1400°C for 2 h. Therefore, we can assume the composition of this powder (after boro/carbothermal reduction) is: 1 mol ZrB_2 , 0.035 mol B_2O_3 (from $\text{B/Zr} = 2.069$), and X mol free carbon, and the oxidized sample composition is 1 mol ZrO_2 and 0.035 mol B_2O_3 , then the yield can be expressed as:

$$(123.2 + 1.035 \times 69.6) / (112.8 + 0.035 \times 69.6 + 12 \times X) = 1.626$$

where 123.2, 69.6, 112.8 and 12 are molecular weights of ZrO_2 , B_2O_3 , ZrB_2 and carbon, respectively. Solving above equation, yields $X = 0.378$, that is, the ratio of free carbon to ZrB_2 is 0.378. From the point view of mass, the content of free carbon to ZrB_2 is 3.89

wt%. Therefore, the product with initial composition of C/Zr = 5 and B/Zr = 3 wasn't pure ZrB₂ but boria and carbon excess although the XRD pattern showed that ZrB₂ was the only crystalline phase after heat treatment at 1400°C for 2 h.

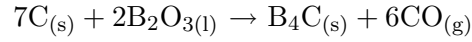
3.1.3 Preparation of the ZrB₂-B₄C Composite

The ZrB₂-B₄C composite was prepared by mixing the ZrB₂ and B₄C sol before concentration. The composition of ZrB₂ sol was the same as before, that is: B/Zr = 3, C/Zr = 5; but some experiments were required to decide upon the composition of B₄C sol.

3.1.3.1 Preparation of B₄C Sol

B₄C sol was prepared by mixing a boron-bearing precursor (boric acid) and a carbon-bearing precursor (phenolic resin) in 2-propanol.

The ideal molar ratio of boron to carbon for preparing stoichiometric B₄C powder should be 4:7 according to the following reaction:



$$\Delta G = -62.29 \text{ kJ/mol, at } 1900 \text{ K}$$

However, the actual ratio of B/Zr should be larger than 4:7 due to the volatility of boron oxide. The compositions we used were: B/C = 4.4/7 and 6/7, and the XRD patterns for those samples heat treatment at 1400°C for 2 h are shown in Figure 3.9. The sample with B/C of 4.4/7 has an almost stoichiometric initial composition, but the XRD (Figure 3.9-a) results showed that there is plenty of free carbon left in this sample after heat treated at 1400°C for 2 h (with a yield of 24.85%). While for the sample with B/C of 6/7 has a much higher yield of B₄C after 1400°C heat-treatment comparing to sample a, that is 61.16%, but the XRD patterns (Figure 3.9-b) showed that almost no boron carbide was formed at 1400°C, therefore this yield is mainly due to the loss of boron. If this is true, then it is calculated that 48.8% of boria was lost during the heat-treatment. Upon further heat treatment at 1600°C, B₄C was the only crystallite phase in the XRD pattern of sample b as shown in Figure 3.9-c. Therefore, excess boria in the initial composition (B/C = 6/7)

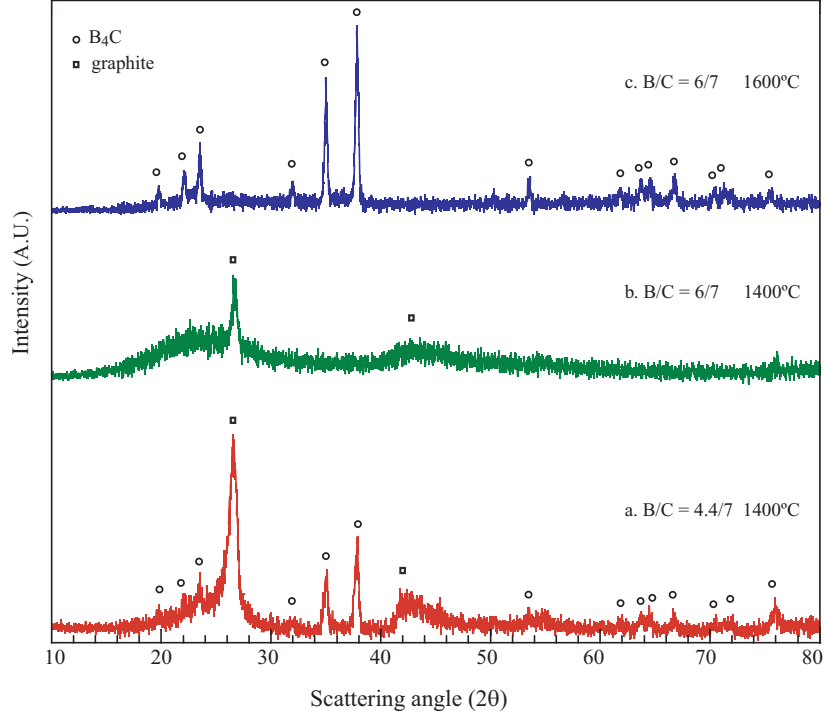


Fig 3.9: XRD patterns for B_4C powder after heat treatment at 1400°C or 1600°C for 2 h. (Initial compositions are indicated in the figure).

was needed to obtain carbon-free B_4C due to significant boria loss via volatilization at temperatures above 1270°C [3].

3.1.3.2 Preparation of ZrB_2 - B_4C composite

The B_4C sol with a composition of $B/C = 6/7$ was added to the ZrB_2 sol, and this mixture was concentrated and dried at 140°C for 3 h. The dry powder was pyrolyzed in an Al_2O_3 -tube furnace at 800°C (heating rate is $5^\circ\text{C}/\text{min}$) for 2 h in flowing $Ar(P(O_2) = 10^{-6})$ to obtain a mixture of boria, zirconia, and amorphous carbon, which was then heat-treated in a graphite furnace (pumped down to ~ 20 mtorr at power output of 31% and then back-filled with argon at output of 50%, the temperature was then controlled automatically with a heating rate of $80^\circ\text{C}/\text{min}$ to a temperature 100°C below the setting temperature, then $40^\circ\text{C}/\text{min}$ to a temperature 50°C lower than setting temperature, then $20^\circ\text{C}/\text{min}$ to a temperature 10°C lower than setting temperature, $5^\circ\text{C}/\text{min}$ to a temperature 5°C lower than setting temperature, finally $1^\circ\text{C}/\text{min}$ to the set temperature) in flowing argon ($P(O_2) = 10^{-6}$) of 0.5 l/h at temperature of 1300°C or 1400°C for boro/carbothermal reduction.

The XRD pattern and yields of powder after heat-treatment at 1300°C or 1400°C for 2 h are shown in Figure 3.10 and Table 3.4, respectively.

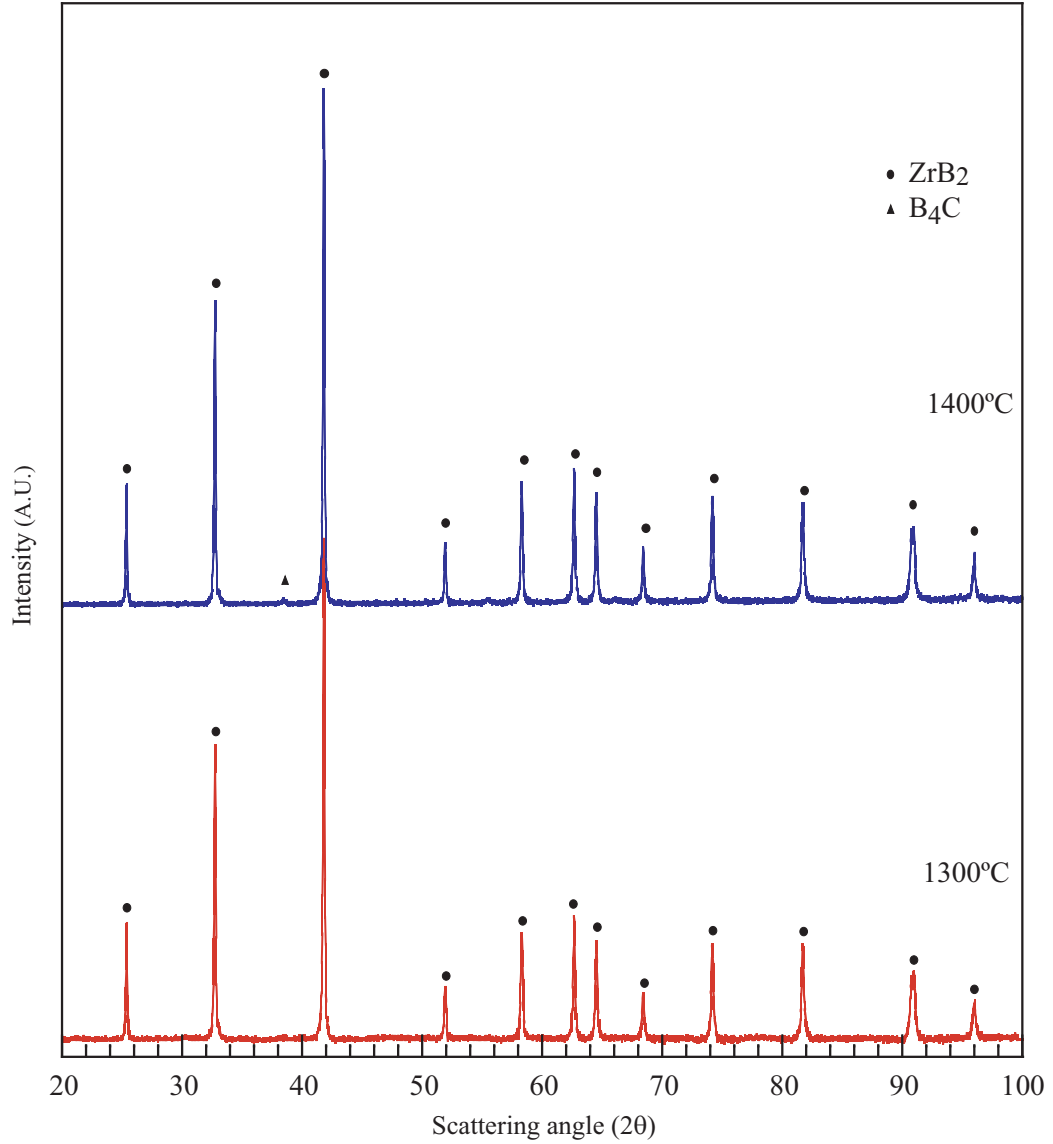


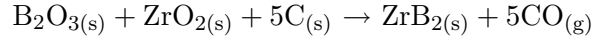
Fig 3.10: XRD patterns for $\text{ZrB}_2\text{-B}_4\text{C}$ powder after boro/carbothermal reduction. Specimens were soaked at 180°C for 2h to eliminate moisture, heated at 5°C/min to 800°C, and soaked 2h for pyrolysis. Specimens were then placed in a graphite furnace and then heated to a) 1300 °C or b) 1400°C and soaked for 2h.

From the yield information, it is interesting to notice that the yields were similar for both heat-treatment at 1300°C or 1400°C, which indicates that the boro/carbothermal reduction had been completed at 1300°C because there is no further weight loss when heat-treated at higher temperature (1400°C). The weight loss in the $\text{ZrO}_2/\text{C}/\text{B}_2\text{O}_3$ system after

Tab 3.4: Heat-treatment results for sample ZB-BC1 (Crystal size determined by XRD line broadening).

| Sample | Heat-treatment condition | Yield, wt% | Crystal size, nm |
|--|--------------------------|---------------|--------------------------|
| ZrB ₂ -3 wt%B ₄ C, | 800°C, 2h | 66.47 | |
| (ZB sol:B/Zr = 3,C/Zr = 5) | 1300°C, 2h | 28.97 | ZB:99.6±4.3,BC:21.8±5.7 |
| (BC sol:B/C=6/7) | 1400°C, 2h | 28.85 | ZB:128.1±7.1,BC:31.5±7.3 |

the above heat-treatments comes from two sources: the release of CO due to carbothermal or borothermal reaction, and the loss of B₂O₃ due to volatilization (and the removal via flowing argon). When the boro/carbothermal reduction was completed, there was no CO produced, therefore, no more weight loss happened even though the sample was further heat-treated. The composition for ZrB₂ sol is: molar ratio of B/Zr = 3, C/Zr = 5, which is boron rich to account for B₂O₃ volatility.



The similarity of XRD patterns in Figure 3.10 proved this conclusion, and there was no more phase development when sample was further heat-treated at higher temperature than 1400°C, but crystal growth. The dominant phases in both of the XRD patterns are ZrB₂, with little amount (weak peak) of B₄C. The particle sizes of ZrB₂ and B₄C are ~700 nm and ~20 nm, respectively determined from the SEM micrograph shown in Figure 3.11. The EDS spectra for large particles showed that they are ZrB₂ phase, while the dominant elements in EDS for small particle are C and Zr, however, there is no ZrC peak observed in its XRD pattern. However, the EDS is not good to tell B and C, while the Zr peak may from the background of the small particle, therefore, the small particle should be B₄C phase. Some oxygen peaks are also observed in EDS patterns.

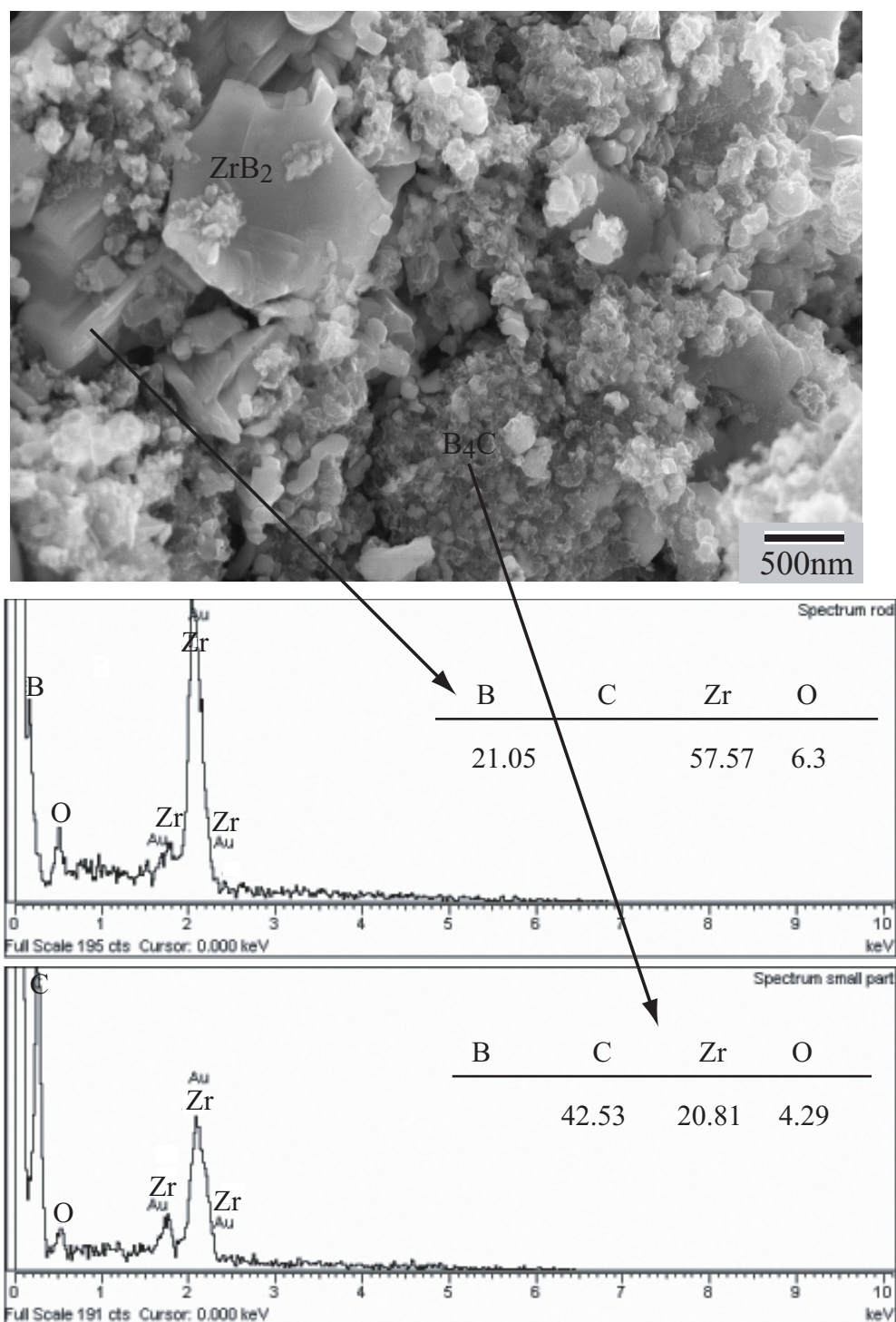


Fig 3.11: SEM photo and EDS of ZrB₂-1wt%B₄C sample heat-treatment at 1400°C for 2 h in a graphite tube furnace.

3.2 *Study on the sinterability of ZrB₂ and ZrB₂-B₄C Mixture*

In this section, the sinterability of pure ZrB₂ powder is compared with a ZrB₂-3 wt% B₄C composite.

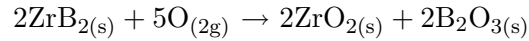
3.2.1 Sintering of ZrB₂ and ZrB₂-B₄C in a Dilatometer

3.2.1.1 Green pellet preparation

1. Preparation of ZrB₂-B₄C Composite Pellet

ZrB₂-B₄C composite heat-treated at 1400°C for 2 h with initial composition of C/Zr = 4.8, B/Zr = 3.0 for ZrB₂ sol, and B/C = 6/7 for B₄C sol was used for sintering. The powder was first ball-milled for 48 h (in methanol, and ZrO₂ was used as media) and then methanol washed for 30 min (twice). The suspension was then dried at ~80°C for dry-pressing and XRD measurement.

The XRD results are shown in Figure 3.12, which implies that some ZrO₂ phase with crystalline size of ~30 nm (the crystal size of ZrB₂ and B₄C after ball-milling were ~64.4 nm and ~27.9 nm (from XRD pattern broadening)) was introduced to the system after the ball-milling compared with its XRD pattern before ball-milling as shown in Figure 3.10-b. The source of the zirconium oxide maybe: (1)the ZrO₂ balls which were used as ball-milling media. (2)The mechanical energy during ball-milling resulted in the oxidation of ZrB₂ according to the reaction:



$$\Delta G = -3828.57 \text{ kJ/mol, at } 298.15 \text{ K, } P(\text{O}_2) = 7 \times 10^{-135}$$

which is highly reactive even at room temperature. The powder and methanol was processed in air atmosphere and ~10 ml air was closed into the bottle with 1.2 g powder. The glass-layer formed on the ZrB₂ surface to protect it from further oxidation was removed by reacting with methanol, and can not protect the ZrB₂ from oxidation. Therefore, significant peaks for ZrO₂ were observed for powder after ball-milling and methanol washing when processed in air.

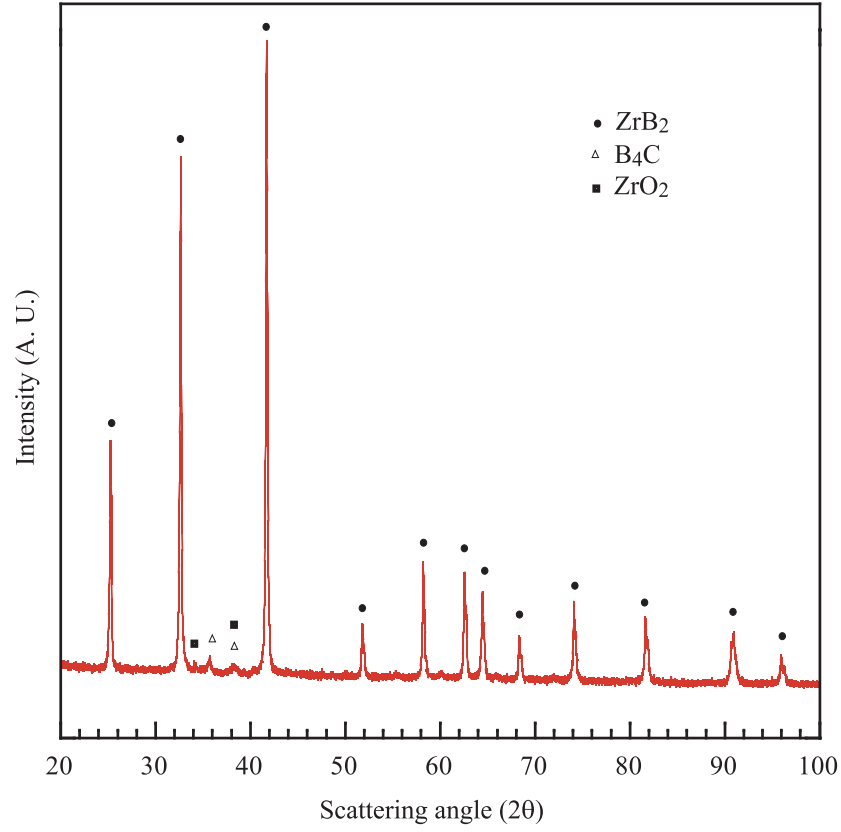


Fig 3.12: XRD pattern for $\text{ZrB}_2\text{-B}_4\text{C}$ powder after ball milling 48 h and methanol washing 30min twice.

Three pellets were prepared by dry pressing at three different pressures of 150 MPa (P1), 300 MPa (P4) and 450 MPa (P5) for 1 min. The dimensions were measured and the green density was calculated. The green density for this sample was low may due to its large differnt of particle size (10 nm to 1 μm) and the shape. Much large ZrB_2 particles are not sphere but flake or prism as shown in Figure 3.11. Increasing pressure from 300 MPa to 450 MPa did not increase the green density, as shown in Table 3.5. The relative green density of pellet prepared at 300 MPa and 450 MPa were almost the same, $\sim 37\%$.

The SEM picture of the $\text{ZrB}_2\text{-3 wt\% B}_4\text{C}$ pellet pressed at 150 MPa is shown in Figure 3.13. Particle sizes ranged from 5-800 nm and there are some large particles with flake shape.

2. Preparation of the $\text{ZrB}_2\text{-1300}^\circ\text{C-2h}$ sample

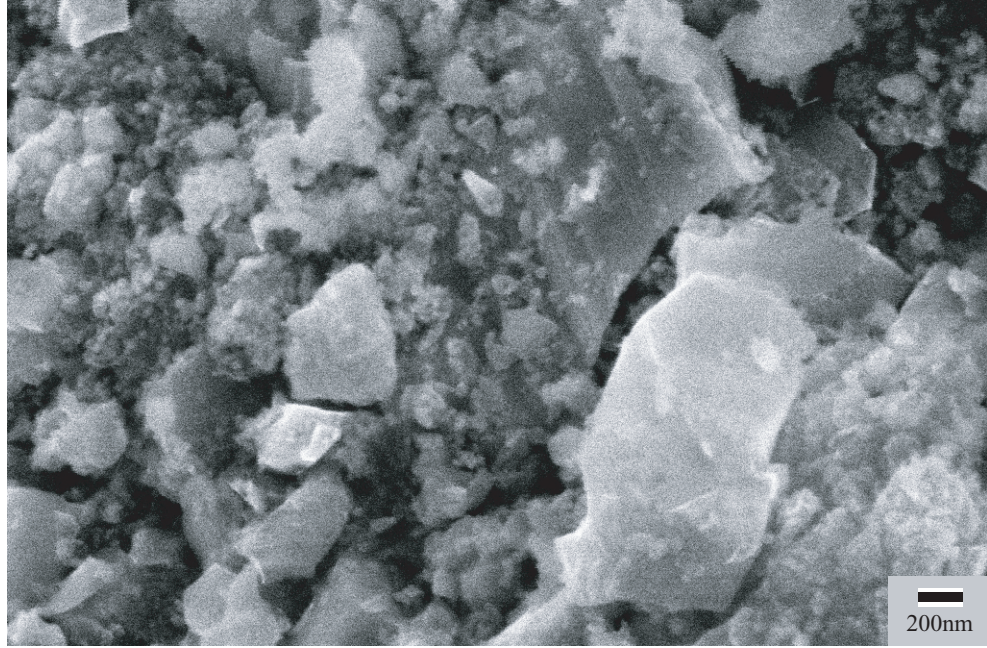


Fig 3.13: SEM of the cross-section of ZrB_2 -3 wt% B_4C green pellet (150 MPa, 1 min) fracture.

The ZrB_2 powder used for sintering was the powder heat-treated at 1300°C for 2 h with initial composition of $\text{C}/\text{Zr} = 5$ and $\text{B}/\text{Zr} = 3.0$. The mean particle size after spex-milling for 30 min are $0.35\ \mu\text{m}$ as shown in Figure 2.6, which was even smaller than the ZrB_2 - B_4C powder ($1.29\ \mu\text{m}$ as shown in Figure 2.7). However, surprisingly, the relative density for green pellet of this ZrB_2 sample was 54% although it was only pressed at 150 MPa for 1 min, much higher than the one for ZrB_2 - B_4C powders ($<37\%$).

The XRD patterns of ZrB_2 powder before and after spex milling are shown in Figure 3.14. The dominant phase before milling was ZrB_2 (crystallite size was 126.7 nm, determined by XRD line broadening) with a trace of t-ZrO_2 . While after milling, WC phase was introduced into the system which came from the coating inside the milling vessel, but the peak for the zirconia phase almost disappeared. The WC may be the reason why the relative density is high for this sample because the theoretical density for calculation we used is that of ZrB_2 , which is $6.085\ \text{g}/\text{cm}^3$, while the density for WC is $15.4\ \text{g}/\text{cm}^3$. The relative density of the ZrB_2 green pellet decreased to 52%, if

Tab 3.5: Dimension and density of pellets (P1:pressure-150 MPa; P4-pressure-300 MPa; P5-pressure-450 MPa. where, ϕ is the diameter of pellets, δ is the thickness of pellets.

| Sample | Condition | Dimension and density | | | | |
|------------------|----------------------|-----------------------|------------------|-----------|-------------------------------|------------------------|
| | | ϕ , mm | δ , mm | Wt, mg | Density, g/cm ³ | Relative density, % |
| ZB-3wt%BC,P1 | Green | 6.59 | 3.92 | 264.03 | 1.98 | 33.83 |
| | Sinter at 2050°C,2 h | 5.02 | 3.01 | 231.41 | 3.89 | 66.66 |
| ZB-3wt%BC,P4 | Green | 6.60 | 3.29 | 243.27 | 2.16 | 37.06 |
| | Sinter at 2050°C,2 h | 5.05 | 2.56 | 215.19 | 4.20 | 71.90 |
| ZB-3wt%BC,P5 | Green | 6.62 | 3.47 | 259.92 | 2.18 | 37.28 |
| | Sinter at 2050°C,2 h | 5.07 | 2.70 | 230.53 | 4.23 | 72.43 |
| ZrB ₂ | Green | 6.45 | 2.47 | 265.54 | 3.29 | 54.10 |
| | 1150°C,2h,Lind | 6.45 | 2.48 | 255.72 | 3.17 | 52.03 |
| | 1600°C-2h,M11 | 6.35 | 2.42 | 224.94 | 2.94 | 48.26 |
| | 1950°C,3h,M11 | 6.06 | 2.32 | 223.62 | 3.34 | 54.95 |
| | 2050°C,2h | 5.83 | 2.27 | 223.59 | 3.70 | 60.80 |

5 wt% WC was introduced to the system.

The green pellet was first pyrolyzed at 1150°C for 2 h to remove organic, and then sintered in the graphite furnace (Centorr M11) at a temperature profile of 1350°C-2 h-1600°C-2 h to remove boria and then held at 1950°C for 3 h. However, the relative density decreased when the pellet was sintered at temperatures lower than 1600°C, and the relative density after further sintering at 1950°C for 3 h was similar to green density. The total dimensional shrinkage for the pellet was only ~ 6 %.

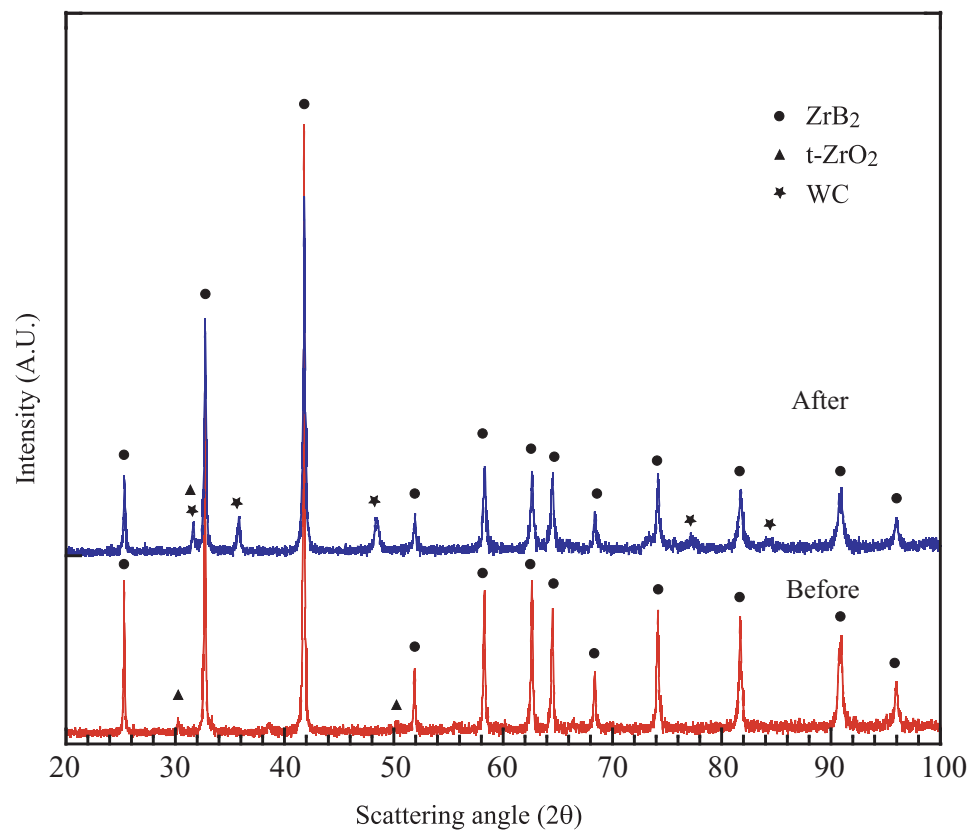


Fig 3.14: XRD pattern of ZrB_2 (1300°C-2h-M11) after and before spex-mill.

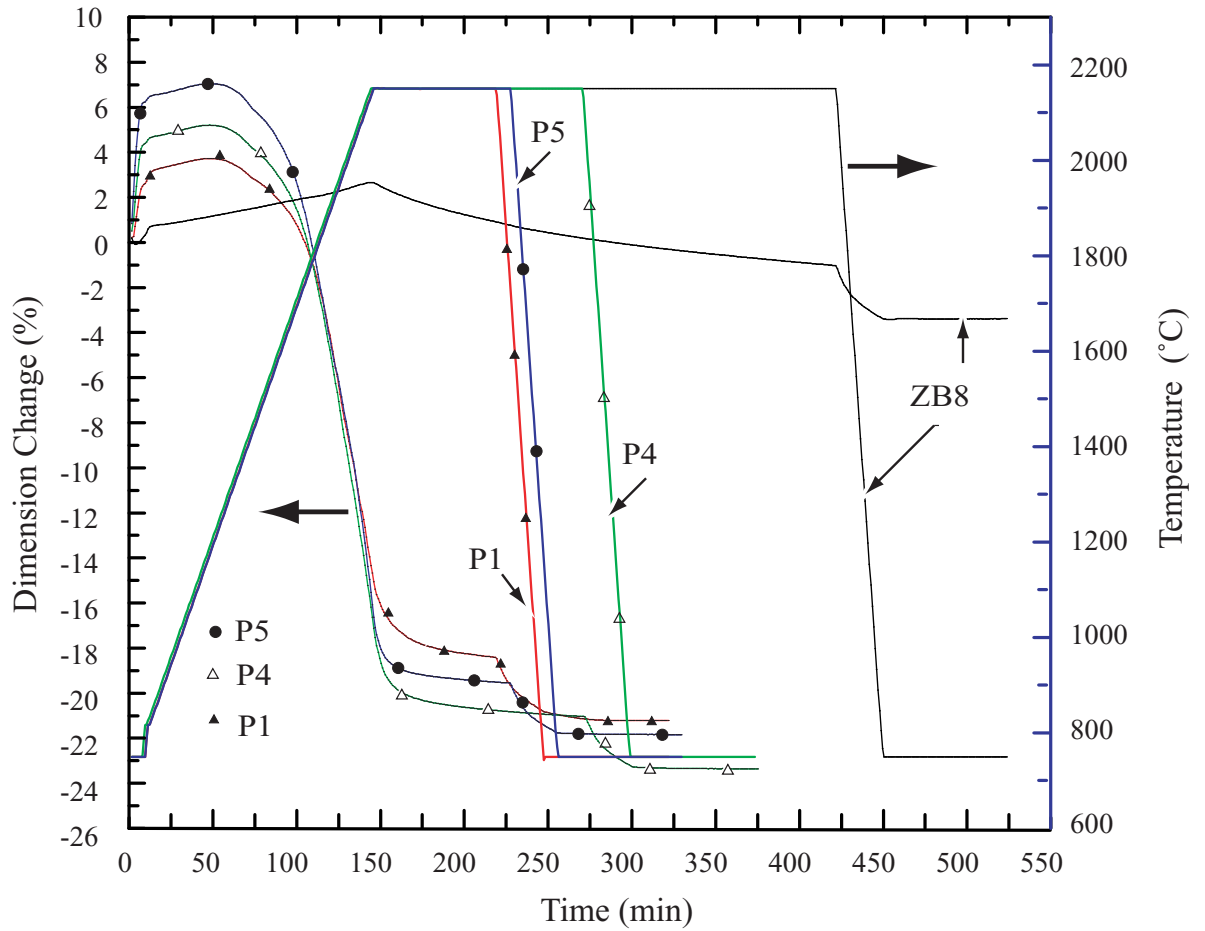


Fig 3.15: Dimension changes of $\text{ZrB}_2\text{-B}_4\text{C}$ (the pressure for pellets P1, P4, and P5 are 150, 300 and 450 MPa, respectively) and ZrB_2 (ZB8, which is first sintered in M11 before load into dilatometer) during sintering at 2050°C in dilatometer.

3.2.1.2 Sintering of ZB-3wt% B_4C pellet at 2050°C in a Dilatometer

Pellets 1, 4 and 5 of ZB-3wt% B_4C (Table 3.5) were dry pressed at different pressures, thus their green densities were a little different. The pellets were loaded into dilatometer and heated at $10^\circ\text{C}/\text{min}$ under a flowing helium atmosphere (flow rate: $0.5\text{ ml}/\text{min}$). Specimens were soaked at 2050°C until their raw expansion rate was less than $0.005\%/ \text{min}$. The holding times for pellets 1, 4 and 5 were 73 min, 126 min and 83 min, respectively. The sintering behavior of those pellets are illustrated in Figure 3.15. For comparison, the expansion of ZrB_2 ($\text{C}/\text{Zr} = 5$, $\text{B}/\text{Zr} = 3$, without B_4C) is also shown in Figure 3.15. $\text{ZrB}_2\text{-B}_4\text{C}$ powder with 3 wt% B_4C was highly active and the shrinkage for all three pellets is higher than 21%, but the final relative densities were still low, $\sim 70\%$ because of the low green density. The

fast expansion at the beginning ($<1300^{\circ}\text{C}$) was because of the evaporation of residual boria in the sample. Since the pure ZrB_2 pellet had been sintered at temperature higher than 1300°C in a graphite-vacuum furnace (M11) for several hours, no residual boria remained in this pellet, therefore, the phenomenon of fast expansion at the beginning ($<1300^{\circ}\text{C}$) was not observed when it was sintered in the dilatometer.

The shrinkage of the pure ZrB_2 pellet sintered at 2050°C was low. The possible reason was the residual ZrO_2 (boria should be removed at 1350°C), which increased the self-diffusion coefficient of ZrB_2 and results in particle coarsening, and thus inhibits the densification [5, 6, 7]. The SEM photo in Figure 3.16b showed that the particle was elongated for pellet ZrB_2 without B_4C , while the grain was equiaxed for $\text{ZrB}_2\text{-B}_4\text{C}$ pellet with B_4C . The B_4C in sample $\text{ZrB}_2\text{-B}_4\text{C}$ can react with residual ZrO_2 according to the following equation, hence inhibiting the extensive grain growth and enhancing the densification.



$$\Delta G = -22.91 \text{ kJ/mol, at } 1500 \text{ K}$$

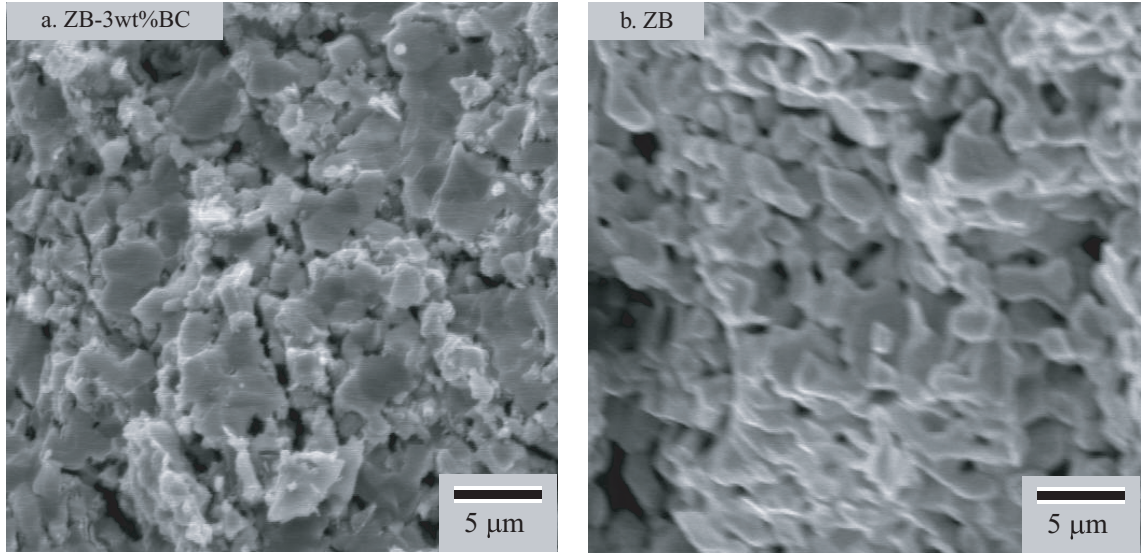


Fig 3.16: SEM photo of pellets sintered at 2050°C in a dilatometer. (a) $\text{ZrB}_2\text{-3 wt}\%\text{B}_4\text{C}$, sintered at 2050°C for 73 min; (b) ZrB_2 , sintered at 1600°C -2 h- 1950°C -2 h in the M11, then 2050°C for 250 min in the dilatometer.

Fahrenholtz [8] reported that the WC introduced to the system during milling could also react with ZrO_2 and remove them, thus enhance densification. However, pure ZrB_2 pellet

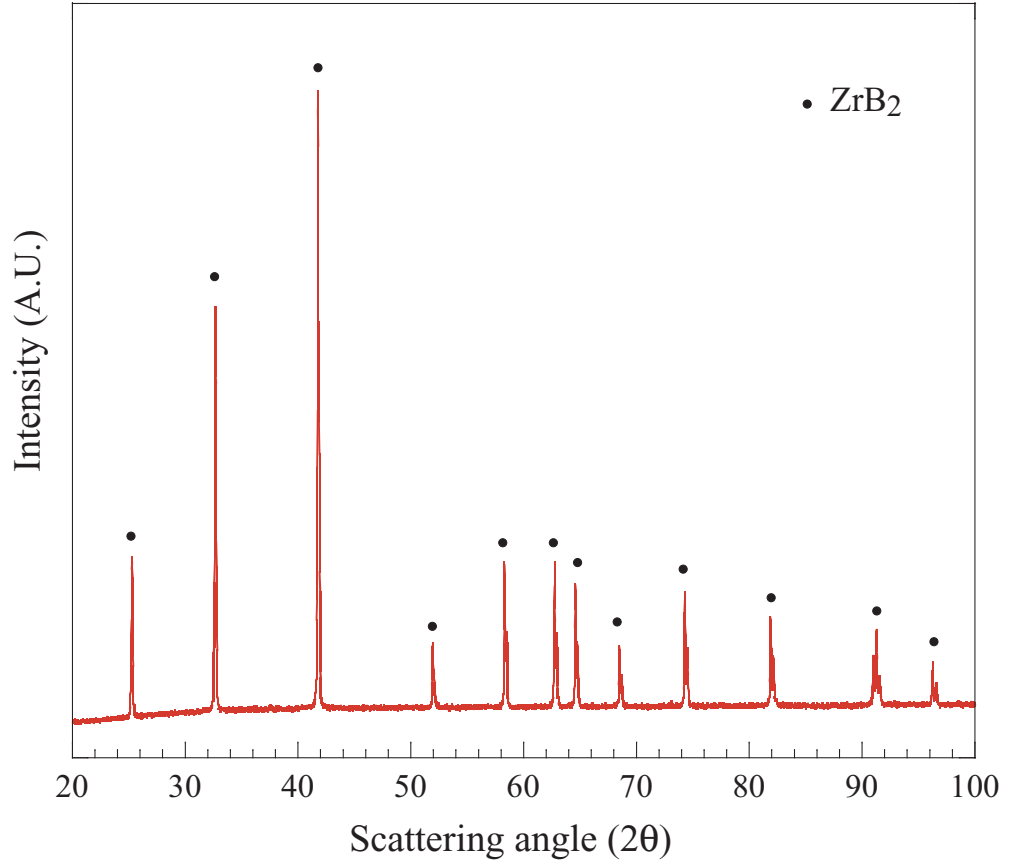
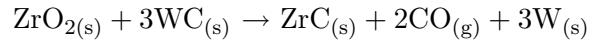


Fig 3.17: XRD pattern of pure ZrB₂ after sintering at 2050°C in the dilatometer.

could not be densified at all even at 2050°C although there were significant amounts of WC in sample ZB8 after spex-milling as shown in Figure 3.14, but the WC peak disappeared after sintered at 2050°C, as shown in Figure 3.17 and no other phases shown in the XRD pattern except ZrB₂.



$$\Delta G = -25.66 \text{ kJ/mol, at } 2300 \text{ K}$$

The XRD patterns of pellets ZrB₂-B₄C are shown in Figure 3.18, which showed that ZrB₂ was still the dominant phase, but a new graphite peak was shown in the figure after sintering at 2050°C. The peaks of B₄C and ZrO₂ (see Figure 3.12) disappeared after sintering.

The B₄C can enhance the sintering of zirconium diboride as aforementioned, however, the zirconium diboride pellet still cannot be densified, and the relative density is only ~72%

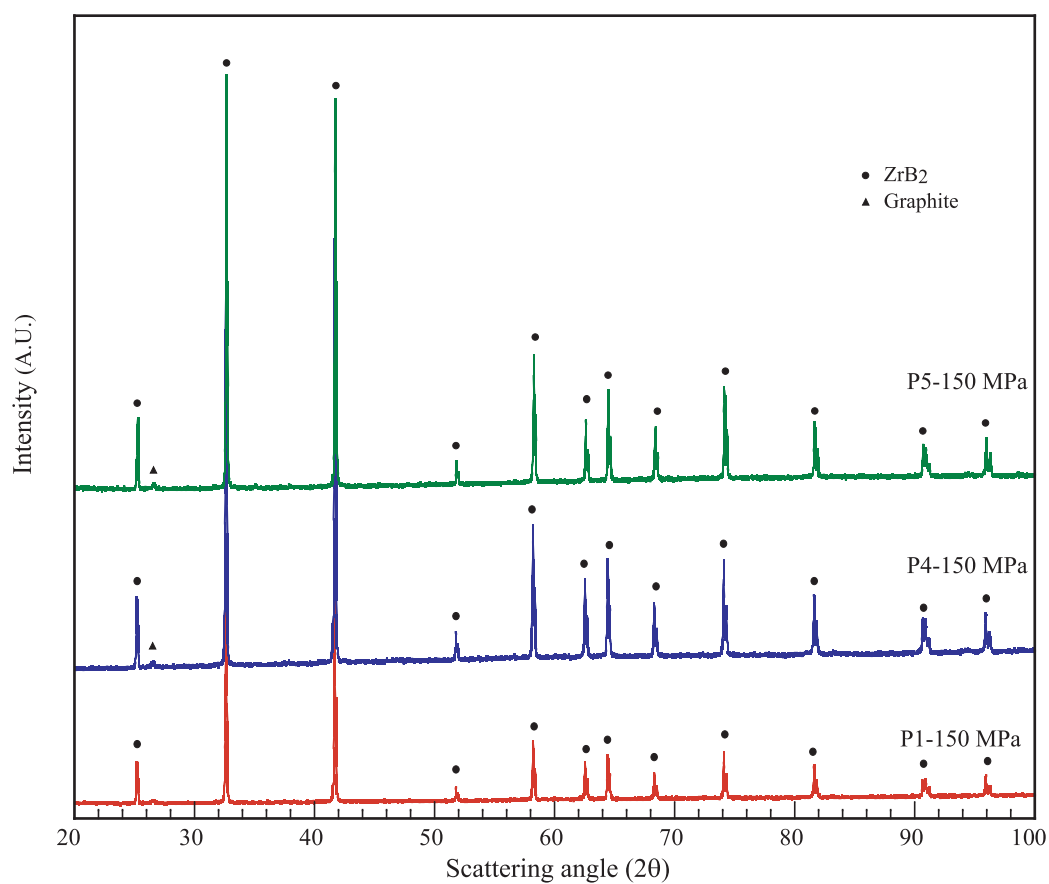
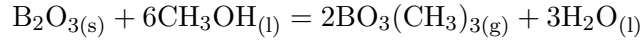


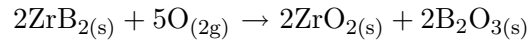
Fig 3.18: XRD pattern of ZrB₂-B₄C after sintering at 2050°C in the dilatometer (the pellet P1, P4 and P5 are all prepared by dry-pressing but the pressure are 150 MPa, 300 MPa and 450 MPa, respectively).

even after sintering at 2050°C for about 1 h. The problem may be:

1. The use of ZrO₂ as media during the ball-milling introduced oxide impurity of zirconium oxide into the system, which inhibited the densification of ZrB₂ pellets [5].
2. Methanol washing was an efficient method to remove the boron oxide on the particle surfaces. However, this step should be repeated several times (6 times)[10]. Sonication broke up the agglomerates, and methanol dissolved the boria (the equation was shown in the following) and formed a gas phase, which was removed from the system by evaporation. 2 times methanol washing was not enough to remove the boron oxide impurities.



3. The solution added and removed was done in air so that oxygen was sealed into the bottle for ball-milling, which may have reacted with the diboride powder and formed oxide, such as ZrO₂ and B₂O₃ as described in the following reaction. Those oxides may bring a significant negative effect on the following densification.



$$\Delta G = -3828.57 \text{ kJ/mol, at } 298.15 \text{ K}$$

The powder processing procedure was then improved according to the problem we found, and some new powder was synthesized and the sinterability was also studied using the new processing method as described in 2.2.2 of Chapter 2.

3.2.2 Sinterability of ZrB₂ and ZrB₂-B₄C Using a New Method

3.2.2.1 Synthesized Powder of ZrB₂ and ZrB₂-B₄C for Sintering

The powder synthesis method was the same as before, but the powder processing method was improved, such as using B₄C as milling media instead of ZrO₂, using methanol washing 4 -6 times, the suspension was transferred and prepared in glove box to avoid introduce oxygen, as described in chapter 2.2.2.

Newly bought zirconium-n-propoxide and 1-propanol were used to synthesize ZrB_2 and $\text{ZrB}_2\text{-B}_4\text{C}$ powder for the sintering research. The microscope photos of ZrB_2 and $\text{ZrB}_2\text{-B}_4\text{C}$ powders after boro/carbothermal reduction at 1400°C for 2 h were shown in Figure 3.19 and Figure 3.20, respectively.

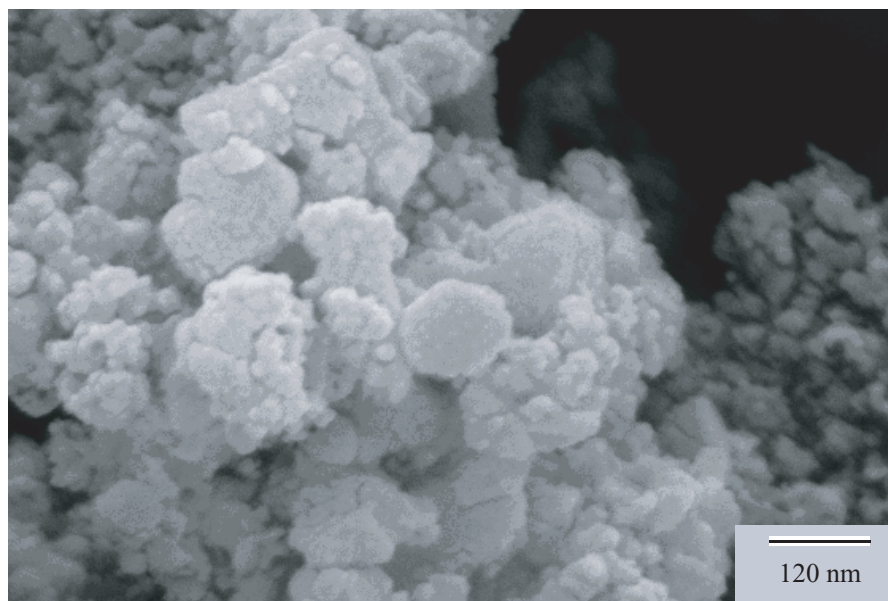


Fig 3.19: SEM photo of ZrB_2 powder heat-treated at 1400°C .

The powders are much uniform and fine compared to previous synthesized powder using old initial materials, and the particle size is $\sim 20\text{ nm}$ - 150 nm for ZrB_2 powder as shown in Figure 3.19, and 50 nm - 300 nm for $\text{ZrB}_2\text{-B}_4\text{C}$ powder as shown in Figure 3.20. Zr-propoxide used as Zr-source is a sensitive material which may react with moisture or air, the property of this material maybe easily changed during storage although they were put into the Glove Box and no obvious precipitates could be observed. But the pH after refluxing with HAcAc is 8.5-10 when using old Zr-propoxide, while the normal pH range after refluxing should be 7-8.

3.2.2.2 Sintering

The ZrB_2 and $\text{ZrB}_2\text{-B}_4\text{C}$ powder after heat-treatment at 1400°C for 2 h were processed and green pellets were prepared as described in II.2 of chapter 2. The green pellet after CIP and debinding were loaded into M11 furnace and sintering at 2020°C for 1 h. The geometric

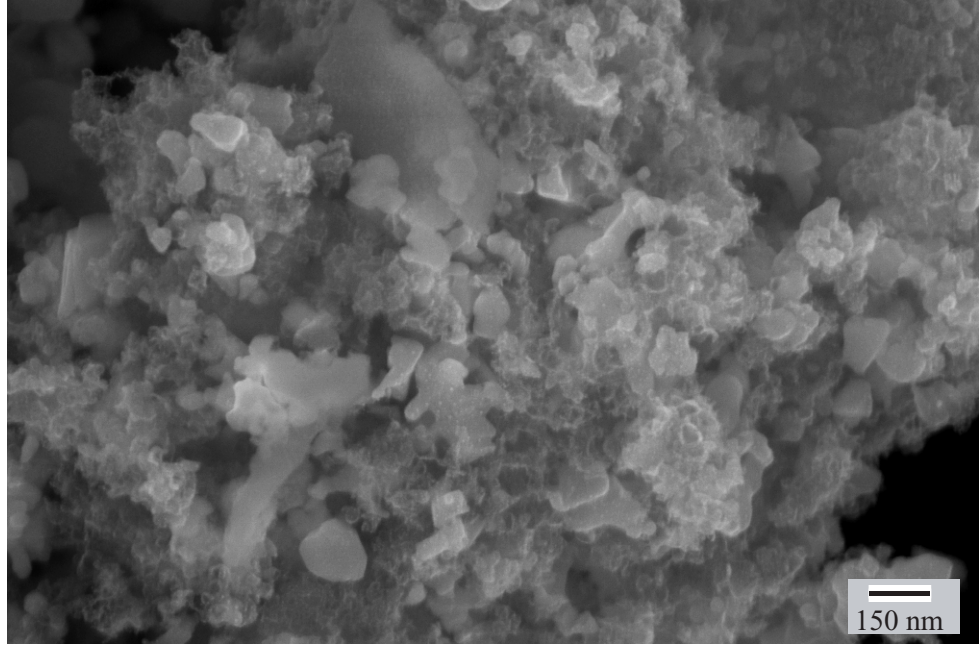


Fig 3.20: SEM photo of $\text{ZrB}_2\text{-B}_4\text{C}$ powder heat-treated at 1400°C .

density of green, after CIP and after sintered are listed in Table 3.6.

Tab 3.6: Dimension and bulk density of ZrB_2 and $\text{ZrB}_2\text{-B}_4\text{C}$ pellets using new processing method where, ϕ is the diameter of pellets, δ is the thickness of pellets.

| Sample | Condition | Dimension and density | | | | |
|-----------------------------------|--------------------------------------|-----------------------|------------------|-----------|-----------------------------|------------------------|
| | | ϕ , mm | δ , mm | Wt, mg | Density, g/cm^3 | Relative density, % |
| ZrB_2 | Green | 6.64 | 5.52 | 402.71 | 2.11 | 34.67 |
| | CIP | 6.61 | 5.29 | 400.8 | 2.21 | 36.32 |
| | Sinter at 2020°C , 1 h | 4.79 | 3.71 | 304.19 | 4.55 | 74.87 |
| $\text{ZrB}_2\text{-B}_4\text{C}$ | Green | 6.55 | 5.21 | 388.97 | 2.22 | 37.96 |
| | CIP | 6.41 | 4.89 | 388 | 2.46 | 42.12 |
| | Sinter at 2020°C , 1 h | 4.7 | 3.586 | 296.71 | 4.77 | 81.70 |

For ZrB_2 pellet, the true density used is 6.09 by assuming it's pure zirconium diboride. The theoretical density for $\text{ZrB}_2\text{-3 wt}\%\text{B}_4\text{C}$ powder was calculated as follows:

$$\text{TD} = 100 / (97 / 6.09 + 3 / 2.52) = 5.84$$

Where, 97 wt% is the weight percent of ZrB_2 in the composite, and 3 wt% is the weight percent of B_4C in the composite; 6.09 is the theoretical density of pure ZrB_2 , and 2.52 is the theoretical density of pure B_4C .

The dimensional bulk density can give us some information on the densification, but it's not accurate because the pellets are not perfect cylindrical and there maybe pores existed in the bulk pellets. Therefore, the Archimedes density of bulk pellets were also measured and the results are listed in Table 3.7.

Tab 3.7: Archimedes density measurement of ZrB_2 and $\text{ZrB}_2\text{-B}_4\text{C}$ pellets sintered at 2020°C for 1 h in M11 furnace where, ϕ is the diameter of pellets, δ is the thickness of pellets.

| Sample | Dry weight, mg | Suspended weight, mg | Saturate weight, mg | open pore, % | Bulk density g/cm^3 | Relative density, % |
|-----------------------------------|----------------|----------------------|---------------------|--------------|------------------------------|---------------------|
| ZrB_2 | 304.23 | 251.32 | 314.84 | 16.7 | 4.78 | 78.62 |
| $\text{ZrB}_2\text{-B}_4\text{C}$ | 297.61 | 244.51 | 303.16 | 9.46 | 5.07 | 86.82 |

The bulk density of ZrB_2 without B_4C after sintering at 2020°C for 1 h is lower than the one of $\text{ZrB}_2\text{-B}_4\text{C}$ composite, they are $\sim 78\%$ and $\sim 86\%$, respectively. The SEM micrograph of these pellet after sintering are shown in Figure 3.21.

The possible reason is the zirconium oxide impurity in the system as shown in Figure 3.23 which results in the extensive crystal growth and inhibited densification [5]. The dominant phase for the sample after heat treatment at 1400°C for 2 h in M11 furnace is ZrB_2 , but there is still a trace of tetragonal zirconia in the pattern. Zirconium oxide can not be completely avoided according to the calculation of oxygen partial pressure as shown in Figure 3.22. The partial pressure in the flowing argon is higher than equilibrium oxygen partial pressure for the oxidization of ZrB_2 so that the oxidation can not be avoided. But the oxygen amount in the flowing argon is low and there should be only trace zirconia residue in the system after the boro/carbothermal reduction complete. For the $\text{ZrB}_2\text{-B}_4\text{C}$ composite, a weak peak of zirconia is also observed in its XRD pattern as shown in Figure 3.24, but the B_4C in the system can react with it during the sintering so as to avoid the negative effect of oxides on the densification. The peak of B_4C is very weak because the content of it is really low, only 3 wt% in the composite, that is 0.06 mol of B_4C for 1 mol ZrB_2 .

However, the peak of zirconia disappears after sintering at 2020°C for 1 h for both pellets with and without B_4C as shown in Figures 3.23 and 3.25, which is unexpected. For

the pellet with B₄C, the residual zirconia can react with it to form ZrB₂:



$$\Delta G = -22.91 \text{ kJ/mol, at } 1500 \text{ K}$$

For the sample without B₄C, the zirconia may react with excess B₂O₃ in the sample if it is present. However, for this sample, the powder had been methanol washed 6 times to remove boria. A possible reason is the methanol washing can only remove the boria on the surface but not those one inside the agglomerate, which may react with the trace zirconia during sintering.

3.3 Conclusion

The nearly stoichiometric ZrB₂ powder with particle size of 20 nm-150 nm from SEM micrograph by a solution-based method was obtained with an initial composition of B/Zr = 3.0 and C/Zr = 5.0 after heat-treatment at 1400°C for 2 h in a graphite tube furnace under flowing argon. Zirconium-n-propoxide was first refluxed with Hacac to form Zr-pentanedinate, which can be hydrolysis under controlled rate so that nanocrystalline powder can be obtained.

ZrB₂-B₄C composite was synthesized by solution-based method after boro/carbothermal reduction at 1400°C for 2 h. The initial composition for ZrB₂ sol is B/Zr = 3 and C/Zr = 4.8, while the initial composition for B₄C sol is B/C = 6/7 with excess boron due to the volatile of boria. The particle size for B₄C was about 20 nm, but the particle size for ZrB₂ in the composite was 50-300 nm.

The difficulty for ZrB₂ densification was the oxide which results in particle coarsening. After carefully processing boride powders, the sinterability of above powders was studied at 2020°C for 1 h in a graphite tube furnace under flowing argon. The relative densities of ZrB₂ and ZrB₂-B₄C bulk density as measured by Archimedes method were 78% and 86%, respectively.

ZrO₂ impurity in ZrB₂ powder can not be avoided during synthesis because the partial oxygen pressure in argon is higher than the pressure needed to oxidize ZrB₂. While B₄C

can react with ZrO_2 can formed ZrB_2 and CO gas, and thus eliminate the negative effect of ZrO_2 on the sinterability, hence improve the densification.

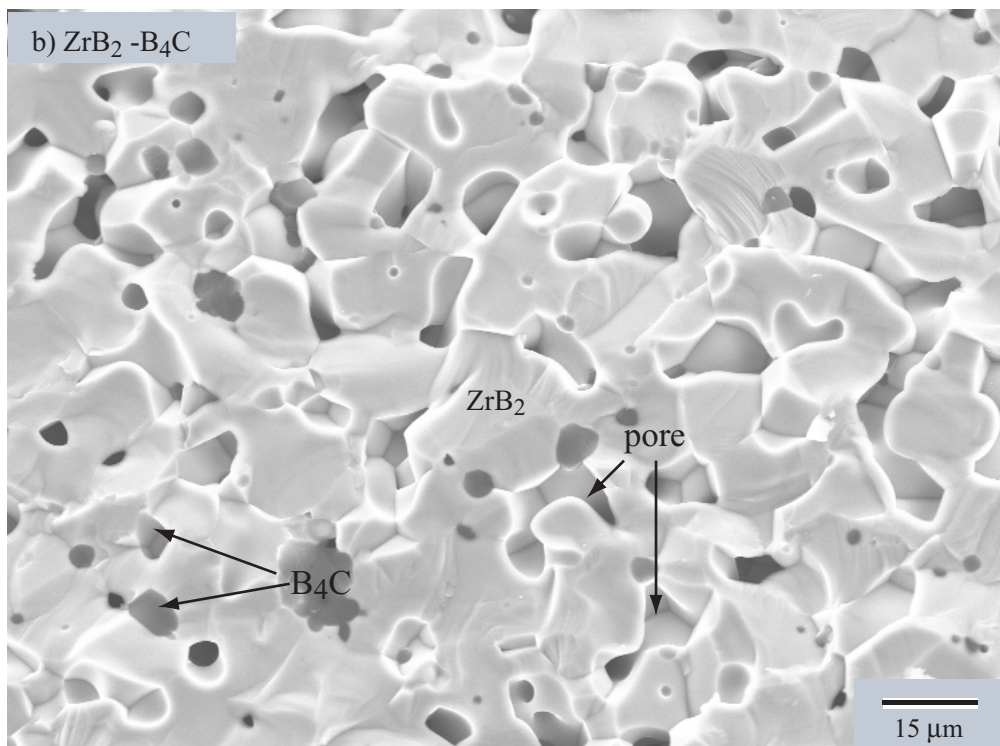
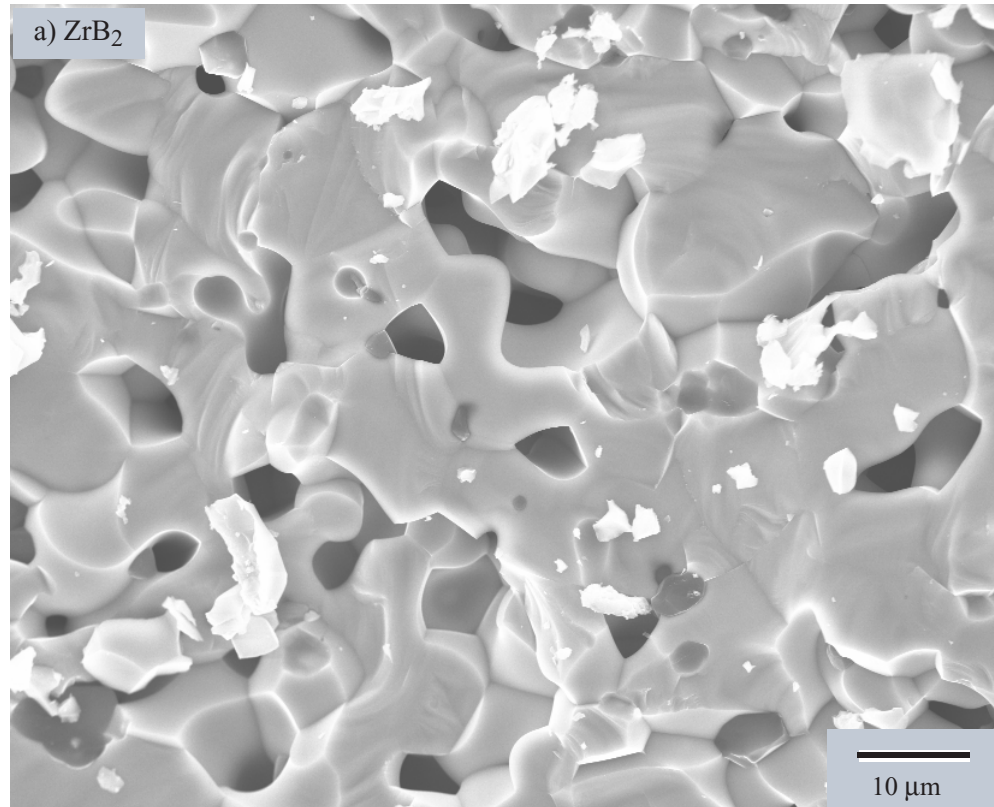


Fig 3.21: SEM micrograph of ZrB_2 and ZrB_2 - B_4C pellets after sintering at 2020°C for 1 h in the M11 furnace.

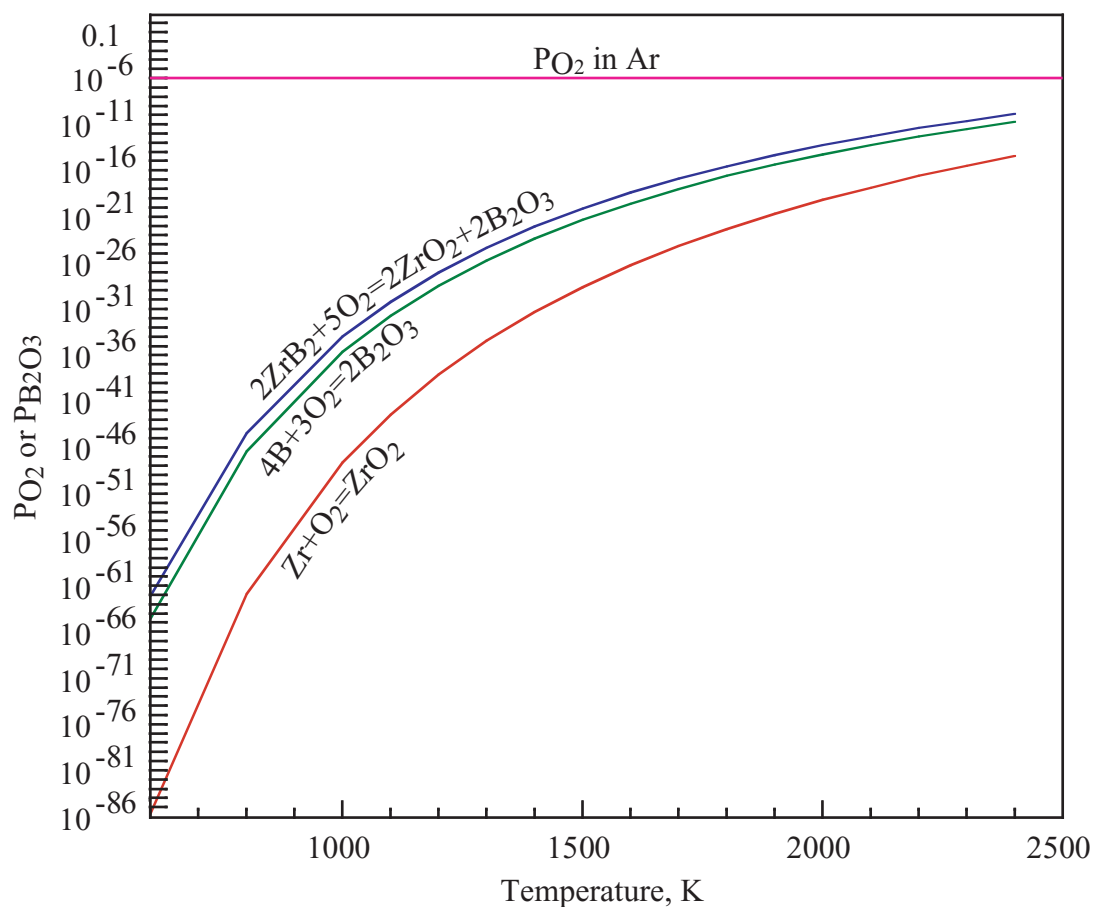


Fig 3.22: Partial pressure of oxygen during the oxidization of Zr, B and ZrB_2 in flowing argon with oxygen partial pressure of 10^{-6} with temperature from thermal calculation (data from NIST-JANAF Thermochemical Tables [9]).

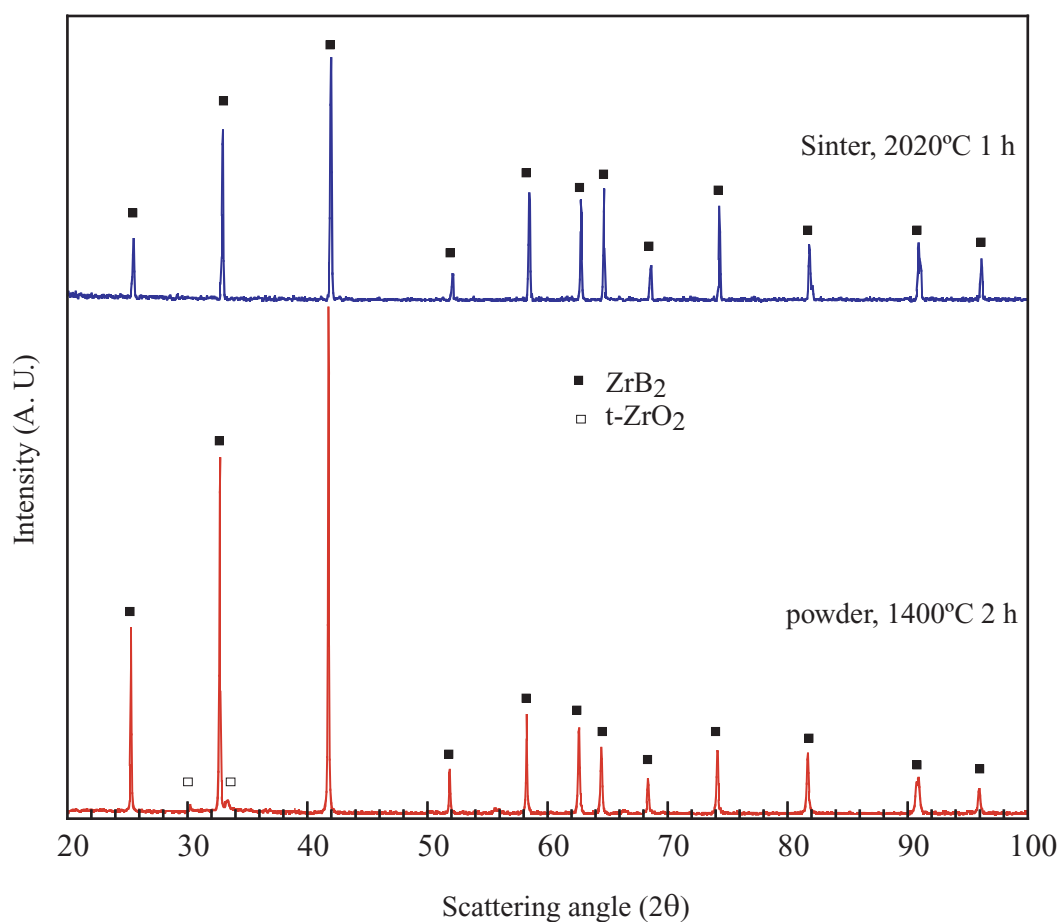


Fig 3.23: XRD Pattern of ZrB_2 powder heat-treated at 1400°C for 2 h used for preparing of a pellet, and the pellet after sintering at 2020°C for 1 h in the M11 furnace.

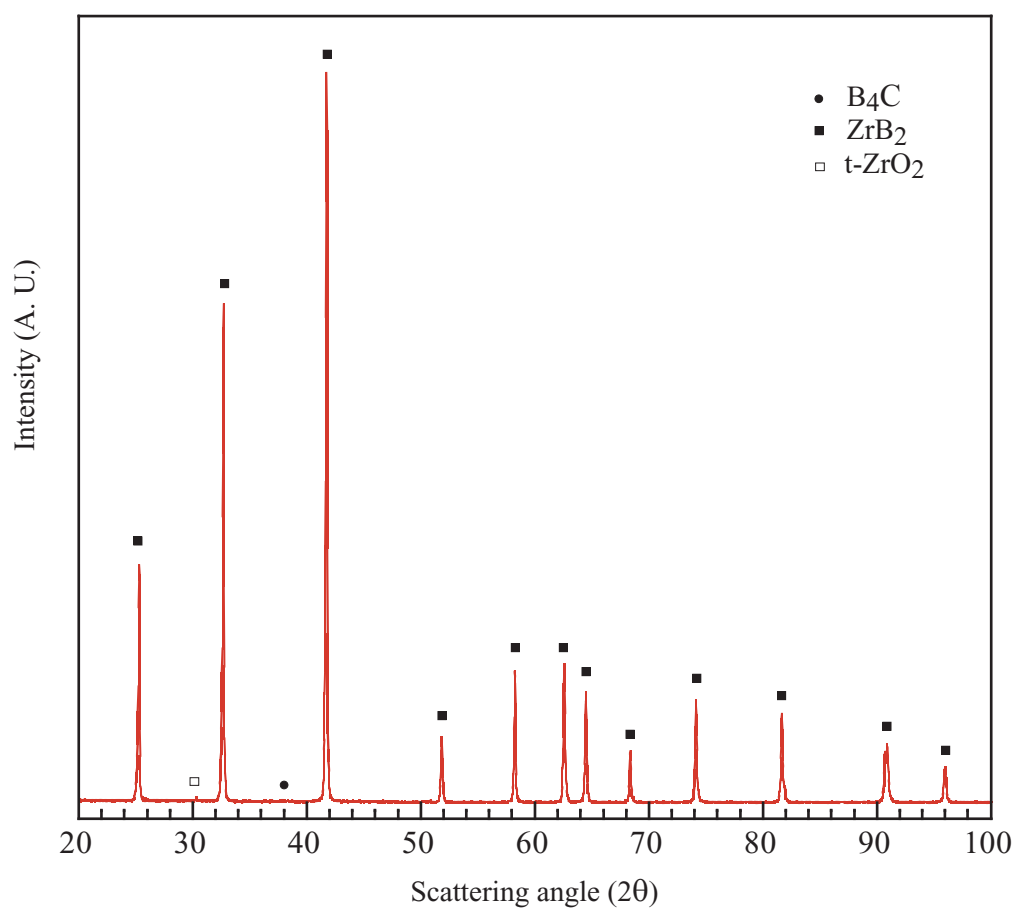


Fig 3.24: XRD Pattern of ZrB_2 - B_4C powder heat-treated at $1400^\circ C$ for 2 h used for preparing of pellet.

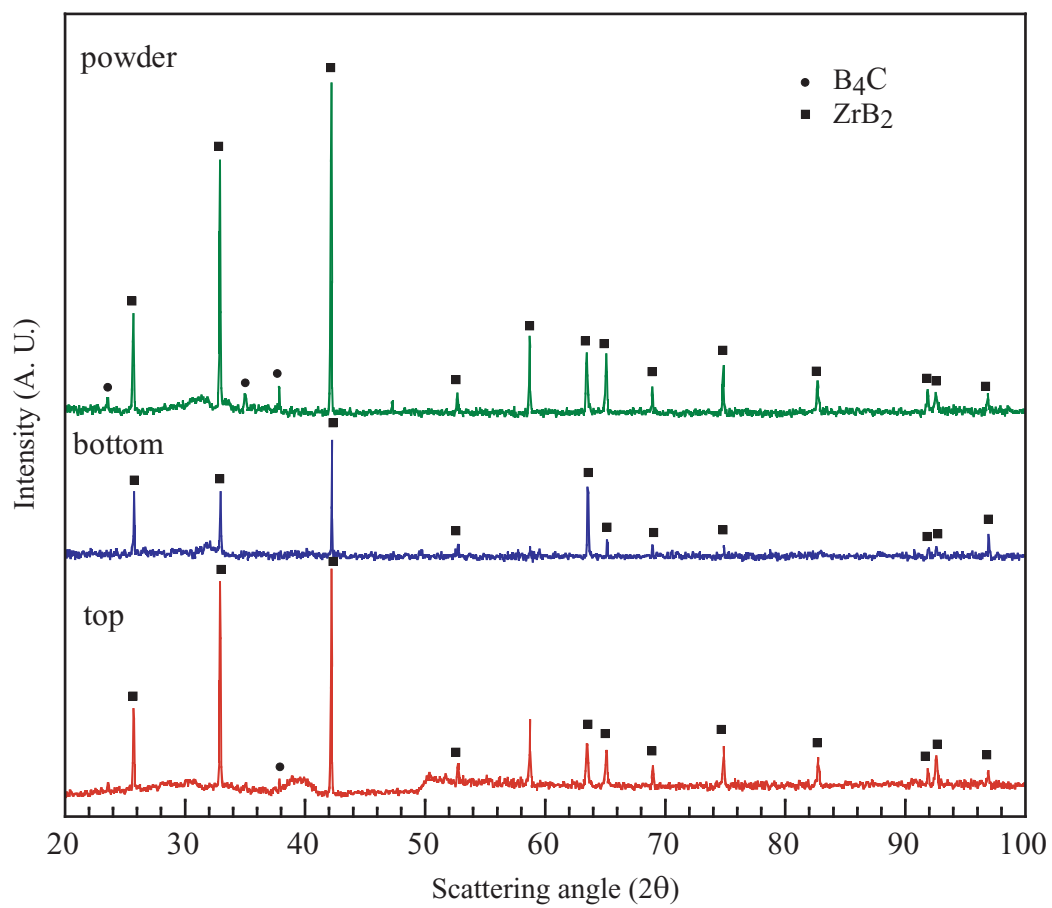


Fig 3.25: XRD pattern of ZrB_2 - B_4C pellet and powder sintered at 2020°C for 1 h in M11 furnace.

REFERENCES

3.4 References

- [1] NLM04 US National Library of Medicine (NLM), ed. Boron oxide. In: The Hazardous Substances Data Bank (HSDB) <http://toxnet.nlm.nih.gov>
- [2] Z. Hu, M. D. Sacks, G. A. Staab, C. A. Wang, and A. Jain, "Solution-Based Processing of Nanocrystalline ZrC," *Ceram. Eng. Sci. Proc.*, **23**[4] 711-717 (2002).
- [3] A. Jain, M. D. Sacks, C. A. Wang, M. Middlemas, and Z. Cheng, "Processing of Nanocrystalline Zirconium Carbide Powders," *Ceram. Eng. Sci. Proc.*, **24**[A] 41-49 (2003).
- [4] Alan W. Weimer, Raymond P. Roach, Christopher N. Haney etc. "Rapid carbothermal reduction of boron oxide in a graphite transport reactor," *AIChE Journal*, **37**[5] 759-768 (1991).
- [5] S. Baik, P. F. Becher, "Effect of Oxygen Contamination on Densification of Titanium Diboride," *J. Am. Ceram. Soc.*, **70** [8] 527-30 (1987).
- [6] M. F. Yan, U. Chowdhry, and R. M. Cannon, "Conditions for Discontinuous Grain Growth with Pore Entrapment or Pore Coarsening," *Am. Ceram. Soc. Bull.*, **57** [3] 316 (1978).
- [7] M. F. Yan, "Microstructural Control in the Processing of Electronic Ceramics," *Mater. Sci. Eng.*, **48** 53-72 (1981).
- [8] A. L. Chamberlain, W. G. Fahrenholtz, and G. E. Hilmas, "High-strength Zirconium Diboride-based Ceramics," *J. Am. Ceram. Soc.*, **87** [6] 1170-1172 (2004).
- [9] "Nist-Janaf Thermochemical Tables" *J. Physi. Chem. Ref. Data*, monograph 9.

- [10] N. Cho, “Processing of Boron Carbide,” *PH. D thesis*, 2006, MSE, Georgia Institute of Technology.

CHAPTER 4

Research on the synthesis of $\text{ZrB}_2\text{-TaB}_2$ and $\text{ZrB}_2\text{-TaB}_2\text{-B}_4\text{C}$ powder and their sinterability

4.1 Synthesis of Nanocrystalline $\text{ZrB}_2\text{-TaB}_2$ based composite by a Solution-based Method

Introducing Tantalum into ZrB_2 can significantly improve the oxidation-resistance of this material [1, 1], therefore, $\text{ZrB}_2\text{-TaB}_2$ based composites were synthesized in this study.

4.1.0.3 Preparation of $\text{ZrB}_2\text{-TaB}_2$ composite

A mixture of tantalum ethoxide and 2,4-pentanedione was added to a mixture of zirconium n-propoxide and 2,4-pentanedione with a molar ratio of $\text{Zr/Ta} = 3$. The solution was then refluxed and hydrolyzed in the same fashion as in the preparation of single phase ZrB_2 . A boron source (boric acid) and an additional carbon source (phenolic resin) were added to the above hydrolyzed solution to make the molar ratio of $\text{C}/(\text{Zr}+\text{Ta}) = 4.8$ and $\text{B}/(\text{Zr}+\text{Ta}) = 3.0$. The mixture was then concentrated, dried and heat-treated as before. The weight loss during heat treatment and corresponding XRD patterns are shown in Figures 4.1 and 4.2, respectively.

Weight loss increased abruptly from 1100°C to 1300°C due to the borothermal/carbothermal reduction reaction, and the weight loss for 1300°C and 1400°C is similar, but there was phase development at 1400°C . A little more weight loss of $\sim 1.37\%$ appeared when the sample was exposed to a higher heat-treatment temperature of 1600°C , compared with 1300 and 1400°C .

The XRD pattern in Figure 4.2 shows that only weak peaks of tantala and zirconia appeared in $\text{ZrB}_2\text{-TaB}_2$ sample heat-treated at 600°C . A compound of zirconium tantalum oxide ($\text{TaZr}_{2.75}\text{O}_8$) formed at 700°C . The relative intensity of this phase ($\text{TaZr}_{2.75}\text{O}_8$)

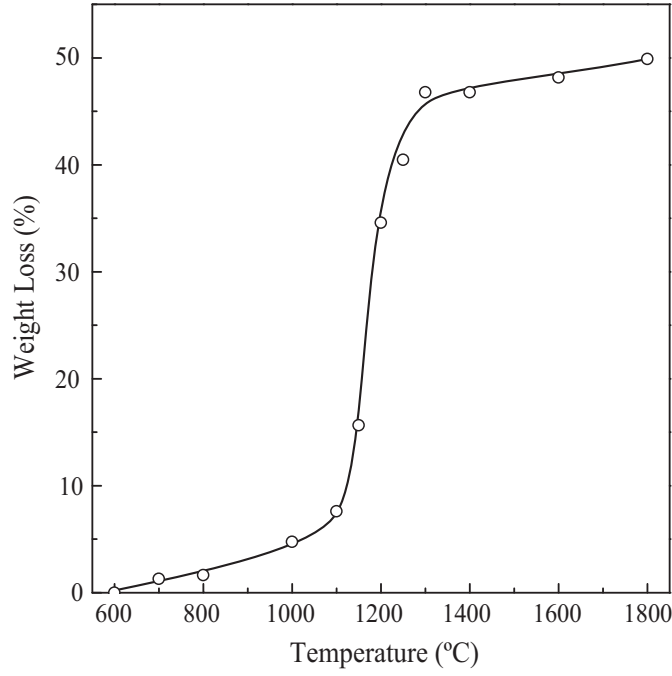
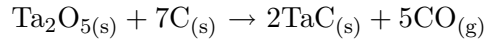
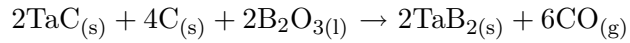


Fig 4.1: Weight loss vs. temperature for a ZrB₂-TaB₂ composite.

increased with temperature up to maximum at 1000°C, and then decreased and finally disappeared at 1200°C. A new phase of TaC was observed at 1000°C, and its intensity increased at 1100°C, and then decreased until disappeared at 1200°C. TaC is an intermediate product, which reacted with boria at higher temperature and formed TaB₂.

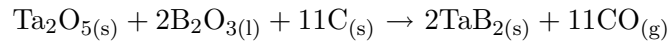


$$\Delta G = -16.46 \text{ kJ/mol, at } 1400 \text{ K}$$



$$\Delta G = -20.14 \text{ kJ/mol, at } 1800 \text{ K}$$

The overall boro/carbothermal reduction reaction was:



$$\Delta G = -21.85 \text{ kJ/mol, at } 1600 \text{ K}$$

ZrB₂ and TaB₂ appeared at 1150°C and developed with increasing temperature. ZrB₂ and TaB₂ was obtained at 1300°C, but the relative intensity of ZrB₂ increased with further

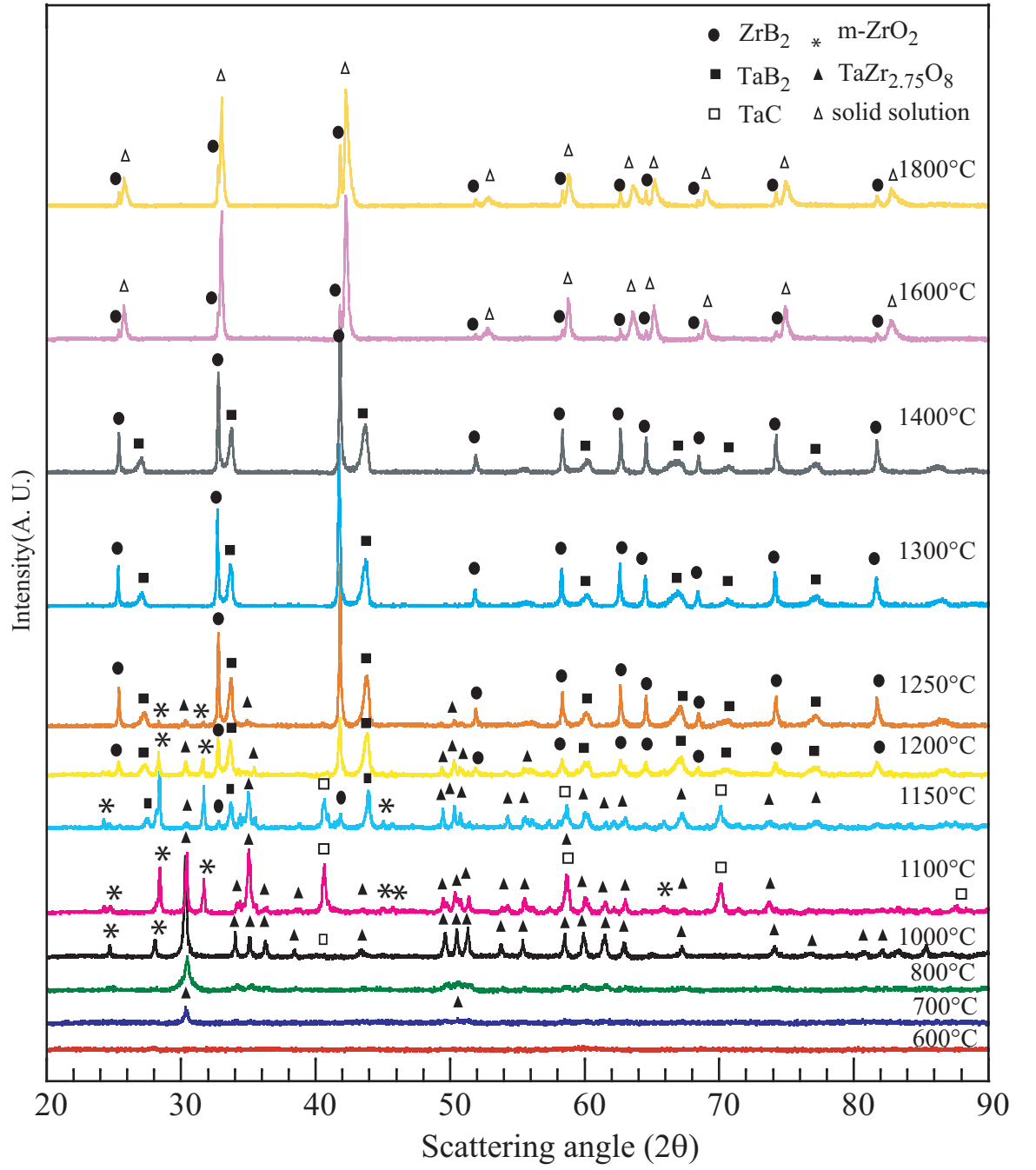


Fig 4.2: XRD patterns for $\text{ZrB}_2\text{-TaB}_2$ heat-treated from 600°C to 1800°C for 2h.

heat-treatment at 1400°C. The intensity of the TaB₂ phase showed no significant change above 1200°C. However, the peaks of ZrB₂ and TaB₂ moved closer with increasing temperature and finally the two phases combined together at 1600°C. The backscattered SEM photo shown in Figure 4.3-(c) proved there is no phase separation for the sample because there is no evidence of compositional contrast. This implies that the ZrB₂ and TaB₂ were soluble in each other and finally formed a complete solid solution, although the present phase diagram does not show this. Figure 4.3-(a) shows the microstructure of the ZrB₂-TaB₂ composite heat-treated at 1300°C for 2 h and EDS analysis showed that the both phases of ZrB₂ and TaB₂ observed in a small of area of a particle. The particle size is ~100-250 nm but increased to ~500 nm after further heat-treated at 1600°C for 2 h as shown in Figure 4.3-(b).

The crystallite sizes (calculated from XRD broadening, the XRD patterns were presented in Figure 4.2) for the same sample are shown in Figure 4.4. The crystallite size for every phase increased significantly with temperature, except for TaB₂. The crystallite size for TaB₂ changed little since 1200°C. This is consistent with the XRD pattern, which showed that the intensity for this phase was almost the same for samples heat-treated from 1200°C to 1400°C.

4.1.0.4 Preparation of ZrB₂-TaB₂-B₄C composite

The sols of ZrB₂-TaB₂ and B₄C were prepared separately, and then they were mixed together, concentrated and dried in a similar fashion to the synthesis of the ZrB₂-B₄C composite described in 2.1.2 of Chapter 2. The initial composition for ZrB₂-TaB₂ batch is $C/(Zr+Ta) = 4.8$, $B/(Zr+Ta) = 3.0$ and $Zr/Ta = 3.0$, while it is $B/C = 6/7$ for B₄C batch. The dry powder was then pyrolyzed at 850°C to obtain fine-scale mixed TaZr_{2.75}O₈/B₂O₃/C powder, which was then heat-treated at higher temperature from 1250°C-1600°C for boro/carbothermal reduction reaction to obtain a ZrB₂-TaB₂-B₄C composite. About 400 mg pyrolysis powder was load into the M11 furnace and heat-treated at desired temperature (such as 1250°C, 1300°C) and held for 2 h. The sample was taken out from the furnace and the weight was measured. The weight loss during heat treatment and

corresponding XRD patterns are shown in Figures 4.5 and 4.6, respectively.

The weight loss increased abruptly from 850°C to 1300°C, especially from 1250-1300°C due to the borothermal/carbothermal reduction reaction, but it slowed down from 1300°C to 1400°C. The weight losses were almost the same for sample heat-treated at temperature higher than 1400°C, hence the boro/carbothermal reduction should be completed after the hold at temperature 1400°C, which is coincident with the XRD pattern shown in Figure 4.6.

The dominant phases in the sample heat-treated at 1250°C for 2 h are ZrB₂ and TaB₂ with traces of tetragonal zirconia, monoclinic zirconia and TaC. Those impurities disappear when heat-treated at the higher temperature of 1300°C, and only the peaks of ZrB₂ and TaB₂ are apparent on the XRD pattern of sample heat-treated at 1300°C for 2 h. The phase developments were not observed for samples further heat-treated at higher temperature of 1400, 1500°C and 1600°C, but the position of peaks for ZrB₂ and TaB₂ shifted together, and they were almost converged at 1600°C. The peak for phase B₄C was not observed in the XRD pattern, the reason maybe the amount of B₄C was too small, 3 wt% of B₄C, that is 0.076 mol compared to 1 mol (Zr+Ta), which may be too low a concentration to be detected.

The particle size for ZrB₂-TaB₂-B₄C composite is from 50 nm to 700 nm after heat-treatment at 1300°C, measured from the SEM photo shown in Figure 4.7. The particle size increased to 100 nm - 820 nm when heat treated at higher temperature of 1400°C, but from then on, the particle size did not change much after further heat treatment at higher temperatures of 1500°C and 1600°C as shown in Figure 4.8. However, the morphology of particles changed significantly. The necking between particles was apparent for the sample heat-treated at 1500°C, while the sample heat-treated at 1600°C appeared liquified and formed glass layer on the surface.

4.2 Sintering of ZrB₂-TaB₂ and ZrB₂-TaB₂-B₄C composites

The powder used for bulk processing were ZrB₂-TaB₂ and ZrB₂-TaB₂-B₄C, heat-treated at 1400°C for 2 h, and the method for pellet preparation was described in II.2 of Chapter 2. The geometric density of pellets in the green, CIP state, and after sintering, are listed in

Table 4.1.

For the ZrB₂-TaB₂ pellet, the theoretical density was calculated by assuming: i) Only ZrB₂ and TaB₂ phases existed in the sample. ii) The molar ratio of Zr to Ta is exactly 3 as desired. iii) The weight percent of ZrB₂ is x , therefore, the weight percent of TaB₂ is $100 - x$

$$(x/112.84)/((100 - x)/202.57) = 3$$

$$x = 62.57$$

The weight percents for ZrB₂ and TaB₂ are 62.57 wt% and 37.43 wt%. The theoretical density of ZrB₂-TaB₂ was:

$$TD = 100/(62.57/6.085 + 37.43/11.15) = 7.33$$

Where, 112.84 g/mol and 202.57 g/mol are the molecular weights of ZrB₂ and TaB₂, respectively. 6.085 g/cm³ and 11.15 g/cm³ are the densities of ZrB₂ and TaB₂.

For ZrB₂-TaB₂-3 wt%B₄C composite (the weight percent of ZrB₂-TaB₂ is 97 wt%), the theoretical density can be calculated similarly:

$$TD = 100/(3/2.52 + 0.97(62.57/6.085 + 37.43/11.15)) = 6.93$$

where 2.52 g/cm³ is the theoretical density of pure B₄C.

The relative bulk density for ZrB₂-TaB₂ and ZrB₂-TaB₂-3wt%B₄C pellets were all over 90%, which are 91.22% and 93.48%. The density was calculated by measuring the dimension of pellets, however, the pellets were not a perfect cylinder shape due to the friction between the die wall and the powder, which results in the transform of the pellet shape when it's removed from the die, and thus the error can not be avoided, although for every dimension, although it's average value for several measurements. To obtain accurate bulk density of sintered pellets, the Archimedes densities were measured and recorded in Table 4.2.

The bulk density of ZrB₂-TaB₂ (Archimedes density) with and without B₄C after sintering at 2020°C for 1 h were 97.21% and 92.26%, respectively, which are much higher than the one for the ZrB₂ sample. The ZrB₂ and TaB₂ have similar crystal structure as shown in Table 4.3, and they may dissolve into each other and form solid solution, which increase the

bulk diffusion and results in improvements in densification. This was implied by their XRD patterns shown in Figures 4.9 and 4.10. The peaks for ZrB_2 and TaB_2 are totally converged together after sintering at 2020°C for 1 h. The results also consistent with Wantanate [4], who found that TiB_2 , TaB_2 can dissolve into CoB when heated at 1800° and formed solid solution.

Figure 4.11 and Figure 4.12 show the SEM micrograph and EDS spectra for pellet $\text{ZrB}_2\text{-TaB}_2$ and $\text{ZrB}_2\text{-TaB}_2\text{-B}_4\text{C}$. No pore was observed for both samples and they are fully densified. For $\text{ZrB}_2\text{-TaB}_2$ sample, no difference observed for the particles, but for $\text{ZrB}_2\text{-TaB}_2\text{-B}_4\text{C}$ sample, there are two phases appeared in the micrograph. EDS analysis shows that the dominate phase for the dark is B_4 , while the for the light phase is $\text{ZrB}_2\text{-TaB}_2$ (EDS can not exactly tell B and C, above conclusion was determined according to the amount of Zr and Ta).

4.3 Conclusion

The $\text{ZrB}_2\text{-TaB}_2$ composite (molar ratio of $\text{Zr}/\text{Ta} = 3$) with crystalline size of 100 nm-250 nm formed by a solution-based method was obtained with an initial composition of $\text{B}/(\text{Zr}+\text{Ta}) = 3.0$ and $\text{C}/(\text{Zr}+\text{Ta}) = 4.8$ after heat-treatment at 1300°C for 2 h in a graphite tube furnace under flowing argon. Zirconium-n-propoxide and tantalum-ethoxide were used as Zr-bearing source and Ta-bearing source, respectively, phenolic resin was used as carbon-bearing source, and propanol was used as mixing solvent.

$\text{ZrB}_2\text{-TaB}_2\text{-B}_4\text{C}$ composite was synthesized by solution-based method after boro/carbothermal reduction at 1400°C for 2 h. The molar ratio for $\text{ZrB}_2\text{-TaB}_2$ sol is $\text{B}/(\text{Zr}+\text{Ta}) = 3.0$, $\text{C}/(\text{Zr}+\text{Ta}) = 4.8$ and $\text{Zr}/\text{Ta} = 3$, while the initial composition for the B_4C sol is $\text{B}/\text{C} = 6/7$ and the weight percent of B_4C in the composite is 3 wt%. The particle size for this composite is 100-820 nm.

The $\text{ZrB}_2\text{-TaB}_2$ and $\text{ZrB}_2\text{-TaB}_2\text{-B}_4\text{C}$ can be easily densified at 2020°C for 1 h due to the solid solution formed between ZrB_2 and TaB_2 , and the relative densities were 97.21% for $\text{ZrB}_2\text{-TaB}_2\text{-B}_4\text{C}$ and 92.26% for $\text{ZrB}_2\text{-TaB}_2$.

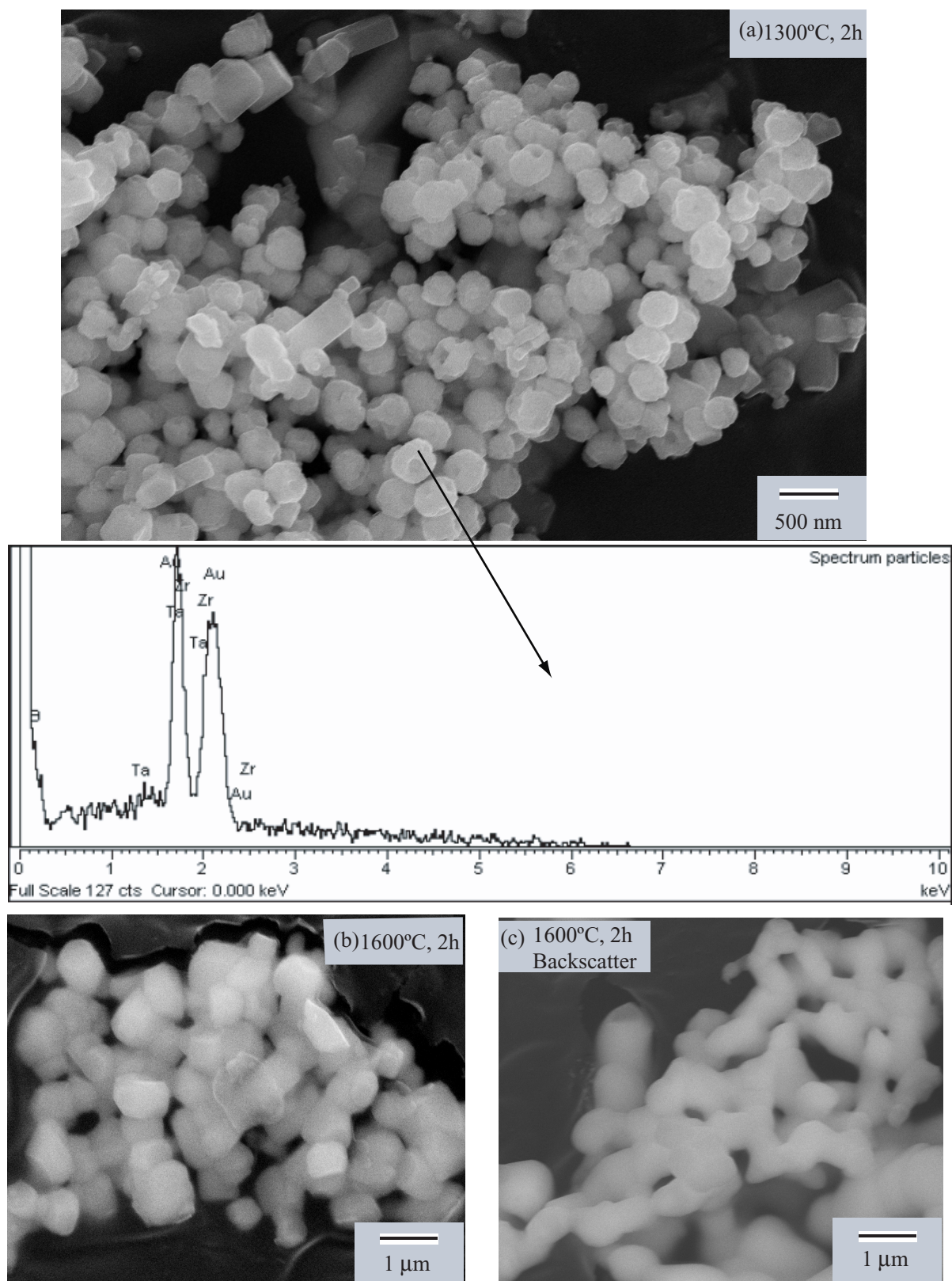


Fig 4.3: SEM micrograph of $\text{ZrB}_2\text{-TaB}_2$ heat-treated at (a) 1300°C-2 h. (b) 1600°C-2 h. (c) 1600°C-2 h-backscatter

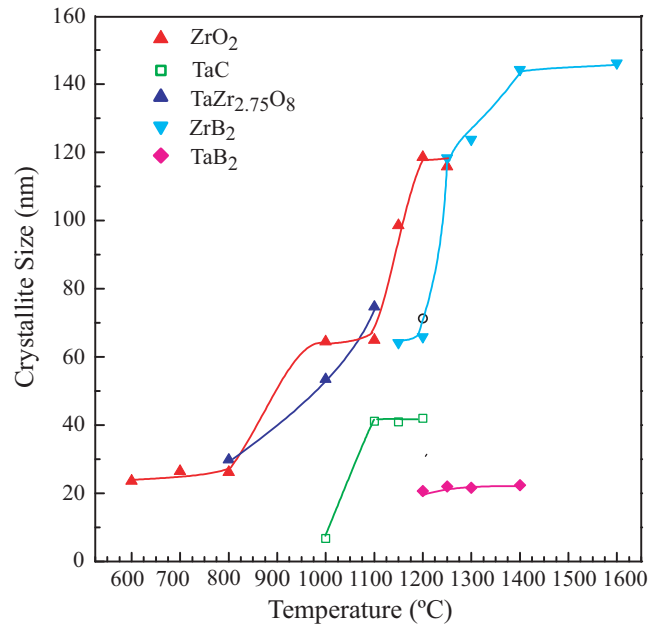


Fig 4.4: Plot of crystallite sizes (determined from XRD measurements) vs. heat treatment temperature for ZrB₂-TaB₂ composite.

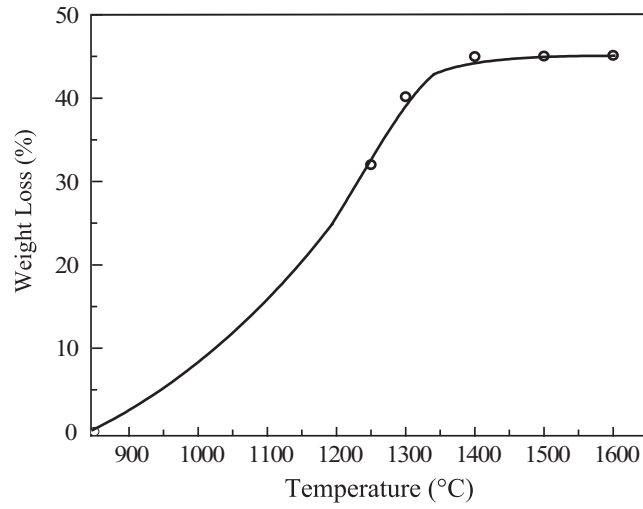


Fig 4.5: Weight loss vs. temperature for a ZrB₂-TaB₂-B₄C composite.

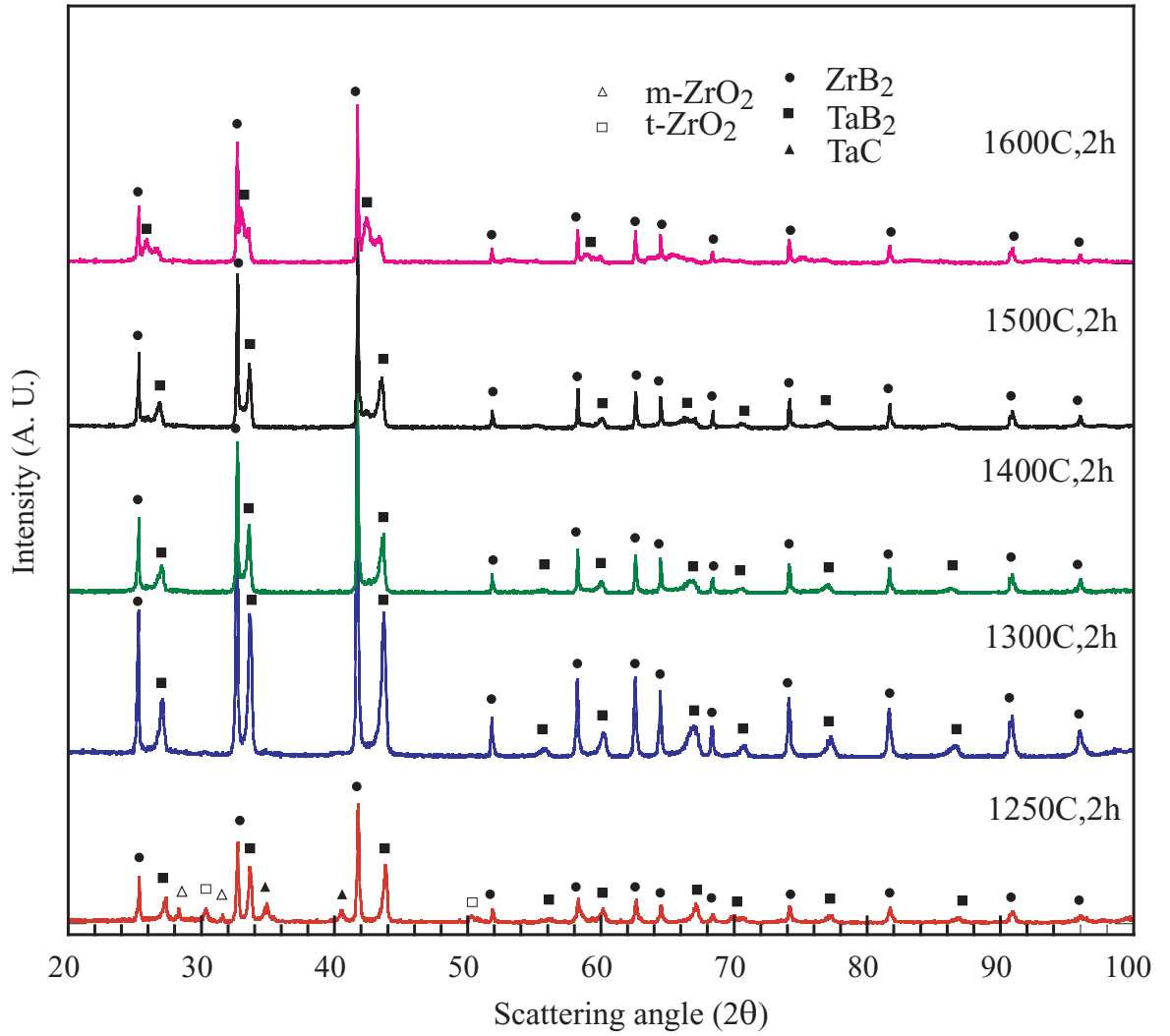


Fig 4.6: XRD patterns for $\text{ZrB}_2\text{-TaB}_2\text{-3wt\%B}_4\text{C}$ heat-treated from 1250°C to 1600°C for 2h.

Tab 4.1: Dimension and bulk density of $\text{ZrB}_2\text{-TaB}_2$ and $\text{ZrB}_2\text{-TaB}_2\text{-B}_4\text{C}$ pellets using new processing method where, ϕ is the diameter of pellets, δ is the thickness of pellets.

| Sample | Condition | Dimension and density | | | | |
|---|--------------------------------------|-----------------------|------------------|-----------|-----------------------------|------------------------|
| | | ϕ , mm | δ , mm | Wt, mg | Density, g/cm^3 | Relative density, % |
| ZrB_2 - TaB_2 | Green | 6.47 | 4.49 | 411.85 | 2.79 | 38.08 |
| | CIP | 6.37 | 3.75 | 411.03 | 3.44 | 46.95 |
| | Sinter at 2020°C , 1 h | 4.97 | 2.85 | 368.88 | 6.69 | 91.22 |
| ZrB_2 - $\text{TaB}_2\text{-B}_4\text{C}$ | Green | 6.48 | 4.37 | 393.26 | 2.73 | 39.40 |
| | CIP | 6.36 | 3.59 | 392.78 | 3.44 | 49.65 |
| | Sinter at 2020°C , 1 h | 5.02 | 2.89 | 369.13 | 6.48 | 93.48 |

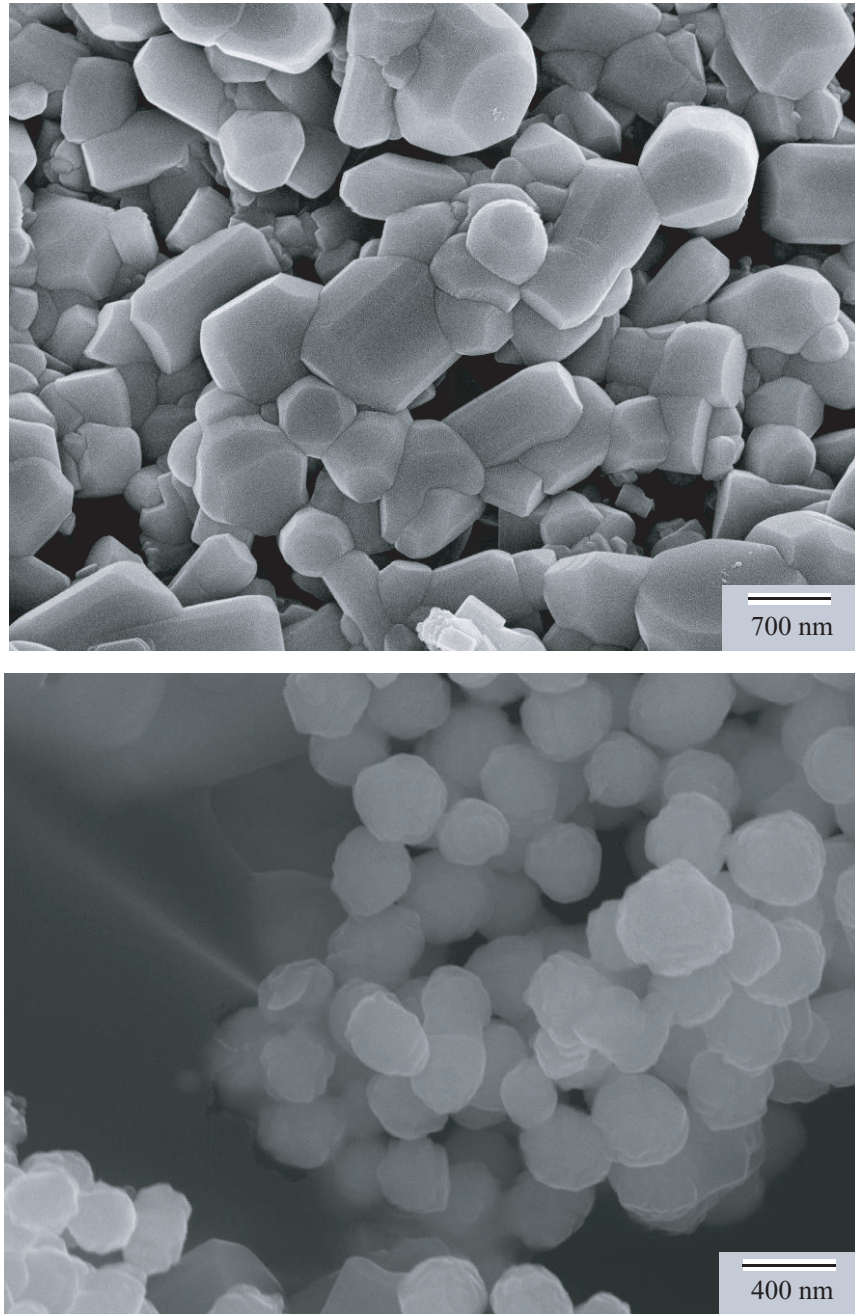


Fig 4.7: SEM micrograph of $\text{ZrB}_2\text{-TaB}_2\text{-3 wt\%B}_4\text{C}$ heat-treated at 1300°C (heating at $80^\circ\text{C}/\text{min}$ to 1225°C , $40^\circ\text{C}/\text{min}$ to 1265°C , $20^\circ\text{C}/\text{min}$ to 1285°C , $5^\circ\text{C}/\text{min}$ to 1295°C , $2^\circ\text{C}/\text{min}$ to 1299°C , and $1^\circ\text{C}/\text{min}$ to 1300°C) for 2 h.

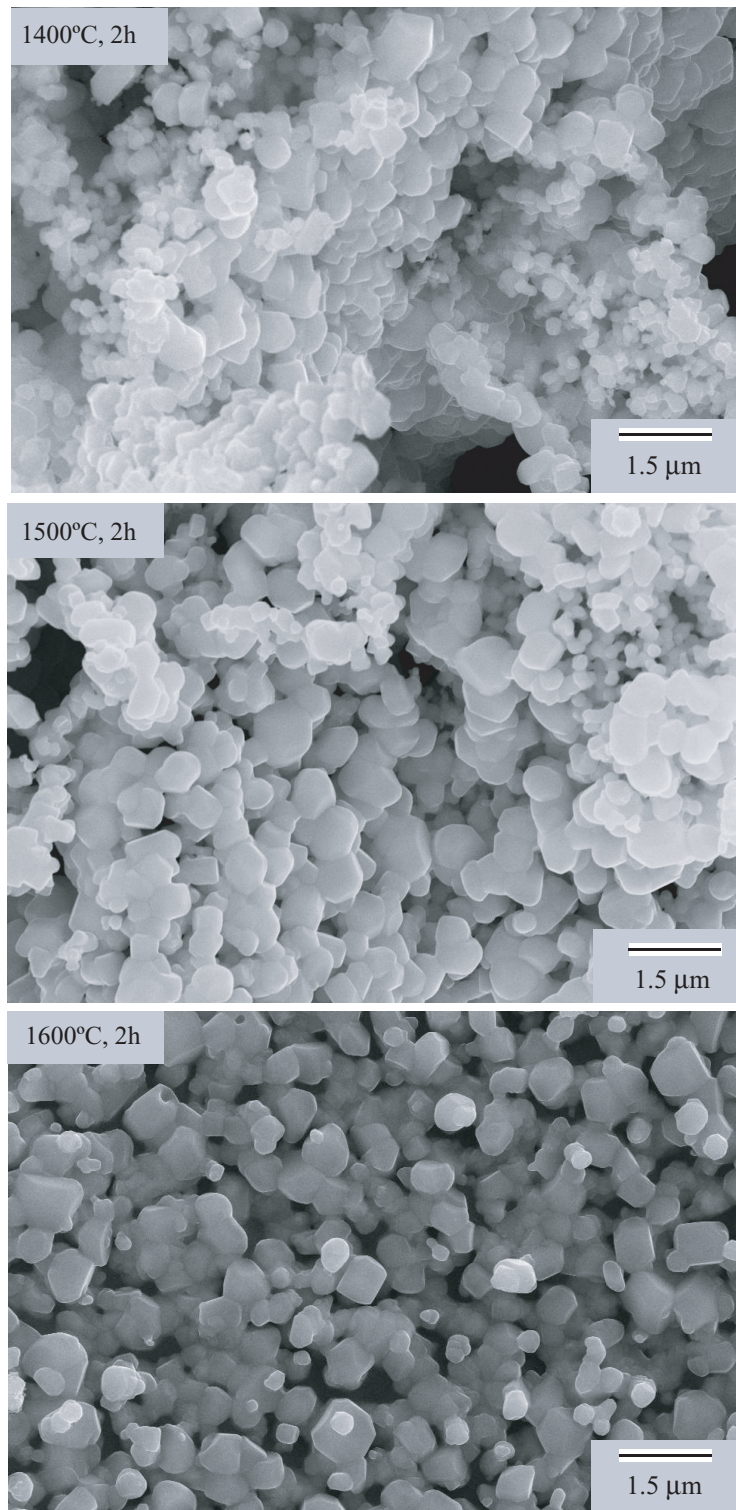


Fig 4.8: SEM micrograph of $\text{ZrB}_2\text{-TaB}_2\text{-3 wt\%B}_4\text{C}$ heat-treated at 1400°C , 1500°C , 1600°C for 2 h.

Tab 4.2: Archimedes density measurement of $\text{ZrB}_2\text{-TaB}_2$ and $\text{ZrB}_2\text{-TaB}_2\text{-B}_4\text{C}$ pellets sintered at 2020°C for 1 h in M11 furnace where, ϕ is the diameter of pellets, δ is the thickness of pellets.

| Sample | Dry weight, mg | Suspended weight, mg | Saturate weight, mg | Bulk Density g/cm^3 | Relative density, % |
|--|----------------|----------------------|---------------------|------------------------------|---------------------|
| $\text{ZrB}_2\text{-TaB}_2$ | 368.99 | 314.43 | 368.93 | 6.76 | 92.26 |
| $\text{ZrB}_2\text{-TaB}_2\text{-B}_4\text{C}$ | 370.97 | 315.22 | 370.00 | 6.76 | 97.21 |

Tab 4.3: Lattice parameter for ZrB_2 and TaB_2 .

| Phase | Sys. | a | c |
|----------------|-----------|---------|---------|
| ZrB_2 | hexagonal | 3.1687 | 3.53002 |
| TaB_2 | hexagonal | 3.09803 | 3.22660 |

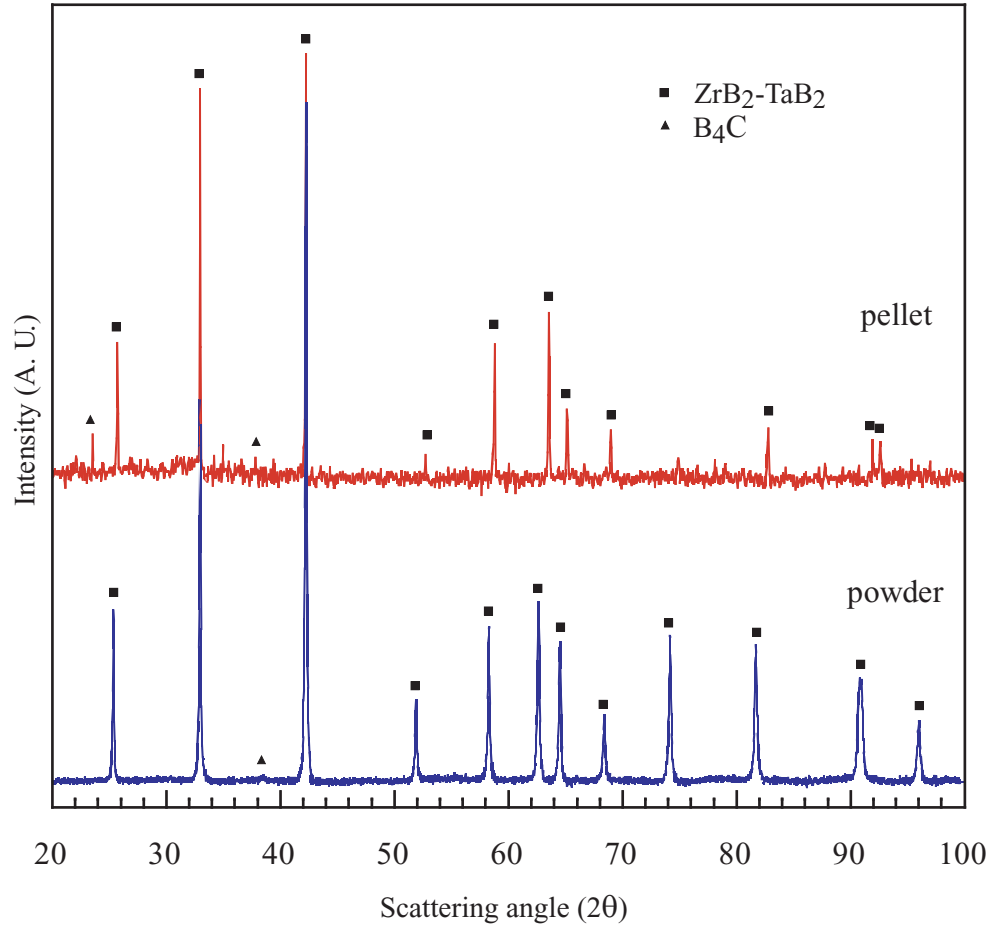


Fig 4.9: XRD patterns for $\text{ZrB}_2\text{-TaB}_2\text{-3 wt}\%\text{B}_4\text{C}$ powder and pellet sintered at 2020°C for 2h.

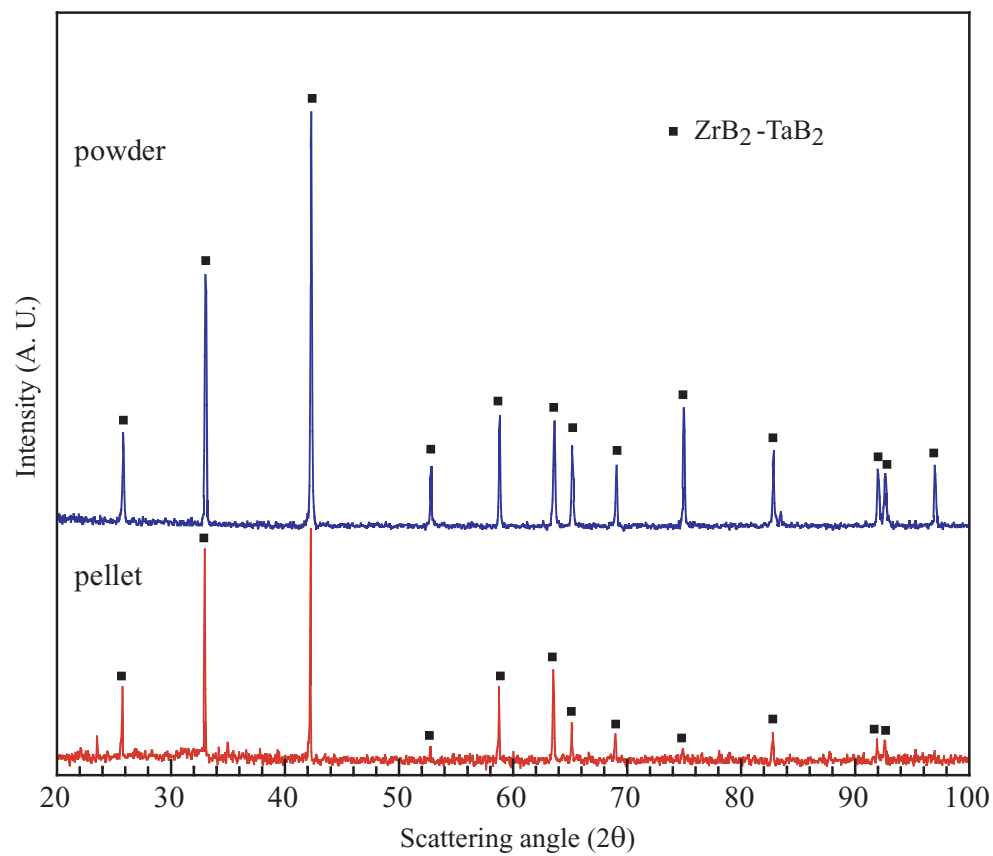


Fig 4.10: XRD patterns for $\text{ZrB}_2\text{-TaB}_2$ powder and pellet sintered at 2020°C for 2h.

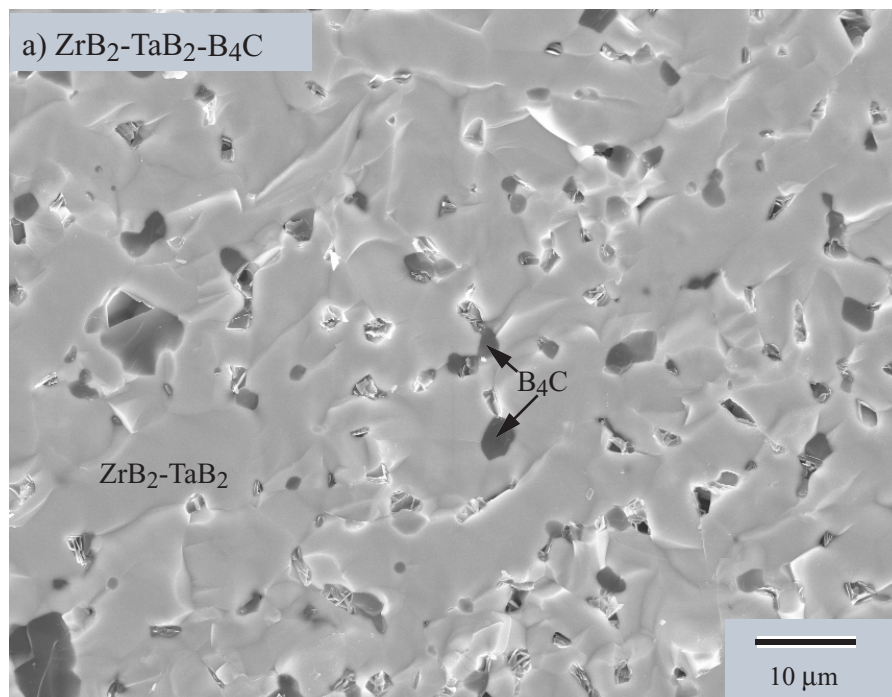
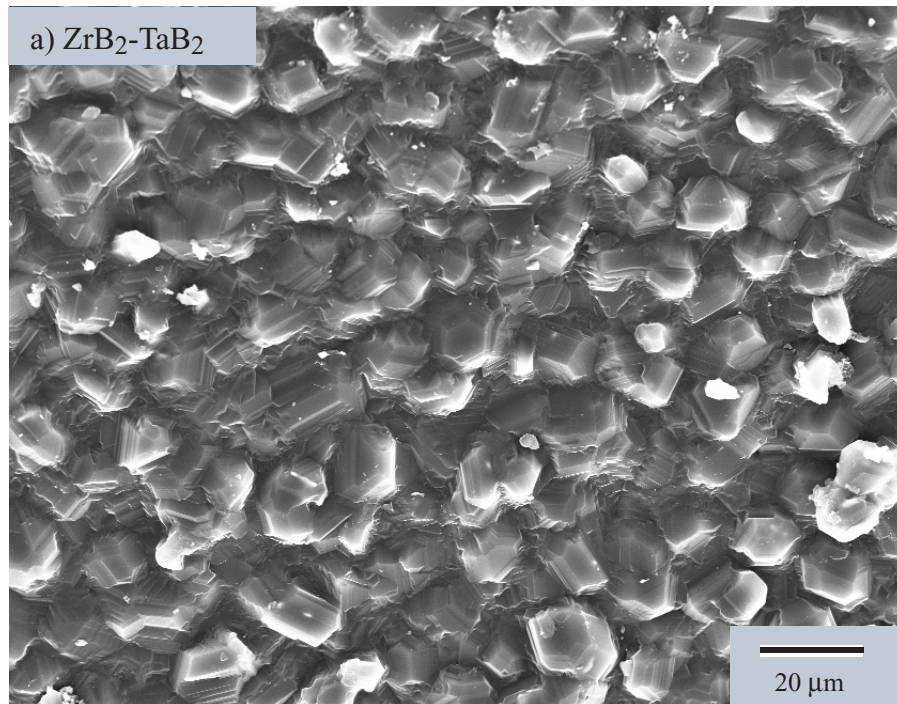


Fig 4.11: SEM micrograph for $\text{ZrB}_2\text{-TaB}_2$ and $\text{ZrB}_2\text{-TaB}_2\text{-B}_4\text{C}$ pellets sintered at 2020°C for 2h (crosssection of fractured pieces).

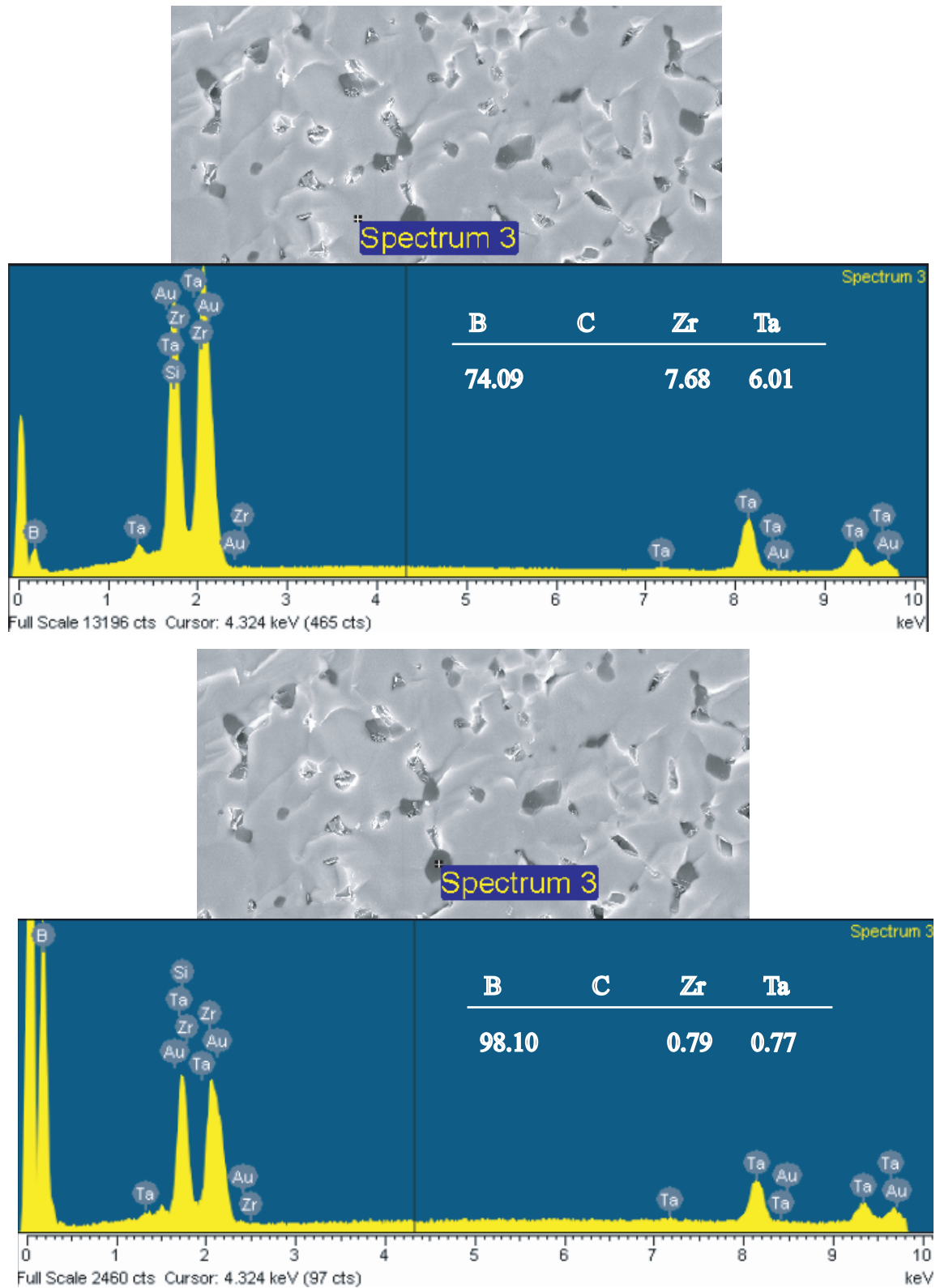


Fig 4.12: EDS spectra of ZrB₂-TaB₂-B₄C pellet sintered at 2020°C for 2h.

REFERENCES

4.4 *References*

- [1] E. Opila, S. Levine, J. Lorincz, “Oxidation of ZrB₂- and HfB₂-based Ultra-high Temperature Ceramics: Effect of Ta Additions,” *J. Mater. Sci.*, **39** 5969-5977 (2004).
- [2] M. Opeka, I. Talmy, J. Zaykoski, “Oxidation-based Materials Selection for 2000°C + Hypersonic Aerosurfaces: Theoretical Considerations and Historical Experience,” *J. Mater. Sci.*, **39** 5887 - 5904 (2004).
- [3] T. Watanabe and S. Kouno, “Mechanical Properties of TiB₂-CoB-metal Boride Alloys,” *Am. Ceram. Soc. Bull.*, **61** [9] 970-973 (1982).

CHAPTER 5

Research on the synthesis of $\text{ZrB}_2\text{-TaSi}_2$ and its sinterability

5.1 Synthesis of Submicron $\text{ZrB}_2\text{-TaSi}_2$ Composite by a Solution-based Method

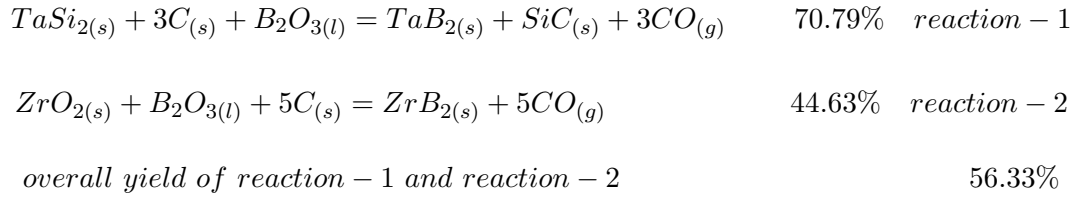
TaSi_2 added to the ZrB_2 powder can significantly improve its oxidation-resistance. However, the TaSi_2 powder was normally mixed with ZrB_2 powder [1] and uniform mixing cannot be obtained between these two phases. In this chapter, the TaSi_2 powder dispersed in 2-propanol was mixed with ZrB_2 -based solution to guarantee homogeneous mixture between TaSi_2 and ZrB_2 .

For this method, 0.06 mol ZrB_2 -based solution was first prepared according to the method described in I.5 of Chapter 2 with initial composition of $\text{C/Zr} = 4.8$, $\text{B/Zr} = 3.0$.

3.8 g (0.016 mol) TaSi_2 (molar ratio of $\text{Zr/Ta} = 3.75$) powder was ball-milled in 2-propanol for 8 h, and then the TaSi_2 slurry was added to above 0.06 mol ZrB_2 -based solution and strong stirring for 1 h. The particle size for TaSi_2 added to the system is ~ 200 nm- $1.2\ \mu\text{m}$ measured from the microscope picture shown in Figure 2.5 in chapter 2. The mixed slurry was initially concentrated by rotary evaporator and then dried at 120°C for 3 h in a vacuum oven. The dry powder was then pyrolyzed at 850°C in an alumina tube furnace under flowing argon to obtain fine-scale mixing of $\text{TaSi}_2/\text{ZrO}_2/\text{B}_2\text{O}_3/\text{carbon}$, which is the prerequisite to obtain products with particle size and uniform dispersion between different phases. This dry powder was heat-treated at higher temperature of 1300°C and 1400°C in a graphite tube furnace under flowing argon (Partial pressure of oxygen is $(1-5)\times 10^{-6}$) for boro/carbothermal reduction to get composite of $\text{ZrB}_2\text{-TaSi}_2$.

The XRD patterns of dry powder, pyrolyzed powder and samples after boro/carbothermal reduction at 1300°C and 1400°C are shown in Figure 5.1. The only phase appeared in the

dry powder is TaSi₂ and the others are amorphous because there are no peaks observed in the XRD pattern. While the dominant phases for pyrolysis powder are TaSi₂ and tetragonal ZrO₂ with trace of monoclinic ZrO₂. Those phases are combined together and the morphology is porous blocks as shown in the SEM photos (Figure 5.2). The peak for tetragonal ZrO₂ disappeared upon further heat treatment at 1300°C, but the peaks for monoclinic ZrO₂ increased and a new phase of TaZr_{2.75}O₈ observed in the XRD pattern of this sample although the dominant phases are ZrB₂, TaB₂ and TaSi₂. Those impurities of oxide disappeared after heat treatment at 1400 °C for 2 h in M11 furnace, and a composite of ZrB₂-TaB₂-TaSi₂ was obtained, which was unexpected. For this system, the possible reactions and their theoretical yield was listed as follows:



The yield for the reactions should be 56.33% if the TaB₂ came from the reaction 1 as described above. However, the yield for this sample heat treated at 1400°C is ~42% as shown in Table 5.1, similar but a little lower than the yield for reaction 2. This is reasonable because we assume that there is no boria evaporation for the reaction, however, it always happens during the boro/carbothermal reduction [3], which lead to more weight loss and results in a lower yield.

The peak of SiC was difficult to be identified in the XRD pattern because most of them overlap with TaSi₂, but SiC was found by EDS when sintering those material at higher temperature as shown in Figure 5.7), which proved reaction 1 should exist when sample heat treated at 1300°C and 1400°C. However, reaction 1 may not be the main reason for the high content of TaB₂ in products because there are much TaB₂ observed in the sample. Investigating the XRD pattern in detail, the typical peaks of tantalum zirconium oxide and ZrSi₂ were observed, but there is no reaction to produce such phases. Therefore, the phases of TaB₂, ZrSi₂ and ZrTa_{2.75}O_{0.8} may be result from the replacement between Zr and Ta. The dissolve between TiB₂, TaB₂ and CoB was also observed by Wantanate [4].

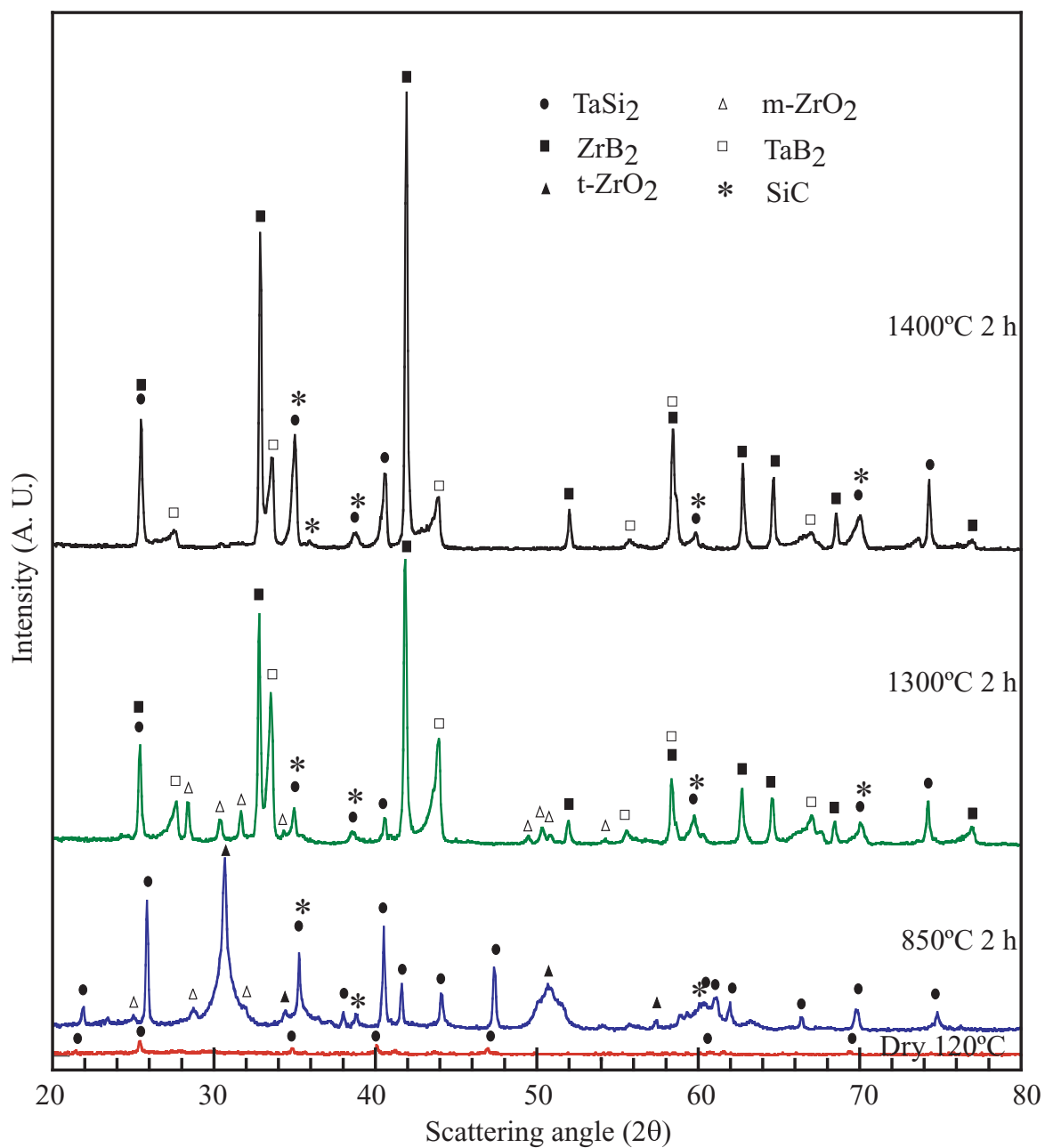


Fig 5.1: XRD patterns for ZrB₂-TaSi₂ pyrolyzed at 850°C and further heat-treated at 1300, 1400°C for 2h.

Tab 5.1: The Yields for ZrB₂-TaSi₂ Heat Treatments

| Temperature | Yield, % | Total yield from dry powder, % |
|-------------|----------|--------------------------------|
| 850, 2 h | 74.48 | |
| 1300, 2 h | 45.85 | 34.14 |
| 1300, 2 h | 46.04 | 34.29 |
| 1300, 2 h | 45.77 | 33.95 |
| 1400, 2 h | 42.70 | 31.80 |
| 1400, 2 h | 42.54 | 31.69 |
| 1400, 2 h | 42.47 | 31.63 |
| 1400, 2 h | 41.92 | 31.21 |
| 1400, 2 h | 42.10 | 31.36 |
| 1400, 2 h | 42.21 | 31.44 |

The particle size for product ZrB₂-TaSi₂ after boro/carbothermal reduction reaction at 1300°C is 50 nm-600 nm, as shown in Figure 5.3, while the particle size increased to 100 nm-800 nm after further heat-treatment at 1400°C as shown in Figure 5.4.

The phases of powder after heat treatment at 1400°C for 2 h are ZrB₂/TaB₂ and TaSi₂/ZrSi₂ are shown in the XRD pattern in Figure 5.1, without any trace of oxides or other impurities were observed. Those powders were used to preparing bulk pellet and their sinterability were also studied in this paper.

5.2 The Effect of Ball Milling on the Particle Size and Morphology of Particles

Ball milling is an efficient method to decrease the particle size and obtain more uniform distributed powders, however, too diluted slurry would decrease the efficient of ball-milling [5]. Therefore, we use ~ 25 ml solvent to disperse 6 g powders we studied.

Approximately 6 g ZrB₂-TaSi₂ powder heat-treated at 1400°C for 2 h were put into a vinyl container with 15 g B₄C media, and then 25 ml methanol was added into the bottle. Above operation were done in a glove box and the bottle was sealed and then taken out for 60 h ball-milling. A drop of suspension was taken out from the bottle and dripped onto the tape on a SEM sample mount when ball milled for 10 h, 40 h and 60 h, respectively. After ball-milling for 60 h, the suspension was dried in rotary evaporator and then methanol was added back and sonicated for 60 min. This step was repeated for at least 3 times. One drop

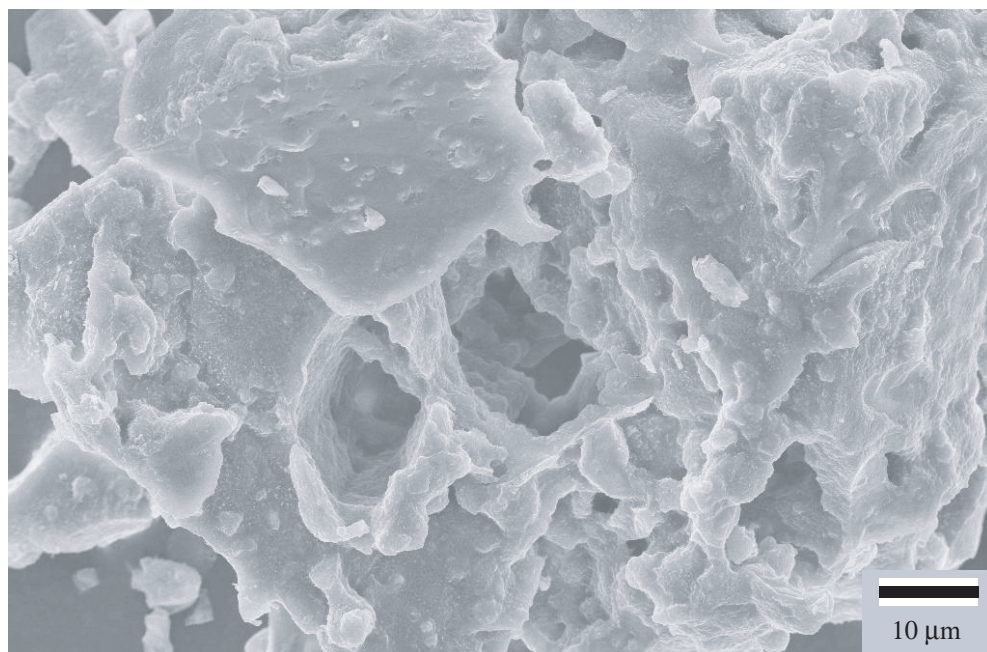


Fig 5.2: SEM micrograph of $\text{ZrB}_2\text{-TaSi}_2$ pyrolyzed at 850°C in Lindberg furnace for 2 h.

of suspension after sonicating was also taken for SEM observation. All the steps related to sample taken or solvent change were done in the glove box to avoid sample exposure to air.

The samples on SEM mounts were dried in air and then coated with gold by sputter coating. Particle sizes and morphologies of the particles were observed by the LEO SEM.

Ball milling was an efficient method to break the agglomerates and obtain fine particle distributions, but it's not an efficient way to break the large solid crystals [5]. For the $\text{ZrB}_2\text{-TaSi}_2$ sample we used, small particles adhered to the surface of large particles and formed huge agglomerates when ball milling for 10 h. The surfaces of the large particles are rough and there was almost no free fine particles observed in the sample (as shown in Figure 5.5-a).

The amounts of free fine particles separated from the others increased with the time of ball-milling. The ratio of fine particles separated from the others to large particles increased from 0 (after ball-milling for 10 h as shown in Figure 5.5-a.) to $\sim 60\%$ after ball-milling for 40 h, as shown in Figure 5.5-b, and $\sim 85\%$ after ball-milling for 60 h as shown in Figure 5.5-c. The surfaces of large particles became smooth after ball-milling for 60 h because the small particles attached to their surfaces were removed and became free fine particles. The sharp

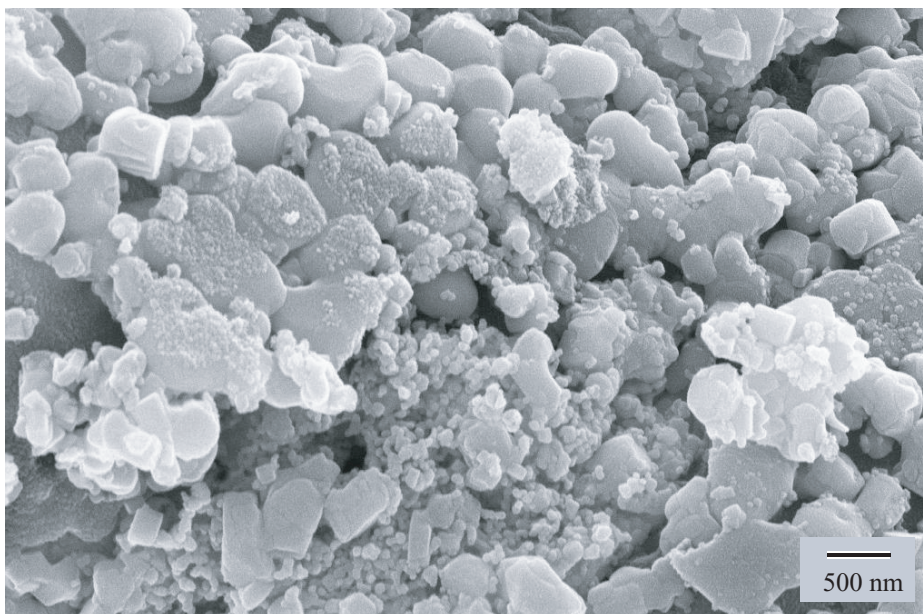


Fig 5.3: SEM micrograph of $\text{ZrB}_2\text{-TaSi}_2$ heat treated at 1300°C in the M11 furnace for 2 h (heating at $80^\circ\text{C}/\text{min}$ to 1225°C , with successively slower rates as 1300°C was approached).

edges also became rounded.

The large particle size also decreased from $\sim 1.2\ \mu\text{m}$ at the beginning to 600 nm after ball-milling for 60 h. The large agglomerates were broken by the mechanical force and shear force from the ball grinding and collision. Ultra sonication was more powerful in breaking agglomerates and powders with much more uniform distribution was observed after sonication for 60 min, as shown in Figure 5.6. The ratio of fine particles to large particles was $\sim 90\%$.

5.3 Sintering of $\text{ZrB}_2\text{-TaSi}_2$ Powder

The powder after ball-milling, sonication and methanol-washing was dried in a rotary evaporator and then further dried in a vacuum oven at 120°C for 3 h. Binder (0.69 wt%PEG and 3.46 wt%PVA) and plasticizer (0.52 wt% Darven 821A) were added to the above dry powder using water (60.71 wt%) as solvent (the weight percent of binder was compared with the weight of dry powder interested), the slurry was then ball-milled for 6 h and then dried similarly. After grinding and sieving, the powder was used for dry pressing.

The bulk pellets were prepared by uniaxial dry pressing and $\sim 400\ \text{mg}$ powder was used

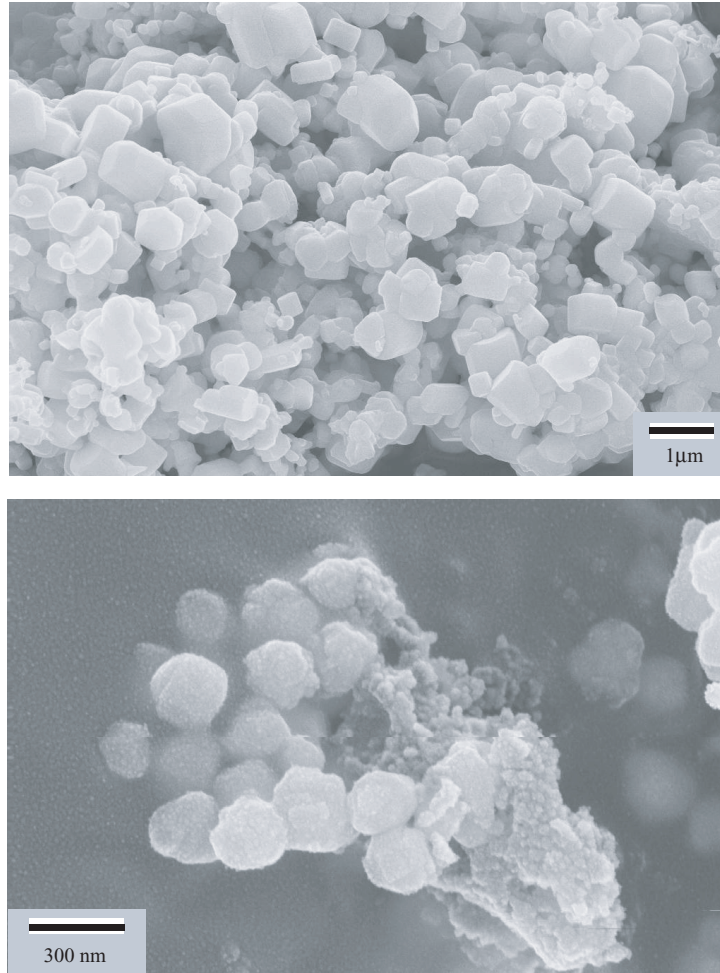


Fig 5.4: SEM micrograph of $\text{ZrB}_2\text{-TaSi}_2$ heat treated at 1400°C in M11 furnace for 2 h (heating at $80^\circ\text{C}/\text{min}$ to 1325°C , with successively slower rates as 1400°C was approached).

for every pellet. The dimensions of the stainless steel die used have a diameter of 6.4 mm and a height of 14 mm. The dry powder was compacted at 150 MP and held for 30 sec. The dimension and weight of the green pellets were measured and the dimensional density was calculated. The green pellets were then cold isostatic pressed (CIP) at 45000 PSI for 30 s. The dimensional density was also measured and calculated. The green density and dimensional density after CIP were recorded in Table 5.2.

The theoretical density was calculated by assuming there was only ZrB_2 and TaSi_2 present in the powder with a composition the same as desired. Considering the loss of TaSi_2 by transferring and ball-milling, it is ~ 3.2 g TaSi_2 (0.0135mol) in 0.06 mol (6.77 g) ZrB_2 , that is 32.1 wt% TaSi_2 and 67.9 wt% ZrB_2 (the molar ratio of $\text{Zr}/\text{Ta} = 4.45$). Therefore,

Tab 5.2: Dimensional density of ZrB₂-TaSi₂-green and pellet after CIP where, ϕ is the diameter of pellets, δ is the thickness of pellets.

| Condition | pellet No ϕ , mm | Dimension and density | | | | |
|-----------|-----------------------------|-----------------------|-----------|-------------------------------|------------------------|-------|
| | | δ , mm | Wt, mg | Density, g/cm ³ | Relative density, % | |
| Green | P1 | 6.41 | 3.46 | 411.15 | 3.68 | 54.02 |
| | P2 | 6.41 | 3.42 | 407.97 | 3.70 | 54.28 |
| | P3 | 6.41 | 3.35 | 397.78 | 3.69 | 54.14 |
| | P4 | 6.40 | 3.43 | 404.01 | 3.66 | 53.73 |
| CIP | P1 | 6.26 | 3.39 | 410.65 | 3.95 | 57.92 |
| | P2 | 6.24 | 3.33 | 407.71 | 4.00 | 58.75 |
| | P3 | 6.25 | 3.33 | 406.71 | 3.99 | 58.47 |
| | P4 | 6.24 | 3.33 | 404.05 | 3.98 | 58.37 |

the theoretical density can be calculated as follows:

$$TD = 100 / (67.9 / 6.085 + 32.1 / 9.14) = 6.81$$

where 9.14 g/cm³ is the theoretical density for TaSi₂, and 6.085 g/cm³ is the theoretical density for ZrB₂

The pellets after CIP were de-bindered at 500°C for 24 h in an alumina tube furnace under flowing argon, with low heating rate of 0.2°C/min to avoid the accumulation of stress which may result in cracks. The pellet were then sintered in a graphite tube furnace at 2020°C for 30 min under a flowing argon atmosphere with a high heating rate of 50°C/min (but the heating rate was decreased when the temperature was near the soak temperature to avoid overshooting).

For sintering, 3 pellets were loaded into the furnace at same time, but the first one was buried in B₄C powder, the second one was put on a ZrB₂ substrate, and the third one was directly put on the graphoil boat to hold these three pellets. The Archimedes' densities of these three pellets after sintering were measured and the results are listed in Table 5.3.

The relative density for the pellet buried in B₄C powder during sintering was 95.73%, but the relative densities for those pellets either on ZrB₂ substrate or on graphoil were very low, only 64%, although all the three pellets were sintered under the same heat-treatment conditions. The reason maybe that zirconium diboride are sensitive to moisture and oxygen, which adsorb moisture when exposed to air and then may oxidized during heat-treatment.

Tab 5.3: Archimedes density measurement of ZrB₂-TaSi₂ pellets sintered at 2020°C for 30 min in M11 furnace.

| Sample | Dry weight, mg | Suspended weight, mg | Saturate weight, mg | Bulk Density g/cm ³ | Relative density, % |
|-----------------------------------|----------------|----------------------|---------------------|--------------------------------|---------------------|
| Buried in B ₄ C powder | 163.32 | 139.82 | 164.85 | 6.52 | 95.73 |
| On ZrB ₂ substrate | 173.93 | 150.39 | 190.00 | 4.39 | 64.42 |
| On graphoil | 335.79 | 289.84 | 369.53 | 4.21 | 61.83 |

We had ever put a pellet with diameter of 1.5 cm and thickness of 3 mm into air overnight and then sintering it at 1800°C for 2 h in flowing argon (partial pressure of oxygen is about 10⁻⁶) when we made the ZrB₂ substrate. The surface of the pellet are white and XRD results showed that the phase is zirconium oxide, but inside is black ZrB₂. While the B₄C can reacted with ZrO₂ and thus let the pellet buried in it being sintered. Figure 5.7 shows the SEM micrograph of pellets put on ZrB₂-substrate or buried in B₄C while sintering. It showed that the pellet not buried in boron carbide was not sintered at all, while for the pellet buried in B₄C sintered well but still some pores were observed. The Archimedes' density of the fracture of pellet buried in B₄C was same as the intact pellet before fracture, which mean that the pore observed should be closed.

Figure 5.8 gives the XRD pattern of those three pellet put on graphoil, ZrB₂-substrate and buried in B₄C powder while sintering, which shows that there was no difference in their XRD patterns except the intensity. The phases observed in the XRD pattern are ZrB₂, TaSi₂ and an unknown phase and ZrB₂ is the dominant phase. The unknown phase may be a solid solution among ZrB₂, TaB₂ and TaSi₂ because they have similar crystal structure (hexagonal), and Zr, Ta can diffuse into each other's lattice, but this was not proven. A powder sample, which was taken out before the ball-milling and following processing, was heat-treated at the same condition as the pellets at 2020°C, but the unknown phase was not observed in its XRD pattern (shown in Figure 5.9) and the peaks for TaSi₂ are more clear compared with the XRD pattern of the pellets.

5.4 Conclusion

Uniformly distributed $\text{ZrB}_2\text{-TaSi}_2$ ($\text{Zr}/\text{Ta} = 4.45$) composite has better oxidation-resistance than pure ZrB_2 , but the mixing of powder do not guarantee homogeneous mixture, thus decrease the advantages of this material. In this study, the slurry of TaSi_2 was mixing with ZrB_2 -based solution to make sure the homogeneous mixing. The particle size of this composite after heat-treating at 1400°C for 2 h in a graphite tube furnace under flowing argon.

The influence of ball-milling on the particle size distribution was studied in this chapter. Ball-milling is an efficient method to break agglomerates and get more uniformly distributed powders. But sonication is more powerful on dispersing powders than ball-milling.

The $\text{ZrB}_2\text{-TaSi}_2$ pellets were sintered at 2020°C for 30 min in the M11 furnace under the same heat treatment condition, but the density of pellet buried in B_4C powder during sintering was much higher than the pellets put on ZrB_2 substrate or on graphoil. The relative density for the pellet buried in B_4C powder is 95%, while for those sintered without being buried in B_4C was only 64%. The reason may be the moisture and air adsorbed on the surface of samples reacted with ZrB_2 and formed ZrO_2 , which is proved to inhibit the densification of this material, while buried in B_4C can avoid such problem and resulted in highly densified pellet.

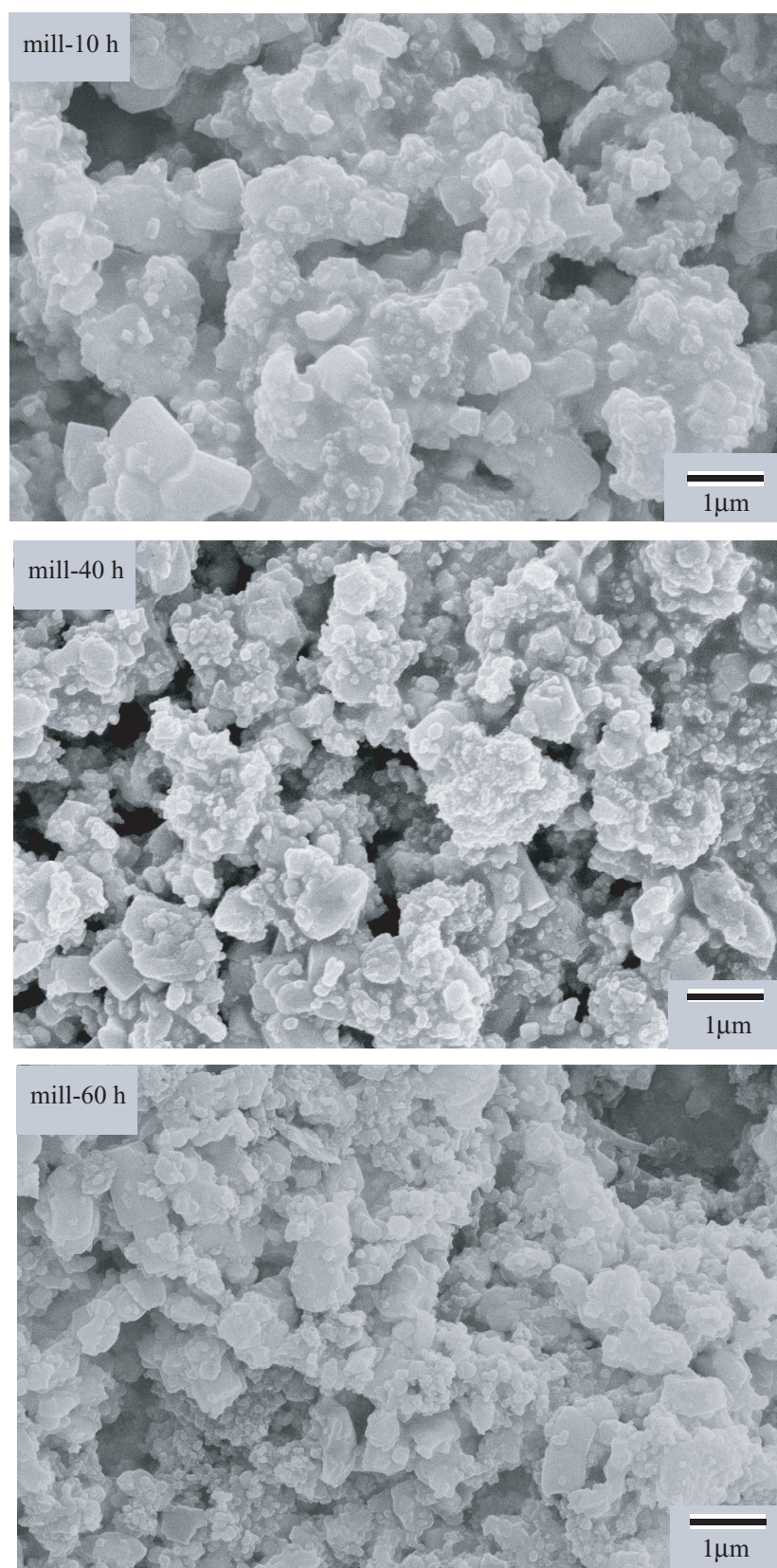


Fig 5.5: SEM micrograph of $\text{ZrB}_2\text{-TaSi}_2$ powder after ball-milling for 10 h, 40 h and 60 h.

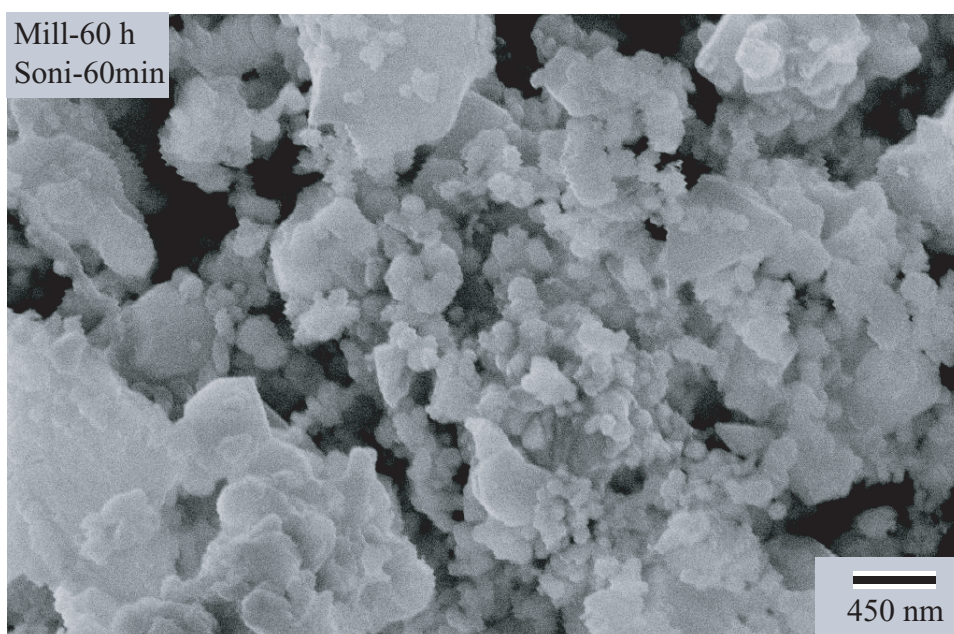
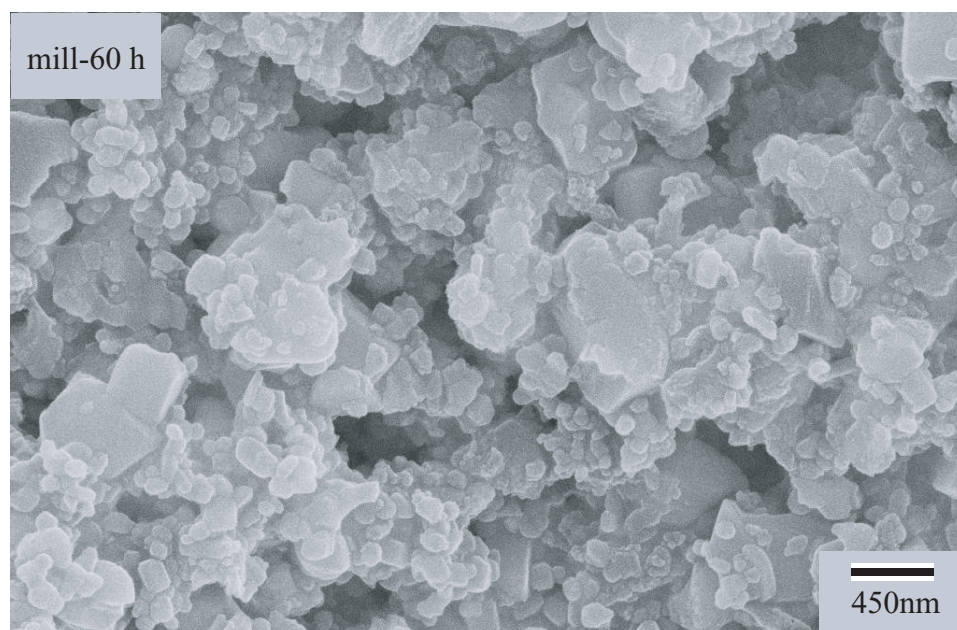


Fig 5.6: (a) SEM micrograph of ZrB₂-TaSi₂ powder after ball-milling for 60 h (b) SEM micrograph of ZrB₂-TaSi₂ powder after ball-milling for 60 h and sonication for 60 min.

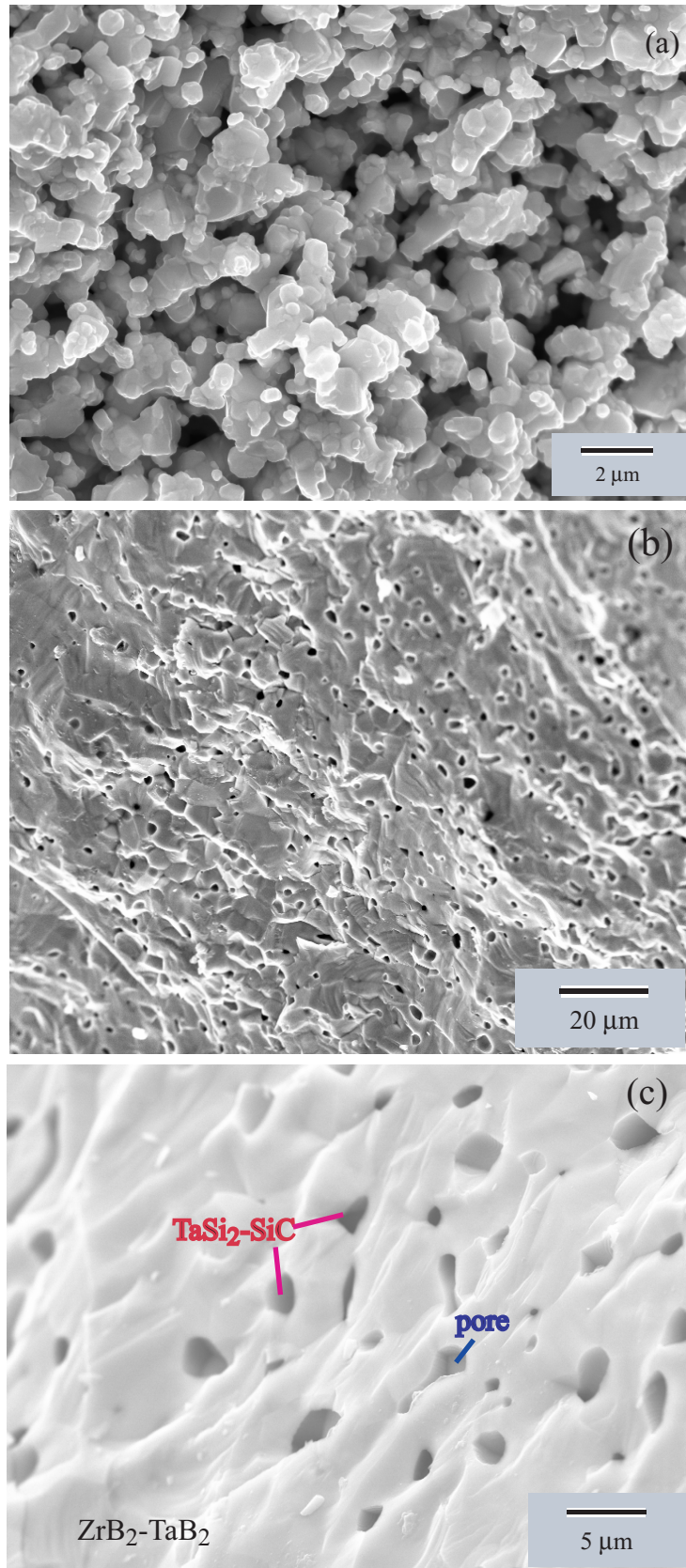


Fig 5.7: SEM micrograph of the crosssection of fractured $\text{ZrB}_2\text{-TaSi}_2$ pellet heat treated 2020°C for 1h. (a) Pellet on ZrB_2 substrate. (b) Pellet buried in B_4C powder. (c) magnification of b.

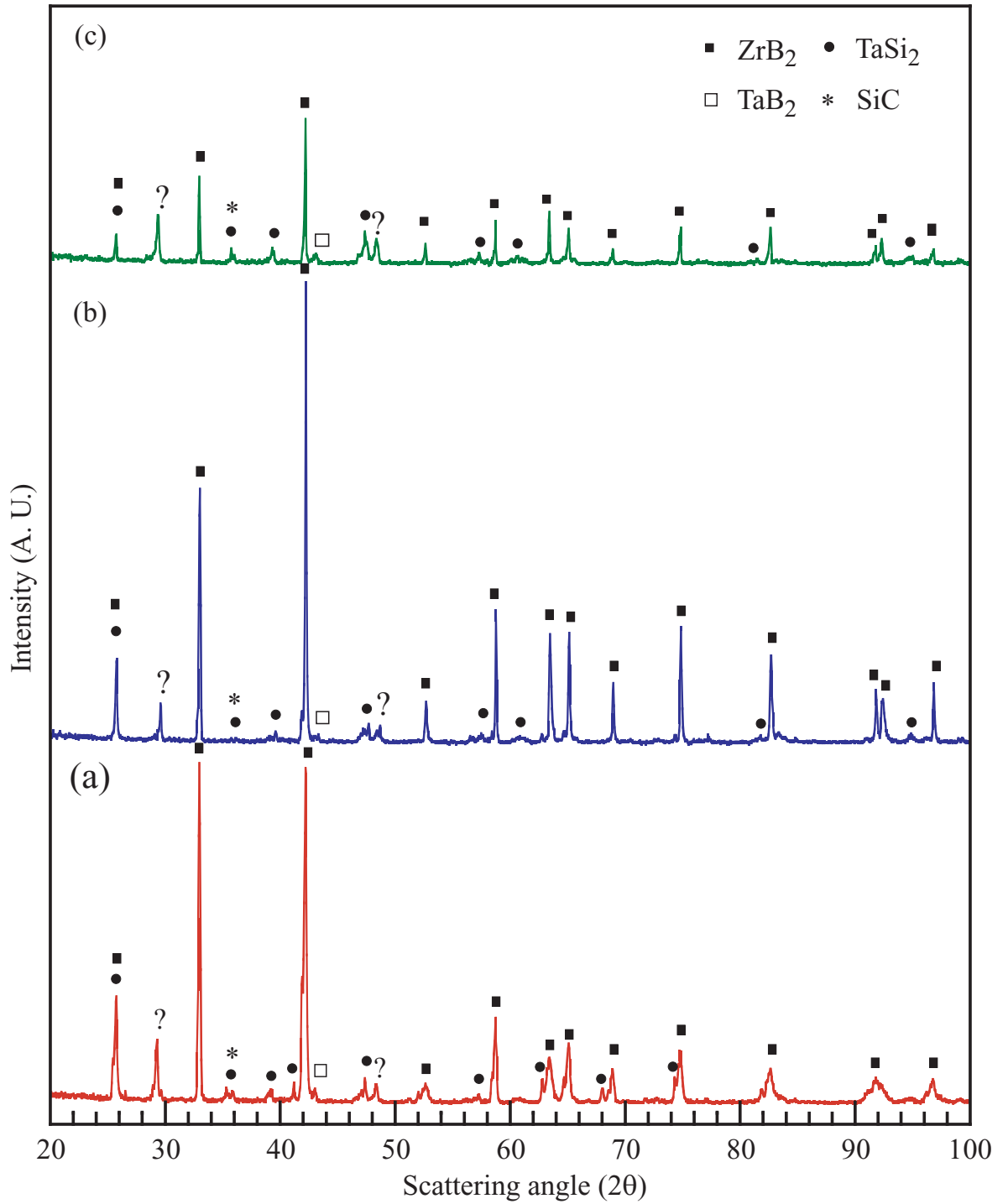


Fig 5.8: XRD patterns for $\text{ZrB}_2\text{-TaSi}_2$ powder and pellet heat treated 2020°C for 1h. (a) Pellet on graphoil. (b) Pellet on ZrB_2 substrate. (c) Pellet buried in B_4C powder. (For the peaks at diffraction angle of ~ 29 and 48°), no ICDD card match them. They may be solid solution between ZrB_2 , TaB_2 or TaSi_2 .

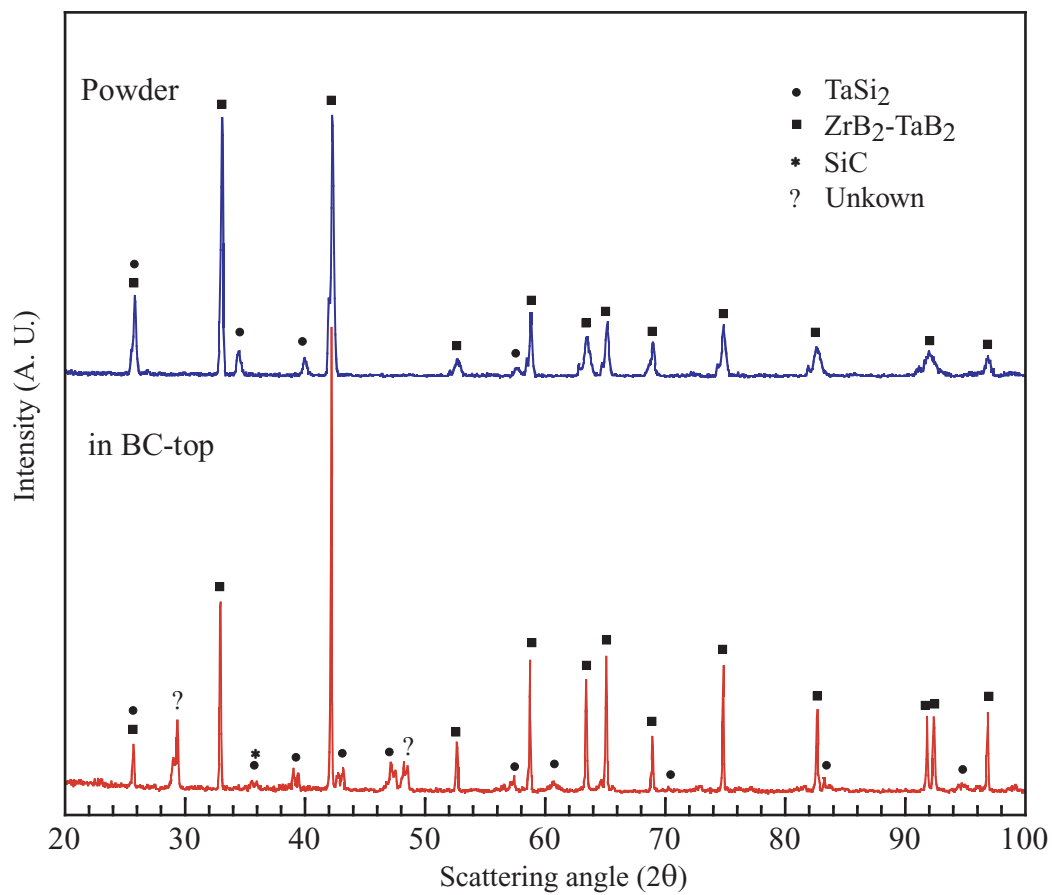


Fig 5.9: XRD patterns for $\text{ZrB}_2\text{-TaSi}_2$ powder and pellet heat treated 2020°C for 1h (For the peaks at diffraction angle of ~ 29 and 48°), no ICDD card match them. They may be solid solution between ZrB_2 , TaB_2 or TaSi_2 .

REFERENCES

5.5 References

- [1] M. Opeka, I. Talmy, J. Zaykoski, “Oxidation-based Materials Selection for 2000°C + Hypersonic Aerosurfaces: Theoretical Considerations and Historical Experience,” *J. Mater. Sci.*, **39** 5887 - 5904 (2004).
- [2] T. Watanabe and S. Kouno, “Mechanical Properties of TiB₂-CoB-metal Boride Alloys,” *Am. Ceram. Soc. Bull.*, **61** [9] 970-973 (1982).
- [3] Alan W. Weimer, Raymond P. Roach, Christopher N. Haney etc. “Rapid carbothermal reduction of boron oxide in a graphite transport reactor,” *AIChE Journal*, **37**[5] 759-768 (1991).
- [4] Mohamed N. Rahaman. *Ceramic Processing*, CRC press, Boca Raton, FL (2007).
- [5] Mohamed N. Rahaman. *Ceramic processing and sintering*, Dekker press, New York (2003).

CHAPTER 6

Research on the Synthesis of Nanocrystalline ZrB₂-based Composites

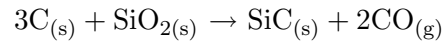
6.1 *Preparation of the Nanocrystalline ZrB₂-based SiC Composite*

6.1.0.5 *Preparation of the Nanocrystalline ZrB₂-based SiC Composite*

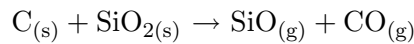
SiC sol was prepared by mixing a silica-bearing precursor (tetraethoxysilane with a formula of (C₂H₅O)₄Si, often referred to as “TEOS”) and a carbon-bearing precursor (phenolic resin). Propanol was used as a mutual solvent. The SiC sol after hydrolysis was mixed with ZrB₂ sol and then concentrated and dried in a vacuum oven as described in I.3.1 of chapter 2. The dry powder was used for pyrolysis and further boro/carbothermal reduction.

Figure 6.1 shows XRD patterns of the ZrB₂/20 vol%SiC composite after pyrolysis at 1100°C and boro/carbothermal reduction at 1400°C for 2h. The XRD pattern for pyrolysis sample showed that the boria, carbon and silica are amorphous in pyrolyzed powder because it only showed peaks of m-ZrO₂ and t-ZrO₂. The sample also showed only ZrB₂ and SiC in the product with crystallite sizes (determined by XRD line broadening) of ~57 nm for ZrB₂ and 15 nm for SiC after borothermal/carbothermal reduction. The SEM photo of this sample is shown in Figure 6.2, which shows that the crystal size of ZrB₂ is in the range of 20-250 nm, and the size for SiC is <20 nm.

The overall carbothermal reduction reaction to form SiC was given by:



However, evidence from previous studies showed that SiC is produced by a multi-step process[1, 2, 3]:



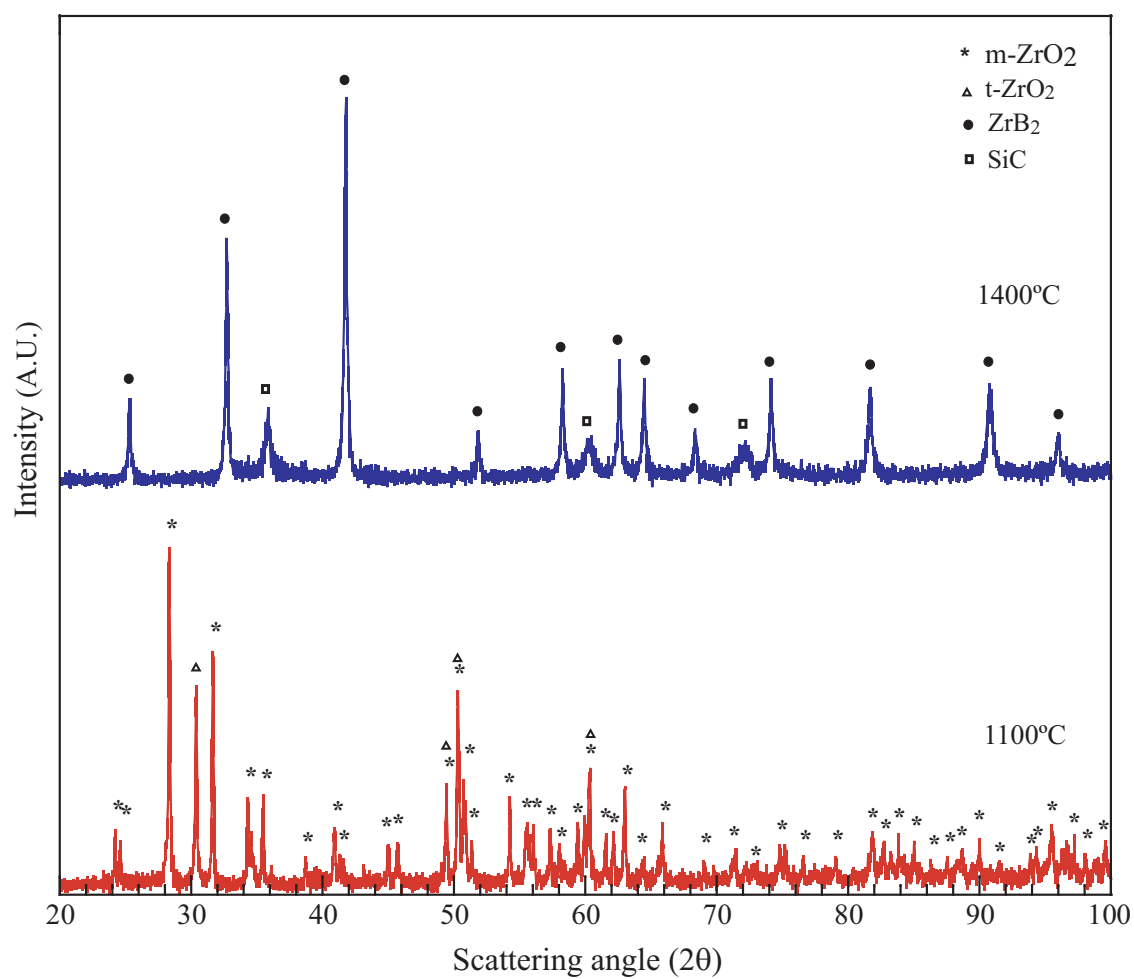


Fig 6.1: XRD pattern for ZrB_2 -20 vol% SiC heat-treated at 1100°C or 1400°C for 2h.

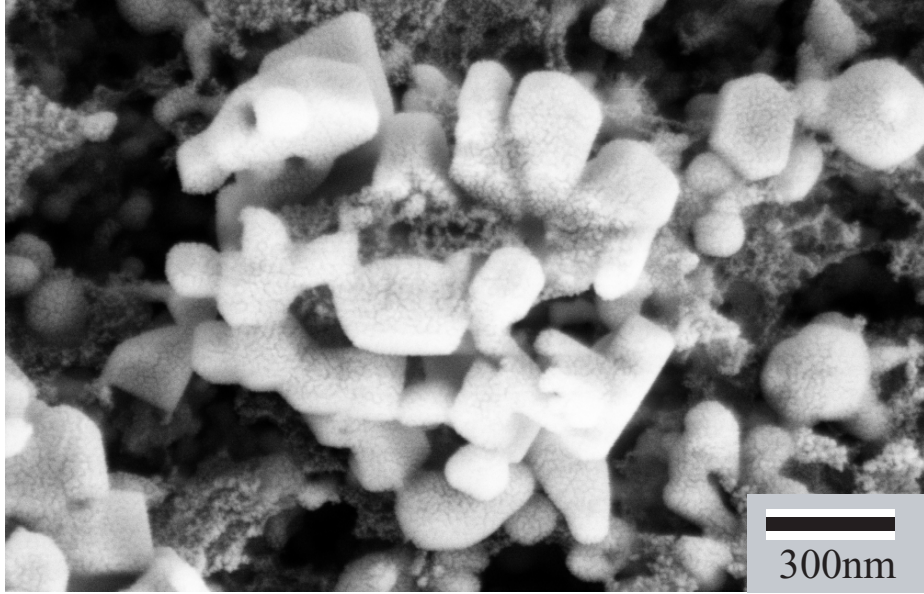
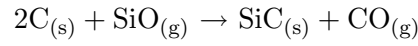


Fig 6.2: SEM photo of ZrB₂-SiC sample heat-treated at 1400°C for 2 h in an alumina tube furnace.



It involves intermediate reactions which generate SiO vapor. Transporting of the SiO vapor to the carbon phase, and subsequent reaction at the carbon surface is necessary to form SiC. A high flow rate would remove the SiO vapor from furnace and could not react with carbon to form SiC, therefore, the argon flow rate should not be too high.

6.1.0.6 Preparation of the ZrB₂-TaB₂-SiC Composite

The ZrB₂-TaB₂-SiC composite was synthesized using the method described in I.4.2 of chapter 2. The dry powder was then pyrolyzed in the Lindberg furnace under flowing argon at 700, 800, 1000, 1100°C for 2 h to obtain a fine-scale mixture of ZrO₂/B₂O₃/SiO₂/carbon. The pyrolyzed powder was then further heat-treated at 1150, 1200, 1300, 1400, 1600 and 1800°C in M11 furnace under flowing argon for boro/carbothermal reduction reaction to obtain a ZrB₂-TaB₂-SiC composite. The powder was heat-treated at multiple temperatures to discern the detail of phase development with temperature; the XRD pattern for this sample is shown in Figure 6.3.

Figure 6.3 showed that the dominant phase in the pyrolyzed powder is a compound of ZrO₂ and Ta₂O₅ with a composition of TaZr_{2.75}O₈. A trace of Ta₂O₅ and t-ZrO₂ was

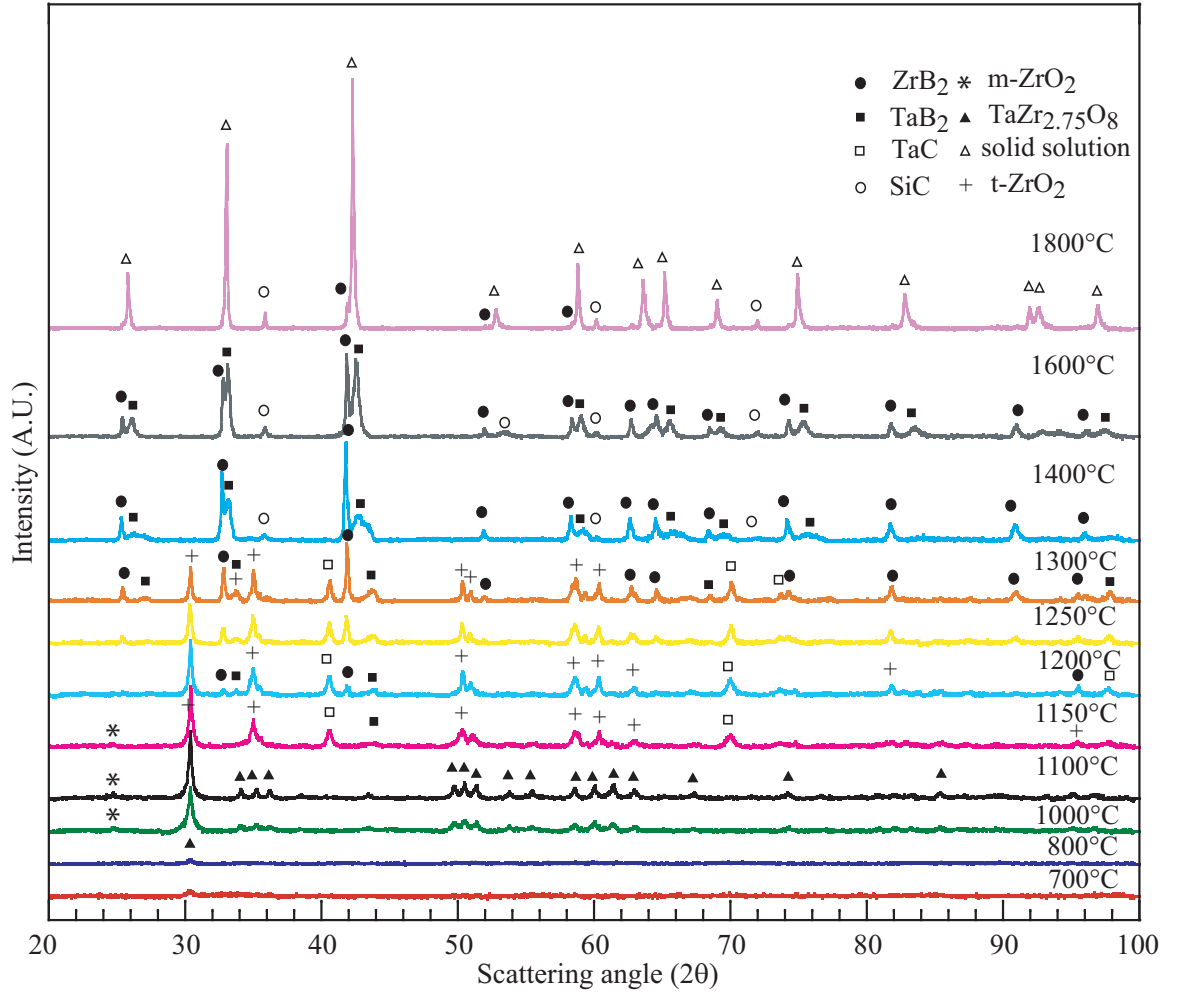
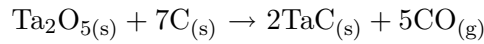
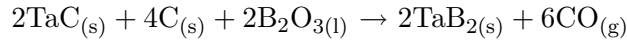


Fig 6.3: XRD patterns for $\text{ZrB}_2\text{-TaB}_2\text{-SiC}$ heat-treated from 700°C and 1800°C for 2h.

also observed in the sample pyrolyzed at 700°C. The peak intensity of TaZr_{2.75}O₈ kept increasing until 1100°C, and then disappeared at 1150°C, at which point the borother-mal/carbothermal reduction began and TaB₂ was observed in the XRD pattern. TaC was also observed at 1150°C, and the phase development finished at 1300°C. The ZrB₂ phase was first observed at 1200°C, and the intensity kept increasing to 1400°C, and then the intensity decreased due to the formation of solid solution with TaB₂. The pure composite of ZrB₂-TaB₂-SiC was obtained at 1400°C, but the intensity of SiC was weak. The intensity of SiC increased after further heat treatment at higher temperature. However, the peak position of ZrB₂ and TaB₂ moved closer gradually forming a mutual solid solution. Finally, the peaks of ZrB₂ and TaB₂ combined together at 1800°C.

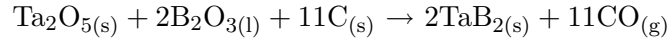


$$\Delta G = -16.46 \text{ kJ/mol, at } 1400 \text{ K}$$



$$\Delta G = -20.14 \text{ kJ/mol, at } 1800 \text{ K}$$

The overall boro/carbothermal reduction reaction was:



$$\Delta G = -115.67 \text{ kJ/mol, at } 1500 \text{ K}$$

Figure 6.4 shows a plot of weight loss vs. temperature from 700°C to 1800°C and the results were consistent with the XRD patterns. It illustrates that a gradual weight loss of 3.55% occurred between 700-1100°C, followed by rapid weight loss at temperature ranges of 1150-1400°C due to the boro/carbothermal reduction reaction. The borother-mal/carbothermal reduction was mostly completed by 1400°C, and the XRD pattern showed that it is a pure composite of ZrB₂-TaB₂-SiC. The weight loss at higher temperature (> 1400°C) was negligible, the total weight loss between 1400-1800°C was only 1.1%, which is interpreted to have resulted from the carbothermal reduction to form SiC, based on phase development of the SiC that was observed in the XRD pattern.

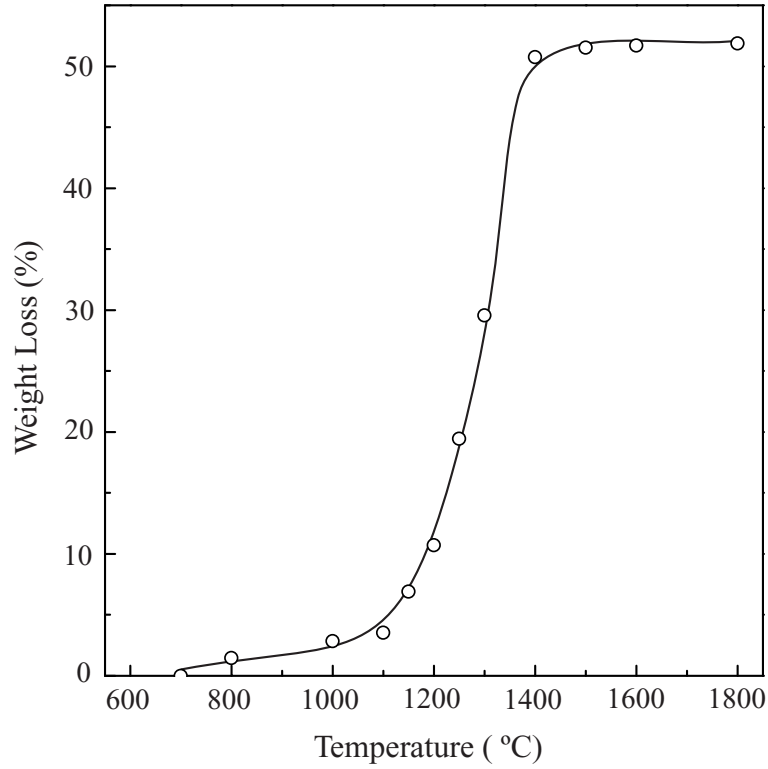


Fig 6.4: Plot of weight loss vs. temperature for $\text{ZrB}_2\text{-TaB}_2\text{-SiC}$ composite.

The particle sizes for sample $\text{ZrB}_2\text{-TaB}_2\text{-SiC}$ heat-treated at different temperature are shown in Figure 6.5. In contrast with $\text{ZrB}_2\text{-TaB}_2$ composite, the crystallite sizes for most phases in this composite, such as $\text{TaZr}_{2.75}\text{O}_8$, ZrB_2 and TaB_2 , did not increase significantly with increasing temperature, except SiC. Apparently, the SiC in the composite inhibited the crystal growth of diborides.

Figure 6.6 shows the appearance and phases determined by EDS of particles heat treated (in flowing argon, partial pressure of oxygen in argon is 10^{-6}) at 1600°C . TaB_2 and ZrB_2 regions were not visibly distinct, whereas regions of smaller SiC particles are apparent. The particle sizes for the combined diborides and SiC were ~ 500 nm and ~ 150 nm, respectively. Oxygen is also observed in EDS patterns in this sample, which is reasonable because the partial pressure of oxygen in the flowing argon is $\sim 10^{-6}$ and higher than the pressure needed to oxidize the boride. However, the oxygen in the argon is low and the amount of oxide should not be too high and it can not be detected by XRD.

The backscatter SEM pictures of this sample heat treated at 1300°C and 1800°C are

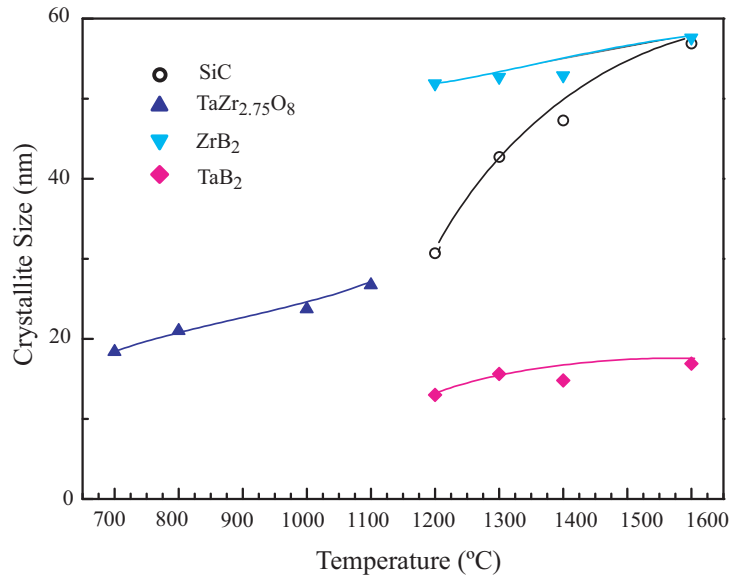


Fig 6.5: Plot of crystallite sizes (determined from XRD measurements) vs. heat treatment temperature for ZrB₂-TaB₂-SiC composite.

shown in Figure 6.7. Compositional contrast was observed for the sample heat treated at 1300°C, which indicated that there are separate phases for this sample. The XRD pattern shown in Figure 6.3 confirmed these results, which illustrates the different phases of ZrB₂, TaB₂, TaC and ZrO₂ coexisted in the sample. No compositional contrast was observed from the backscatter photos for the sample heat treated at 1800°C for 2 h. This is reasonable because the XRD pattern showed that the peaks of ZrB₂ and TaB₂ converged together after heat treatment at high temperature of 1800°C and formed a solid solution, which consistent with the research of Watanable [4].

6.2 *Synthesis ZrB₂-based Composite by Adjusting the Precursor Adding Sequence*

The effect of sequence of precursor addition on the product property was studied in this chapter. The main purpose was to check if the sequence of precursor addition would affect the segregation and particle size distribution of the product. The sequences that were checked are listed below:

- (a) Reflux - hydrolysis -addition of boric acid - addition of phenolic (cloudy)
- (b) Reflux - addition of boric acid - hydrolysis - addition of phenolic (phase separation)

after dry)

(c) Reflux - addition of boric acid - addition of phenolic - hydrolysis (cloudy)

(d) Reflux - (addition of boric acid and phenolic mixture) - hydrolysis (cloudy)

(e) Reflux - hydrolysis - (addition of boric acid and phenolic mixture)

In our experiments, five samples were prepared from the same batch of refluxed sol to minimize the inaccuracy. The same $B/Zr = 3.0$ and $C/Zr = 5.0$ ratios were used for all five samples. For sample (b), (c), (d) no additional water was added since water from boric acid solution already gave a higher H_2O/Zr ratio than 24, which was used as in sample (a), (e). Acid/Zr ratio was kept the same for all five samples. After hydrolysis and concentration, five samples were dried and pyrolyzed under same conditions. The phenomena which happened during the synthesis is listed in Table 6.1.

Tab 6.1: Observations for synthesizing of ZrB_2 with different precursor adding sequence

| sample | before hydrolysis | after hydrolysis | after dry |
|--------|---|-----------------------------|-------------------|
| a | clear solution | cloudy when adding phenolic | uniform |
| b | clear solution | clear solution | phase segregation |
| c | cloudy when adding phenolic | clear after adding water | uniform |
| d | cloudy when adding mixture of phenolic and boric acid | clear after adding water | uniform |
| e | clear solution | clear solution | uniform |

The precursor adding sequence affected the synthesis results significantly. Only sequence e was a clear solution during the whole synthesis procedure and yielded a uniform dry powder. For adding sequence a, c and d, solutions became cloudy during the synthesis procedure, resulting from uncontrolled hydrolysis, which may lead to large particle sizes after later heat treatment. Adding sequence b was clear solution during the synthesis but a color difference was observed for dry powder, which implies segregation of phases. Therefore, the adding sequence e is the best method for synthesis of homogeneous powder with small size. The XRD patterns for samples heat treated at 1300°C for 2 h in the M11 furnace with precursor different adding sequence as described above is shown in Figure 6.8. The dominant phases are ZrB_2 for all those three samples, but the second phases of ZrC , or tetragonal zirconium oxide, or monoclinic zirconium oxide are observed for sample with

adding sequence c, d, a which become cloudy during the synthesis. The XRD pattern for sample b, e are single phase of ZrB_2 which are clear during the synthesis. The cloudy during synthesis described that uncontrolled hydrolysis happened and precipitate of solid formed, which may result in large particle size of precursor mixture and need higher temperature to complete the boro/carbothermal reduction. Therefore, the XRD pattern showed impurities of oxide for those cloudy sample with adding sequence a, c, d at same heat-treatment temperature of sample b, e.

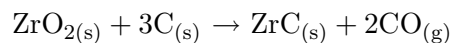
6.3 Preparation of the Nanocrystalline ZrB_2/ZrC or $\text{ZrB}_2/\text{ZrO}_2$ Composite by Solution-based Method

6.3.1 Synthesis of ZrB_2/ZrC or $\text{ZrB}_2/\text{ZrO}_2$ Composite by Adjusting the Initial Concentration of C/Zr and B/Zr

Composites of ZrB_2/ZrC or $\text{ZrB}_2/\text{ZrO}_2$ were obtained by adjusting the concentrations (ratio of C/Zr, B/Zr) of the starting materials during solution processing of ZrB_2 , ZrB_2/ZrC or $\text{ZrB}_2/\text{ZrO}_2$ composite materials could be produced under the same heat treatment conditions, as illustrated by the XRD patterns in Figure 6.9.

The XRD-based crystallite size for ZrB_2 was 50-130 nm, and 50 nm for ZrC , 120 nm for ZrO_2 .

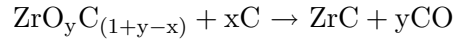
Figure 6.10 is the XRD pattern for a sample with same composition of starting materials as the one in Figure 6.9-b, which shows that the ZrO_2 phase observed in the 1300°C (2 h) pattern disappears after further heat-treatment (1400°C, 2 h) and a ZrB_2/ZrC composite is obtained. The crystallite size of ZrB_2 remained <130 nm and ZrC <95 nm at 1950°C, which is consistent with the SEM results shown in Figure 6.11. The crystal size was small compared to pure ZrB_2 sample because the second phase of ZrC inhibited the crystal growth of ZrB_2 . The reason why the ZrO_2 shown in 1300°C disappeared at higher temperature is there was enough carbon in the system, and zirconia reacted with carbon at higher temperature (1400°C) according to following reaction:



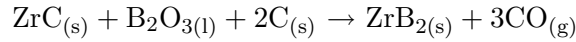
$\Delta G = -23.57 \text{ kJ/mol}$, at 2000K The

particle size (measured from their SEM pictures shown in Figure 6.12 and 6.13) increased with temperature but not as significantly as for the single phase ZrB₂ sample. The particle sizes are in the range of 10 nm-300 nm for the samples heat treated from 1300°C to 1950°C. However, the morphology of the particles changed from round shape at temperature of 1300°C to elongated shape when heat treated at 1950°C for 2 h.

Figure 6.14 shows the weight loss vs. temperature during heat-treatment. It illustrates that there was a further weight loss at 1800°C, even though the XRD pattern shows no residual ZrO₂ in the sample heat-treated at 1400°C or higher temperature. This can be explained by a carbothermal reduction reaction in which the reactants were zirconium oxycarbide (formed by dissolving zirconia into the zirconium diboride) and free carbon[5]:



If the ratio of B/Zr is increased from 2.2 to 3, the ZrC XRD peak will also disappear by reacting with B₂O₃, forming ZrB₂, as shown in Figure 3.4. ZrC is the intermediate product during ZrB₂ synthesis, which forms at lower temperature (~1300°C), and then reacts with boria to form diboride at higher temperature (1400°C) according to following reaction:



$$\Delta G = -8.24 \text{ kJ/mol, at } 1300 \text{ K}$$

6.3.2 Synthesis of ZrB₂/ZrC or ZrB₂/ZrO₂ Composite by Adjusting the Initial Concentration of C/Zr

6.3.2.1 Synthesis dry powder

ZrB₂/ZrC or ZrB₂/ZrO₂ composites were obtained by changing the initial molar ratio of C/Zr and B/Zr as described above. However, similar composites can be obtained by adjusting the initial C/Zr while keeping the B/Zr = 3.0 (which is the molar ratio to obtain stoichiometric ZrB₂ from our research).

Three samples with different initial concentration were prepared. The initial B/Zr ratios of these three samples were kept as 3, while C/Zr ratios varied for those samples: (a) C/Zr =

5.0, (b) C/Zr = 4.5, and (c) C/Zr = 5.5. It should be pointed out that these C/Zr ratios are based on the assumptions that (1) a C/Zr ratio of 2.0 is from the decomposition of refluxed ZrPM sol; and (2) carbon yield from phenolic is 44.46% based on previous experimental work in ZrC synthesis.

For these three samples, the same refluxed sol was used for the synthesis and the same sequence of precursor addition was adopted: Reflux - hydrolysis - addition of mixture of boric acid and phenolic resin. It can be seen that these three batches are almost identical in terms of composition except for the C/Zr ratio. Drying was conducted in a vacuum oven in the temperature range of 110 to 130°C. All pyrolysis works were carried out in Lindberg furnace at 1100°C for 2h under flowing argon with flow rate of 80 ml/min. Further heat-treatments or reactions were carried out in the M11 at 1300°C for 2h or longer time.

6.3.2.2 *Heat-treatment of samples*

For all three samples, the dominant phase in the pyrolyzed sample was monoclinic zirconia, and a trace of tetragonal zirconia. In the pyrolyzed sample, B₂O₃ and carbon are believed to be amorphous because no peaks for these phases were observed in the XRD pattern.

The XRD patterns of these three samples after the carbo/borothermal reduction at 1300°C for 2 h in the M11 furnace are shown in Figure 6.15. The dominant phase in all three samples is zirconium diboride, while sample (c), with the highest C/Zr ratio of 5.5 among the three, yields an almost crystalline phase-pure product after the reaction, with just a trace of ZrC and ZrO₂. Sample (b) had the lowest C/Zr ratio of 4.5 in the pyrolysis materials, which results in much more monoclinic zirconia in the reacted products. Sample (a) has a medium C/Zr ratio of 5.0, and the phase impurity from XRD measurement lies between (b) and (c).

To estimate the extent of the carbo/borothermal reduction of these samples, longer reaction times of 4 h and 8 h were used for the heat treatments on sample (b) and (c). Here, we still used 1300°C as the reaction temperature because we did not want to permit vigorous volatilization of boria which is expected to occur at higher temperature.

Figure 6.16 showed the XRD patterns of sample (b) after 1300°C 4 h and 8 h heat-

treatment. It can be seen that there is almost no difference between them and the 1300°C-2h sample. Yields of the sample after heat-treatments at 1300°C for 2 h, 4 h and 8 h were 45.18%, 44.89% and 43.30%. There was not too much difference between the yields from different heat treatment times, which showed that the carbo/borothermal reduction was almost complete after 1300°C-2 h heat treatment. The little additional weight loss might be due to the loss of boria or the completion of the reaction.

The boro/carbothermal reduction reaction was completed after heat-treatment at 1300°C for 2 h, there was phase development and weight loss from further heat-treatment. However, the particle size increased with the heat-treatment time increasing. The particle size increased from 20-500 nm after heat treatment at 1300°C for 2 h to 100 nm-2 μm after further heat-treatment reduction at 1300°C for 4 h as shown in Figure 6.17. The morphology of the particle changed from a nearly round shape for heat treatment 2 h sample to elongated shape after heat-treating for 4 h. Therefore, the boro/carbothermal should be stopped right after the reaction is finished, further heat-treatment may result in extra coarsening and lead to necking between particles.

Figure 6.18 shows the XRD patterns of sample (c) after heat-treatment at 1300°C for 2 h, 4 h and 8 h respectively. It can be seen that ZrC is no longer present in the 1300°C-4 h sample, which is associated with a slight weight loss from 1300°C-2 h (47.38%) to 1300°C-4 h (46.19%). After heat-treatment at 1300°C for 8 h, the XRD pattern showed no difference from the 1300°C-4 h sample. There is also no additional weight loss from 1300°C-4 h sample (46.19%) to 1300°C-8 h sample (46.27%).

6.4 Conclusions

1. ZrB₂-20vol%SiC composite was synthesized by solution based method, using Zr-n-propoxide as Zr-bearing source and TEOS as Si-bearing source. Pure-phase ZrB₂-20vol%SiC was obtained after heat treating at 1400°C for 2 h in M11 furnace under flowing argon. The particle sizes for ZrB₂ (smaller than pure ZrB₂ particle because the second phase SiC block the grain growth of ZrB₂) and SiC are 20-250 nm and \sim 20 nm, respectively.

2. ZrB₂-TaB₂-SiC composite was synthesized using Zr-n-propoxide as Zr-bearing source, Tantalum ethoxide as Ta-bearing source and TEOS as Si-bearing source. Pure-phase ZrB₂-TaB₂-20vol%SiC was obtained after heat treating at 1600°C for 2 h in M11 furnace under flowing argon. The particle sizes for ZrB₂-TaB₂ and SiC are 500 nm and ~150 nm, respectively.
3. ZrB₂-based composite with ZrC or ZrO₂ can be obtained by adjusting the initial concentration. ZrB₂-ZrC composite with crystalline size of 50-130 nm for ZrB₂ and 50 nm for ZrC was obtained when use initial concentration of B/Zr =6.0, C/Zr = 4.0, which is boron in excess and carbon in short. ZrB₂-ZrO₂ composite with crystalline size of 50-130 nm for ZrB₂ and 120 nm for ZrO₂ was obtained when use initial concentration of B/Zr =2.2, C/Zr = 6.0, which is boron in short and carbon in excess.
4. Excess heat-treatment at higher temperature may lead to excess grain growth, which result in product with large particle size and elongated shape. Therefore, heat treatment should be stopped right after the boro/carbothermal reduction reaction was completed.
5. Precursor adding sequence had significant effect on the product property. Phenolic resin solution added to the system before hydrolysis might result in uncontrolled hydrolysis (the solution become cloudy) and results in large particle size, as a result, need heat-treated at higher temperature to complete boro/carbothermal reduction. The best precursor adding sequence is: Reflux - hydrolysis - (addition of boric acid and phenolic mixture).

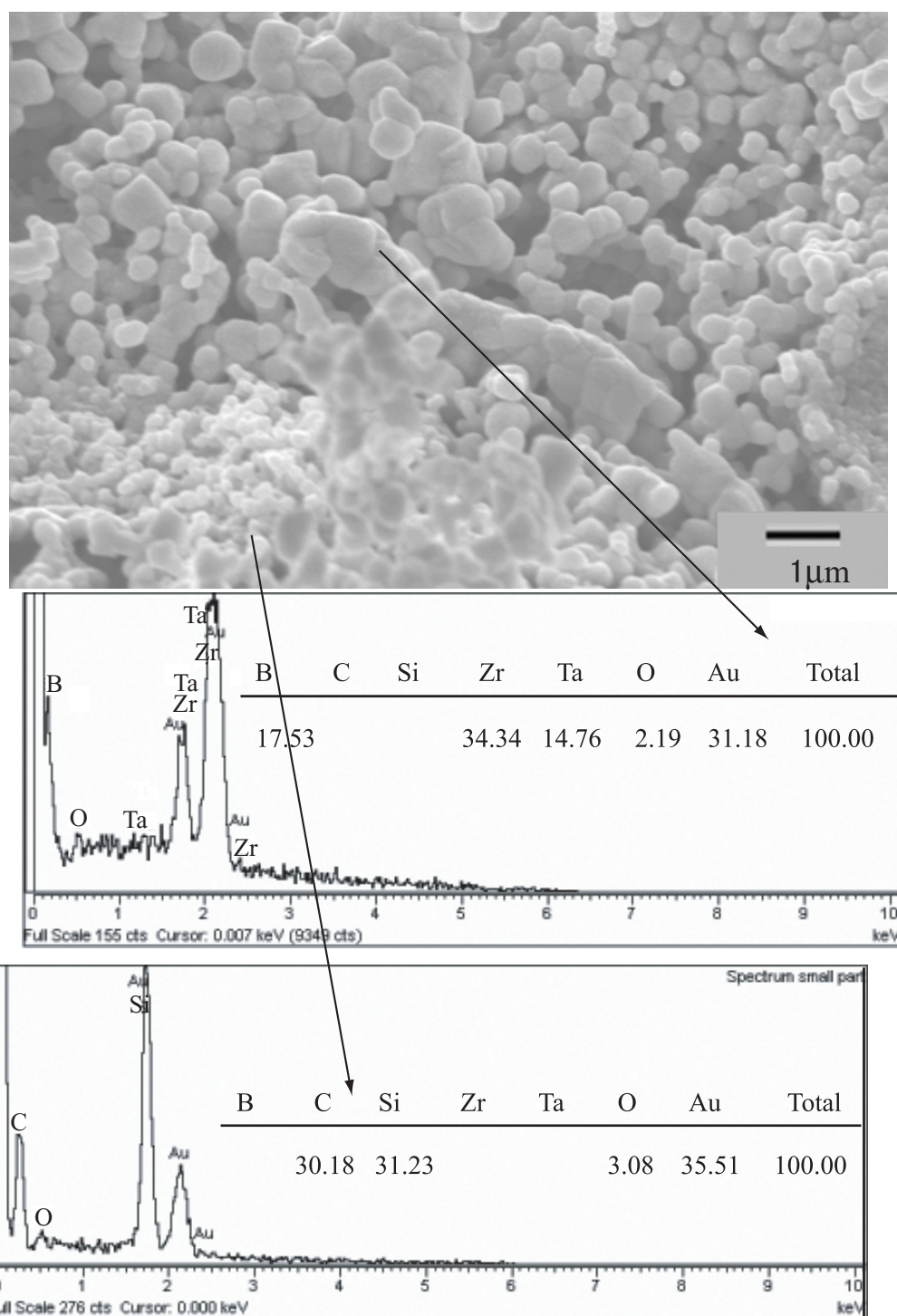


Fig 6.6: SEM micrograph and EDS pattern of $\text{ZrB}_2\text{-TaB}_2\text{-SiC}$ heat-treated at 1600°C (heating at $80^\circ\text{C}/\text{min}$ to 1525°C , with successively slower rates as 1600°C was approached) for 2 h. Indicated phases are based on EDS analysis.

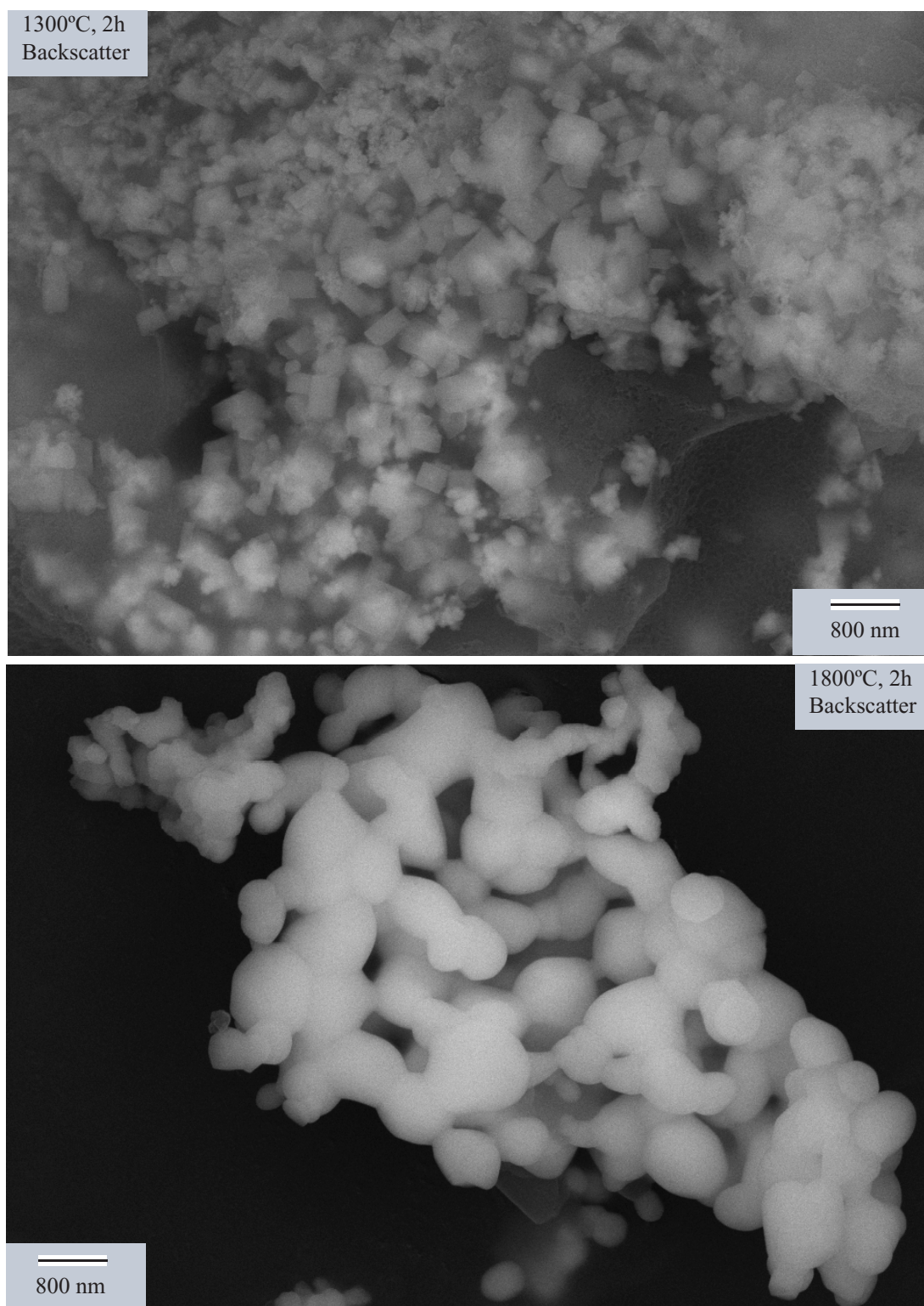


Fig 6.7: Backscatter SEM micrograph of $\text{ZrB}_2\text{-TaB}_2\text{-SiC}$. (a) Heat-treated at 1300°C for 2 h. (b) Heat-treated at 1800°C for 2 h.

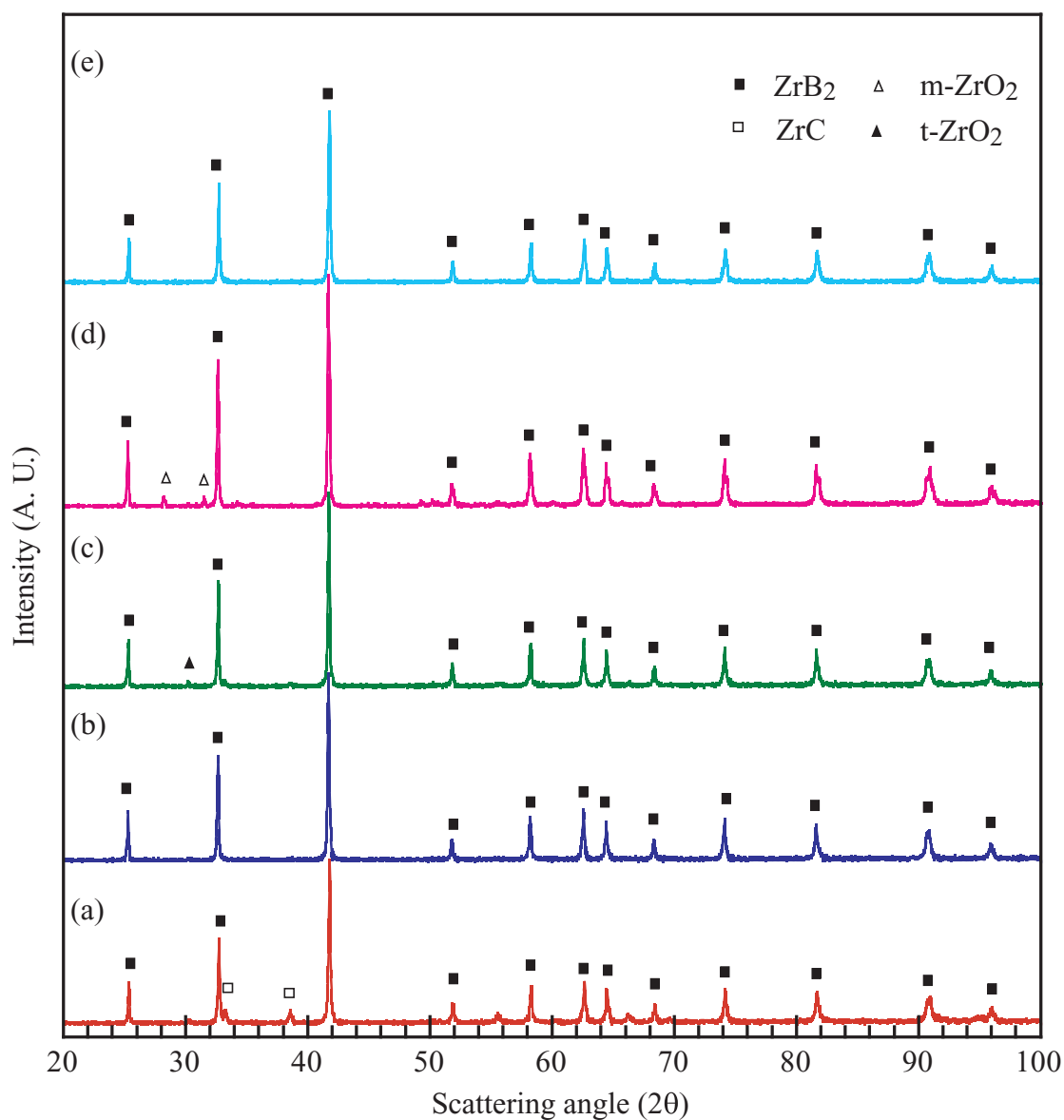


Fig 6.8: XRD patterns of ZrB_2 samples heat-treated at 1300°C for 2 h in M11 furnace with different precursor adding sequence as follows: (a) Reflux - hydrolysis - addition of boric acid - addition of phenolic. (b) Reflux - addition of boric acid - hydrolysis - addition of phenolic. (c) Reflux - addition of boric acid - addition of phenolic - hydrolysis. (d) Reflux - (addition of boric acid and phenolic mixture) - hydrolysis. (e) Reflux - hydrolysis - (addition of boric acid and phenolic mixture).

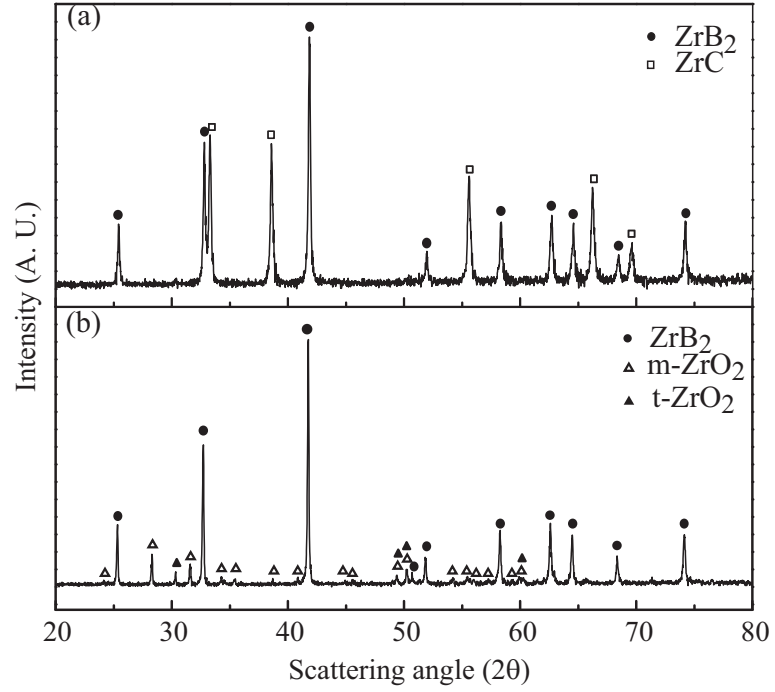


Fig 6.9: XRD pattern for two compositions heat-treated at 1300°C for 2 h (a. $B/Zr = 6.0$, $C/Zr = 4.0$; b. $B/Zr = 2.2$, $C/Zr = 6$).

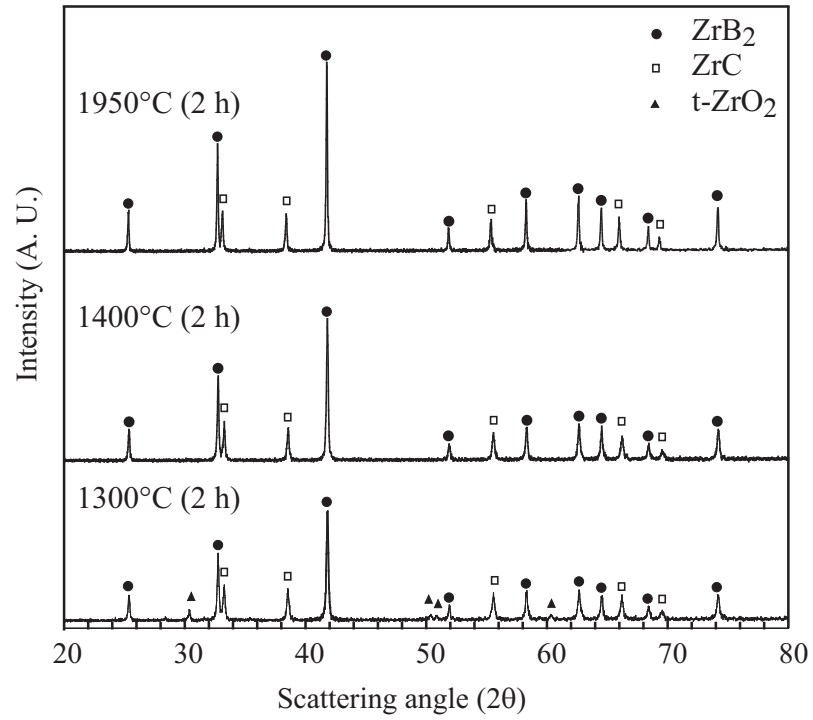


Fig 6.10: XRD for phase development of sample ZrB_2 as a function of soaking temperature ($B/Zr = 2.2$, $C/Zr = 6$).

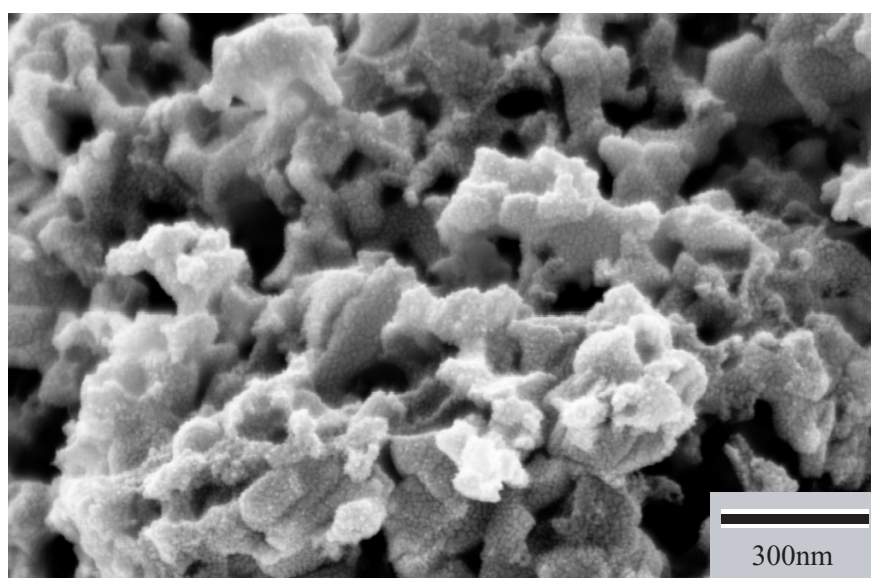


Fig 6.11: SEM photomicrograph of ZrB₂-ZrC sample heat-treated at 1400°C for 2 h in a graphite-tube furnace.

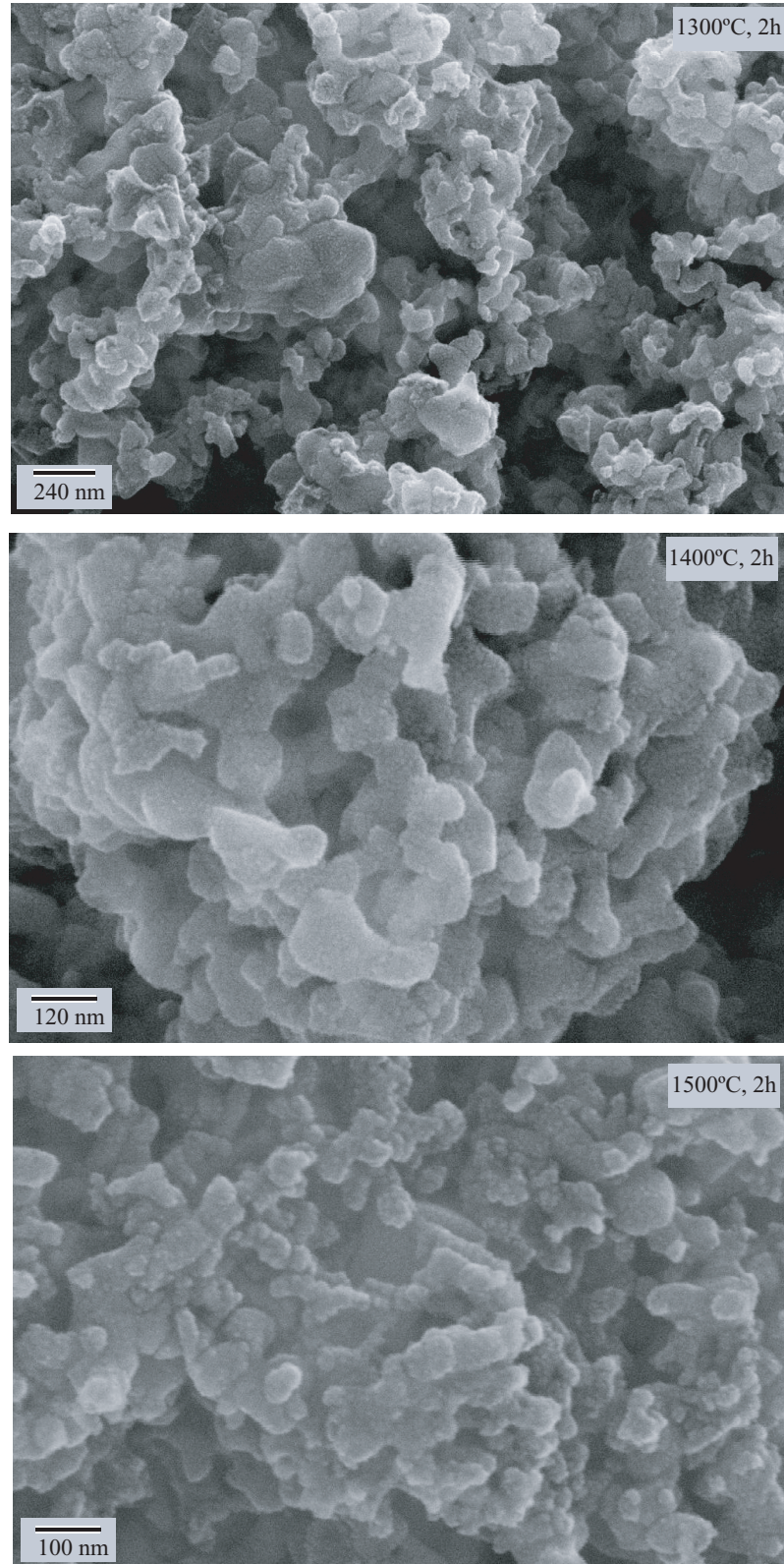


Fig 6.12: SEM photomicrograph of $\text{ZrB}_2\text{-ZrC}$ sample heat-treated at 1300°C, 1400°C and 1500°C for 2 h in a graphite-tube furnace.

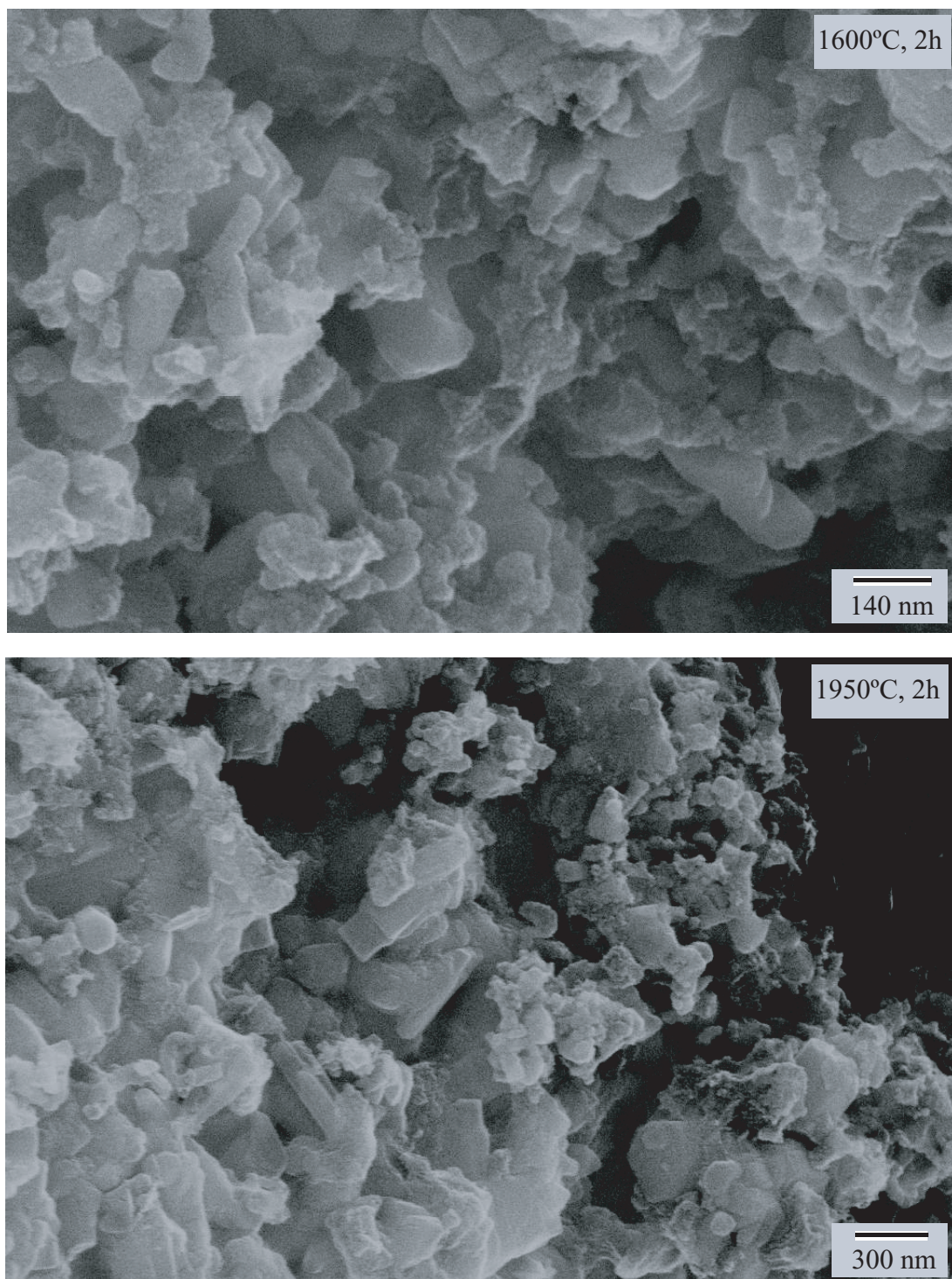


Fig 6.13: SEM photomicrograph of ZrB₂-ZrC sample heat-treated at 1600°C and 1950°C for 2 h in a graphite-tube furnace.

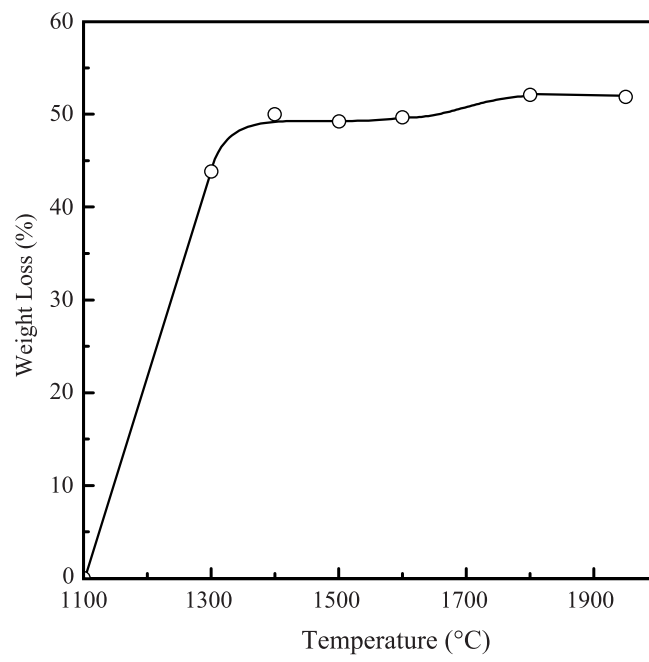


Fig 6.14: Plot of weight loss vs. temperature for ZrB₂ composite (B/Zr = 2.2, C/Zr = 6).

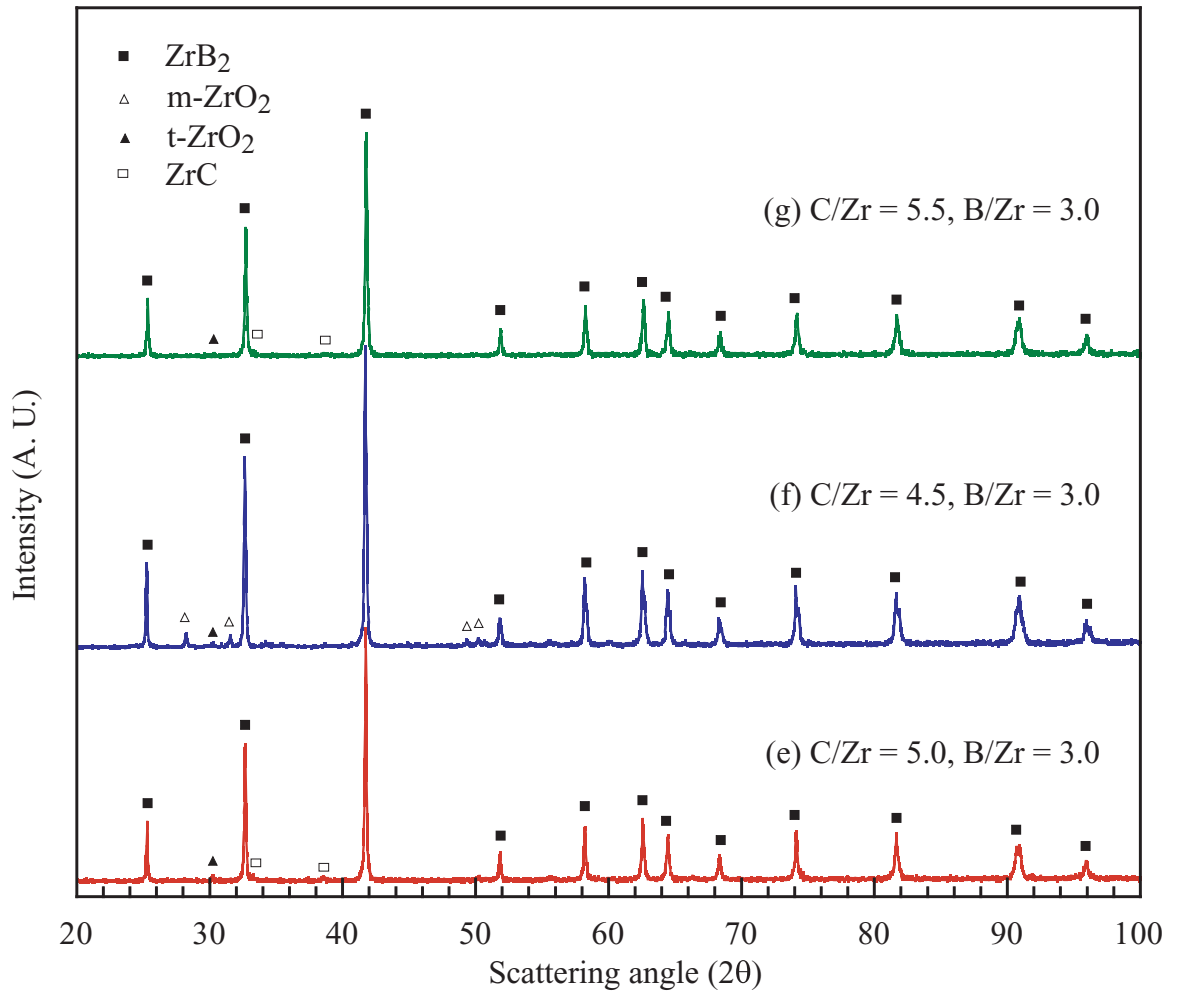


Fig 6.15: XRD pattern of ZrB₂ sample with different initial C/Zr heat-treated at 1300°C for 2 h in M11 furnace. (e) C/Zr = 5.0 (b) C/Zr = 4.5. (c) C/Zr = 5.5 .

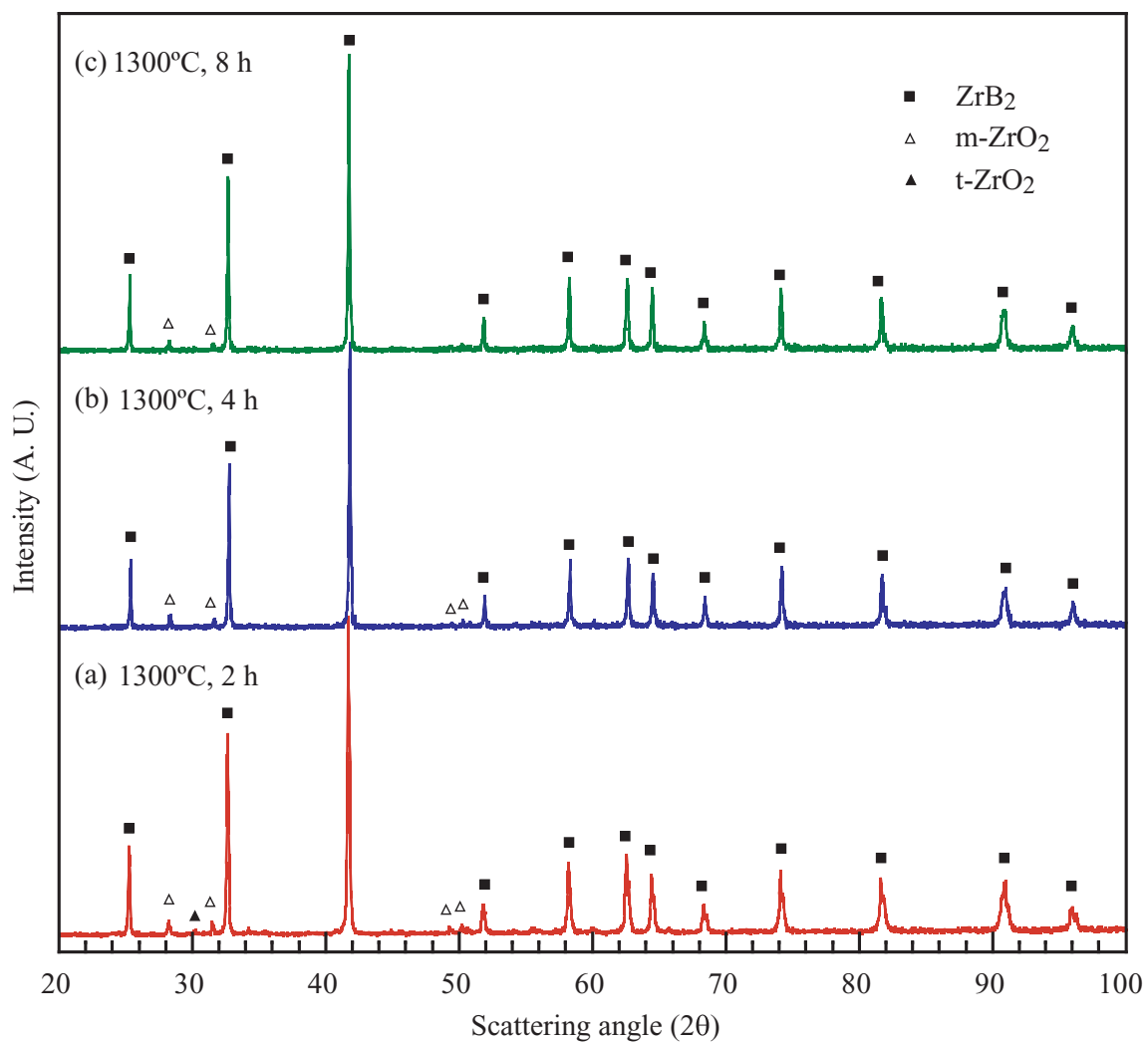


Fig 6.16: XRD pattern of ZrB₂ sample (with initial C/Zr = 4.5) heat-treated at 1300°C for (a) 2 h. (b) 4 h. (c) 8 h in a graphite-tube furnace.

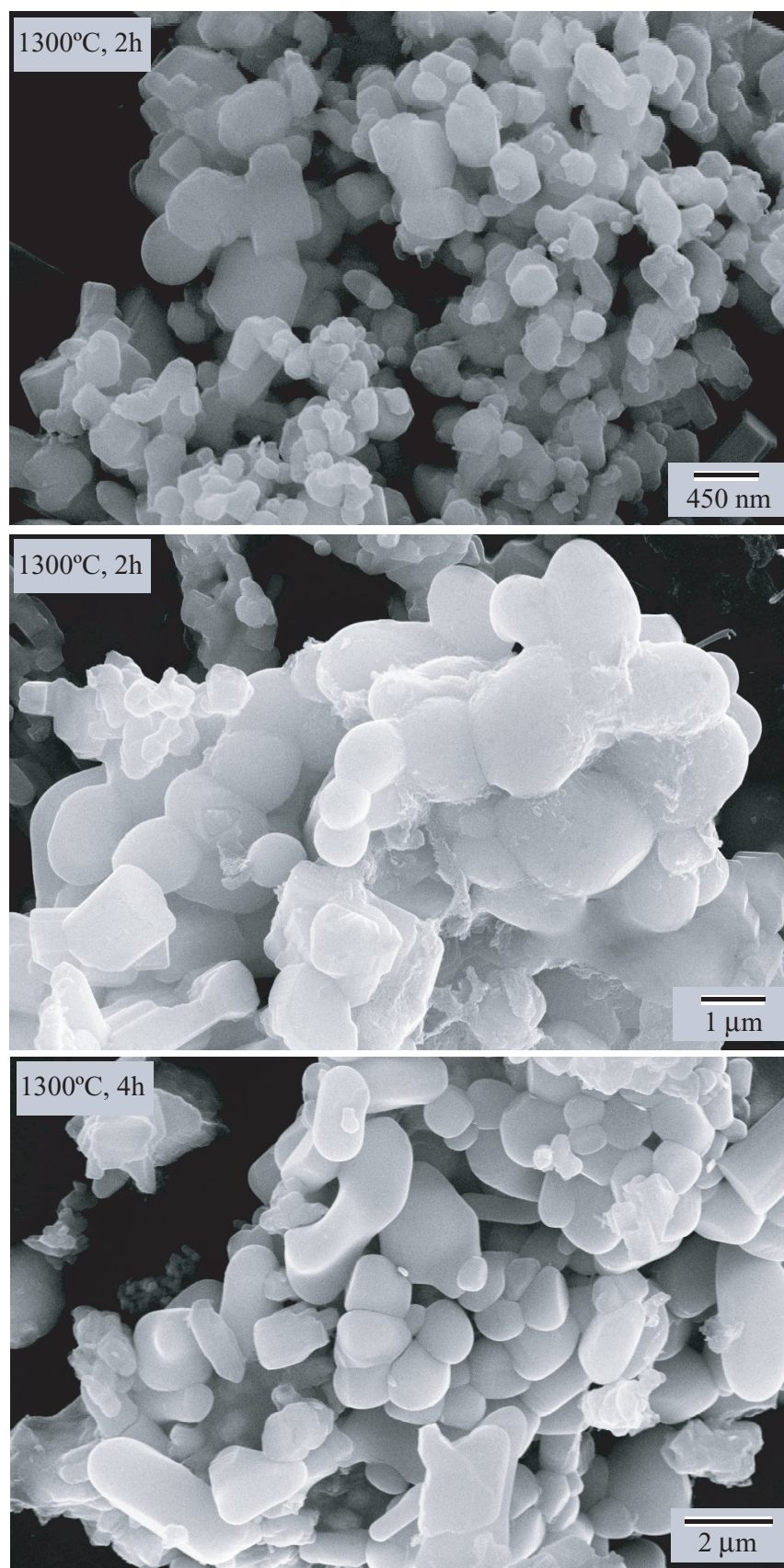


Fig 6.17: SEM photomicrograph of $\text{ZrB}_2\text{-ZrC}$ sample heat-treated at 1300°C for 2 h and 4 h in a graphite-tube furnace.

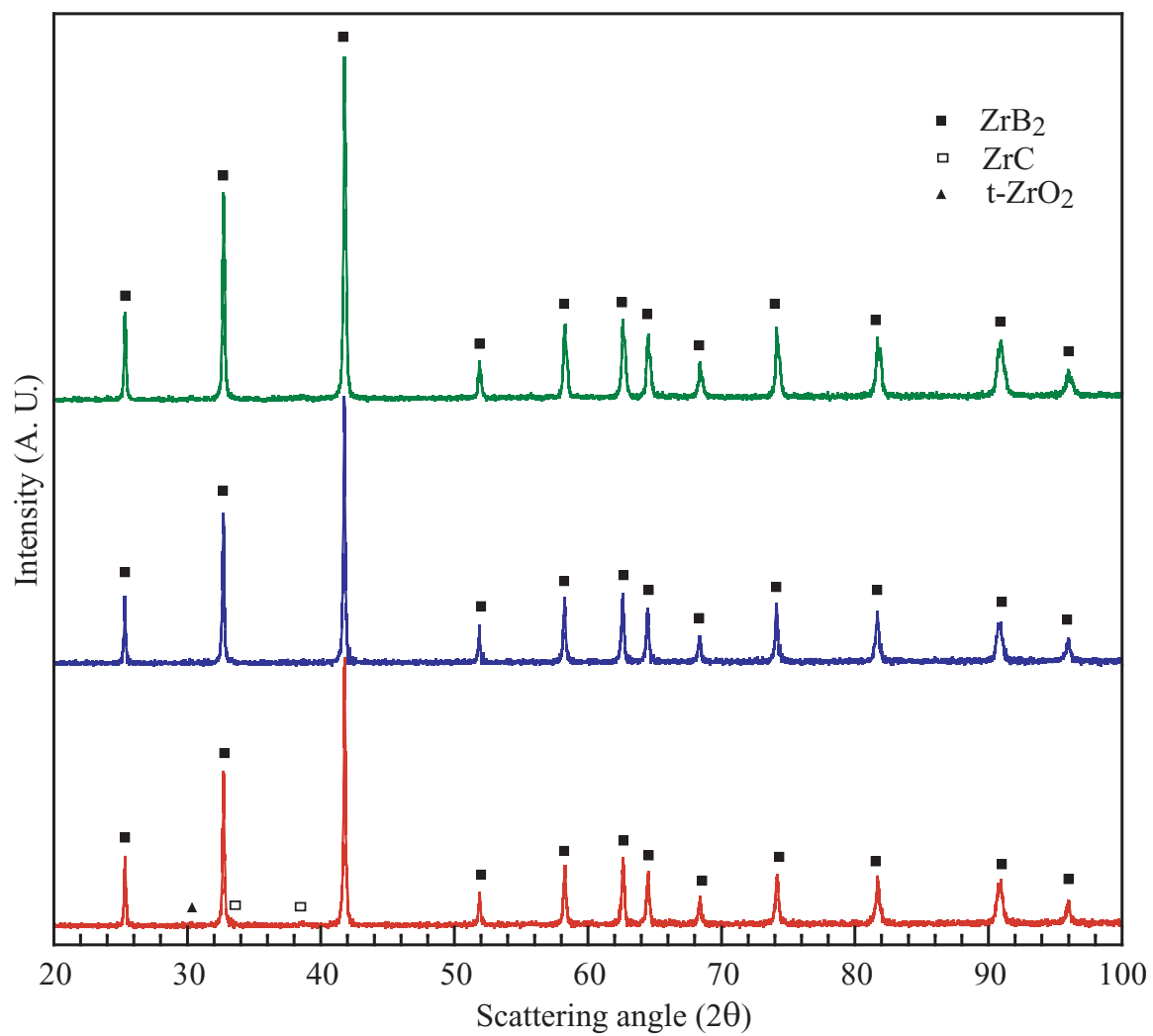


Fig 6.18: XRD pattern of ZrB_2 sample (with initial $\text{C}/\text{Zr} = 5.5$) heat-treated at 1300°C for (a) 2 h. (b) 4 h. (c) 8 h in a graphite-tube furnace.

REFERENCES

6.5 *References*

- [1] J. L. Blumenthal, M. J. Santy, and E. A. Burns, “Kinetics Study of High-temperature Carbon-silica Reactions in Charred Silica-reinforced Phenolic Resins,” *J. AIAA*, **4** [6] 1053-1057 (1966).
- [2] V. M. Kevorkijan, M. Komac, and D. Kolar, “Low Temperature Synthesis of Sinterable SiC Powders by Carbothermic Reduction of Colloidal SiO₂,” *J. Mater. Sci.*, **27** [10] 2705-2712 (1992).
- [3] A. W. Weimer, K. J. Nilson, G. A. Cochran and R. P. Roach, “Kinetics of Carbothermal Reduction Synthesis of Beta Silicon Carbide,” *J. AICHE*, **39** [3] 493-503 (1993).
- [4] T. Watanabe and S. Kouno, “Mechanical Properties of TiB₂-CoB-metal Boride Alloys,” *Am. Ceram. Soc. Bull.*, **61** [9] 970-973 (1982).
- [5] Z. Hu, M. D. Sacks, G. A. Staab, C. A. Wang, and A. Jain, “Solution-Based Processing of Nanocrystalline ZrC,” *Ceram. Eng. Sci. Proc.*, **23**[4] 711-717 (2002).

CHAPTER 7

conclusions

7.1 Nanocrystalline Powder Synthesis

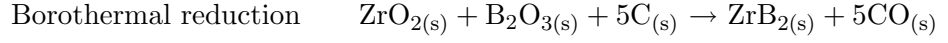
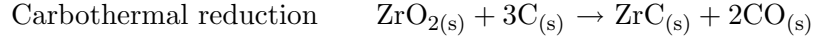
7.1.1 Nanocrystalline ZrB₂ Powder Synthesis

The nearly stoichiometric ZrB₂ powder with crystalline size of 20 nm-150 nm from SEM photo was produced by boro/carbothermal reduction reactions using fine-scale ZrO₂/B₂O₃/C mixtures as the starting materials. The reactant mixtures were prepared by pyrolytic decomposition of solution-derived precursors. The initial compositions for synthesis pure ZrB₂ are B/Zr = 3.0 and C/Zr = 5.0.

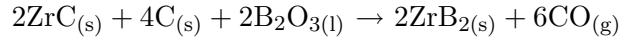
The Zr-bearing source (zirconium-n-propoxide) was first refluxed with Hacac to partially or fully convert the Zr alkoxy groups to a chelated zirconium diketonate structure, which allows greater control over the hydrolysis and condensation reaction. The condition for controlled hydrolysis was: H₂O/Zr = 24 and HNO₃/Zr = 0.27. Phenolic resin was used as the carbon-bearing source, boric acid was used as the boron-bearing source, and propanol was used as a mixing solvent. Boric acid/water/2-propanol solution, which is used as a boron-bearing source was first mixed with phenolic resin/2-propanol (carbon-bearing source), and then the mixture was added to the above hydrolysis solution. After concentrating and drying, amorphous dry precursor was obtained for further heat treatment.

The precursors were pyrolyzed at 800-1100°C for 2 h in a alumina tube furnace under flowing argon with a flow rate of 80 ml/min to produce a fine-scale of tetragonal or monoclinic ZrO₂ with amorphous B₂O₃ and carbon mixture. The pyrolysis powder was then heat-treated at higher temperature of 1300°C or 1400°C for 2 h in a graphite tube vacuum furnace for boro/carbothermal reduction reaction to obtain the desired

product. The boro/carbothermal reaction to produce ZrB_2 is shown in the following:



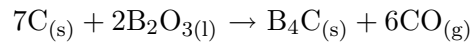
ZrC is an intermediate phase which first appeared at 1200°C and disappeared at 1300°C . ZrC reacts with B_2O_3 and carbon later at higher temperature to form ZrB_2 .



Chemical analysis by titration and ICP showed that the molar ratio of B/Zr is 2.069, which means there is excess boron in the ZrB_2 product. The free carbon in the product is ~ 0.378 compared to ZrB_2 .

7.1.2 Nanocrystalline ZrB_2 - B_4C Composite Synthesis

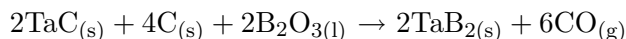
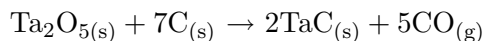
ZrB_2 - B_4C composite was synthesized by the solution-based method after boro/carbothermal reduction at 1400°C for 2 h. The initial composition for ZrB_2 sol is $\text{B/Zr} = 3$ and $\text{C/Zr} = 4.8$, while the initial composition for B_4C sol is $\text{B/C} = 6/7$. The particle size for B_4C and ZrB_2 in the composites was 20 nm and 50-300 nm, respectively. The reaction to produce B_4C is



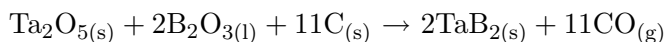
7.1.3 Synthesis of Nanocrystalline ZrB_2 - TaB_2 Based Composite

The ZrB_2 - TaB_2 composite (molar ratio of $\text{Zr/Ta} = 3$) with crystalline size of 100 nm-250 nm by the solution-based method was obtained with initial composition of $\text{B/(Zr+Ta)} = 3.0$ and $\text{C/(Zr+Ta)} = 4.8$ after heat-treated at 1300°C for 2 h in a graphite tube furnace under flowing argon. The synthesis method is similar to the ZrB_2 powder except the zirconium-n-propoxide (Zr-bearing source) and tantalum-ethoxide (Ta-bearing source) was first mixed in 1-propanol before refluxing with H₂ gas.

The boro/carbothermal reactions to produce TaB₂ are:



The overall boro/carbothermal reduction reaction was:



TaC is an intermediate product which appeared at 1150°C and disappeared at 1300°C.

ZrB₂-TaB₂-B₄C composite was synthesized by a solution-based method after boro/carbothermal reduction at 1400°C for 2 h. The molar ratio for ZrB₂-TaB₂ sol is B/(Zr+Ta) = 3.0, C/(Zr+Ta) = 4.8 and Zr/Ta=3, while the initial composition for B₄C sol is B/C=6/7 and the weight percent of B₄C in the composite is 3 wt%. The particle size for this composite was 100-820 nm.

7.1.4 Synthesis of Submicro-size ZrB₂-TaSi₂ Composite

The ZrB₂-TaSi₂ composite with particle size of 50 nm-800 nm by solution-based method was obtained with an initial composition of B/Zr = 3.0 and C/Zr = 4.8 after heat-treatment at 1400°C for 2 h in a graphite tube furnace under flowing argon.

The solution of ZrB₂ batch was synthesized the same as pure ZrB₂ powder, but TaSi₂/2-propanol slurry was added to the solution before it was concentrated. The particle size of TaSi₂ added to the system is ~200 nm-1.2 μm, as a result, only a submicron-size product was obtained.

7.1.5 Synthesis of Nanocrystalline Diboride-SiC Composite

A ZrB₂-20vol%SiC composite was synthesized by a solution-based method, using Zr-n-propoxide as the Zr-bearing source and TEOS as the Si-bearing source. Phase-pure ZrB₂-20 vol%SiC was obtained after heat-treatment at 1400°C for 2 h in the M11 furnace under flowing argon. The particle sizes for ZrB₂ and SiC were 20-250 nm and ~20 nm, respectively.

A $\text{ZrB}_2\text{-TaB}_2\text{-SiC}$ composite was synthesized using Zr-n-propoxide as the Zr-bearing source, tantalum ethoxide as the Ta-bearing source and TEOS as the Si-bearing source. Phase-pure $\text{ZrB}_2\text{-TaB}_2\text{-20vol\%SiC}$ was obtained after heat-treatment at 1600°C for 2 h in the M11 furnace under flowing argon. The particle sizes for $\text{ZrB}_2\text{-TaB}_2$ and SiC were 500 nm and ~ 150 nm, respectively.

7.1.6 Synthesis of other diboride-based Composites

ZrB_2 -based composite with ZrC or ZrO_2 could be obtained by adjusting the initial concentration. A $\text{ZrB}_2\text{-ZrC}$ composite with crystalline size of 50-130 nm for ZrB_2 and 50 nm for ZrC was obtained when using an initial concentration of $\text{B/Zr} = 6.0$, $\text{C/Zr} = 4.0$, which has excess boron and deficient carbon. A $\text{ZrB}_2\text{-ZrO}_2$ composite with crystalline size of 50-130 nm for ZrB_2 and 120 nm for ZrO_2 was obtained when using an initial concentration of $\text{B/Zr} = 2.2$, $\text{C/Zr} = 6.0$, which is boron deficient and excess carbon.

Excess heat-treatment at higher temperature or holding for longer times may lead to excess coarsening, which results in a product with a large particle size and elongated shape. Therefore, heat treatment should be stopped right after the boro/carbothermal reduction reaction is completed.

Precursor-adding sequence had a significant effect on the product properties. Phenolic resin solution added to the system before hydrolysis might result in uncontrolled hydrolysis and the solution became cloudy. The best precursor adding sequence was: Reflux - hydrolysis - (addition of boric acid and phenolic mixture).

7.2 Bulk Pellet Processing

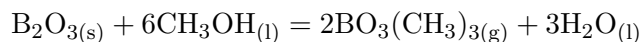
ZrB_2 pellet is difficult to densify, not only because its high melting temperature, but the oxide impurities, even in trace amounts, can result in excess coarsening instead of densification, therefore, there are some tricks to processing the powder containing diborides.

7.2.1 Ball-milling

Ball-milling is an efficient method to break up agglomerates in the powder and obtain a more uniform dispersion of particles. The media used for ball-milling should not be oxide, and B₄C media was used for our research. The atmosphere in the bottle contained powder interested should be inert gas. For our research, the powder was put into the bottle with media and methanol solvent in a glove box with circulating argon.

7.2.2 Methanol-washing

Methanol washing can remove the boron oxide on the particle surface efficiently. However, this step should be repeated several times (6 times). The sonication break up the agglomerates, while methanol dissolve the boria and formed a gas phase of BO₃(CH₃)₃, which volatile from the system and was removed.



7.2.3 Binder

Nanoscale powder is difficult to obtain higher green density by dry pressing, while binder can help pellet formation and increase green density from 34% to nearly 40%. The binder we used was 0.02 g/ml polyvinyl alcohol-polyvinyl acetate copolymer and 0.1 g/ml polyethylene glycol, while 40 % solution of Darven 821A was a deflocculant and used to disperse ceramic suspensions to minimize the water content. The amounts of binder compared with the weight of dry powder were 3.46 wt% PVA, 0.69 wt% PEG, 0.52 wt% Darwen 821A and 60.71 wt% water.

For debinding, the heating rate should be slow to avoid stress accumulation which may lead to cracking. For our research, the heating rate for debinding was 0.2°C/min to 500°C, holding for 24 h.

7.2.4 CIP

Cold isostatic pressing can significantly increase the green density, which is necessary for powder with nanosize. The green density was increased about 5% - 10% by CIP.

7.3 *Research on the Sinterability of Nanocrystalline Diboride Powders*

7.3.1 Sinterability of ZrB₂ and ZrB₂-B₄C Composite

The pellet made from nanosize powder was highly active and the shrinkage was higher than 21% measured by dilatometer. However, the pure ZrB₂ powder was difficult to densify due to the oxide impurity. The sinterability of the composite of ZrB₂-B₄C was much better than pure ZrB₂. The density for ZrB₂-B₄C after sintering at 2020°C for 1 h was 8% higher than the one for ZrB₂ because B₄C can react with oxide impurity ZrO₂ and the excess coarsening resulted by oxide was avoided.

The reaction between B₄C and ZrO₂ is:



7.3.2 Sintering of ZrB₂-TaB₂ and ZrB₂-TaB₂-B₄C Composite

The powder used for sintering was ZrB₂-TaB₂ and ZrB₂-TaB₂-B₄C heat-treated at 1400°C for 2 h. Those samples could be easily densified at 2020°C for 1 h due to the solid solution formed between ZrB₂ and TaB₂, and the relative density were 97.21 % for ZrB₂-TaB₂-B₄C, and 92.26 % for ZrB₂-TaB₂.

7.3.3 Sintering of ZrB₂-TaSi₂ Composite

The ZrB₂-TaSi₂ pellets made from the powder heat treated at 1400°C for 2 h were sintered at 2020°C for 30 min in the M11 furnace under same heat treatment condition, but one pellet was buried in B₄C powder, the others were put on ZrB₂ substrate or on graphoil. The relative density for the pellet buried in B₄C powder was 95%, while for those sintered without buried in B₄C was only 64%. The material is sensitive

to moisture and adsorbed H_2O quickly when exposed to air, which then reacted with ZrB_2 and formed ZrO_2 . Zirconium oxide is proved to be the dominate reason to inhibit the densification of this material, while B_4C covered the sample can react with Zr_2 and removed the oxide, hence avoiding such problem and improving the sinterability.

Reference ICDD Card

Tab 1: Reference ICDD card number.

| Identified phases | Sys. | Reference ICDD |
|-------------------------------------|--------------|----------------|
| ZrB ₂ | hexagonal | 34-0423 |
| TaB ₂ | hexagonal | 38-1462 |
| TaSi ₂ | hexagonal | 38-0483 |
| SiC | cubic | 29-1129 |
| ZrC | cubic | 35-0784 |
| B ₄ C | rhombohedral | 35-0798 |
| WC | hexagonal | 25-1047 |
| ZrO ₂ | monoclinic | 37-1484 |
| ZrO ₂ | tetragonal | 42-1164 |
| Ta ₂ O ₅ | monoclinic | 33-1391 |
| TaZr _{2.75} O ₈ | orthorhombic | 42-0060 |
| C | hexagonal | 41-1487 |